Universitat de Girona

ELECTRONIC STRUCTURE, CHEMICAL BONDING, AND ELECTRONIC DELOCALIZATION OF ORGANIC AND INORGANIC SYSTEMS WITH THREE-DIMENSIONAL OR EXCITED STATE AROMATICITY

Ouissam El Bakouri El Farri

Universitat de Girona

DOCTORAL THESIS:

Electronic structure, chemical bonding, and electronic delocalization of organic and inorganic systems with three-dimensional or excited state aromaticity

Ouissam El Bakouri El Farri

2017

Doctoral programme in Chemistry

Supervised by: Dr. Miquel Solà i Puig, Dr. Jordi Poater Teixidor and Dr. Ferran Feixas Geronès
Tutor: Dr. Miquel Solà i Puig

Presented in partial fulfillment of the requirements for a doctoral degree from the University of Girona

Prof. Dr. Miquel Solà i Puig, and Dr. Ferran Feixas Geronès from University of Girona; and Dr. Jordi Poater Teixidor from University of Barcelona,

WE DECLARE:

That the thesis entitled Electronic structure, chemical bonding, and electronic delocalization of organic and inorganic systems with three-dimensional or excited state aromaticity, presented by Ouissam El Bakouri El Farri to obtain the doctoral degree, has been completed under our supervision and meets the requirements to opt for an International Doctorate.

For all the intents and purposes, we hereby sign this document.

Prof. Dr. Miquel Solà i Puig   Dr. Jordi Poater Teixidor

Dr. Ferran Feixas Geronès

Girona, September 25th, 2017

Dedicated to my family

"However difficult life may seem,
there is always something you can do and succeed at."

Stephen Hawking

Full list of publications

List of publications resulting from this thesis

1) <u>El Bakouri, O.</u>; Duran, M.; Poater, J.; Feixas, F.; Solà, M. Octahedral aromaticity in $^{2S+1}A_{1g}$ X_6^q clusters (X = Li–C and Be–Si, S = 0–3, and q = −2 to +4). *Phys. Chem. Chem. Phys.* **2016**, *18*, 11700.

2) <u>El Bakouri, O.</u>; Solà, M.; Poater, J. Planar *vs.* three-dimensional X_6^{2-}, $X_2Y_4^{2-}$, and $X_3Y_3^{2-}$ (X, Y = B, Al, Ga) metal clusters: an analysis of their relative energies through the turn-upside-down approach. *Phys. Chem. Chem. Phys.* **2016**, *18*, 21102.

3) <u>El Bakouri, O.</u>; Poater, J.; Feixas, F.; Solà, M. Exploring the validity of the Glidewell–Lloyd extension of Clar's π-sextet rule: assessment from polycyclic conjugated hydrocarbons. *Theor. Chem. Acc.* **2016**, *135*, 205.

4) Jorner, K.; Dreos, A.; Emanuelsson, R.; <u>El Bakouri, O.</u>; Fdez. Galván, I.; Börjesson, K.; Feixas, F.; Lindh, R.; Zietz, B.; Moth-Poulsen, K.; Ottosson, H. Unraveling factors leading to efficient norbornadiene–quadricyclane molecular solar-thermal energy storage systems. *Mater. Chem. A* **2017**, *5*, 12369.

5) Ayub, R.; <u>El Bakouri, O.</u>; Jorner, K.; Solà, M.; Ottosson, H. Can Baird's and Clar's Rules Combined Explain Triplet State Energies of Polycyclic Conjugated Hydrocarbons with Fused 4nπ- and (4n + 2)π-Rings? *J. Org. Chem.* **2017**, *82*, 6327.

6) <u>El Bakouri, O.</u>; Postils, V.; Garcia-Borràs, M.; Duran, M.; Luis, J. M.; Matito, E.; Calvello, S.; Soncini, A.; Feixas, F.; Solà, M. Metallaelectrides: A molecular model for the metallic bonding. *To be submitted.*

7) <u>El Bakouri, O.</u>; Postils, V.; Feixas, F.; Solà, M.; Matito, E. Electride, metal, and metallaelectride behavior in lithium metal clusters. *To be submitted.*

8) <u>El Bakouri, O.</u>; Garcia-Borràs, M.; M. Girón, R.; Filippone, S.; Martín, N.; Solà, M. On the regioselectivity of the Diels-Alder cycloaddition to C_{60} in high spin states. *To be submitted.*

My contribution to the publications discussed: As the first author, I carried out the calculations and the writing of the draft for articles 1, 2, 3, 6, 7 and 8. As a co-author, I performed part of the computational study, discussion and revision of papers 4 and 5.

List of publications not included in this thesis

9) El-Hamdi, M.; <u>El Bakouri, O.</u>; Salvador, P.; Abdelouahid, B. A.; El Begrani, M. S.; Poater, J.; Solà, M. Analysis of the Relative Stabilities of Ortho, Meta, and Para MClY(XC$_4$H$_4$)(PH$_3$)$_2$ Heterometallabenzenes (M = Rh, Ir; X = N, P; Y = Cl and M = Ru, Os; X = N, P; Y = CO). *Organometallics* **2013**, *32*, 4892.

10) <u>El Bakouri, O.</u>; Fernández, M.; Brun, S.; Pla-Quintana, A.; Roglans, A. A simple catalytic system based on $PdCl_2(CH_3CN)_2$ in water for cross-coupling reactions using diazonium salts. *Tetrahedron* **2013**, *69*, 9761.

11) <u>El Bakouri, O.</u>; Cassú, D.; Solà, M.; Parella, T.; Pla-Quintana, A.; Roglans, A. A new mild synthetic route to N-arylated pyridazinones from aryldiazonium salts. *Chem. Commun.* **2014**, *50*, 8073.

12) <u>El Bakouri, O.</u>; Jorner, K.; Solà, M.; Ottosson, H. Triplet states of pentalenes intrafused with benzo- and naphtho-segments: When Baird-aromatic and when Hückel-aromatic? *To be submitted.*

13) <u>El Bakouri, O.</u>; Feixas, F.; Solà, M. Critical assessment of aromaticity indices. *To be submitted.*

List of acronyms

Abbreviation	Description
ACID	Anisotropy of the Induced Current Density
AIM	Atom In a Molecule
AO	Atomic Orbital
AOM	Atomic Overlap Matrix
ASE	Aromatic Stabilization Energy
BCP	Bond Critical Point
CASSCF	Complete Active Space Self-Consistent field
CBD	Cyclobutadiene
CCP	Cage Critical Point
CCSD	Coupled Cluster Singles and Doubles
CCSD(T)	Coupled Cluster Singles, Doubles and perturbative Triples
CI	Conical Intersection
CMO	Canonical Molecular Orbital
COT	Cyclooctatetraene
CP	Critical Point
Cp	Cyclopentadiene
CROHF	Coupled-perturbed Restricted Open-Shell Hartree-Fock
CTOCD	Continuous Transformation Of Current Density
DA	Diels-Alder
DI	Delocalization Index
DFT	Density Functional Theory
EDA	Energy Decomposition Analysis
EMF	Endohedral Metallofullerenes
ESI	Electronic Sharing Indices
FLU	Aromatic Fluctuation Index
FC	Franck-Condon
GIMIC	Gauge-Including Magnetically Induced Current
HOMA	Harmonic Oscillator Model of Aromaticity

HOMO	Highest Occupied Molecular Orbital
IPR	Isolated Pentagon Rule
ISC	Intersystem Crossing
ISE	Isomerization Stabilization Energy
LI	Localization Index
MCI	Multicenter Index
MO	Molecular Orbital
MP2	Second-order Moller-Plesset Perturbation Theory
MR	Membered-Ring
NBO	Natural Bond Orbital
NBD	Norbornadiene
NCI	Noncovalent Interactions
NCP	Nuclear Critical Point
NICS	Nucleus-Independent Chemical Shift
NNA	Non-Nuclear Attractor
PAH	Polycyclic Aromatic Hydrocarbon
PCH	Polycyclic Conjugated Hydrocarbon
PDI	Para-Delocalization Index
PEN	Pentalene
PES	Potential Energy Surface
QC	Quadricyclane
QCISD	Quadratic Configuration Interaction with Single and Double Excitations
QTAIM	Quantum Theory of Atoms in Molecules
RCP	Ring Critical Point
SOMO	Singly Occupied Molecular Orbital
TDDFT	Time-Dependent Density Functional Theory
XCD	Exchange-Correlation Density

List of figures

List of schemes

List of tables

Acknowledgements

This work would not have been possible without the following financial support:

En aquest punt ja puc dir que estic a les portes de finalitzar una de les etapes més importants i desafiants de la meva vida (*check!!*). En certa manera, això és com si hagués estat fent una ruta. Et vas topant amb dificultats i obstacles que has d'anar superant i encara que et quedis estancat en algun punt, sempre hi haurà algú al teu voltant disposat a donar-te un cop de mà i tirar cap endavant. Per això, dedico aquestes primeres pàgines a les persones que han estat presents i m'han ajudat en aquest llarg viatge inoblidable.

Primerament, dono infinites gràcies als meus directors de tesi, Miquel, Jordi i Ferran, per obrir-me el camí per fer la tesi, per confiar amb mi durant tot aquest temps, i per la gran ajuda que m'han proporcionat en tot moment. Encara recordo el primer cop que vaig parlar amb en Miquel (a pràctiques de primer a TBLs) fa uns set anys (com passa el temps!!) i al mateix any, curiosament, vaig conèixer en Jordi (a Mètodes Químics Informatitzats).

Ara li toca al grup, amb qui he compartit molt de temps i que, sense la seva presència, l'experiència no hauria estat la mateixa.

Tot va començar al Jaume Casademont. Tot i estar molt poc temps en aquells despatxos, vam passar molts bons moments. I després hi va haver l'èpic trasllat cap al Monturiol. Tot i que durant aquells dies vam acabar esgotats, tots plegats vam fer una molt bona feina! En aquest punt, juntament amb l'Adrià, vam ser els primers a colonitzar un espai molt "especial" que posteriorment vam batejar com a PEIXERA on encara ara, PhDs i TFGs, cuinen els seus projectes.

Adrià (*aka* Dj. Romero, quin tiu!!!), un tiu collonut, amb qui he compartit molts bons moments tant a la peixera com a fora i que m'ha acompanyat des dels inicis d'aquest viatge. Mai oblidaré l'experiència a Uppsala (el *hiking* etern sobre neu, gel i fang... encara no sé com

vam sobreviure després de 8 hores) i al dia següent, per acabar-ho de rematar, a Estocolm. Moltíssimes gràcies per haver-te passat per allà!! No ho hagués gaudit millor!!

Ferran (*aka the competitive guy*)!! En primer lloc, t'agraeixo molt haver estat sempre al meu costat per ajudar-me a solucionar qualsevol problema i, en certa manera, tot el que semblava impossible ho has fet possible i admiro la teva capacitat de desencallar les coses amb facilitat. Moltes gràcies per la paciència que has tingut durant aquests anys, de debò! També et vull tornar a donar les gràcies per lo de Vall Ter, una experiència que tornaria a repetir (com oblidar-ho!).

Marc ("se atormenta una vecina")! T'agraeixo tant tota l'ajuda que m'has proporcionat tan en els projectes de ful·lerens com per tots consells que m'has donat. M'han servit moltíssim!! Deixant de banda la recerca, no oblidaré mai els tes i els dinars amb tu i les mil històries que has explicat. Moltes gràcies per tot!!

Sílvia O. (*the Queen of Enzymes*)!! Encara que no hàgim col·laborat científicament, he gaudit molt de la teva companyia, sobretot en els tes i els dinars. I com oblidar del triple combo (RyC + Starting + FPdGi) i l'ICREA! Sincerament, me n'alegro molt per tu, i espero que la teva carrera científica continuï creixent i perdurant.

Vero! Tampoc vull deixar de donar-te les gràcies per tota l'ajuda proporcionada durant el màster, el doctorat i en especial, en el tema dels electrurs. Edu! Gràcies també per donar-me un cop de mà amb tot el tema dels electrurs. He après molt! Per cert, no oblidaré pas les teves anècdotes èpiques.

I tampoc m'oblido de l'Abril, en Mauricio, l'Eloy, l'Albert, en Pedro i l'Steven, amb qui hem compartit molt bons moments.

Quim ("el jefecito")!! Has tingut un paper molt important durant aquest viatge i no em vull estar d'agrair-te tot el que has fet per mi i en especial no em vull oblidar del tema de mobilitat ja que sense tu, no hauria anat pas a Uppsala. Trobaré molt a faltar les teves frases típiques com: "necessitaràs alguna cosa de dalt?". Segurament molts estaran d'acord però et trobem molt a faltar ja que sense tu el Parc ja no continuarà sent el mateix Parc: ets únic i insubstituïble!! Molta sort d'ara endavant!!

Carme i Maria! Moltes gràcies pel tema papeleo! I Dani! T'agraeixo l'ajuda proporcionada en tot moment pel tema tècnic i per aconseguir que el *beta* mai mori!

Passem al sector CompBioLab! La peculiaritat d'aquest grup és que hi passa de tot en un temps infinitesimal. I com ha anat creixent! Entre tots heu animat moltíssim l'ambient (Adrià, Eila, Lorenzo, Miguel Ángel, Javi, Miquel E., Christian, Carla i Guillem). Eila ("apamplao")! Gràcies per passar pel despatx de tant en tant! M'ha vingut genial desconnectar de tant en tant. *Lorenzo and Miguel Ángel (aka the bothering committee!) Something I will never forget about you is that, when you are both combined, someone special is about to appear, you know!! Thanks for the great time together!* A les noves incorporacions, Carla, Guillem, Christian i Miquel E., molta sort d'ara endavant i que els JACS, Nature, Angewandte, etc. estiguin sempre a favor vostre!! Guillem! Gràcies per compartir les mil històries sobre les calories!! He après moltíssim!!

Now... Davide ("black and blue never match")!!! Who forgets a guy like you??!! Thanks for being my office partner for more than one year! It has been a pleasure having such a guy like you! Great things, great time and the craziest histories happened in this office! I will never forget them! Also it is important mentioning the significant influence of the bothering committee over you. I will never forget them neither! Finally, I wish you the best for your life and researcher career.

Now let's move to Uppsala!! First, I want to thank Prof. Henrik Ottosson for giving me the chance to join his group! It was a great experience that I enjoyed a lot!! I also want to thank the members of this group, Kjell, Rabia, Raffaello and Aleksandra, for all the help you provided me! Thanks for all the advices! I would not have learnt those things without you guys! Thanks to the great time we have had out of the workplace, especially in Gamla Uppsala. Kjell!! Thanks for helping me from the first day in the airport to reach the apartment comfortably and also to get back the last day! I appreciate it a lot!! I do not forget the farewell neither. The fika was very delicious!! And finally, what do I say? Simply and obviously, it was a great pleasure to be part of this group!! Thanks a lot!!

En últim lloc però amb el mateix grau d'importància, dono les gràcies als meus pares pel seu suport continu, per les seves ganes incansables d'animar-me a no rendir-me mai i tirar cap endavant davant de qualsevol adversitat que es presenti, als meus germans (Yasmina, Ali i Mohamed) per estar amb mi en el dia a dia i als meus nebots amb qui he pogut desconnectar de tant en tant. Us estimo moltíssim a tots!

Contents

Summary of the Thesis

Aromaticity is a key concept in chemistry, used by chemists to explain the structure, stability, and reactivity of many compounds. Aromatic compounds are present in industrial processes as well as in living systems. Initially, the realm of aromatic molecules was limited to cyclic benzenoid systems. Over the years, this concept has been expanded to heterosystems, metal clusters, fullerenes, and more exotic molecules. Aromaticity is not an observable property and, thus, a direct or a universal measure does not exist. Therefore, finding a good indicator of the aromatic character of a given molecule has become a challenge. Computational chemistry has provided many qualitative and quantitative methods based on geometric, electronic, magnetic and thermodynamic properties.

The aromatic character has been always attributed to the concept of cyclic electron delocalization, thus the chemical bonding features of a molecule play a significant role. It is worth highlighting that cyclic electron delocalization can be manifested in both electronic ground and excited states of any compound.

Until now, the concept of (anti)aromaticity has found a large number of applications in a wide variety of systems, although the advances in this field are continually evolving. Computational methods can be leveraged to rationalize the concept of (anti)aromaticity for a large number of systems that expands from planar organic systems and metal clusters to three-dimensional compounds. Besides, it allows for the exploration of the intricate chemical bonding properties of some metal clusters.

The $4n+2$ rule for the ground state and the $4n$ Baird's rule for the lowest-lying triplet state are used to predict the aromatic and antiaromatic character of annulenes. For polycyclic conjugated hydrocarbons (PCHs), the latter rules fail. Instead, one must use the Clar's and Glidewell-Lloyd's rules. With regard to the Glidewell-Lloyd's rule, neither computational nor experimental studies have analyzed its validity. In the first part of this thesis, we assess the validity of this rule using Density Functional Theory (DFT) calculations and different aromaticity criteria (Chapter 4).

The second part of this thesis is centered upon the study of the aromaticity of organic compounds in their excited states. First, we start the section with three-dimensional organic

systems like fullerenes. In particular, we attempt to rationalize, in terms of aromaticity the inversion of the regioselectivity of the Diels-Alder (DA) reaction between C_{60} and cyclopentadiene (Cp) between the singlet and the triplet state (Chapter 5.1). Chapters 5.2 and 5.3 contain two collaborations with Prof. Henrik Ottosson's group at Uppsala University. These works are related with the study of excited state (anti)aromaticity of different organic systems. Specifically, we study the aromatic character of the enclosed organic systems by means of aromaticity electronic descriptors in order to support and further understand their theoretical and experimental observations.

The last part of this thesis focuses on the analysis of aromaticity and chemical bonding of metal clusters. Chapter 6.1 centers upon the analysis of the chemical bonding of the B_6^{2-} and Al_6^{2-} clusters. Even though both systems are based on atoms that belong to the same group, they prefer different molecular structures. An energy decomposition analysis (EDA) has been used to justify the structural preference of the B_6^{2-} and Al_6^{2-} clusters. In Chapter 6.2, we analyse the aromaticity of octahedral metal species and we attempt to find a possible rule to predict the aromaticity of octahedral systems. Among the compounds that have been studied in Chapter 6.2, two of them present non-nuclear attractors (NNAs), a property that is typical of electrides. To determine whether they behave as electrides or not, a detailed analysis of the chemical bonding has been performed (Chapter 6.3). At this point, the term *metallaelectride* is proposed to describe these systems since their NNAs present more electron delocalization than the NNAs of electrides that are more localized. Finally, to complement the previous study, we aim to provide a recipe that allows categorizing a series of lithium clusters, which also possess a large number of NNAs, into electrides or metallaelectrides, although a mixture of both properties could be observed in some of the clusters (Chapter 6.3).

Resum de la Tesi

L'aromaticitat és un concepte clau en química, utilitzat pels químics per explicar l'estructura, l'estabilitat i la reactivitat de molts compostos. Els compostos aromàtics estan presents tant en els processos industrials com en sistemes vius. Inicialment, l'àmbit de les molècules aromàtiques estava limitat a sistemes benzenoids cíclics. Amb el pas del temps, aquest concepte s'ha ampliat a sistemes heterocíclics, clústers metàl·lics, ful·lerens i altres molècules més exòtiques. L'aromaticitat no és una propietat observable i, per tant, no existeix una mesura directa o universal. Per tant, trobar un bon indicador del caràcter aromàtic d'una determinada molècula ha esdevingut un repte. La química computacional ha proporcionat molts mètodes qualitatius i quantitatius basats en propietats geomètriques, electròniques, magnètiques i termodinàmiques.

El caràcter aromàtic sempre s'ha atribuït al concepte de deslocalització cíclica d'electrons, de manera que el tipus d'enllaç químic d'una molècula té un paper significatiu. Cal destacar que la deslocalització cíclica d'electrons es pot manifestar tant a l'estat fonamental com en els estats excitats de qualsevol compost.

Fins ara, el concepte d'aromaticitat o antiaromaticitat ha trobat una gran quantitat d'aplicacions en una àmplia varietat de sistemes, tot i els avenços continus en aquest camp. Els mètodes computacionals permeten racionalitzar el concepte d'aromaticitat i antiaromaticitat per a una gran quantitat de sistemes que s'expandeixen des dels sistemes orgànics planers i clústers metàl·lics fins a compostos tridimensionals. A més, això permet explorar també les complexes propietats de l'enllaç químic de clústers metàl·lics.

La regla $4n+2$ per a l'estat fonamental i la regla $4n$ Baird per a l'estat triplet més baix en energia s'utilitzen per predir el caràcter aromàtic i antiaromàtic d'anul·lens monocíclics. Per als hidrocarburs policíclics conjugats, aquestes últimes regles fallen. Com a alternativa, cal utilitzar les regles Clar i Glidewell-Lloyd. Pel que fa a la regla Glidewell-Lloyd, cap estudi computacional ni experimental ha analitzat la seva validesa. A la primera part d'aquesta tesi, valorem la validesa d'aquesta regla utilitzant els càlculs de la Teoria Funcional de Densitat i els diferents criteris d'aromaticitat (Capítol 4).

La segona part d'aquesta tesi es centra en l'estudi de l'aromaticitat de compostos orgànics en els seus estats excitats. Primer, iniciem la secció amb sistemes orgànics tridimensionals com els ful·lerens. En particular, intentem racionalitzar en termes d'aromaticitat la inversió de la regioselectivitat de la reacció de Diels-Alder entre C_{60} i ciclopentadiè entre l'estat singlet i l'estat triplet (Capítol 5.1). Els capítols 5.2 i 5.3 inclouen dos col·laboracions amb el grup del Prof. Henrik Ottosson de la Universitat d'Uppsala. Aquests treballs estan relacionats amb l'estudi de l'aromaticitat en estats excitats de diferents sistemes orgànics. Específicament estudiem el caràcter aromàtic de sistemes orgànics mitjançant descriptors electrònics d'aromaticitat per tal de donar suport i comprendre les seves observacions teòriques i experimentals.

L'última part d'aquesta tesi se centra en l'anàlisi de l'aromaticitat i l'enllaç químic de clústers metàl·lics. El Capítol 6.1 està centrat en l'anàlisi de l'enllaç químic dels clústers B_6^{2-} i Al_6^{2-}. Tot i que tots dos sistemes es basen en àtoms que pertanyen al mateix grup, prefereixen estructures moleculars diferents. L'anàlisi de descomposició energètica ha estat utilitzada per justificar la preferència estructural dels clústers B_6^{2-} i Al_6^{2-}. En el Capítol 6.2, analitzem l'aromaticitat de les espècies metàl·liques octaèdriques i intentem trobar una possible regla per predir l'aromaticitat dels sistemes octaèdrics. A partir dels compostos que s'han estudiat al Capítol 6.2, dos d'ells presenten atractors no nuclears (NNAs), una propietat típica dels electrurs. Per determinar si es comporten com a electrurs o no, s'ha realitzat una anàlisi detallada de l'enllaç químic (Capítol 6.3). En aquest punt, es proposa el terme metal·laelectrur per descriure aquests sistemes, ja que el seus NNAs presenten més deslocalització electrònica que els NNAs de les electrurs que estan més localitzats. Finalment, per complementar l'estudi anterior, es pretén proporcionar una recepta que permeti classificar una sèrie de clústers de liti, que també posseeixen una gran quantitat de NNAs en electrides o metal·laelectrurs, tot i que es podria observar una barreja d'ambdues propietats en algunes dels clústers (Capítol 6.3).

Resumen de la Tesis

La aromaticidad es un concepto clave en química, utilizado por los químicos para explicar la estructura, la estabilidad y la reactividad de muchos compuestos. Los compuestos aromáticos están presentes tanto en los procesos industriales como en sistemas vivos. Inicialmente, el ámbito de las moléculas aromáticas estaba limitado a sistemas benzenoids cíclicos. Con el paso del tiempo, este concepto se ha ampliado a sistemas heterocíclicos, clústeres metálicos, fulerenos y otras moléculas más exóticas. La aromaticidad no es una propiedad observable y, por tanto, no existe una medida directa o universal. Por lo tanto, encontrar un buen indicador del carácter aromático de una determinada molécula se ha convertido en un reto. La química computacional ha proporcionado muchos métodos cualitativos y cuantitativos basados en propiedades geométricas, electrónicas, magnéticas y termodinámicas.

El carácter aromático siempre se ha atribuido al concepto de deslocalización cíclica de electrones, por lo que las características de enlace químico de una molécula tienen un papel significativo. Cabe destacar que la deslocalización cíclica de electrones se puede manifestar tanto en el estado fundamental como en los estados excitados de cualquier compuesto.

Hasta ahora, el concepto de aromaticidad o antiaromaticitat ha encontrado una gran cantidad de aplicaciones en una amplia variedad de sistemas, aunque los avances en este campo nunca terminan. Los métodos computacionales permiten racionalizar el concepto de aromaticidad y antiaromaticitat para una gran cantidad de sistemas que se expanden desde los sistemas orgánicos planos y clústeres metálicos hasta compuestos tridimensionales. Además, esto permite explorar también las complejas propiedades del enlace químico de clústeres metálicos.

La regla $4n+2$ para el estado fundamental y la regla $4n$ Baird para el estado triplete más bajo en energía se utilizan para predecir el carácter aromático y antiaromático de anulenos monocíclicos. Para los hidrocarburos policíclicos conjugados, estas últimas reglas fallan. Como alternativa, hay que utilizar las reglas Clar y Glidewell-Lloyd. En cuanto a la regla Glidewell-Lloyd, ningún estudio computacional ni experimental ha analizado su validez. En la primera parte de esta tesis, valoramos la validez de esta regla utilizando los cálculos de la Teoría Funcional de Densidad y los diferentes criterios de aromaticidad (Capítulo 4).

La segunda parte de esta tesis se centra en el estudio de la aromaticidad de compuestos orgánicos en sus estados excitados. Primero, iniciamos la sección con sistemas orgánicos tridimensionales como los fulerenos. En particular, intentamos racionalizar en términos de aromaticidad la inversión de la regioselectividad de la reacción de Diels-Alder entre C_{60} y ciclopentadieno entre el estado singulete y el estado triplete (Capítulo 5.1). Los capítulos 5.2 and 5.3 incluyen dos colaboraciones con el grupo del Prof. Henrik Ottosson de la Universidad de Uppsala. Estos trabajos están relacionados con el estudio de la aromaticidad en estados excitados de diferentes sistemas orgánicos. Específicamente, estudiamos el carácter aromático de sistemas orgánicos mediante descriptores electrónicos de aromaticidad para apoyar y comprender sus observaciones teóricas y experimentales.

La última parte de esta tesis se centra en el análisis de la aromaticidad y el enlace químico de los clústeres metálicos. El Capítulo 6.1 está centrado en el análisis del enlace químico de los clústeres B_6^{2-} y Al_6^{2-}. Aunque ambos sistemas se basan en átomos que pertenecen al mismo grupo, prefieren estructuras moleculares diferentes. El análisis de descomposición energética ha sido utilizado para justificar la preferencia estructural de los clústeres B_6^{2-} y Al_6^{2}. En el Capítulo 6.2, analizamos la aromaticidad de las especies metálicas octaédricas e intentamos encontrar una posible regla para predecir la aromaticidad de los sistemas octaédricos. A partir de los compuestos que se han estudiado en el Capítulo 6.2, dos de ellos presentan atractores no nucleares (NNAs), una propiedad típica de los electruros. Para determinar si se comportan como electruros o no, se ha realizado un análisis detallado del enlace químico (Capítulo 6.3). En este punto, se propone el término metaloelectruro para describir estos sistemas, ya que sus NNAs presentan más deslocalización electrónica que los NNAs de los electruros que están más localizados. Finalmente, para complementar el estudio anterior, se pretende proporcionar una receta que permita clasificar una serie de clústeres de litio, que también poseen una gran cantidad de NNAs en electruros o metaloelectruros, aunque se podría observar una mezcla de ambas propiedades en algunos de los clústeres (Capítulo 6.3).

CHAPTER 1:

INTRODUCTION

1.1 The concept of aromaticity

Chemists continuously deal with aromatic molecules due to their interesting properties as building blocks of many relevant compounds.[1] Aromaticity is not an observable molecular property in quantum mechanics because we cannot directly get a measure by an action of an "aromaticity" operator on the wavefunction. Therefore, aromaticity is not a well-defined magnitude such as the position, the dipolar moment, or the energy. Yet, any of the known observables can quantify directly the aromatic character of a molecule. Even though many definitions of aromaticity have been proposed, nowadays this concept is still blurry. For instance, in 2005, Schleyer *et al.* defined it as "a manifestation of electron delocalization in closed circuits, either in two or in three dimensions (…)".[2] Nevertheless, according to IUPAC's definition, aromaticity is "a concept of spatial and electronic structure of cyclic molecular systems displaying the effects of cyclic electron delocalization which provide for their enhanced thermodynamic stability (relative to acyclic structural analogues) and tendency to retain the structural type in the course of chemical transformations(…)".[3] It is worth highlighting that both definitions share an important key concept: the electron delocalization.

1.2 Summary of the key developments in aromaticity

The next table summarizes significant contributions in the field of aromaticity that will be briefly mentioned in the following sections. The ones highlighted in blue are related to metalloaromaticity, that is, molecules that contain metal atoms in the aromatic ring, and the ones in brown are related to aromatic organic systems.

Table 1. List of the key advances of the concept of aromaticity listed in chronological order.

Year	Main contributor(s)	Contribution
1825	Faraday[4]	Isolation of benzene, high carbon-hydrogen ratios
1865	Kekulé[5]	Cyclohexatriene benzene formula; structural basis of aromaticity
1866	Erlenmeyer[6]	Reactivity basis for aromaticity: substitution is more favorable than addition
1911	Willstätterand Waser[7]	Synthesis of the first antiaromatic compound: COT
1922	Crocker[8]	Aromatic sextet
1925	Armit and Robinson[9]	Aromatic sextet; inscribed circle notation
1931	Hückel[10]	Theory of cyclic $(4n+2)\pi$-electron systems
1933	Pauling[11]	Valence bond method and resonance
1945	Calvin and Wilson[12]	Chelatoaromaticity introduced to explain the stability of Cu(II)-1,3-diketonate complexes
1964	Heilbronner[13]	Möbius aromaticity
1965	Breslow[14]	Distinction between aromaticity and antiaromaticity
1971	Wade[15,16]	$2n+2$ Wade's rule for closoboranes
1972	Mingo[17,18]	$4n+2$ Mingo's rule for closoboranes
1972	Clar[19]	Clar's aromatic sextet
1972	Baird[20]	Triplet state aromaticity
1978	Aihara[21]	Three-dimensional aromaticity in metal clusters
1979	Bursten and Fenske[22]	Metalloaromaticity is used to describe CBD metal complexes
1979	Thorn and Hoffmann[23]	Metallacyclopentadienes and metallabenzenes predicted through computation
1979	Dewar[24]	σ–Aromaticity
1984	Glidewell and Lloyd[25]	Extension of the Clar's rule
1985	Shaik and Hiberty[26]	π–electron distortivity
1985	Kroto and Smalley[27]	Discovery of fullerenes
2000	Hirsch[28]	Spherical aromaticity in closed-shell fullerenes
2001	Boldyrev and coworkers[29]	All-metal aromaticity; double σ– and π–aromaticity
2003	King[30]	σ–Aromaticity in transition metal rings
2003	Boldyrev and coworkers[31]	All-metal conflicting aromaticity; σ–aromaticity and π–antiaromaticity
2003	Herges and coworkers[32]	First Möbius annulene synthesized
2005	Schleyer and coworkers,[33] Tsipis and coworkers,[34] Wang and coworkers[35]	d-Orbital aromaticity
2007	Boldyrev and coworkers[36]	δ-aromaticity
2007	Averkiev and Boldyrev[37]	Triple σ-, π-, and δ-aromaticity
2008	Fowler and Soncini[38]	Extension of Hückel-Baird rules
2008	Rzepa[39]	Linking number rule. Generalized Hückel-Möbius rules
2011	Poater and Solà[40]	Spherical aromaticity in open-shell fullerenes
2013	Herges and coworkers[41]	First triple twisted Möbius annulene

1.3 The beginning of aromaticity and antiaromaticity

The origin of the concept of aromaticity starts with the discovery of benzene. In 1825, benzene was isolated by Michael Faraday from the oil mixture used to store gaseous fuel at high pressures giving it the name of bicarburet of hydrogen.[4] After a decade, Eilhard Mitscherlich obtained the same compound from gum benzoin by heating benzoic acid. He found that its empirical formula was CH and finally recognized that the molecular formula was C_6H_6. As it was derived from gum benzoin, he named it benzin,[42] which at the end became benzene when it was translated into English. Many years later, compounds like benzoic acid or phenol with similar properties were detected in the oil mixture. So, one can easily imagine that these compounds are extremely stable. The high stability of these unsaturated compounds suggested that they are less reactive than the typical alkenes or alkynes despite the presence of multiple unsaturated bonds. Systems like benzene or phenol were categorized as aromatic compounds because of their distinct odor or aroma.

Many researchers tried to find the best model structure for explaining the high stability and chemical bonding of benzene. In 1865, F. Kekulé[5,43] proposed a cyclic arrangement of six carbon atoms with alternating single and double bonds and A. W. Hofmann[44] applied the term aromatic to compounds containing a benzene ring. Yet, Kekulé's structure only explains the spatial distribution of the atoms of the molecular formula. Later, thanks to the aromaticity sextet concept introduced by Crocker[8], Robinson and Armit related the aromaticity with the number of electrons through their Aromatic Sextet Theory.[9] The latter researchers postulated that each carbon was contributing with one p_z-electron to form a circuit of six electrons that circulate around the molecule triggering the aromatic properties. In 1933, through the valence bond theory, developed by Pauling,[11,45] it was stated that the extra stability of benzene was mainly attributed to the high contribution of two Kekulé resonance structures (Figure 1).

On the other hand, in 1911, the synthesis of an eight-membered carbon ring (8-MR) with alternating single and double bonds, known as cyclooctatetraene (COT)[7] (Figure 1), revealed that its reactivity was significantly different from benzene, and for this reason it was classified as an antiaromatic compound. Remarkably, it is worth noting that for antiaromatic systems (see 1.4.1 for more details on antiaromaticity), like COT, the Pauling's resonance theory fails because, even though the system presents conjugation, the extra stabilization does not exist.
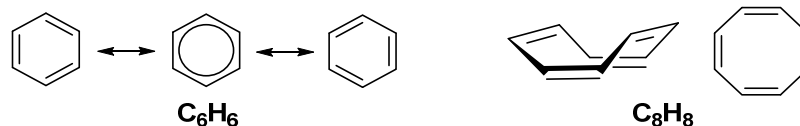
Figure 1. Resonance structures of benzene (left) and geometry of COT (right).

1.4 Aromaticity in organic chemistry

In this section, we are going to walk through the basics of the different simple rules that are used to predict which molecules are potentially aromatic. These rules are widely used to qualitatively assign an aromatic character to a molecule. The classification of molecules as aromatic is a difficult task and rules are needed to establish a border between aromatic and non-aromatic molecules. Then, the influence of such rules in organic chemistry will be discussed with some examples.

1.4.1 Hückel's $4n+2$ rule

The most popular rule of aromaticity among the chemistry community is probably the Hückel's $4n+2$ rule, which is used as a tool to predict qualitatively whether a molecule will be aromatic or not. First, we go through the basics of this rule. According to the molecular orbital (MO) theory, the benzene molecule displays three bonding (Ψ_1, Ψ_2 and Ψ_3) and three antibonding (Ψ_4, Ψ_5 and Ψ_6) π-MOs, which involve the six carbon atoms of the molecule (Figure 2). Moreover, it was argued that the delocalization of the three pairs of electrons, which belong to the three bonding orbitals, was the responsible for the high stability of benzene. These observations were confirmed by Hückel in 1931. Being able to split the MOs into σ and π orbitals, Hückel demonstrated that six electrons have π character and they are completely delocalized through the carbon atoms of the ring.[10,46] He concluded that this π-electron delocalization as well as the three occupied bonding MOs and the presence of two degenerated highest occupied molecular orbitals (HOMOs) (Ψ_2 and Ψ_3), is what makes benzene significantly stable and aromatic. Then, from these findings, the $(4n+2)\pi$ rule was formulated to predict whether a system is aromatic or not based on the number of π-electrons. Therefore, a system will be aromatic if it possesses $(4n+2)\pi$-electrons. Otherwise, it will be considered antiaromatic or non-aromatic (see below for more details). Interestingly, in 1954, the synthesis of the tropylium cation verified Hückel's $4n+2$ rule.[47] Here, it is worth noting that the carbon-carbon bond length equalization is an important feature that arises in

Hückel aromatic systems, opposite to what happens in antiaromatic species (further details below).
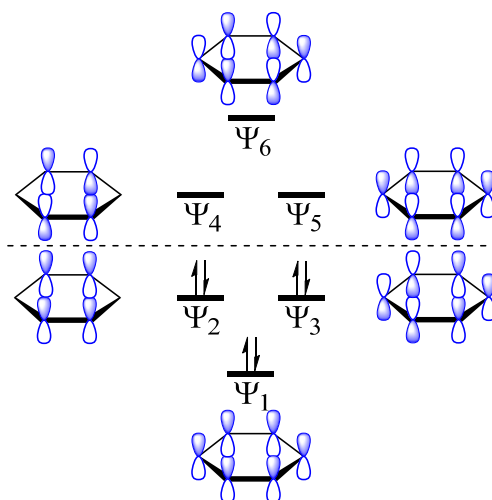
Figure 2. Schematic π-MOs of benzene in its S_0 state.

In 1964, Heilbronner[13] introduced the concept of Möbius aromaticity. He predicted that $4n\pi$- and $(4n+2)\pi$-conjugated molecules with Möbius topology should be aromatic and antiaromatic, respectively. Thus, the Möbius aromaticity, which follows the opposite Hückel's rule, is characterized for possessing a single twisted one-sided topology (Figure 3), like a Möbius strip, in $4n\pi$-conjugated systems. Yet, if the molecule is characterized by a double-twisted Möbius strip, we move towards a "twisted Hückel" topology. In 2008, Rappaport and Rzepa[39] introduced the linking number as a numerical invariant that describes the linking of two closed curves in three-dimensional space. Intuitively, the linking number represents the number of times that each curve winds (writhe and twist) around the other. Rappaport and Rzepa generalized the Hückel-Möbius rules by stating that cyclic conjugated annulenes that have an even value of the linking number (even number of writhes and twists) follow Hückel's $(4n+2)\pi$-electron rule of aromaticity for the closed-shell ground state, whereas those having an odd linking number obey the Möbius 4n π-electron rule.[39]

Hückel
twist = 0º
aromatic: 4n+2
antiaromatic: 4n

Möbius
twist = 180º
aromatic: 4n
antiaromatic: 4n+2

Twisted Hückel
twist = 360º
aromatic: 4n+2
antiaromatic: 4n
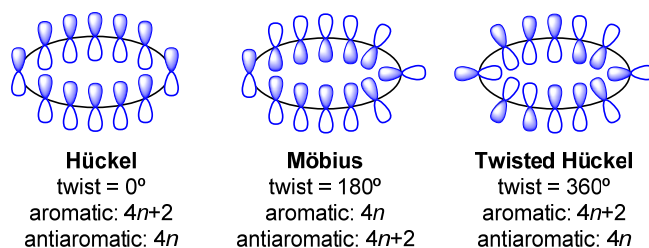
Figure 3. Hückel and Möbius topologies.

A representative case of aromatic Möbius [4n]annulene is the $C_{10}H_{10}^{2-}$ anion previously reported by Mucke *et al.*[48] $C_{10}H_{10}^{2-}$ anion is able to adopt two conformations: Hückel or Möbius. Figure 4 shows how the Möbius structure displays a single twisted MO while in the Hückel conformer this twist is not present. It is also worth mentioning that the most stable structure is the Möbius one. Porphyrins such as the recently synthesized [28]hexaphyrin[49] are molecules that present Möbius aromaticity and antiaromaticity due to mainly the conformational flexibility shown by the macrocyclic π-conjugated system. These systems present interesting photophysical properties.[50,51]
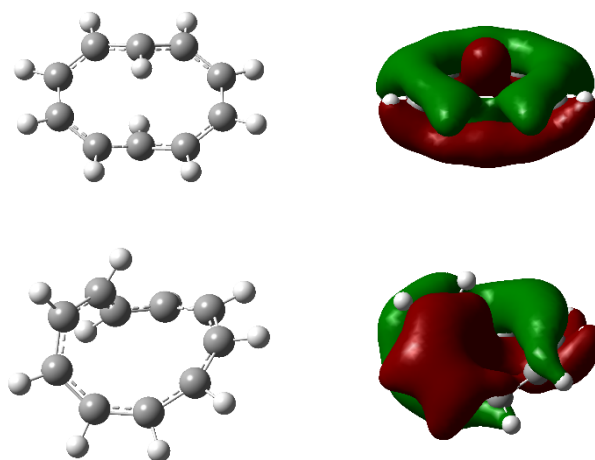
Figure 4. Most stable Hückel (top) and Möbius (bottom) isomers of $C_{10}H_{10}^{2-}$ with their most respective representative π-MOs. Geometries obtained from reference [48]. Isosurface value at 0.02 a.u.

In 1965, R. Breslow assigned the term "antiaromaticity"[52] to systems with 4nπ-electrons. In contrast to the concept of aromaticity, antiaromatic systems would be destabilized with respect to open chain analogues. Therefore, molecules such as cyclobutadiene (CBD) (with 4π-electrons) or COT (with 8π-electrons) are antiaromatic. It is worth highlighting that, apart from the bond length alternation, the non-planarity is an important feature for antiaromatic systems, which is mainly observed in large rings, like COT. Cyclopropenyl anion, which has 4π-electrons, was the first system analyzed to proof the validity of this hypothesis.[53] The schematic MO diagram of cyclopropenyl cation (D$_{3h}$) (Figure 5) showed that it is composed of an occupied π-bonding MO (Ψ_1) and two unoccupied non-bonding (Ψ_2) and π-antibonding (Ψ_3) MOs, so those Ψ_2 and Ψ_3 are degenerated. In the cyclopropenyl anion (C$_{2v}$), the two extra π-electrons occupy Ψ_2 so that the D$_{3h}$ symmetry is lost and consequently the initial degeneracy of Ψ_2 and Ψ_3 is destroyed. This destabilization of the MOs is the reason

that makes the cyclopropenyl anion antiaromatic instead of aromatic. And for such, the properties of this molecule will be completely different from the ones observed in benzene.
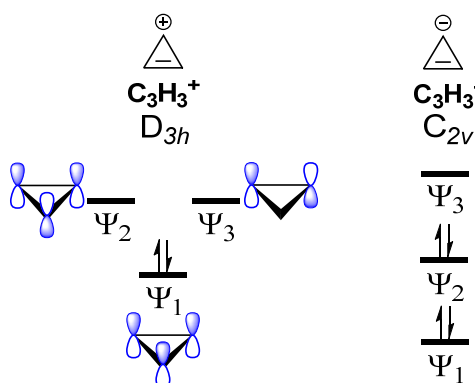
Figure 5. Schematic π-MOs of cyclopropenyl cation (left) and anion (right).

Thus, Hückel's rule states that monocyclic planar conjugated hydrocarbons with $(4n+2)\pi$-electrons are aromatic whereas systems with $4n\pi$-electrons are antiaromatic. Further, the stability is gained when bonding orbitals are populated (aromaticity) but is lost if the electrons occupy antibonding or non-bonding orbitals (antiaromaticity).[10] So the number of π-electrons plays an essential role in determining the stability, structure, and reactivity of aromatic and antiaromatic systems. We have to also mention that Hückel's rule is exclusively valid and only works for closed-shell monocyclic species.

1.4.2 Clar's and Glidewell-Lloyd's rule

The $4n+2$ rule works remarkably well for annulenes with rings of different size. However, for large PCHs, Hückel's rule does not correctly predict their aromatic behavior. Among many attempts to extend this rule to polycyclic systems, the most successful one was the Clar's sextet rule[19] that was proposed in 1972. This rule is mainly based on the Armit and Robinson's work[9] where they used the term "aromatic π-sextet" for the first time. Basically, the Clar's rule states that the Kekulé resonance structure with the largest number of separated aromatic π-sextets is the most significant one to describe the properties of the polycyclic aromatic hydrocarbons (PAHs). Aromatic π-sextets are defined as six π-electrons localized in a single six-membered ring (6-MR) separated from adjacent rings by formal C-C single bonds. It is also demonstrated that isomers with a certain number of aromatic π-sextets are kinetically more stable than isomers with less number of aromatic π-sextets.[54–56]

Figure 6 shows all possible resonance structures, with the Clar ones highlighted in red that can be generated from phenanthrene (**A**) and anthracene (**C**), and the Clar structure for triphenylene (**B**). For **A**, according to Clar's rule, the most stable structure should be the second one due to the presence of more aromatic π-sextets and in fact this is also supported by computational studies[57–59]. For **C**, there are three structures that have only one Clar's sextet localized in one of the three rings. The three structures are equivalent according to Clar's rule and the Clar structure is better described by a superposition of these three structures.
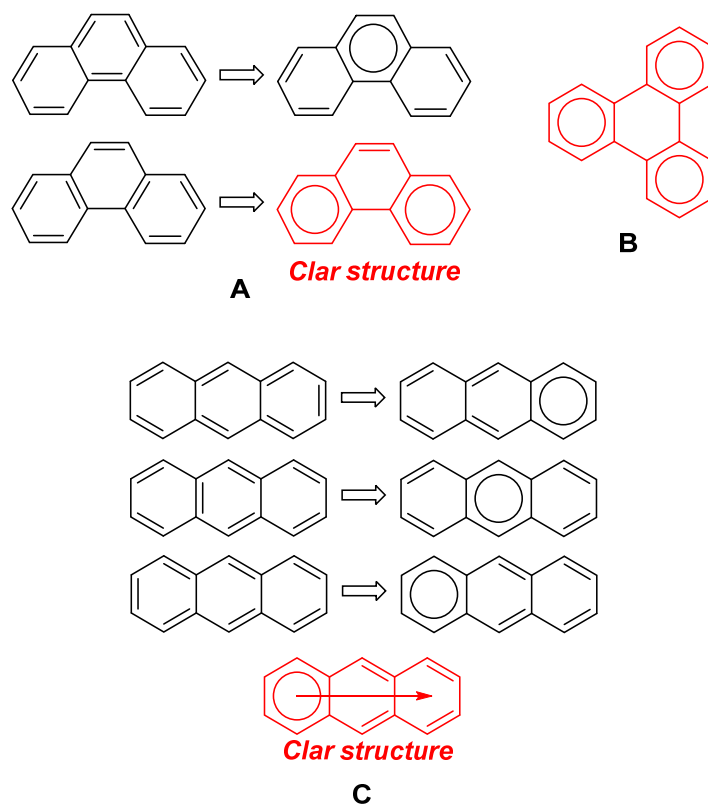
Figure 6. Resonance and Clar (in red) structures of phenanthrene (**A**) and anthracene(**C**) and Clar structure of triphenylene (**B**). Reproduced/adapted with permission from reference [60].

From the previous findings concerning the systems in Figure 6, one can classify the 6-MRs of benzenoid species in four types of rings: aromatic sextets (like phenanthrene external ring), migrating sextets (like anthracene rings), empty rings (like triphenylene central ring) and rings with localized double bonds (like the phenanthrene central ring). Note that Clar's rule only works with PAHs involving 6-MRs. This represents an advance with respect to the $4n+2$ rule but still presents some limitations.

Twelve years later, Glidewell and Lloyd[25] proposed to extend the Clar's rule to PCHs with rings constituted by an even number of carbon atoms, *i.e.*, non-benzenoid PAHs. Glidewell and Lloyd's rule affirms that the total population of π-electrons in conjugated polycyclic systems tends to form the smallest $4n + 2$ groups and to avoid the formation of the smallest $4n$ groups.[60] Figure 7 shows three non-benzenoid PAHs in which the application of the Glidewell and Lloyd rule leads to the conclusion that the resonance structures highlighted in blue are the most relevant to explain the electronic and molecular properties of these systems. For instance, for case **A** (Figure 7), which is composed of fused COT and CBD rings, the resonance structure that better defines the molecular and electronic structure of this compound is the one that places eight π-electrons in the 8-MR and two in the 4-MR.

A   **B**   **C**
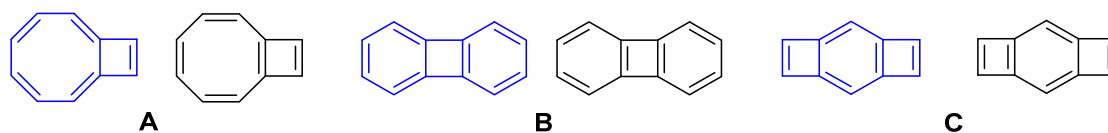
Figure 7. Different resonance structures for three selected cases of PCHs. Blue resonance structures are those that better describe the structural and electronic properties of these PCHs according to the Glidewell-Lloyd's rule.

1.4.2.1 The usefulness of Clar's sextet rule

At first glance, one can state that the concept of Clar's sextet rule is only employed from the theoretical point of view to explain the physical and chemical properties of PAHs. However, during the last decade, this concept has received more attention and it has become a powerful tool for experimentalists to design novel molecules with properties of interest.

For instance, in 2015, Matsumoto and coworkers reported the synthesis and physical properties of a peripentacene derivative which has eight benzene rings (**A**, Figure 8) that follow Clar's rule according to aromaticity studies.[61] While neutral PAHs are very common in chemistry, cationic species are not easy to obtain due to their high reactivity. Actually, these cationic species play a significant role as intermediates in organic synthesis and have found interesting applications in fields such as molecular electronics.[62] Recently, the same researchers synthesized a number of perylene dications (**B** and **C**, Figure 8) and for the first time successfully crystallized the perylene dication **B**.[63] The crystal structure of **B** confirmed the validity of Clar's sextet rule. Actually, by combining experimental and computational

studies they demonstrated that Clar's aromatic π-sextet rule can explain and predict the reactivity and structure of dicationic PAHs in a very simple manner.
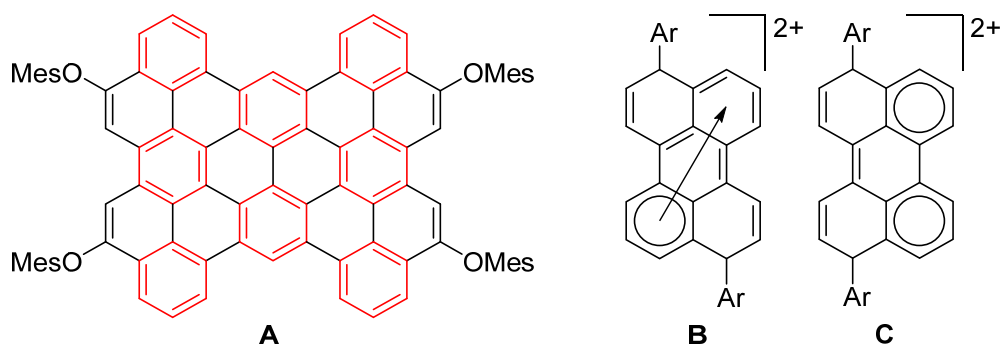
Figure 8. Structure of tetrabenzoperipentacene (**A**) and Clar structures of perylene dications (**B** and **C**).

1.4.3 Baird's rule

As we said above, Hückel's rule can be only applied to closed-shell systems and therefore it cannot be applied to systems other than the (singlet) electronic ground state. Aromaticity can play an important role in photochemistry[64] and, therefore, it is important to be able to assign the aromatic character of excited states species.

By using the perturbation molecular orbital (PMO) theory, Baird[20] revealed in 1972 that aromatic singlet annulenes (like benzene) are antiaromatic in the lowest-lying excited π-π^* triplet state (T_1), while antiaromatic singlet annulenes are aromatic in the triplet state. Thus, Baird's rule states that $4n\pi$ monocycles (like CBD or COT) are aromatic in the T_1 state as well as in the S_1 state.[65–67] Indeed, triplet ground states of cyclopentadienyl (Cp^+, $C_5H_5^+$) and pentachlorocyclopentadienyl (PCp^+, $C_5Cl_5^+$) cations were detected experimentally[68–70] reporting the first evidence that the triplet states of these systems really exist as predicted by Baird. Opposite to Hückel aromaticity, the bond equalization of Baird aromatic systems arises at T_1 state but, for antiaromatic species, it is not present. To understand where the stabilization comes from we analyze in detail the MOs of $C_5H_5^+$. Its MO diagram (Figure 9) shows that, in S_0, four electrons are distributed in two π-MOs (Ψ_1 and Ψ_2). This electronic distribution is ruled by the Jahn-Teller effect. Nevertheless, at T_1, two degenerated half-filled MOs are formed and this fact instigates stabilization of Ψ_3. So in that way, this stabilization that is gained makes the system aromatic. In addition to this, it is worth highlighting that,

from S_0 to T_1, we obtain a more symmetric (D_{5h}) structure compared with S_0 (C_{2v}) leading to a situation with bond length equalization typical of aromatic systems.
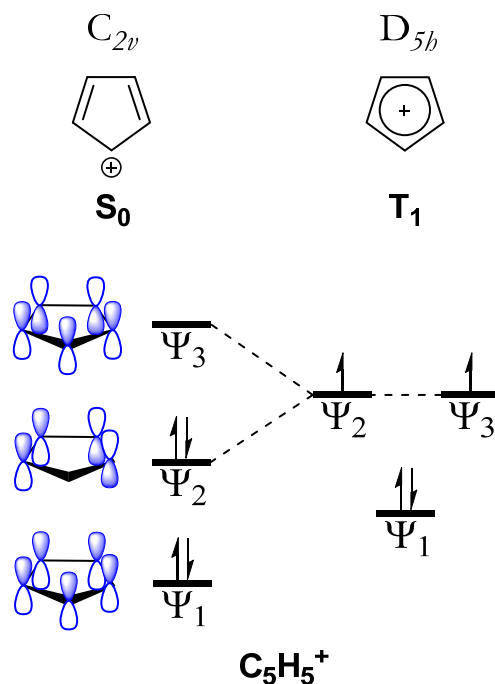
Figure 9. Schematic MO of cyclopentadienyl cation in the S_0 and T_1 states.

1.4.3.1 The importance of Baird's rule

The number of studies regarding the aromatic character of excited state species is less frequent in comparison with the ground-state literature. Nonetheless, recently excited-state aromaticity has received an increased attention because this property allows us to rationalize a number of photophysical and photochemical reactions.[64] Due to the large number of studies, we focus this section only on a couple of recent studies in which the (anti)aromaticity has a significant impact on photochemical reactions to show the power of the Baird's rule.

<u>Photosilylations and transfer photohydrogenations of benzenoid hydrocarbons and graphene</u>

Generally, it is difficult to make aromatic species reactive in the ground state due to the endergonicity of these processes unless we use drastic conditions such as high pressures and temperatures. Yet, a number of computational studies proved that the aromaticity of benzene decreases drastically in the T_1 and S_1 states and therefore benzene can easily undergo

photochemical reactions.[71] For instance, that would be the case of the first hydrogenation step of benzene in S_0, which is endothermic because the aromaticity of the ring must be destroyed, contrary to the hydrogenation of alkenes. Nonetheless, according to Baird's rule, benzene should experience the hydrogenation reaction easily in T_1 and S_1 because in both states benzene is antiaromatic.
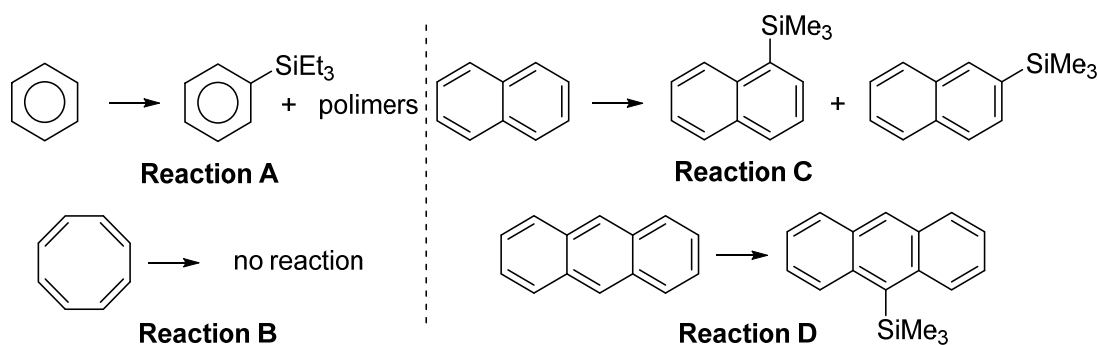
Figure 10. Experimental results on metal-free photosilylations of benzene (Reaction A), COT (Reaction B), naphthalene (Reaction C) and anthracene (Reaction D) under *hv* and Et₃SiH.

With regard to the previous reaction, very recently, Papadakis *et al.* took advantage of Baird's rule to show that benzene and several PAHs experience metal-free photochemical (hydro)silylations and transfer-hydrogenations at mild conditions.[72] First, their computations showed that in general the hydrogenation of [4n+2] annulenes takes place in an exergonic process in T_1 while for [4n] annulenes the reaction is endergonic. So this demonstrates that their initial hypothesis about the influence of Baird-antiaromaticity on these reactions is valid. Besides, experimental photosilylation reactions of benzene, COT and larger PAHs such as naphthalene, phenanthrene and anthracene were carried out using Et₃SiH as a hydrogen abstractor. Interestingly, these experiments show that all the reactions work giving the desired product except for the reaction with COT which does not take place due to the high endergonicity of this process (Figure 10). With regard to the photoreactivities of the PAHs towards Et₃SiH, several factors lower them when compared with benzene. The computed activation energies for H-atom abstraction from HSiMe₃ gradually increase with the size of the PAHs showing that other factors than excited-state antiaromaticity also influence the activation barriers and reactivities of larger T_1 state PAHs. In particular, it was argued that the formation of excimers (as they are less antiaromatic) could be one of those factors that lower the reactivity of large PAHs. Finally, they have examined the photohydrogenations and

photohydrosilylations of graphene. They observed that graphene is more reactive than large PAHs due to two important features. First, the T_1 antiaromaticity localizes to the edges of the molecule. And second, the formation of two T_1 state antiaromatic five-membered rings (5-MRs) from an antiaromatic 14π-electron perimeter (Stone–Wales defects[73,74]) could be presented. So at least two possibilities for triplet-state antiaromaticity localization exist in graphene.

The results obtained in this study emphasize that the excited state antiaromaticity is important and beneficial for triggering photoreactivity.[71]

Excited state intramolecular proton transfer reactions

Excited state intramolecular proton transfer (ESIPT) reactions, which have found interesting applications in photochemistry, are essentially based on keto-enol phototautomerizations. Systems like *o*-hydroxybenzaldehyde (OHBA)[75], *o*-nitrobenzaldehyde (NBA)[76] or salicylideneaniline (SA)[77] are compounds that experience these kind of reactions. In this section we are going to focus on the case of SA.

SA is an aromatic Schiff base which shows a photochromic behavior.[78] Experimental and theoretical studies reveal that the proton transfer reaction of SA takes places essentially in S_1 because, in this state, this step is (π,π^*) barrierless.[79,80] Scheme 1 shows schematically the ESIPT process in SA (ignoring the isomerization processes).[81] Basically, the photoreaction begins with the excitation of the enol tautomer by light to the S_1 state. Then the tautomerization reaction takes place in this excited state forming the keto form. Once the keto tautomer is formed, the reaction can easily return to the enol form through the ground state.

As it can be seen, the formation of one tautomer or the other is influenced by the electronic state. Consequently, the enol form cannot be transformed to the keto form in the ground state due to the endergonicity of this process. The opposite situation is observed if one wants to obtain the keto tautomer from the enol one through the S_1 state.
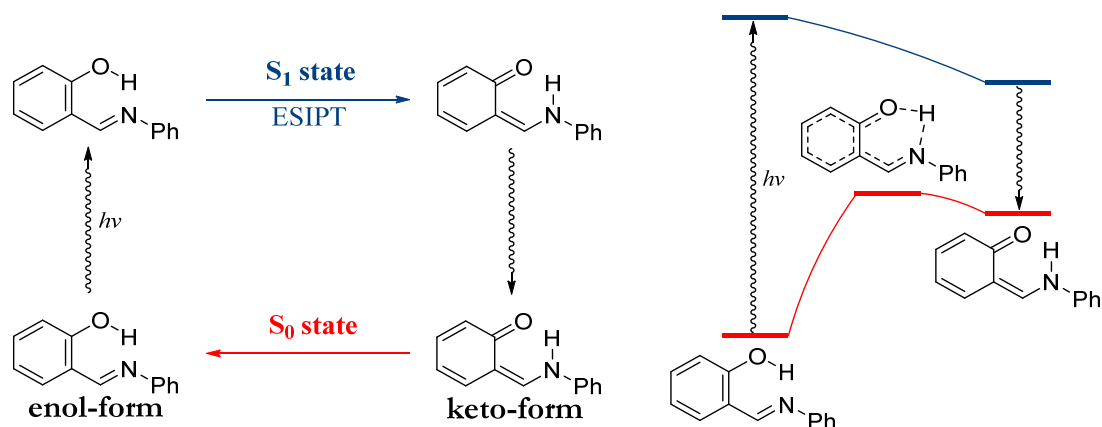
Scheme 1. Schematic ESIPT mechanism of the SA.

SA as well as OHBA or NBA involves a benzene moiety (phenol ring) in its structure. So one could wonder if aromaticity may play a role in these reactions. In 2015, Gutiérrez-Arzaluz and collaborators found, through time-dependent density functional theory (TDDFT) calculations, that the ESIPT of SA is driven by changes in the aromaticity of the system upon excitation.[81] Their results showed that the different reactivity between the S_0 and S_1 states is attributed to a loss of aromaticity of the phenol moiety after the photoexcitation, letting a redistribution of electron density to facilitate the tautomerization reaction. In fact, in the S_1 state the aromatic character of the phenol moiety is practically kept along the reaction coordinate. Contrarily, in the ground state, a significant change of aromaticity is observed. Concerning the aromaticity of the $-C_6H_5$ group, even though it is reduced after photoexcitation, the changes in the aromatic character of the aniline ring are smaller than those of the phenol moiety.

We must highlight that, in the previous study, the Baird (anti)aromaticity concepts, which are used to rationalize photochemical reactions, could have been used to explain the ESIPT. Thus, if we do so, the first point we notice is that the benzene ring becomes Baird antiaromatic (or "Mr Hyde" as stated by Ottosson and coworkers)[71] in S_1 due to the formation of a biradical because of the π-π* character that destroys the aromaticity (we put one electron from a bonding orbital to an antibonding). In general it is assumed that, in the S_1 state, these systems prevent the aromatic sextet in the benzene moiety by favoring the enol form.[82,83] So in terms of Baird aromaticity, one can also argue that the antiaromaticity in the first excited electronic state during the ESIPT reaction is the responsible for the reactivity of the enol tautomer.

Final remarks

Nowadays, Baird-aromaticity concept is continually evolving and it is receiving huge attention. Here, we have shown the high importance of the T_1-aromaticity through different recent studies. Even though one can study the electronic structure of an organic system, it is crucial to link it with experiments to achieve a solid rationalization of the molecular properties that a molecule exhibits in both ground and excited states.

1.4.4 Rules of spherical aromaticity

Fullerenes are polycyclic π-conjugated 3D structures and there is a certain interest to find out some way to predict their aromatic character and its role in fullerene reactivity. Fullerenes possess a molecular structure close to a sphere. Taking advantage of this feature, in 2000, the $2(n+1)^2$ rule postulated by Hirsch appeared and considered that the π-electron system of a spherical carbon cluster can be approached by a spherical electron gas surrounding the surface of the sphere.[28,84,85] The
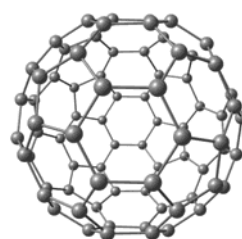
Figure 11. C_{80}^{5-} (S=7/2) structure.

corresponding wavefunctions of this electron gas are characterized by the angular momentum quantum number l (l = 0, 1, 2...), with each energy level being $2l+1$ times degenerated, and consequently all π-shells are completely filled when we have 2, 8, 18, 32, 50… electrons, *i.e.*, $2(n+1)^2$ electrons. Thus, spherical closed-shell carbon cluster that has $2(n+1)^2$ π-electrons are aromatic. According to this rule, systems like C_{20}^{2+} (I_h), C_{60}^{10+} (I_h) or C_{80}^{6+} (D_{5d}) are aromatic. Their aromatic character was assessed in terms of nucleus-independent chemical shifts (NICS) (see 2.3.3 for more details).[28]

Hirsch's rule is the analogue to the $4n+2$ rule for two-dimensional polycyclic annulenes postulated by Hückel. In 2013, Poater and Solà extended the Hirsch's rule to open-shell fullerenes, like Baird did for $4n$π open-shell annulenes.[40] In that case, they took the same type of wavefunctions as in Hirsch's rule and demonstrated that an aromatic situation with the degenerate HOMOs occupied with half-filled electrons in parallel spin with the rest of the lower level orbitals being fully-filled is reached for a number of electrons equal to 1, 5, 13, 25, 41…, *i.e.*, for spherical species with $2n^2 + 2n+1$ electrons and with an electronic spin of (S=n+½). Hence, carbon clusters like C_{20}^{5-} (I_h, S=7/2), C_{60}^{1-} (I_h, S=11/2), C_{60}^{19+} (I_h, S=9/2) and C_{80}^{5-} (I_h, S=13/2) are aromatic because they obey this rule. Their aromatic character was

evaluated in terms of multicenter index (MCI) (see 2.3.1 for more details) and NICS (see 2.3.3 for more details).

1.4.4.1 Recent research on the aromaticity of fullerenes

In 1987, Kroto[86] proposed the Isolated Pentagon Rule (IPR) as a simple criterion to relate the stability of fullerene isomeric carbon cages and the disposition of their twelve pentagonal rings with different isomers. This rule states that most stable fullerene isomers are those where the twelve pentagons are isolated on the fullerene surface, for instance in C_{60} where pentagonal rings are surrounded by five hexagonal rings. When two pentagonal rings occupy adjacent positions on a spherical fullerene structure, a high steric tension is produced due to the geometrical restrictions, in addition to the destabilizing effect on the π-electron structure of the molecule. According to Hückel's rule, π–electron stabilization of 6-MRs is greater than for 5-MRs and 7-MRs and in 4-MRs and 8-MRs it is even less. Hence, the IPR rule indicates that the final stability of fullerenes is given by an equilibrium between steric tension and π-electron structure. At this point, it is worth highlighting that depending on the molecular structure of the fullerene, we have different types of bonds (Figure 12) which are significant from the reactivity point of view. Actually, depending on the type of the reaction, one bond or another will be involved.
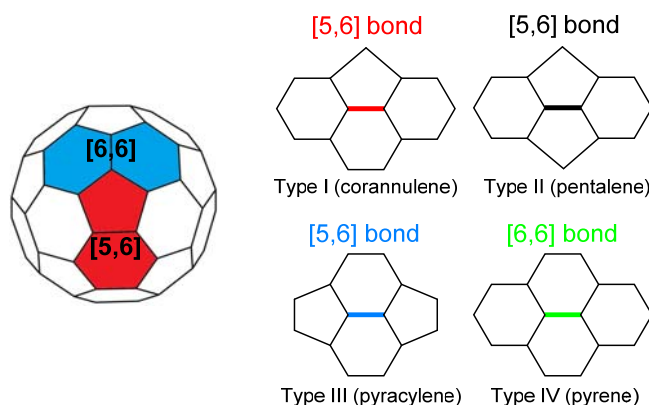
Figure 12. Representation of some of the different types of bond in fullerenes.

Garcia-Borràs's doctoral thesis[87] included many works where the aromaticity plays a significant role in determining the reactivity and regioselectivity as well as stability of fullerenes. In this section we briefly discuss two representative studies to highlight the importance of aromaticity in fullerene reactivity.

Diels-Alder reaction

In 2013, Garcia-Borràs *et al.*[88] studied the aromaticity of the successive electron additions in C_{60} and its role in the reactivity. This work has an important impact on the fullerene reactivity of the Diels-Alder (DA) reaction between C_{60}^n (n=0, -1…, -6) as a dienophile and cyclopentadienyl as a diene. C_{60} follows the IPR and consequently has two types of bonds, the [5,6] and [6,6] bonds.

So basically the cycloaddition is a regioselective process because the reaction can occur either on the [5,6] or on the [6,6] bonds. Besides, it is well-known that dienophiles tend to react on the [6,6] bond of an empty fullerene because it is thermodynamically more favored than the [5,6] attack.[88] Yet, they saw that if they put electrons to the system then the regioselectivity of the DA reaction is significantly changed and the reaction takes place preferably on the [5,6] bond instead of [6,6] bond. The aromatic character was evaluated in terms of MCI (see 2.3.1 for more details). According to the analysis of aromaticity, the change of the reactivity is attributed to the strong aromatic character of the 5-MRs when the electron addition increases.
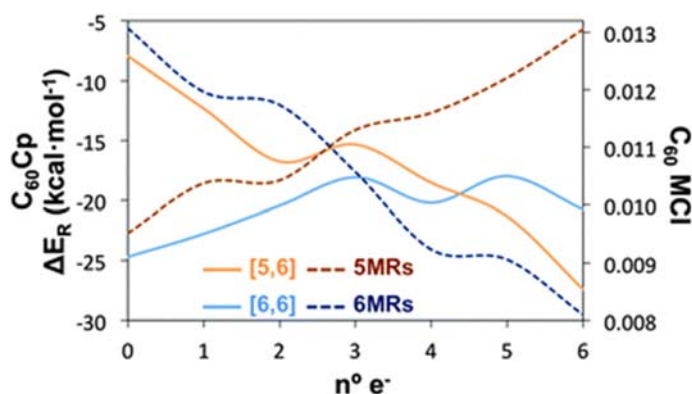
Figure 13. Schematic representation of the reaction energies (ΔE_R) for the DA addition of cyclopentadiene (Cp) to the [6,6] and [5,6] bonds of C_{60} and MCI values (dashed lines) of the 5-MRs and 6-MRs in C_{60}^n when the charge *n* changes. Reproduced with permission from reference [88].

Stability of Bingel-Hirsch monoadducts by homoaromaticity

The Bingel-Hirsch (BH) reaction, a [2+1] cycloaddition reaction,[89] between bromomalonate and fullerenes or endohedral metallofullerenes (EMFs) was shown to be a very powerful and versatile tool for functionalizing EMFs in a rapid and efficient manner.[90] In the first step, the

bromomalonate carbanion (which is an enolate formed through deprotonation by the presence of a strong base) attacks the fullerene cage *via* nucleophilic addition in a barrierless process. During the second step, a cyclopropane ring closure takes place when the newly generated carbanion on the fullerene cage displaces the bromine anion in an intramolecular nucleophilic substitution (Figure 14).
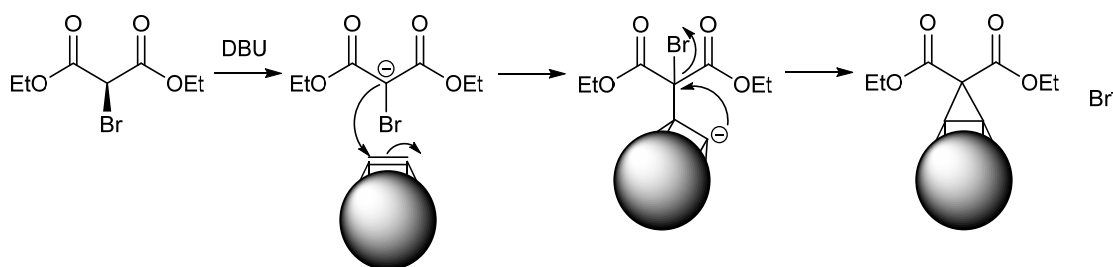
Figure 14. Bingel-Hirsch reaction mechanism. Adapted from reference [91].

In 2013, Garcia-Borràs *et al.* reported that there exists a direct relationship between the stabilities of the BH monoadducts and their degree of aromaticity.[91,92] Considering that the main driving force that determines the most stable isomeric cage is the aromatic character, Garcia-Borràs and coworkers defined the Maximum ARomaticity Criterion (MARC)[93] which states that the most stable anionic fullerene isomer is the one whose total aromaticity is maximized. Yet, the authors demonstrated that the MARC also applies for the BH monoadducts thermodynamic stabilities (*i.e.* "the most aromatic adduct = the most stable").[92]
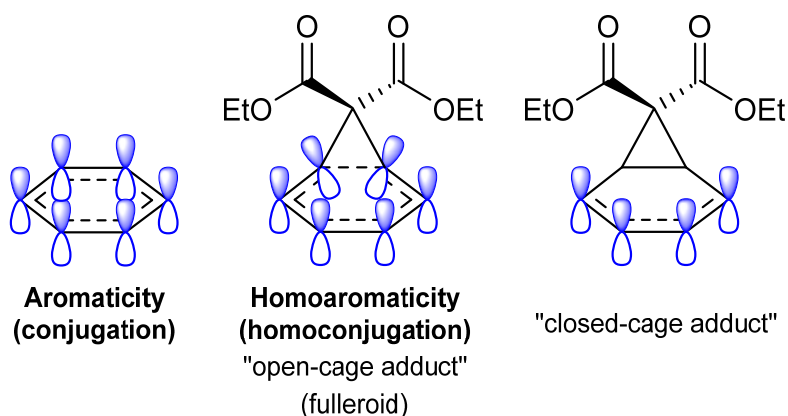
Figure 15. Schematic representation of aromaticity and homoaromaticity.

Previous studies proved that, in some cases, the addition to a certain C–C bond of a fullerene led to the breaking of the attacked C–C bond and the formation of adducts called fulleroids with an open bond on the surface of the cage that are more stable than their closed bond

counterparts.[94] Actually, in the open-cage structures, all carbon cage atoms kept their sp^2 hybridization (Figure 15) forming homoaromatic rings (homofullerenes). At this point, it is worth mentioning that, Winstein[95] was the first scientist that introduced the concept of homoaromaticity when he was studying the tris-homocyclopropenyl cation. He suggested that even though the continuous π-electron conjugation in a ring is interrupted by the presence of a single sp^3 hybridized atom, this discontinuity is bridged by the p-orbital overlap to keep a continuous delocalization of π-electrons that confers an extra stability to the system. Regarding the previous study,[92] the Additive Local Aromaticity (ALA) index (see section 1.6.4 for more details) pointed out that the aromaticity enhanced by the presence of these homoaromatic rings in the BH adducts was responsible for the better stabilization of the open-cage fulleroids in contrast to the closed-cage adducts, where the hybridization of the attacked carbon atoms changed towards sp^3 without allowing π-electron delocalization.[92,93]

1.5 Metalloaromaticity

The concept of metalloaromaticity was used to describe cyclic species with at least one metal atom in the ring where the aromatic character has an important role in their stability. Since the aromaticity of organic compounds is always associated with highly delocalized electrons, that concept can be used to characterize also metalloaromatic species. At the moment, many types of metalloaromatic compounds have been discovered. In this section, first we will walk through the beginnings of metalloaromaticity by exploring in detail its role in the stabilization of alkali and alkaline earth metal clusters, inorganic metal clusters, as well as transition metal-based clusters.

1.5.1 Beginnings of metalloaromaticity

The chelatoaromaticity concept, which was introduced by Calvin and Wilson[12] in 1945, was used to explain the stability of Cu(II)-1,3-diketonate complexes (**A**, Figure 16). Later this concept was replaced by metalloaromaticity as a general term that refers to any cyclic system that involves at least one (or more) metal atoms. Actually, the concept of metalloaromaticity was employed for the first time to describe cyclobutadienemetal complexes.[22] Then, Thorn and Hoffmann[23] predicted computationally the existence of metallacyclopentadienes and metallabenzenes. The latter systems refer to analogues of cyclopentadiene and benzene, respectively, where one (or more) of the CH groups is replaced by a transition metal.

However, it was not proved till 1982 when Roper *et al.* synthetized the first metallabenzene,[96] an osmabenzene (**B**, Figure 16), and that opened the doors to extending the concept of metalloaromaticity to more intricate systems.
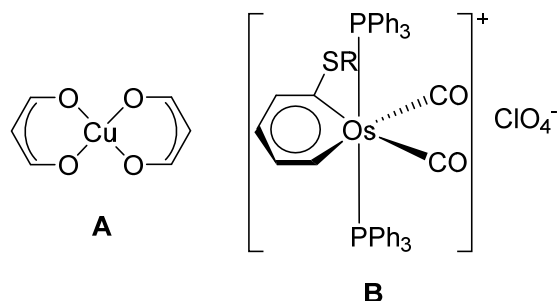
Figure 16. Molecular structure of Cu(II)-1,3-diketonate complex (**A**) and osmabenzene derivatives (R=H, Me) (**B**).

1.5.2 Aromaticity in inorganic metal clusters

The Bi_5^- cluster or the Ga_3 triangular unit of $Na_2[[(2,4,6-Me_3C_6H_2)_2C_6H_3]Ga]_3$ (Figure 17) were the first all-metal clusters that were studied from the aromaticity point of view to interpret their properties and chemical bonding features.[97,98] Nonetheless, the first pure all-metal cluster was not proposed till 2001.[29]
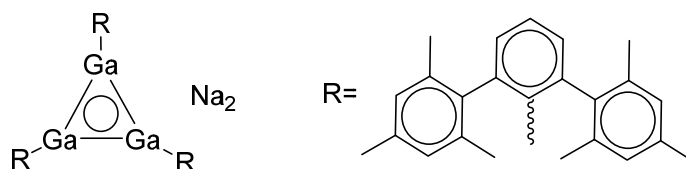
Figure 17. Molecular structure of $Na_2[[(2,4,6-Me_3C_6H_2)_2C_6H_3]Ga]_3$.

In 2001, Wang and coworkers were the first to broad the concept of metalloaromaticity into all-metal clusters. By experimental (photoelectron spectroscopy) and theoretical studies (*ab initio* calculations), they were able to find the first evidence of aromaticity in MAl_4^- clusters (M = Cu, Li, Na).[29] In addition to this, they also found that the global minimum adopts a square pyramidal geometry where the M^+ cation is coordinated to a square planar Al_4^{2-} unit. The aromatic character of these clusters was revealed by analyzing the MOs. The Al_4^{2-} unit has seven valence MOs where four are linear combination of 3s orbitals on each of the aluminum atoms, two are σ-delocalized and the last one is π-delocalized. Thus, the presence of only one π occupied MO was indicative of aromaticity according to Hückel's rule.

Interestingly, Wang and collaborators also extended the study to the heterocyclic 4-MR all-metal systems, XAl_3^- (X = Si, Ge, Sn, Pb), in which their stability is ruled fundamentally by the π-electron delocalization if the electronegativity of X is similar, and thus all of them present aromatic properties.[99]

Yet, the σ-delocalization that was observed in the MOs of Al_4^{2-} triggered a new concept: the σ-aromaticity. Actually, it was Dewar who used for the first time the term σ-aromaticity to describe the σ-conjugation in alkanes (or historically named paraffins).[24,100] σ-aromaticity (σ-tangential and σ-radial) became an important concept to take into account when one describes the chemical bonding of metal clusters like Al_4^{2-} as well as valence isoelectronic Hg_4^{6-}, Ga_4^{2-} and In_4^{2-}.[101,102] Conceptually, radial MOs are composed of orbitals directed towards the center of the cyclic structure (formed by p_σ-radial atomic orbitals (AOs)), while tangential MOs are composed of orbitals that are perpendicular to the radial ones (formed by p_σ-tangential AOs) (Scheme 2).
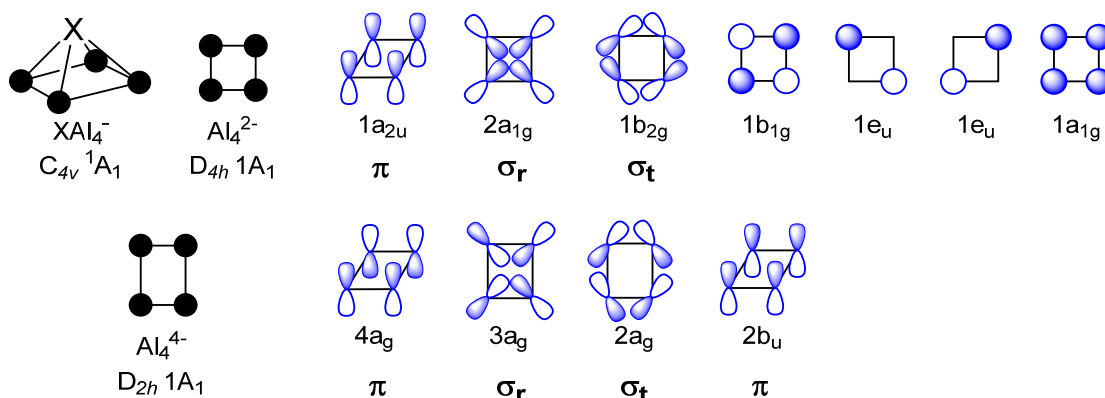
Scheme 2. Schematic structures of XAl_4^- (X=Cu, Li, Na), Al_4^{2-} and Al_4^{4-}, the MOs of Al_4^{2-} and the four HOMOs of Al_4^{4-}.

As we have seen before, the π-aromatic character in Al_4^{2-} comes from the occupied π-bonding MO according to the Hückel's rule. Applying the same rule individually to the σ-tangential and radial MOs, we obtain that these MOs are also aromatic. Particularly, two electrons on the radial MO make this cluster σ_r-aromatic and, on the other hand, two electrons on the tangential MO make it σ_t-aromatic. So this cluster is an example of double (σ_r, σ_t and π) aromaticity. Actually, at first, Fowler and coworkers assessed the ring current in Al_4^{2-} and MAl_4^- and concluded that σ-electrons are responsible for the diamagnetic ring current.[103] But then, Sundholm and co-workers concluded that π-electrons also contribute to diatropic ring current as well, and therefore those molecules are considered both σ- and π-

aromatic.[104] Besides, Boldyrev and Kuznetsov confirmed that the presence of one π-bond and two σ-bonds implicates a high resonance energies for Na_2Al_4 and Na_2Ga_4 and that was in fact indicative of σ- and π-aromaticity fingerprint.[105]

The fact that Al_4^{2-} is σ- and π-aromatic is clear, but occasionally conflicting aromaticity could occur in certain species. That is the case of Al_4^{4+}. This species has two σ MOs, a π-bonding MO and an occupied π-antibonding orbital because of the presence of two extra electrons in the system that Al_4^{2-} did not possess. So this is an example of conflicting aromaticity because, according to the Hückel's rule, Al_4^{4+} would be σ-aromatic, as it has two σ_t–electrons and two σ_r–electrons, and π-antiaromatic with four π-electrons.[106] This conflict appears because, in comparison with Al_4^{2-}, the D_{4h} symmetry is lost leading to a less symmetrical structure (D_{2h}) due to the involvement of an occupied π-antibonding orbital. However, the aromaticity comes mainly from the σ-MOs.

1.5.3 Aromaticity in alkali and alkaline earth metal clusters

In general, alkali metal M_3^+ clusters (M=Li, Na, K, Rb, Cs) are well-known for presenting σ-aromaticity, while M_3^- clusters (M=Li, Na, K, Rb, Cs) are considered σ antiaromatic. Alexandrova and co-workers were the first researchers that extended the aromaticity concept to σ-aromatic alkali metals as well as alkali earth metal clusters. In their study, they assessed the aromatic character of Li_3^+ and Li_3^- to explain their relative stability.[107]

In particular, the D_{3h} Li_3^+ structure ($1a_1^{'2}$) has two σ-electrons and therefore it satisfies the Hückel's rule. Therefore, only one σ delocalized bonding orbital makes this cluster aromatic. In addition to this, even though current density maps showed that σ-aromaticity on Li_3^+ does not exist, magnetic indicators and the fulfillment of the $4n+2$ rule indicated that the metal cluster is σ-aromatic.[108]
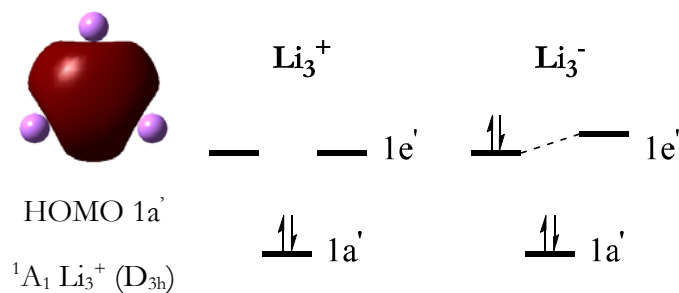
Figure 18. HOMO of the Li_3^+ cation and schematic MOs of Li_3^+ cation and Li_3^- anion (D_{3h}). Isosurface value at 0.03 a.u.

Contrarily, M_3^- (M=Li, Na, K, Rb, Cs) anions, which have a $1a'^2 1e'^2$ configuration at the D_{3h} symmetry, are hypothetic examples of σ antiaromatic cluster due to the four σ-electrons.[107] As it can be seen in Figure 18, adding two electrons to the Li_3^+ means that one degenerated orbital (1e') must be filled. So the degeneracy of the 1e' orbitals is broken and therefore their triangular structures undergo a Jahn–Teller distortion. Indeed, that explains its instability and why it is not a minimum in the D_{3h} symmetry. If we let this molecule relax then we obtain a linear Li_3^- structure $(D_{\infty h})$[109] with two valence MOs that can be localized into two 2c-2e bonds. Actually, this behavior is similar to the antiaromatic CBD.

Regarding to the aromaticity of alkali earth metal clusters, Solà and collaborators[110] found that the singlet state of the isolated *cyclo*-$[Mg_3]^{2-}$ unit (with D_{3h} symmetry) also has exclusively σ-aromaticity (Figure 19). Yet, Kuznetsov and Boldyrev[111] found that this σ-aromaticity of this unit is lost in $NaMg_3^-$ and Na_2Mg_3 because it has a pair of π-electrons which gives π-aromaticity to this cluster without formation of the σ-framework (Figure 19). Therefore, it seems that the interaction of Na^+ with that unit triggers off an unprecedented shift from the σ-aromatic cluster to π-aromatic species, $NaMg_3^-$ and Na_2Mg_3.[112,113]

Mg_3^{2-} $NaMg_3^-$ Na_2Mg_3
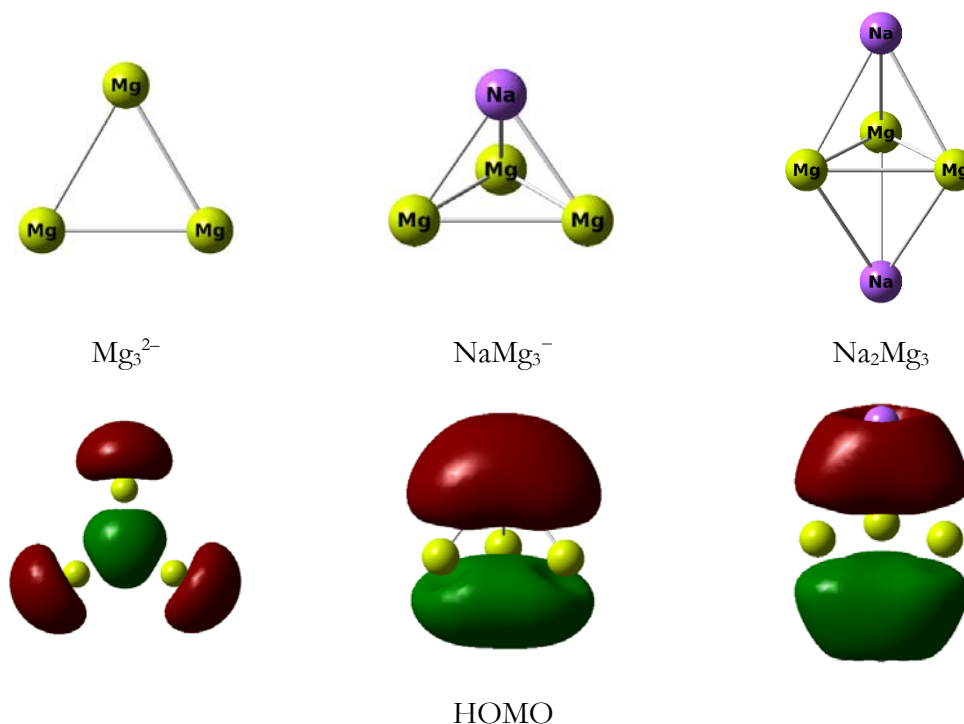
HOMO

Figure 19. Molecular structures and HOMOs of Mg_3^{2-}, $NaMg_3^-$ and Na_2Mg_3 species. Isosurface value at 0.03 a.u.

1.5.4 Aromaticity in transition metal clusters

As we have mentioned above, the metalloaromaticity of all-metal clusters based on inorganic, alkali or alkali earth atoms is attributed to either s- or p-AOs. Yet, when a system involves transition metal atoms, apart from s and p orbitals, d orbitals may trigger aromatic character as well.

By means of computational and experimental studies, Huang and collaborators[35] reported for the first time evidence of d-orbital aromaticity in two early 4d and 5d transition metal oxide clusters, that is $M_3O_9^-$ and $M_3O_9^{2-}$ (M=Mo, W). $M_3O_9^-$ and $M_3O_9^{2-}$ possess one (anionic) and two (dianionic) extra electrons, respectively, that are responsible for direct metal-metal bonding, assuming that the oxidation state of oxygen is -2. The HOMO presents a completely bonding situation with a three-center σ-bond formed by in-plane d-AOs of the metal (Figure 20). So because of the fact that these metal clusters have HOMOs that are σ-delocalized and formed from d-orbitals of transition metals, they have been described as the first d-orbital-based σ-aromatic species. Yet, d-orbital-based double (σ and π) aromaticity can also be present in systems like X_3^- (X=Sc, Y, La) clusters.[114,115]
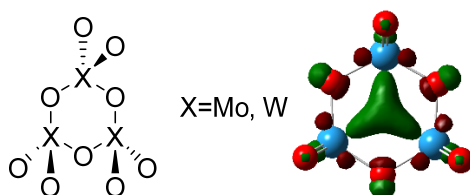
Figure 20. Molecular structure of M_3O_9 and HOMO of $[W_3O_9]^-$. Isosurface obtained at 0.07 a.u. and geometry obtained from reference [35].

δ-aromaticity can also be present in transition metal cluster and basically it comes from delocalized orbitals with δ-symmetry. The first example of δ-aromaticity was reported by Zhai and collaborators[36] in $Ta_3O_3^-$ which has a closed-shell D_{3h} structure (Figure 21). If we assign the oxidation state -2 to oxygen, the formal oxidation of Ta is 1.66 and we get ten electrons that are responsible for the direct metal-metal bonding. The five MOs responsible for

Figure 21. Molecular structure of $Ta_3O_3^-$.

the delocalized metal-metal bonding can be classified in σ-, π- and δ-MOs. Yet, the delocalized σ-bonding is canceled as the doubly degenerate bonding/antibonding-HOMO (4e') and bonding-MO (3a₁') are completely occupied. So the bonding character of 3a₁' is

canceled by the antibonding nature of 4e'. Besides, the MO diagram (Figure 22) shows a completely bonding δ-MO (4a₁') and π-MO (2a₂") and that is indicative of the presence of double (δ and π) aromaticity according to the Hückel's rule in the cyclic systems with $n=0$, applied separately to δ- and π-electrons.
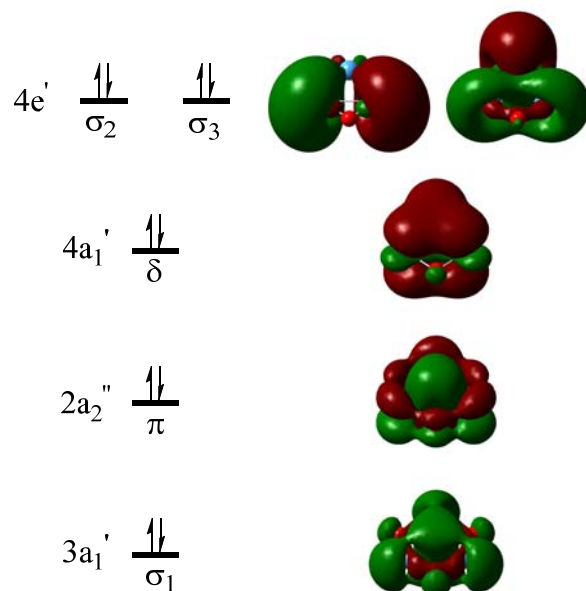
Figure 22. MOs of $Ta_3O_3^-$. Isosurfaces obtained at 0.018 a.u. and geometry obtained from reference [36].

Three-fold (σ, π, δ) aromaticity was detected for the first time in the Hf_3 cluster which adopts a D$_{3h}$ structure (Figure 23).[37] This system has three 2c-2e Hf-Hf σ-bonds formed of hybrid 6s- and 5d-MOs and three completely delocalized bonds formed of pure d-AOs (Figure 24): one bonding 3c-2e d-radial-based σ-bond responsible for the presence of σ-aromaticity, one bonding 3c-2e d-radial-based π-bond responsible for the presence of π-aromaticity and one bonding 3c-2e d-AO-based δ-bond responsible for the presence of δ-aromaticity (for each kind of aromaticity, the $4n+2$ rule is followed). It is worth highlighting that the triple aromaticity is consistent with the bond equalization and high symmetry of Hf_3.
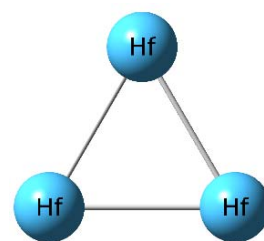
Figure 23. Molecular structure of Hf_3.
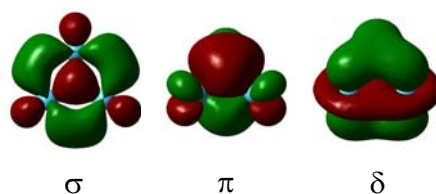
Figure 24. Representative MOs of Hf_3. Isosurfaces obtained at 0.02 a.u. and geometry obtained from reference [37].

1.5.5 Three-dimensional aromaticity

The *closo* borohydride $B_{10}H_{10}^{2-}$ (Figure 25) [116,117] as well as derivatives of closo-dodecaborate and closo-decaborate[118,119] were indeed the first inorganic clusters that expanded the concept of aromaticity from two to three dimensions. Wade proposed several empirical rules, which had a theoretical interpretation by MO theory, and were based on connecting the structure with the number of electrons in polyhedral boranes. At this point, the term *three dimensional aromaticity* appeared, analogous to Hückel aromaticity. For instance,
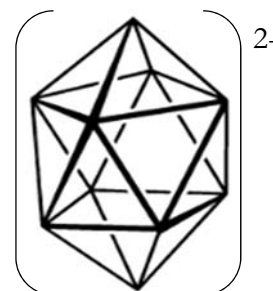
Figure 25. Molecular structure of $B_{10}H_{10}^{2-}$.

closo borohydride clusters with the formula $[B_nH_n]^{2-}$ that follow either Wade's $2n+2$ electron rule,[15,16] where *n* is the number of vertexes of the polyhedron, or Mingo's $4n+2$ rule,[17,18] are considered aromatic systems. Both rules are equivalent. In particular, Wade's rule states to the skeletal electrons (all valence electrons except those of the B–H bonds), while Mingo's rule incorporates also the exo electrons corresponding to the B–H bonds, thus referring to the total number of valence electrons. In 1978, Aihara presented a theoretical basis for the concept of three-dimensional aromaticity of polyhedral boranes.[21] And quite recently, a relationship between the $4n+2$ Hückel's and Wade-Mingo's rules was established.[120] Even more recently, the cubic aromaticity has been described as a new form of 3D aromaticity (Zn^I_8) and the $6n+2$ rule (with $n=1$ for Zn^I_8) was proposed for this type of 3D aromaticity.[121]

1.5.6 Recent research about metalloaromaticity

Currently, metalloaromaticity is really progressing. Major advances have been made to understand the chemical bonding, structure and fluxionality of several large planar boron clusters where the (anti)aromaticity plays a significant role.[122]

The doubly σ- and π- aromatic B_9^- cluster,[123] the aromatic B_{16}^{2-} and B_{17}^- clusters[124,125] with ten π-electrons analogues to the well-known aromatic naphthalene, the antiaromatic B_{16} cluster with eight π-electrons,[126] or the concentric double π-aromatic B_{19}^- cluster[127] with a spider-web-like structure, are some examples of large planar boron systems. Particularly, the double π-aromaticity of the latter case comes from the fact that two concentric delocalized π systems are detected and besides, each of the two π systems obeyed the $4n+2$ rule. Thus, the B_{19}^- cluster was considered to be a concentric doubly π-aromatic species.[127]

Aromatic borometallic molecular wheels[128] are another potential and novel compounds. An electronic design principle for metal-centered boron wheels with different ring sizes, $M^{(x)}@B_n^{k-}$, has been proposed. It is also demonstrated that, if the valence of M (x) and the ring size satisfy the equation, $x+n+k=12$, the boron wheel should be a stable electronic system with double aromaticity. Based on this principle, Boldyrev and coworkers have synthesized and characterized a series of transition metal centered molecular wheels for $n=8$–10.[129–132] For instance, $Co@B_8^-$ and $Ru@B_9^-$ are two metal-centered monocyclic boron rings which present double (π,σ) aromaticity.[129]

One of the most recent advances is the application of this concept to solid-state compounds. In this section we discuss briefly two recent and interesting works regarding the previous application.

<u>π-antiaromatic all-metal clusters</u>

The synthesis of solid-state compounds with antiaromatic building blocks has been a challenge because of their low stability and high reactivity. Yet, Min and coworkers[133] synthetized and structurally identified the first π-antiaromatic all-metal systems in solid state, $[Ln(\eta^4\text{-}Sb_4)_3]^{3-}$ (Ln=La, Y, Ho, Er, Lu). These metal clusters adopt a quasi-D_{3h} symmetry where the lanthanide atom is coordinated to three Sb_4 rhombic units (ligands). At first glance, this system has a positive charge +3 on Ln which would lead to negative charge -2 on each *cyclo*-Sb_4 unit. The peculiarity of these systems is that the *cyclo*-Sb_4 unit possesses a rhombic structure which is a direct consequence of its antiaromaticity due to their four π-electrons.
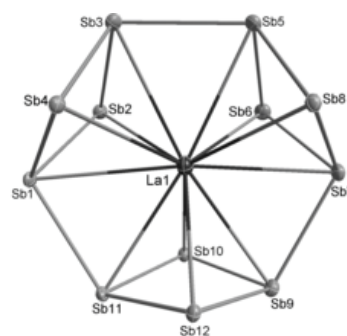
Figure 26. Molecular structure of $[Ln(\eta^4\text{-}Sb_4)_3]^{3-}$. Reproduced with permission from reference [133].

Tsipis[134] demonstrated on the basis of NICS indices that the Sb_4^{2-} dianion is antiaromatic. Additionally, the multicenter indices calculations (see section 2.3.1 for more details), which were previously shown to give excellent results for all-metal compounds,[106] revealed strong similitude with CBD, thus confirming the antiaromatic character of the Sb_4 units.[133] In fact, the coordination of the three Sb_4^{2-} units with the Ln^{3+} ion drastically reduces the aromaticity of the Sb_4 fragments and gives values of multicenter indices that are very close to those of the antiaromatic CBD.

σ-aromatic solid-state all-metal clusters

Among all the all-metal aromatic fragments that have been synthesized in the solid state up to date, there were only two delocalized electrons responsible for the σ-aromaticity of the compounds, as exemplified by the cases of Au_3^+,[135] $TiSn_2$,[136] and Pd_3^+ [137] clusters. However, in 2016 Popov *et al.*[138] isolated the first solid-state all-metal cluster $[Au_2Sb_{16}]^{4-}$ as a stable $[K([2.2.2]crypt)]^+$ salt, that contains two all-metal
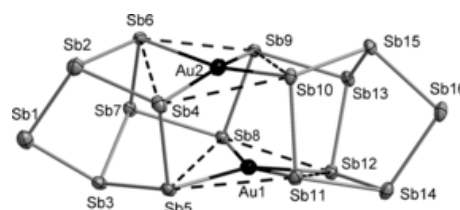
Figure 27. Molecular structure of $[Au_2Sb_{16}]^{4-}$. Reproduced with permission from reference [138].

aromatic $AuSb_4$ fragments with six delocalized σ-electrons each (*n*=1 according to the 4*n*+2 rule). The quasi-planarity of these two $AuSb_4$ fragments is quite peculiar because they do not have equal Sb–Sb bond lengths as expected for aromatic systems. In order to test the importance of aromaticity in $[Au_2Sb_{16}]^{4-}$, electronic multicenter indices have been computed and proved that the two quasi-planar $AuSb_4$ moieties in $[Au_2Sb_{16}]^{4-}$ are indeed σ-aromatic due to the high delocalization of the Au atom with four neighboring Sb atoms.

Hence, the 6 σ-electron aromatic fragments found in the $[Au_2Sb_{16}]^{4-}$ cluster in this study expand the family of storable aromatic metal clusters thus strengthening usefulness of the σ-aromaticity concept in the solid state.

1.6 How to recognize aromaticity and antiaromaticity in organic compounds?

Rules of aromaticity are significantly useful to initially classify a compound as aromatic or not. But as we have shown above, they present some limitations because of the variety of

aromatic molecules that exists. Up to now, it has not been found a single measure that clearly tells if a system is aromatic or not. However, the field of computational chemistry is continuously advancing and, in this way several aromaticity indicators to evaluate and demonstrate the aromaticity or antiaromaticity of a broad variety of compounds have been proposed. Here, we should emphasize that each of these aromatic indices follows a specific criteria based on the properties that present the aromatic molecules. In this section, we are going to discuss briefly the four most relevant criteria that can be used to assess local and global aromaticity.

1.6.1 Energetic criterion

Aromatic cyclic-conjugated molecules are more stable than their open-chain analogues, while antiaromatic cyclic-conjugated species are less stable. Therefore calculating the relative energy (thermodynamic stability) between them gives a measure of the stability of the cyclic-conjugated with respect to the acyclic analogue that can be linked to the aromatic character of the cyclic molecule.

Resonance energy was the first quantitative descriptor of aromaticity introduced by Pauling and Sherman.[11] This term gives us information about the relative stability of the aromatic system with respect to its olefinic analogue, which can be related with the aromatic character of the molecule. However, we must point out that sometimes the choice of the analogues can be difficult. Later, the use of the resonance energy as an aromaticity descriptor was replaced by the aromatic stabilization energy, ASE,[139] which is defined as a virtual (homodesmotic[140] or isodesmic[141]) reaction leading to products with the same number of CH bonds and atoms in the appropriate hybridization states. For instance, an example of a classical isodesmic (or bond separation) reaction for benzene would be,

$$3 \text{ H}_2\text{C}=\text{CH}_2 + 3 \text{ H}_3\text{C-CH}_3 \rightarrow \text{C}_6\text{H}_6 + 6 \text{ CH}_4$$

In this reaction, the number of the chemical bonds of each type (like carbon‑carbon formal single and double bonds) is the same on both sides of the reaction and the reaction energy (which would be the ASE) indicates the stabilization due to the aromaticity of benzene. However, the ASE values fluctuate depending on the computational method and the reference system that are used, which limits its applicability. The isomerization stabilization energy (ISE),[142] which is a way to obtain more reliable ASE, is measured as the difference

between the total energies calculated for a methyl derivative of an aromatic system and the corresponding nonaromatic exocyclic methylene isomer. In general, the ISE approach is independent of the isomers chosen. Besides from ASE and ISE, there is also an approach for the estimation of the aromaticity based on the energy decomposition analysis (EDA).[143]

1.6.2 Geometric criterion

The aromatic character of a ring can be related with the molecular geometry. The bond length between the atoms that form the ring has been the main parameter that researchers focused their attention. In principle, in aromatic systems, we do not expect to find bond length alternation between the bonded atoms of the ring but if it exists, it will not be very significant. In other words, this means that the bond equalization must be induced by the aromaticity of the system. Thus, any deviation from equalization (as well as planarity) makes the aromatic character of the molecule decrease. There are several geometry-based aromaticity indicators. The Julg index[144] and the harmonic oscillator model of the aromaticity (HOMA)[145,146] are some of them. The Julg index was the first quantitative approach to the definition of aromaticity based upon geometry. It is obtained from a normalized function of the C-C bond lengths variance in a perimeter of a cyclic π-electron system. HOMA is currently the most employed (see section 2.3.1 for more details). The harmonic oscillator stabilization energy (HOSE),[147,148] Bird's aromaticity indices I_5 and I_5,[149–151] the heat and formation from atoms estimated from molecular geometry (HtFfa)[151] or the harmonic oscillator model of electron delocalization (HOMED)[152] are other geometric-based indices.

1.6.3 Magnetic criterion

The magnetic criteria is based on the measure of the induced ring currents which are related with cyclic delocalization of electrons. These ring currents are related to magnetic properties. The relation of aromaticity with ring currents was introduced for the first time by Mallion.[153,154] The molecules with diamagnetic ring current are diatropic and those with a paramagnetic ring current are paratropic. A diatropic (paratropic) ring current is associated with aromaticity (antiaromaticity) and therefore, also with electronic delocalization (localization) (see section 2.3.3 for more details). Many descriptors have been proposed along the years that try to relate aromaticity with magnetic properties. In the past, NMR was probably the most direct (experimental) method to observe the effects of the ring currents.

In particular, one can measure ^{1}H NMR chemical shifts since it is known that chemical shifts for external protons in aromatic molecules are deshielded. ^{1}H NMR chemical shifts of ~7 ppm are attributed to "aromatic protons" while values of ~5 ppm and ~1 ppm are associated with olephinic and aliphatic protons, respectively. However, sometimes the frontier between aromatic and antiaromatic compounds is not clear. The main limitation of ^{1}H NMR chemical shifts is that we cannot measure them for all the molecules.

Nucleus–independent chemical shift (NICS), which is probably one of the most used measures of aromaticity nowadays, was introduced by Schleyer *et al.*[155] NICS is defined as the negative value of the absolute magnetic shielding usually computed at the geometric centers of aromatic or antiaromatic rings. The negative NICS value refers to aromaticity and positive NICS refers to antiaromaticity (see section 2.3.3 for more details). One of the advantages of this index is that it gives a clear separation among aromatic, antiaromatic and non-aromatic systems. However, the ring current strength is not properly evaluated by a single NICS calculation and in some cases this could lead to erroneous chemical interpretations.[156] In another words, the calculated NICS in a specific point of the molecule has more global sense than local. Stanger[157,158] and Jiménez-Halla and collaborators[159] developed a unique scheme of scanning the single NICS values (NICS scan) up to a certain distance from the ring center in order to explain the aromaticity/antiaromaticity in various systems. That tool gives us evidence of local and/or global aromaticity.

Current density maps are often used to analyze induced ring currents in aromatic and antiaromatic systems. The current density is a vector field obtained by calculating the current induced by an external magnetic field at each point in space. A magnetic field induces a current that follows the left hand rule. From the ring current maps, the diatropic and paratropic character of rings can be evaluated in both visual and numerical ways. Among many methods to compute and visualize ring currents, we highlight the anisotropy of the induced current density (ACID) plots developed by Herges *et al.*[160] and the continuous transformation of origin of current density-diamagnetic zero method, CTOCD-DZ,[161,162] provided by Fowler and coworkers.[103,163] Regarding numerical methods, it is worth mentioning the gauge-including magnetically induced current (GIMIC) methods designed by Sundholm and collaborators.[164,165]

ACID provides a measure of the anisotropy of the density of induced currents at each point in space. This quantity is visualized using the ACID function which is a scalar function

(similar to the electron density) that represents delocalization and does not depend neither on the magnitude nor the direction of the applied magnetic field. So this function only plots an isosurface around the molecule. Since the current density (vector field) is difficult to visualize over a 3D isosurface (a vector is assigned to each point in space), a reference plane in which the current vectors are projected is usually selected. The current densities provide exhaustive information about electron delocalization, degree of aromaticity, and electron-current and spin-current pathways in molecules. These currents are represented by arrows which are interpreted as mobile or delocalized electrons.[166] For instance, Figure 28b contains the ACID plot for benzene. In this particular case, currents follow the "left hand rule" and therefore they are diatropic (clockwise), which is characteristic of aromatic molecules. Yet, for antiaromatic molecules such as CBD the rule is not obeyed and therefore the currents are anticlockwise with respect to the direction of the external magnetic field (Figure 28c).
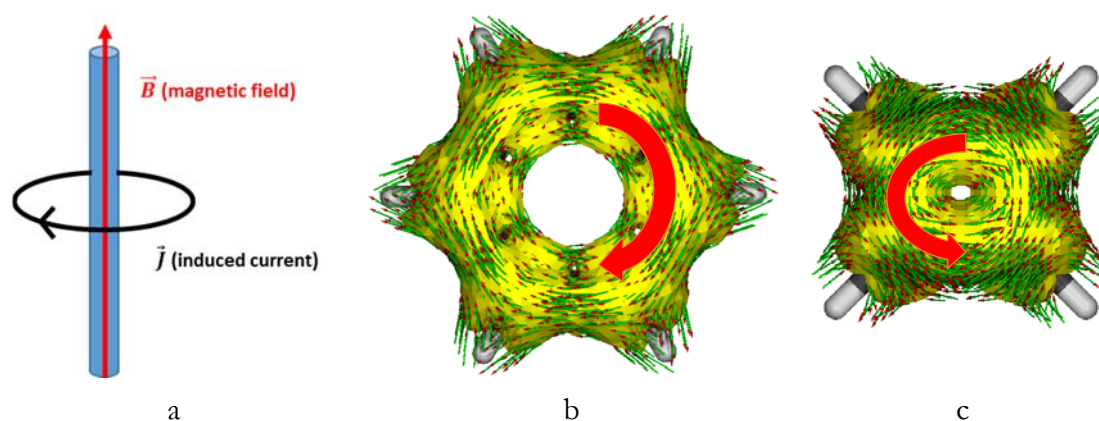
Figure 28. a) The left hand rule for determining the direction of the induced current. b) and c) Isosurface (yellow, 0.05) and current density vectors (green lines) calculated by ACID for benzene (b) and CBD (c).

CTOCD-DZ[161,162] is another qualitative method to obtain current density maps as well as current strengths in aromatic systems. The main limitation of this method is that the current densities can be only calculated at coupled Hartree-Fock (CHF) and Density Functional Theory (DFT) methods while current strengths can only be obtained at CHF level of theory.

The GIMIC method[164,165] is used for calculating magnetically induced current and spin-current densities in molecules. As opposed to ACID and CTOCD-DZ methods, GIMIC is quantitative in the sense that one obtains quantitative values for the induced rings, by numerical integration of the current flow.

1.6.4 Electronic criterion

The aromatic character is strongly connected to the electronic structure of the system. From the very beginnings, measures like the electrostatic potential or the polarizability, were used as electronic-based indicators of aromaticity.[167] Yet, the degree of electron localization and delocalization is considered a relevant electronic measure to quantify the aromatic character as well as the conjugation and hyperconjugation in order to explain the structure, stability and reactivity of a system. Nowadays, the scope of electronic descriptors is large[168–171] and it is a field in constant progression. Here we are going to mention and describe briefly only the most widely used indices. Descriptors of electron localization and delocalization can be classified in three groups: those obtained from a wavefunction, those constructed directly from the electron density and those derived from first- and higher-order density matrices.

In the first group, among the several electron delocalization descriptors, we have to mention the ones that are used for the recognition of localized bonds and lone pairs using the MO theory. This information can be obtained by natural bond orbital (NBO) analysis.[172,173] Similarly, the adaptive natural density partitioning (AdNDP) method[174,175] is used for obtaining patterns of chemical bonding which represents the electronic structure in terms of n-center 2-electrons (nc-2e) bonds. Even more recently, Alcoba and co-workers developed a method based on electron localization function[176] which localizes the MOs in regions that have the highest probability for finding a pair of electron (ELF-LOC).[177–179]

In the second group of delocalization indicators based on the analysis of the electron density, we have the Laplacian of the electron density $(\nabla^2\rho(\boldsymbol{r}))$[180,181] or the noncovalent interaction index (NCI),[182] among others.

The third group gathers a large number of electron delocalization descriptors. Actually, this high number of indicators is attributed to the fact that the identification of electron pairs involves two spatial coordinates and, thus, methods based on functions of two (or more) electronic positions such as the first-order density matrix and the two-electron density or pair density are more suitable to analyze electron localization and delocalization than the electron density. Here we are going to only pay attention to the electron sharing indices (ESIs) that are obtained from the pair-density. ESIs inform us about the electrons shared between two different atoms or groups of atoms. Therefore, the definition of ESI can be generalized to describe delocalization between two atoms or multicenter delocalization. The

localization and delocalization index (LI and DI),[183–185] I_{ring}[186] and its normalized version (I_{NG}), the multicenter index (MCI)[187] and its normalized version (I_{NB}), the *para*-delocalization index (PDI),[188] or the aromatic fluctuation index (FLU),[189] are some of the ESIs that have been developed and applied to discern between aromatic and antiaromatic molecules.

1.6.4.1 Quantification of aromaticity in fullerenes

Fullerenes are based on different types of rings and, therefore, depending on how these are connected, we can have different isomers. To discuss the aromaticity of these isomers, one strategy is to measure the aromaticity of these isomers locally using electronic descriptors. Then, to quantify the global aromaticity of fullerene isomers, one can use the Additive Local Aromaticity (ALA) index,[190] which is defined as the sum of the local aromaticity of all the rings:

$$ALA = \sum_{i=1}^{n} A_i$$

where A_i is the local aromaticity of ring i and n is the total number of rings in the fullerene including 5- and 6-MRs. Electronic as well as geometric indices can be used to compute the local aromaticity of the rings. If the aim is to compare fullerenes of different sizes, then it is advisable to use the normalized ALA index (ALA$_N$) given as,

$$ALA_N = \frac{1}{n}\sum_{i=1}^{n} A_i$$

where n is the number of rings of the fullerene structure.[191]

1.7 Measuring metalloaromaticity

The descriptors of aromaticity we have commented before are mainly applied to organic compounds where the aromaticity fingerprint comes from π-electron delocalization. Yet, can we use the same descriptors to evaluate metalloaromaticity? For instance, if we compare an organic molecule like benzene with a metal cluster such as Al_4^{2-}, we will see that both molecules share a large list of similar properties: geometrically, both are planar and present bond equalization; magnetically, both present a ring current and magnetic susceptibility; and electronically, both cases present a high electron delocalization. Nonetheless, as we have

mentioned before, metalloaromaticity is not always based only on π-electron delocalization, but also σ- or δ- delocalization could be present. So it is important to find descriptors that are able to distinguish the different types of delocalization in metal-based molecules.

First it is worth mentioning that not all the methods designed to measure the aromaticity of organic compounds, can be used to measure metalloaromaticity. In this section we concisely discuss the possibility of applying the most popular descriptors to metalloaromatic systems as well as the advantages and drawbacks of each index.

Energetic descriptors of metalloaromaticity

Energetic-based indicators like ASE are difficult to compute in metalloaromatic species due to the lack of appropriate reference systems.[192] In 2012, Frenking and Hopffgarten developed a tool that evaluates the interaction between different fragments based on the energy decomposition analysis (EDA)[193] (see section 2.4 for more details). Initially, this method was applied to assess conjugation and hyperconjugation effects, to study metal–ligand interactions, or to describe the nature of multiple metal–metal bonding.[193,194] But recently it has found interesting applications in the field of aromaticity. Among other applications it has been used to compute ASE for studying aromaticity in metallabenzenes,[195] or to analyze the propensity of σ- and π-electrons to localize or delocalize in archetypical X_4^{2-} (Al, B, Ga) aromatic clusters.[196]

Geometric descriptors of metalloaromaticity

HOMA is the most used geometric descriptor but its definition depends on reference values, mostly bond lengths that are derived from organic compounds. So if we want to apply this index to metals, then we must redefine these references values.

Magnetic descriptors of metalloaromaticity

The NICS index is the most popular among the magnetic descriptors because it can be applied to a broad range of different systems. The best method to analyze the multifold aromaticity in metal compounds is provided by the NICS contribution of each canonical molecular orbital (CMO)-NICS that allows the decomposition of NICS into σ- and π-orbital contributions (see section 2.3.3 for more details).[197] Yet, as we have mentioned before, a

single point NICS value is not fully reliable.[156] Besides, it is said that NICS and induced magnetic field are strongly influenced by the relativistic corrections especially in spherical metalloaromatic systems based on heavy atoms.[198] So we must take into account this effect to avoid erroneous predictions of the electron delocalization.

ACID, GIMIC and CTOCD-DZ, which have been discussed above, can be applied to inorganic systems and metal clusters as well. With regard to the CTOCD-DZ method, it is worth highlighting that Tauber and collaborators[199] have shown that the inclusion of dynamic correlation must be considered and it is important for obtaining current strengths for inorganic open-shell systems.

<u>Electronic descriptors of metalloaromaticity</u>

Boldyrev *et al.* proposed the AdNDP method,[174] which allows to reconcile a localized bonding with a delocalized one in one molecular method. Basically, this method is an extension of the NBO analysis developed by Weinhold.[172,200]

With regard to ESIs, descriptors such as FLU or the bond order index of aromaticity (BOIA)[187] cannot be employed in metal compounds without redefining the reference values on which their definitions depend. However, I_{ring} and MCI are good options to measure the electron delocalization among the members of the ring of metal compounds.[106] Interestingly, MCI can be exactly splitted into σ- and π- contributions providing an easy way to evaluate the multifolding aromaticity. However, the separation is not strictly exact in δ-aromatic systems, which is only present in metal transition compounds, due to the overlap between σ- and δ-orbitals.[106]

CHAPTER 2:

METHODOLOGY

2.1 Atoms in molecules (AIM)

It is important to characterize the role of each atom that forms a molecule because it allows describing its electronic structure and molecular properties. Thus, it is important to define an atom in a molecule (AIM). To characterize atoms inside a molecule we should partition the molecular space into atomic regions. To this end, a well-defined method to subdivide the atoms in a molecule is required. An atomic partition provides the means to define atomic properties, *i.e.* partial charges that can be used to (chemically) rationalize the electronic structure of a given molecule. There are two ways to partition the molecular space into atoms: a) by partitioning the Hilbert space (the mathematical space where the wavefunction is defined) or b) by partitioning the real 3D space that the molecular structure occupies. It is worth mentioning that it is important to know the limitations and the drawbacks of each partition scheme.

When a molecule is split atomically through a Hilbert space partition, the atom in a molecule is defined as a set of atomic functions centered over that atom. Then, to obtain the atomic contributions to a certain property, the atomic property must be computed for the set of basis functions that correspond to each atom. The Mulliken population analysis[201] is the most common Hilbert-space based partition because it is available for any *ab initio* calculation provided by most of the current computational programs. Even though this partitioning method allows to easily obtain properties such as the atomic populations due to its low computational cost, it is highly basis-set dependent.

The real 3D space partition methods are based on assigning every three-dimensional point of the real space to a particular atom. The methods can be gathered into two groups depending on the definition of the boundaries of the regions. In the first group, we have the

ones that possess sharp boundaries like the Electron Localization Function (ELF)[202] or the Quantum Theory of Atoms in Molecules (QTAIM)[180] method (see section 2.1.1), which is described in the next section. The second group is based on partitioning methods that make use of fuzzy schemes. These fuzzy schemes do not have sharp boundaries and exhibit a continuous transition from one region to another. The most popular definition is the *fuzzy atom*,[203,204] proposed by Salvador and Mayer which will also be described in the following sections.

2.1.1 Quantum theory of atoms in molecules

The quantum theory of atoms in molecules (QTAIM) was introduced by Richard F. W. Bader.[180] This theory uses the electron density to partition the molecular space because it is able to explain the behavior and the distribution of the electrons in a molecule. So the only robust way to deal with the electron density is by using quantum mechanics. The AIM within QTAIM is a quantum subsystem which is a bounded region (open system) that interacts with others and can be obtained from the topological division of the electronic distribution of the density. Thus, QTAIM defines precisely the properties of the atoms (such as the atomic energies and the atomic charges) and chemical bonds that are linked in a molecule in terms of electron density (Figure 29 shows the shape of the electron density in benzene). These molecular properties can be partitioned into atomic contributions by integrating the electron density over the region assigned by the topological partition of the electron density (see section 2.1.1.1 for more details).

I   II
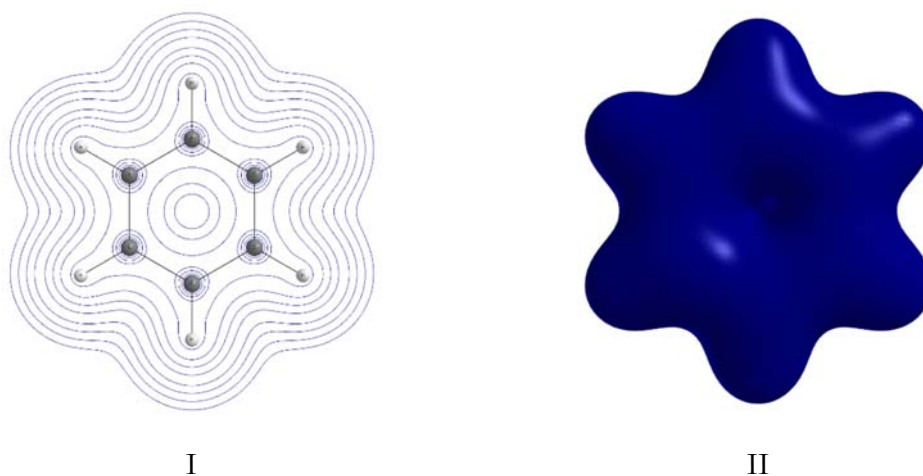
Figure 29. QTAIM analysis. I) Contour map of the electron density $\rho(\vec{r})$ of C_6H_6; II) isosurface of the electron density $\rho(\vec{r})$ of C_6H_6 obtained at 0.02 a.u.

The main benefit of QTAIM is that it can provide an efficient way to describe the properties of the molecules, which are classically represented by a set of atoms connected by bonds, in the framework of quantum mechanics. Yet, the numerical integrations can be sometimes expensive due to the complicated shapes of the basins but also the size of the system and the level of theory used.

From the topological partition of the electron density, one can describe the chemical bonding, structure and reactivity of the molecules. In the following section, the topology of the electron density will be concisely discussed.

2.1.1.1 The topology of the electron density

The density, which is quantum-mechanical observable, is a continuous nonnegative function defined at every point of the real space. Since the electrons are indistinguishable the probability to find one electron is

$$\rho(\vec{x}_1) = N d\vec{x}_1 \int \Psi(\vec{x}_1, \vec{x}_2, \dots, \vec{x}_N)\Psi^*(\vec{x}_1, \vec{x}_2, \dots, \vec{x}_N) d\vec{x}_2 \dots d\vec{x}_N$$
$$\vec{x} = (s, \vec{r})$$

(1)

where $\rho(\vec{x})$ is the so-called density function and $\vec{x}$ contains both position and spin coordinates. Its integration with respect to the spin coordinates leads to the probability density, well-known as the electron density, $\rho(\vec{r})$,

$$\rho(\vec{r}_1) = \int \rho(\vec{x}_1)\, ds_1$$
$$= N d\vec{x}_1 \int \Psi(\vec{x}_1, \vec{x}_2, \dots, \vec{x}_N)\Psi^*(\vec{x}_1, \vec{x}_2, \dots, \vec{x}_N) d\vec{s}_1 d\vec{x}_2 \dots d\vec{x}_N$$

(2)

The first derivative of the electron density (the gradient) provides the set of critical points:

$$\vec{\nabla}\rho(\vec{r}) = \vec{\imath}\frac{\partial\rho(\vec{r})}{\partial x} + \vec{\jmath}\frac{\partial\rho(\vec{r})}{\partial y} + \vec{k}\frac{\partial\rho(\vec{r})}{\partial z} = \vec{0}$$

(3)

$\vec{0}$ means that each individual component of the gradient must be equal to zero (this condition is satisfied at ∞ and at the critical point). The analysis of the second derivative of the density allows us to characterize the nature of the different critical points (maximum, minimum or a saddle point). So at the end, the topology of the electron density is characterized by the

second derivatives, gathered in the so-called Hessian matrix **H** that depends on the position of the critical points r_c

$$H[\rho](\vec{r_c}) = \begin{pmatrix} \dfrac{\partial^2 \rho(\vec{r_c})}{\partial x^2} & \dfrac{\partial^2 \rho(\vec{r_c})}{\partial x \partial y} & \dfrac{\partial^2 \rho(\vec{r_c})}{\partial x \partial z} \\[3mm] \dfrac{\partial^2 \rho(\vec{r_c})}{\partial y \partial x} & \dfrac{\partial^2 \rho(\vec{r_c})}{\partial y^2} & \dfrac{\partial^2 \rho(\vec{r_c})}{\partial y \partial z} \\[3mm] \dfrac{\partial^2 \rho(\vec{r_c})}{\partial z \partial x} & \dfrac{\partial^2 \rho(\vec{r_c})}{\partial y \partial z} & \dfrac{\partial^2 \rho(\vec{r_c})}{\partial z^2} \end{pmatrix} \tag{4}$$

$H[\rho](\vec{r_c})$ is a real symmetric matrix and therefore it can be diagonalized through a unitary transformation using the unitary matrix **U**,

$$U^{-1}H[\rho](\vec{r_c})U = \Lambda \tag{5}$$

The diagonalization is equivalent to the rotation of the coordinate system $\vec{r}(x, y, z) \rightarrow \vec{r_1}(x_1, y_1, z_1)$ that has been performed by a unitary transformation $\vec{r_1} = \vec{r}U$, where **U** is the unitary matrix. Once $H[\rho](\vec{r_c})$ is transformed into its diagonal representation through the previous unitary transformation, the resulting expression is

$$\Lambda = \begin{pmatrix} \dfrac{\partial^2 \rho(\vec{r_c})}{\partial x_1^2} & 0 & 0 \\[3mm] 0 & \dfrac{\partial^2 \rho(\vec{r_c})}{\partial y_1^2} & 0 \\[3mm] 0 & 0 & \dfrac{\partial^2 \rho(\vec{r_c})}{\partial z_1^2} \end{pmatrix} = \begin{pmatrix} \lambda_1 & 0 & 0 \\ 0 & \lambda_2 & 0 \\ 0 & 0 & \lambda_3 \end{pmatrix} \tag{6}$$

where λ_1, λ_2 and λ_3 are the three eigenvalues of the Hessian matrix, *i.e.*, the curvatures of the density according to the three principal axes, x_1, y_1 and z_1, respectively. It is worth highlighting that the trace of the Hessian matrix Λ (which is invariant to the rotation of the coordinate system) is known as the Laplacian of the ρ defined as

$$\vec{\nabla}^2 \rho(\vec{r_c}) = \vec{\nabla} \cdot \vec{\nabla}\rho(\vec{r_c}) = \frac{\partial^2 \rho(\vec{r_c})}{\partial x^2} + \frac{\partial^2 \rho(\vec{r_c})}{\partial y^2} + \frac{\partial^2 \rho(\vec{r_c})}{\partial z^2} = \lambda_1 + \lambda_2 + \lambda_3 \tag{7}$$

The sign of the Laplacian of ρ provides evidence of electron localization or delocalization. A positive value ($\vec{\nabla}^2 \rho(\vec{r_c}) > 0$) is indicative of regions with depletion of the electron density (presence of a minimum of the function) while a negative value ($\vec{\nabla}^2 \rho(\vec{r_c}) < 0$) reveals regions with concentration of the electron density (existence of a maximum of the function). Figure

30 shows how the $\vec{\nabla}^2\rho(\vec{r})$ looks like for benzene. Blue regions (positive values) are characteristic of ionic or Van der Waals interactions while in red regions (negative values) the charge is localized in the bonding region, typical of covalent interactions.

I   II
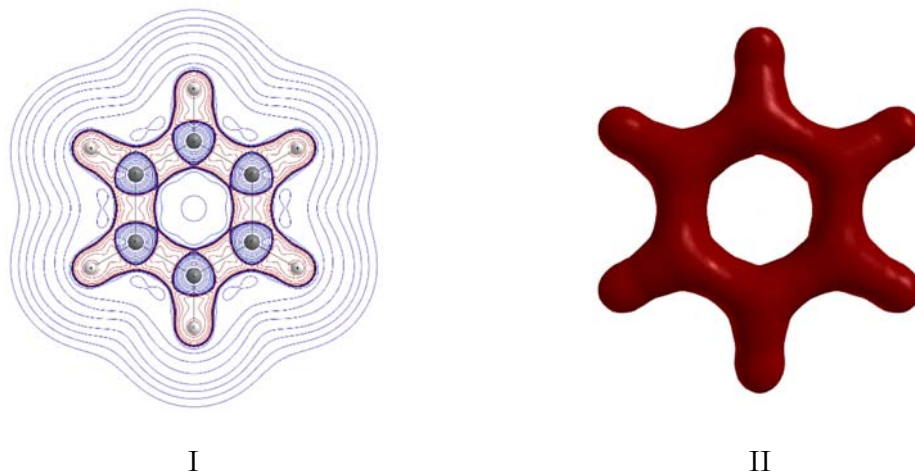
Figure 30. QTAIM analysis. I) Contour map of the Laplacian of the electron density $\vec{\nabla}^2\rho(\vec{r})$ of C_6H_6 (positive and negative values in blue and red, respectively); II) Laplacian isosurface $\vec{\nabla}^2\rho(\vec{r})$ of C_6H_6 obtained at -0.02 a.u.

Classification of the critical points

Each critical point (CP) can be classified with two numbers: ω and σ (ω, σ). ω is the rank which is the number of non-zero curvatures and σ is the signature which depends on the sign of its curvatures assuming non-zero eigenvalues. Each positive curvature contributes +1 to the σ and each negative curvature adds -1. Thus, there are four possible σ values for critical points of rank 3:

- **(3, -3). Nuclear Critical Point (NCP).** All the curvatures are negative, and thus this CP is a maximum of the ρ. These regions usually coincide with an atomic position and an atom-in-molecule within QTAIM theory is characterized by one and only one NCP. However, it is possible but not usual to obtain a maximum of ρ which does not coincide with an atomic position; those are known as non-nuclear attractors (NNA).

- **(3, -1). Bond Critical Point (BCP).** A BCP presents two negative curvatures (λ_1 and $\lambda_2 < 0$) and a positive one ($\lambda_3 > 0$). The BCP is found between two NCPs. The positive curvature corresponds to a saddle point of order 1, which is a maximum of

the electron density and it is related to the direction connecting the two NCP; and the negative eigenvectors form a plane in the perpendicular direction. Actually, the presence of the BCP is usually indicative of a chemical bond between the atoms identified by two NCPs.

- **(3, +1). Ring Critical Point (RCP).** A RCP has two positive curvatures (λ_1 and λ_2 > 0) and a negative one (λ_3 < 0). The two positive curvatures are related to a saddle point of order 1 defined as the plane formed by the positive eigenvectors and the maximum of the electron density in the perpendicular direction. The presence of a RCP indicates a ring structure. If the molecule is planar the RCP is located in the minimum of the electron density inside the ring structure.

- **(3, +3). Cage Critical Point (CCP).** A CCP has three positive curvatures (λ_1, λ_2, and λ_3 > 0) and it is thus a (local) minimum of the electron density. Its presence indicates a cage structure and the CCP is located close to its center: *e.g.* the center of C_{60}.

The number and type of CPs that can coexist in a molecule must follow strictly the Poincaré–Hopf relationship[180] which states that:

$$n_{NCP} + n_{RCP} - n_{BCP} - n_{CCP} = 1 \tag{8}$$

In the case that the previous expression is not fulfilled, then one must check carefully the molecular structure and try to find the missing CPs. Coming back to the case of benzene, twelve NCPs, twelve BCPs and one RCP are detected (Figure 31) and these CPs indeed satisfy the Poincaré–Hopf relationship (12 + 1 – 12 – 0 = 1).
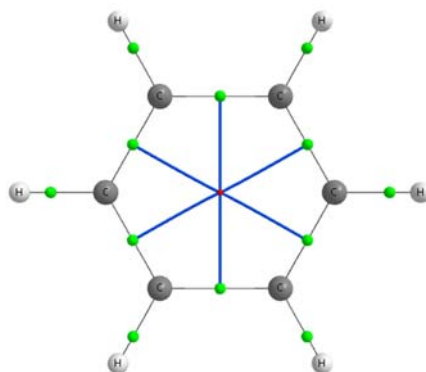
Figure 31. QTAIM analysis. Topology and critical points of C_6H_6: BCPs in green, RCPs in red, bond paths in black and ring paths in blue.

Defining an atom in a molecule from the topology analysis of the electron density

The pronounced maxima in the electron density of the nuclei give rise to a rich topology because its attractive force determines the electronic distribution around its field. This topology represents a natural partitioning of the molecular space into separate mononuclear regions, Ω, identified as atoms in molecules. The atoms in a molecule as defined by QTAIM have their boundaries limited by the zero-flux surface in the gradient vector field of the electron density. This zero-flux surface is given by:[180]

$$\nabla \rho(\vec{r}) \cdot n(\vec{r}) = \vec{0} \qquad \forall r \in S(\Omega) \tag{9}$$

where $\vec{r}$ is the position vector and $n(\vec{r})$ the unit vector normal to the zero-flux surface $S(\Omega)$. The zero-flux surfaces split the molecular space into separate mononuclear "atomic basins". Gradient vector field lines belonging to an atomic basin converge all to one nucleus which acts as an attractor to these gradient vector field lines. Thus, an atom in a molecule is simply defined as the union of a nucleus and its associated basin or, in other words, as a region of space bounded by one or more zero-flux surfaces (Figure 32).
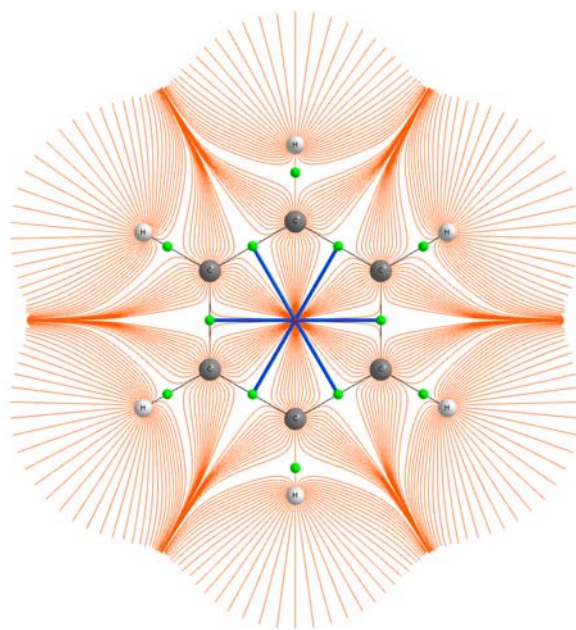
Figure 32. QTAIM analysis. Two-dimensional basin paths (in orange) of C_6H_6.

Rarely, NNAs, which are a maximum of the electron density, could appear at positions other than those of atomic nuclei, especially in metals.[205,206] These NNAs are topologically indistinguishable from the nuclear maxima. A NNA is associated with a basin swept by

gradient vector field lines and is bounded by a zero-flux surface. Consequently, NNA basins constitute proper open quantum systems and are therefore termed "pseudoatoms". Pseudoatoms can be bonded (*i.e.* share a common interatomic zero-flux surface, a BCP, and a bond path) to atoms and other pseudoatoms in a molecule. It is worth highlighting that NNAs and their basins are of great importance in characterizing metallic bonding and are of significant theoretical interest.

The partitioning of the molecular space into atomic basins enables the partitioning of electronic properties into atomic contributions in one consistent theoretical framework. In particular, in the QTAIM framework, we can obtain atomic and bonding properties.

Gradient lines are those which a pair of CPs are connected with. For example, the line that connects two NCPs (or atomic regions) through a BCP is known as *bond path*. It is important mentioning that the BCP corresponds to the lowest value of the electron density along the bond path. According to Bader's theory,[207] the bond path is a widely used indicator of chemical bonding or bonding interaction between two atoms, although some controversy[208–213] have been generated.

On the other hand, the atomic population or the atomic charge are atomic properties. The first measure provides the total electron population of an atom in a molecule defined as:

$$N_A = \int_A \rho(\boldsymbol{r})dr \tag{10}$$

The sum of all atomic populations, *i.e.* $N_A + N_B$ ..., must give the total number of electrons of the molecule. From the electron population, one can define the atomic charge as:

$$q_A = Z_A - N_A \tag{11}$$

where Z_A is the atomic number.

2.1.1.2 Protocol of a typical QTAIM calculation

To perform a QTAIM analysis of the topology of the electron density we can employ many different programs. AIM2000[214], AIMAll[215] and AIMPAC[216] are some of the programs that theoretical chemists usually use. The main steps in a simple QTAIM calculation are shown in Scheme 3.

Get the electronic structure through *ab initio* calculations using theoretical-based software such as Gaussian	Extraction and analysis of the information located in the .int files. For instance, to compute delocalization indices, overlap matrices must be used.
Generate the wavefunction file (.wfn) related to the previous electronic structure	1) Generate an input files (.inp) for each atom of the molecule. 2) Perform individual atomic integrations using basin integration methods such as proaim or promega. The .inp and .wfn files are needed for this calculation. 3) Once the integration is performed to the desired accuracy, an output files (.int) are generated for each atomic integration. The accuracy of the integration is measured by the value of the integrated Laplacian.
Find critical points (NCP, BCP, RCP, CCP and NNA) and both paths using programs like EXTREME or AIMAll (the previous information is reported in .crt and .extout files, respectively)	

Scheme 3. Main steps in a simple QTAIM calculation.

2.1.2 Fuzzy partitioning method

An alternative to QTAIM within 3D-space analysis are atomic definitions that introduce overlapping or "*fuzzy*" atoms. Overlapping atomic partitions define atoms as fuzzy entities that interpenetrate each other and extent all over the space. This means that the atomic domains do not have sharp boundaries but there is a continuous transition from one region to another. The atomic domains are represented by assigning a nonnegative atomic weight function $w_A(\vec{r})$ to each atom A fulfilling the following condition when summing over all the atoms of the system:

$$\sum_A w_A(\vec{r}) = 1 \quad \forall \vec{r} \tag{12}$$

So each atom is assigned a weight function (defined between 0 and 1) that gives the contribution of the atom in each point of the molecular space. It is worth mentioning that the definition of overlap populations is carried out by classical Mulliken analysis.

The fuzzy atoms were first introduced by Hirshfeld.[217] In the Hirshfeld method, the weight $w_A(\vec{r})$ is identified with the ratio of its isolated atomic density $\rho_A^0(\vec{r})$ and the promolecular density $\sum_A \rho_A^0(\vec{r})$, obtained by simple superposition of isolated atomic densities:

$$w_A(\vec{r}) = \frac{\rho_A^0(\vec{r})}{\sum_A \rho_A^0(\vec{r})} \qquad (13)$$

The promolecule is a molecule formed by superposing the densities of the isolated atoms (or fragments). One of the main uses of the Hirshfeld method lies in the population analysis. Atomic populations can be obtained by integration of the atomic density of the AIM:

$$N_A = \int \rho_A(\vec{r})d\vec{r} = \int w_A(\vec{r})\rho(\vec{r})d\vec{r} \qquad (14)$$

The main criticism to this classical Hirshfeld method is that the choice of the electronic state of the isolated atoms can influence the resulting atomic population. This drawback has been overcome by Bultinck *et al.* with the Iterative Hirshfeld approach (Hirshfeld-I).[218,219] On the other hand, we also have the multicenter integration technique defined by Becke, which assigns weights to atoms in the molecule and it was used by Mayer and Salvador[203] to define the *fuzzy atom* partition. Particularly, they use the following weight functions:

$$w_A(\vec{r}) = \frac{f_A(\vec{r})}{\sum_B f_B(\vec{r})} \qquad (15)$$

These functions $f_A(\vec{r})$ are obtained from empirical atomic radii. *Becke-rho* partition (used in this thesis) is an alternative to the *fuzzy atoms* which uses the BCP (or in the absence of the BCP the point with the lowest density in the straight line connecting two atoms) instead of the atomic radii.[220,221]

As we commented previously, the numerical integrations over QTAIM atomic basins are sometimes expensive due to the rather complicated shapes they may exhibit. In the case of *Becke-rho*, even though we obtain values close to the QTAIM ones, the integrations are much more straightforward, accurate enough and have a reduced computational cost. APOST-3D,[222] which was developed by Salvador and Ramos-Córdoba, is one of the few programs that is able to deal with the *fuzzy* scheme mentioned above.

2.2 Electron sharing indices

The bond order has been the key to explain the chemical bonding because it is able to quantify the number of chemical bonds between a pair of atoms. In 1939, Coulson[223] provided a measure of the bond order based on application of the Hückel molecular orbital (HMO) theory, known as Coulson Bond Order (CBO), to explain the electronic structure of

some polyenes and aromatic molecules. The concept of bond order is limited to bonded pairs of atoms. So to avoid the controversy, the term bond order was suggested to be replaced by ESI by Fulton,[224] which gives a measure of the extent of electron sharing between any pair of atoms.

Since Coulson's study, many ESIs have been described in the literature. In MO theory, the Mulliken population analysis,[201] where the population of the MOs is decomposed into atomic populations and diatomic overlap populations, importantly influenced the formulation of bonding concepts, even though it does not describe a bond order itself. On the basis of the Mulliken population analysis, Mayer introduced a popular definition of the number of bonds between two centers, so-called as Mayer Bond Order (MBO),[225–228] originally formulated for single-determinant wavefunctions.

In this section we will briefly discuss the ESIs that are calculated from the Exchange–Correlation Density (XCD), which is given by,

$$\gamma_{xc}(\vec{r_1}, \vec{r_2}) = \rho_2(\vec{r_1}, \vec{r_2}) - \rho(\vec{r_1})\rho(\vec{r_2}) \tag{16}$$

The XCD compares a *fictitious* pair density of independent electron pairs $[\rho(\vec{r_1})\rho(\vec{r_2})]$ with the real pair density $\rho_2(\vec{r_1}, \vec{r_2})$. The pair density contains information about the relative motion of two electrons. The XCD represents the difference between the conditional and unconditional probability densities of finding two electrons, one at $\mathbf{r_1}$ and the other at $\mathbf{r_2}$. The larger the difference, the more dependent and the more coupled the electrons are. Nonetheless, the smaller the difference, the more independent the electrons in these positions are. So we should expect large XCD values for pairs of electrons shared between pairs of atoms located close one to each other in space like in the case of lone pairs.

ESI such as the delocalization index (DI) is based on the XCD. Specifically, the DI, $\delta(A, B)$, is obtained by the double integration of the XCD ($\gamma_{XC}(\vec{r_1}, \vec{r_2})$) over the atomic basins, as defined in the AIM theory,[229] of atoms A and B:

$$\delta(A, B) = -2 \int_A \int_B \gamma_{XC}(\vec{r_1}, \vec{r_2}) d\vec{r_1} d\vec{r_2} \tag{17}$$

For single-determinant wavefunctions (including density functional approaches), $\delta(A, B)$ is expressed in terms of atomic overlaps as:

$$\delta(A,B) = 4 \sum_{i,j}^{occ.MO} S_{ij}(A)S_{ij}(B) \tag{18}$$

The sums run over all the occupied MO. $S_{ij}(A)$ is the overlap between MOs i and j within the basin of atom A. We have made use of the AIM atomic partition defined from the condition of zero-flux gradient in one-electron density $\rho(\mathbf{r})$ to compute $S_{ij}(A)$ values.[180,181]

The term $\delta(A,B)$ gives a quantitative idea of the number of electrons delocalized or shared between A and B.[183,185] Contrarily, the LI, $\lambda(A)$,[230] gives the number of electrons that are not delocalized through other regions:

$$\lambda(A) = -\int_A \int_A \gamma_{XC}(\vec{r_1},\vec{r_2})d\vec{r_1}d\vec{r_2} \tag{19}$$

By integrating the XCD over the number of electrons, one can split the electrons as localized and delocalized and assign them to atoms (localized) and pairs of atoms (delocalized). Thus, that obeys the following sum rule:

$$N = \sum_A (N_A) = \sum_A \sum_{B,A<B} \delta(A,B) + \lambda(A) \tag{20}$$

An electron equally shared between two atoms contributes ½ to the LI and ½ to the DI of a given atom. On the other hand, a fully localized electron in an atom contributes 1 to the LI.

Besides, one can also define the number of electrons of an atomic region as the sum of localized and delocalized electrons:

$$\frac{1}{2}\sum_{A\neq B} \delta(A,B) + \lambda(A) = N_A \tag{21}$$

where the first term is related to the total delocalization in a given atom and $N(A)$ is the average population of an atom A defined as follows:

$$\langle N \rangle_A = N_A = \int_A \rho(\vec{r})d\vec{r} \tag{22}$$

The percentage of localization can be calculated through the following expression,

$$\%LI = \frac{\lambda(A)}{N_A} \cdot 100 \tag{23}$$

Multicenter indices

The Lewis theory is based on the idea of electrons pairs described as two-center two-electron bond (2c-2e) which has been used to describe the structure of most of the molecules. However, this theory fails towards systems that have more complex bond patterns. For example, that would be the case for the structure of boranes, known as electron deficient molecules, which are characterized by 3c-2e bonds. Thus, expressions that take into account multicenter bonding are important to completely characterize the electronic structure. Yet, $\rho(\vec{r})$ cannot be used to characterize three-center interactions because its topological analysis can only define bonds between pairs of atoms. In contrast to $\rho(\vec{r})$, the definition of ESI can be generalized to study the electron delocalization between three or more atoms, so-called multicenter bond indices developed by Giambiagi and coworkers.[231] The generalization of multicenter bond indices in QTAIM's framework was provided by Bochicchio and collaborators.[232] For instance, the 3-center ESI depends on the third order density, $\gamma_3(\vec{r_1}, \vec{r_2}, \vec{r_3})$.[232] Therefore, the calculation of multicenter bond indices at the correlated level implies the extraction of high-order densities which are expensive.[233] Nonetheless, at the HF level, this expression can be written comprehensibly in terms of atomic overlap matrix (AOM),

$$\delta(A, B, C) = 8 \sum_{ijk} S_{ij}(A) S_{jk}(B) S_{ki}(C) \tag{24}$$

Equation 24 is a generalization of equation 18 in the case of three center delocalization. Remarkably, positive $\delta(A, B, C)$ values indicate 3c-2e bonds and negative values correspond to 3c-4e bonds. One of the main and potential applications of the multicenter indices is the quantification of aromaticity (see section 2.3.1 for more details).[186,187]

2.3 Descriptors of aromaticity

Nowadays, a large amount of descriptors to evaluate the aromatic character exists. Yet, as we have commented before, not all the indices work for all systems because each of these indices covers a specific property. Of course, one can combine all these descriptors to get a

global index able to assess the aromaticity, but unluckily we still do not have it. This section will be focused on the theoretical basis of several indices of aromaticity and several examples will be given. First, each indicator of aromaticity will be introduced, then an example of its applications will be given and finally a few advantages or drawbacks will be discussed.

2.3.1 Geometric-based indices

HOMA

The harmonic oscillator model of aromaticity (HOMA) index is a geometric-based indicator defined by Kruszewski and Krygowski[145,146] as:

$$HOMA = 1 - \frac{\alpha}{n} \sum_{i=1}^{n} (R_{opt} - R_i)^2 \tag{25}$$

where n is the number of bonds considered, α is an empirical constant (for C–C, C–N, C–O, and N–N bonds α = 257.7, 93.5, 157.4, and 130.3, respectively), R_{opt} is an optimal bond value (1.388, 1.334, 1.265, and 1.309 Å for C–C, C–N, C–O, and N–N bonds, respectively) and R_i stands for a running bond length. This expression is optimized to give HOMA = 0 for a model nonaromatic system (bonds not equal to an optimal value R_{opt}), and HOMA = 1 for fully aromatic systems with all bonds equal to R_{opt}. Negative HOMA values usually indicate antiaromaticity.

From the HOMA model, two terms EN and GEO that account for the decrease of aromaticity, can be obtained:

$$HOMA = 1 - \frac{\alpha}{n} \sum_{i=1}^{n} (R_{opt} - R_i)^2 = 1 - \left[\alpha (R_{opt} - R_{av})^2 + \frac{\alpha}{n} \sum_{i=1}^{n} (R_{av} - R_i)^2 \right]$$
$$= 1 - EN - GEO \tag{26}$$

where R_{av} is an averaged bond length, $R_{av} = \frac{1}{n} \sum_{i=1}^{n} (R_i)^2$ and $\alpha (R_{opt} - R_{av})^2$ and $\frac{\alpha}{n} \sum_{i=1}^{n} (R_{av} - R_i)^2$ represent EN and GEO terms, respectively. EN describes the contribution due to the bond elongation with respect to the reference fully aromatic system and GEO describes the contribution due to the bond length alternation.

<u>Example: C_6H_6 in its S_0 state as aromatic molecule and T_1 state as antiaromatic molecule.</u>

<div align="center">

C_6H_6 (S_0 state) C_6H_6 (T_1 state)

HOMA = 0.98   HOMA = -0.49

</div>
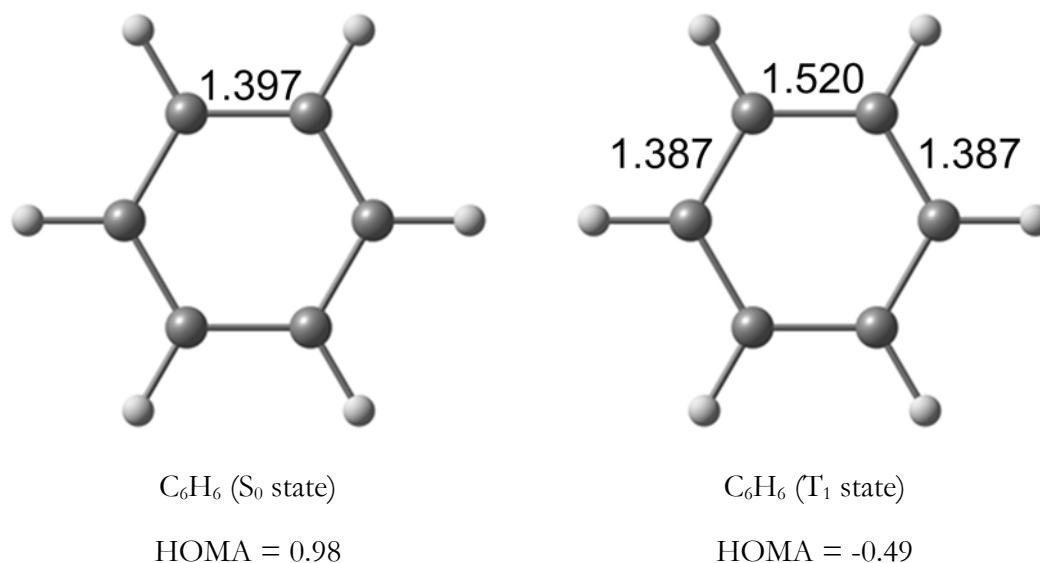
Figure 33. HOMA values for benzene in the S_0 and T_1 states obtained at B3LYP/6-311+G(d,p) geometry. Values in the geometries are bond lengths in Å.

Interpretation: in the S_0 state, HOMA is close to 1 meaning that benzene is aromatic. In the T_1 state, according to Baird's rule, benzene should be antiaromatic and that is reflected by the negative HOMA value.

Drawbacks: HOMA uses reference parameters from well-established aromatic compounds. So even though it seems that HOMA can work fine in small organic molecules, it gives problems when describing the aromaticity of complex inorganic systems, or the aromaticity change along a reaction path when the separation from equilibrium structures is large.[234]

2.3.2 Electronic sharing indices (ESIs)

<u>PDI</u>

Bader and co-workers found that the electron delocalization in benzene is greater between *para*-related carbons in comparison with the *meta*-related ones, even though the larger distance between the atoms in *para* position.[185,235] Considering this discovery, Poater *et al.* introduced the *para*-delocalization index (PDI)[188] given by:

$$PDI = \frac{\delta(A_1, A_4) + \delta(A_2, A_5) + \delta(A_3, A_6)}{3} \tag{27}$$

Basically, PDI is defined as the mean of all delocalization indices (DIs), $\delta(A,B)$,[183,185] of *para*-related carbon atoms in a given 6-MR. $\delta(A,B)$, which is derived from the AIM theory, is the DI between atoms A and B (see section 2.2).

Example: C_6H_6 in its S_0 state as aromatic molecule and T_1 state as antiaromatic molecule.

C₆H₆ (S_0 state)

PDI = 0.105

C₆H₆ (T_1 state)

PDI = 0.043
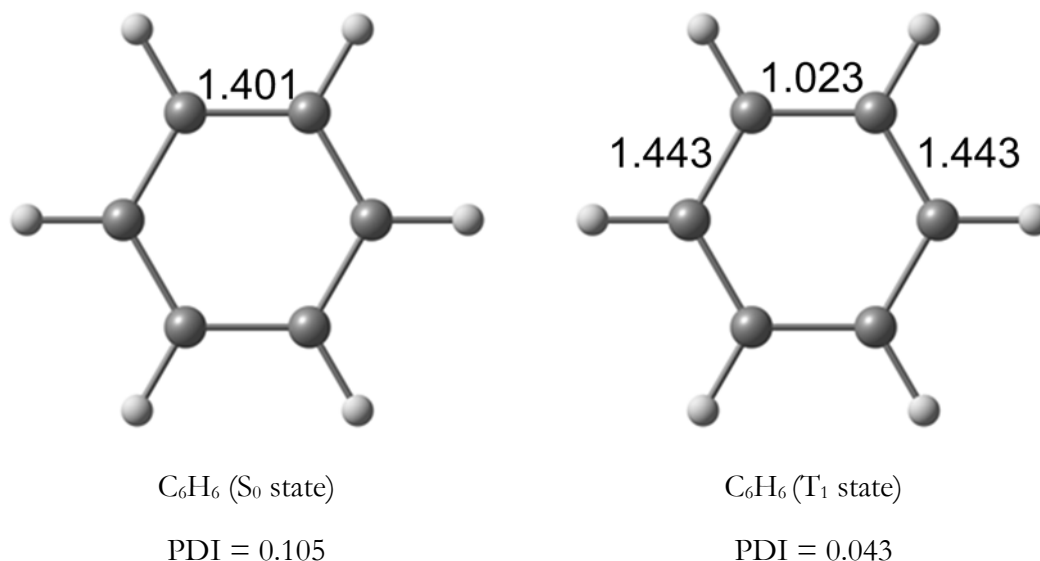
Figure 34. PDI values for the S_0 state and T_1 state of benzene obtained at B3LYP/6-311+G(d,p) geometry. Values in the geometries are DIs expressed in electrons.

Interpretation: the largest PDI value corresponds to benzene in the S_0 state due to its significant aromaticity compared to the T_1 state. A larger PDI value means that the electron delocalization with *para*-related carbon atoms is larger in the S_0 state that in the T_1.

Drawbacks: an obvious disadvantage of PDI is that it only works for 6-MRs. Besides from that, previous studies have shown that PDI does not treat correctly the aromaticity in out-of-plane deformations of aromatic rings and rings with different atoms types (*i.e.* with heteroatoms)

FLU

The aromatic fluctuation index (FLU),[189] developed by Matito and collaborators, is given by:

$$FLU(\mathcal{A}) = \frac{1}{N} \sum_{i=1}^{N} \left[\left(\frac{V(A_i)}{V(A_{i-1})} \right)^{\alpha} \left(\frac{\delta(A_i, A_{i-1}) - \delta_{ref}(A_i, A_{i-1})}{\delta_{ref}(A_i, A_{i-1})} \right) \right]^2 \tag{28}$$

where the string $A = \{A_1, A_2, \ldots, A_N\}$ contains the ordered elements according to the connectivity of the N atoms in a ring and $A_0 \equiv A_N$, $V(A_i)$ is defined as:

$$V(A_i) = \sum_{A_j \neq A_i} \delta(A_i, A_j) \tag{29}$$

α is a simple function to make sure that the first term is always greater or equal to 1, thus taking the values:

$$\alpha = \begin{cases} 1 & V(A_i) > V(A_{i-1}) \\ -1 & V(A_i) \leq V(A_{i-1}) \end{cases} \tag{30}$$

The DI reference values depend on the level of theory we use. For instance, at the B3LYP/6-311+G(d,p) level, the $\delta_{ref}(C, C)$ reference value used of 1.389 e is the $\delta(C, C)$ of benzene, the $\delta_{ref}(C, N)$ reference value used of 1.113 e is the $\delta(C, N)$ of pyridine, and the $\delta_{ref}(C, O)$ reference value used of 0.971 e is the $\delta(C, O)$ of furan. In these cases, all reference values are obtained in their ground states. FLU is close to 0 in aromatic species, and differs from it in non-aromatic ones. However, one can also compute $FLU^{1/2}$ instead of FLU since $FLU^{1/2}$ values are scattered over a wider range and, therefore, the trends derived are clearer. Matito *et al.*[236] have shown that $FLU^{1/2}$ presents better correlations with classical aromaticity indices.

For the FLU_σ ($\sigma = \alpha$ or β) calculations, the same equations can be used but now considering only the α or β molecular spin-orbitals (MSOs) in FLU($\mathcal{A}$) and taking the $\delta_{ref}(C, C)$ reference value as half the reference value used for non-spin split FLU calculations. The main reason for splitting FLU in α and β contributions is to analyze the Baird or Hückel aromatic character of compounds in their triplet states. Whereas identical or very similar values of FLU_α and FLU_β are expected in Hückel-aromatic species, significant differences ($\Delta FLU_{\alpha\beta} = FLU_\alpha - FLU_\beta \neq 0$) are anticipated in Baird-aromatic systems. As an indicator of Hückel (low values) or Baird (high values) aromatic character, one can use the γ descriptor defined as the absolute value of the $\Delta FLU_{\alpha\beta}/FLU$ ratio. As defined, γ allows consistent comparisons between species with different absolute aromaticity FLU values.[237]

Example: $C_5H_5^+$ in its S_0 state as antiaromatic molecule and T_1 state as aromatic molecule.

<div align="center">
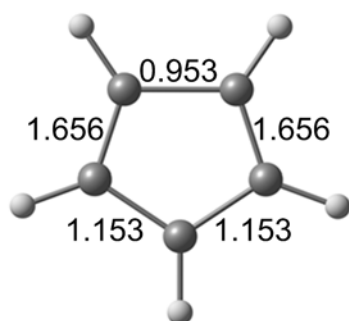
$C_5H_5^+$ (S_0 state)

FLU = 0.048
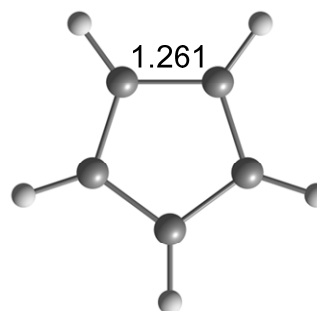
$C_5H_5^+$ (T_1 state)

FLU = 0.010

$FLU_\alpha = 0.000$; $FLU_\beta = 0.037$

$(FLU_\alpha - FLU_\beta)/FLU = 3.7$

</div>

Figure 35. FLU values for the S_0 state and T_1 state of the cyclopentadienyl cation obtained at B3LYP/6-311+G(d,p) geometry. Values in the geometries are DIs expressed in electrons.

Interpretation: It is known that $C_5H_5^+$ is antiaromatic in the S_0 state while it is Baird-aromatic in T_1. FLU in the T_1 state is smaller than the S_0 state indicating that the species is more aromatic in the T_1 state. At the same time, $(FLU_\alpha - FLU_\beta)/FLU$ of 3.7 in the T_1 state reveals that $C_5H_5^+$ is Baird-aromatic.

Drawbacks: FLU, same as HOMA, depends on reference values (DIs). These differ depending on the level of theory. Besides, this electronic index fails when describing geometries far from equilibrium bond distances, like in the analysis of aromaticity along a reaction.[234]

Multicenter indices

The multicenter index (I_{ring}) of Giambiagi[186] *et al.* reads:

$$I_{ring}(\mathcal{A}) = \sum_{i_1, i_2, \dots i_N} n_{i_1} \dots n_{i_N} S_{i_1 i_2}(A_1) S_{i_2 i_3}(A_2) \dots S_{i_N i_1}(A_N) \tag{31}$$

where $S_{ij}(A)$ is the overlap of natural orbitals i and j in the atom A defined in the framework of the QTAIM,[180] and n_i are their occupancies. For a closed-shell monodeterminantal wavefunction we have:

$$I_{ring}(\mathcal{A}) = 2^N \sum_{i_1, i_2, \dots i_N}^{occ.\ MO} S_{i_1 i_2}(A_1) S_{i_2 i_3}(A_2) \dots S_{i_N i_1}(A_N) \tag{32}$$

Equation 32 is a generalization of equation 18 for *n*-centers. Recently, the I_{ring} expression has been split (in a similar way to FLU) in contributions of α and β MOs separately (I_{ring}^{σ}, where σ can be α or β). So taking into account this partition, the I_{ring} can be easily redefined as,

$$
\begin{aligned}
I_{ring}(\mathcal{A}) &= I_{ring}^{\alpha}(\mathcal{A}) + I_{ring}^{\beta}(\mathcal{A}) \\
&= \sum_{\substack{i_1, i_2, \dots i_N}}^{\alpha\ MO} n_{i_1} \dots n_{i_N} S_{i_1 i_2}(A_1) S_{i_2 i_3}(A_2) \dots S_{i_N i_1}(A_N) \\
&+ \sum_{\substack{i_1, i_2, \dots i_N}}^{\beta\ MO} n_{i_1} \dots n_{i_N} S_{i_1 i_2}(A_1) S_{i_2 i_3}(A_2) \dots S_{i_N i_1}(A_N)
\end{aligned}
\tag{33}
$$

A normalized version of the I_{ring} index,[238] has also been recently introduced, the so-called I_{NG}, which appears to be less dependent on the ring size than its unnormalized homologue, and it is written for aromatic species as:

$$I_{NG}(\mathcal{A}) = \frac{\pi^2}{4 N N_{\pi}} I_{ring}^{1/N} \tag{34}$$

where N is the total number of atoms in the ring and N_{π} the total number of π-electrons. I_{NG} has the peculiarity of reproducing the so-called topological resonance energy per electron (TREPE)[239] values at the Hückel Molecular Orbital (HMO) level of theory.

Bultinck and coworkers worked on a particular extension of the I_{ring} index. According to these authors summing up all the I_{ring} values resulting from the permutations of indices A_1, $A_2, \dots, A_N$ defines a new index of aromaticity, the so-called multicenter index (MCI).[240] MCI provides a measure of electron sharing among the atoms considered and it is defined as a sum of all the I_{ring} values resulting from the permutations of indices A_1, A_2, ..., A_N (N is the number of atoms in the ring):

$$MCI(\mathcal{A}) = \frac{1}{2N} \sum_{P(\mathcal{A})} I_{ring}(\mathcal{A}) \tag{35}$$

where $P(\mathcal{A})$ stands for a permutation operator which interchanges the atomic labels A_1, A_2 ... A_N to generate up to the $N!$ permutations of the elements in the string $\mathcal{A}$. Generally, the values of MCI and I_{ring} are in tight correlation because the dominant contribution to MCI is

the Kekulé structure, nonetheless some exceptions may arise.[238] Table 2 collects MCI values for several systems. As one can notice, Baird-aromatic species present higher MCI values in the T_1 state that in the S_0 state. For Hückel-aromatic compounds, one can appreciate the opposite behavior. Currently, the information of these split values (MCI_{T1}^{α} and MCI_{T1}^{β}) provide remains unknown. Whereas FLU_{α} and FLU_{β} can provide us an easy manner to identify the degree of Baird-aromaticity in opened-shell systems, we cannot argue the same for I_{ring} values because currently it is still blurry.

Table 2. MCI for S_0 and T_1 states and MCI_{T1}^{α} and MCI_{T1}^{β} for T_1 state of molecules for each membered-ring (MR) that follow Baird's and Hückel's rule. Values obtained at B3LYP/6-311++G(d,p) level of theory.

Type	Molecule	MR	MCI_{S0}	MCI_{T1}	MCI_{T1}^{α}	MCI_{T1}^{β}	MCI_{T1}^{α} - MCI_{T1}^{β}
BAIRD	C_4H_4	4	0.010	0.124	0.036	0.089	-0.053
	$C_5H_5^+$	5	-0.021	0.098	0.041	0.057	-0.016
	$C_6H_6^{2+}$	6	-0.013	0.079	0.041	0.038	0.003
	$C_7H_7^-$	7	-0.003	0.031	0.005	0.026	-0.021
	C_8H_8	8	0.000	0.027	0.008	0.019	-0.011
	$C_9H_9^+$	9	-0.004	0.021	0.009	0.013	-0.004
	$C_{10}H_{10}^{2+}$	10	-0.004	0.016	0.008	0.008	0.000
HÜCKEL	$C_4H_4^{2+}$	4	0.183	-0.021	-0.022	0.000	-0.022
	$C_5H_5^-$	5	0.068	0.024	0.034	-0.010	0.044
	C_6H_6	6	0.072	0.000	0.001	-0.001	0.003
	$C_7H_7^+$	7	0.057	-0.005	-0.001	-0.003	0.002
	$C_8H_8^{2+}$	8	0.041	-0.004	-0.004	0.000	-0.004
	$C_9H_9^-$	9	0.015	-0.002	0.000	-0.002	0.001
	$C_{10}H_{10}$	10	0.014	-0.002	0.000	-0.001	0.001

Finally, there is a normalized version of the MCI index for aromatic rings,[238] the so-called I_{NB}, given by:

$$I_{NB}(\mathcal{A}) = \frac{C}{NN_{\pi}}[2N \cdot MCI(\mathcal{A})]^{\frac{1}{N}} \tag{36}$$

where $C \approx 1.5155$. One can also obtain I_{ring}, I_{NG}, MCI, and I_{NB} indices at a correlated level with the MP2 and CCSD methods but now natural spin orbitals (NSO) must be taken into account.[67] Yet, to obtain the correlated versions of the PDI and FLU indices the following substitution is needed:

$$S_{ij}(A) \rightarrow \frac{\sqrt{n_i n_j} S_{ij}^{NO}(A)}{2} \tag{37}$$

The higher the multicenter index (I_{ring}, I_{NG}, I_{NB} and MCI) values as well as HOMA and PDI, the more aromatic are the rings. An obvious advantage of multicenter indices is that they can be applied quite generally even in the situation where PDI, FLU or HOMA cannot be used. One of the disadvantages of using those ESIs is the computational cost when large rings are present. Nonetheless, it is worth noting that recently, Matito[241] developed a new descriptor for large rings, named AV1245, which is based on an average of the 4-center multicenter indices (MCI) along the ring that keeps a positional relationship of 1, 2, 4, 5… The key point of this new method is its low computational cost in comparison with other ESIs and besides it does not rely on reference values, does not suffer from large numerical precision errors, and it does not present any limitation on the nature of atoms, the molecular geometry or the level of calculation.[241]

Example I: $C_5H_5^+$ in its S_0 state as antiaromatic molecule and T_1 state as aromatic molecule.

$C_5H_5^+$ (S_0 state)

I_{ring} = 0.000

I_{NG} = 0.015

MCI = -0.038

I_{NB} = -0.042

$C_5H_5^+$ (T_1–state)

I_{ring} = 0.034

I_{NG} = 0.042

MCI = 0.098

I_{NB} = 0.050
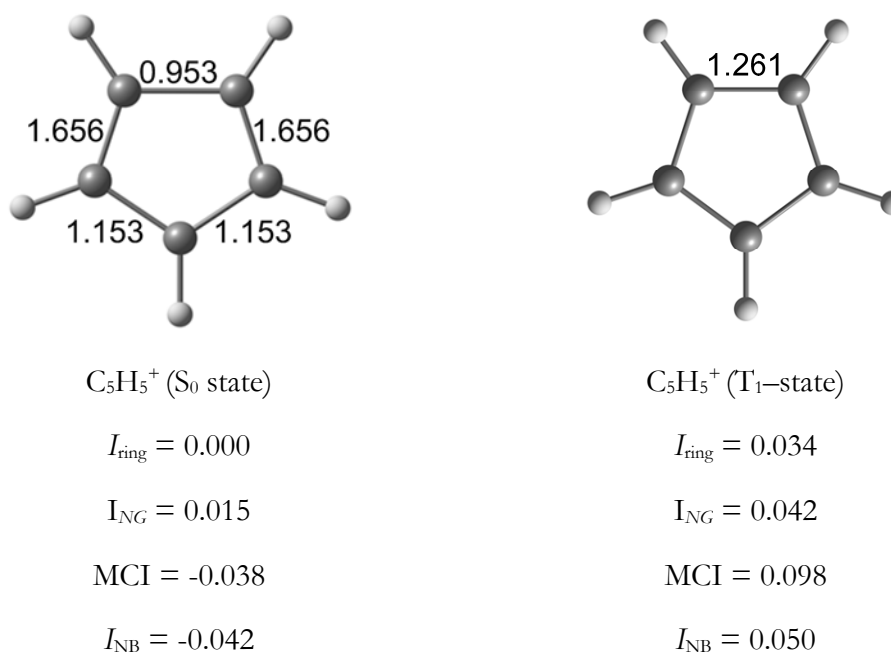
Figure 36. I_{ring}, I_{NG}, MCI and I_{NB} values for the S_0 state and T_1 state of the cyclopentadienyl cation obtained at B3LYP/6-311+G(d,p) geometry. Values in the geometries are DIs expressed in electrons.

Example II: Al_4^{2-} and Al_4^{4-} as metal clusters with double ($\sigma+\pi$) aromaticity and σ-aromaticity.

2.592

| Al_4^{2-} | Al_4^{4-} |

Al_4^{2-}	Al_4^{4-}
MCI = 0.356	MCI = 0.222
MCI_σ = 0.169	MCI_σ = 0.210
MCI_π = 0.187	MCI_π = 0.012
Type of aromaticity = $\sigma+\pi$	Type of aromaticity = σ
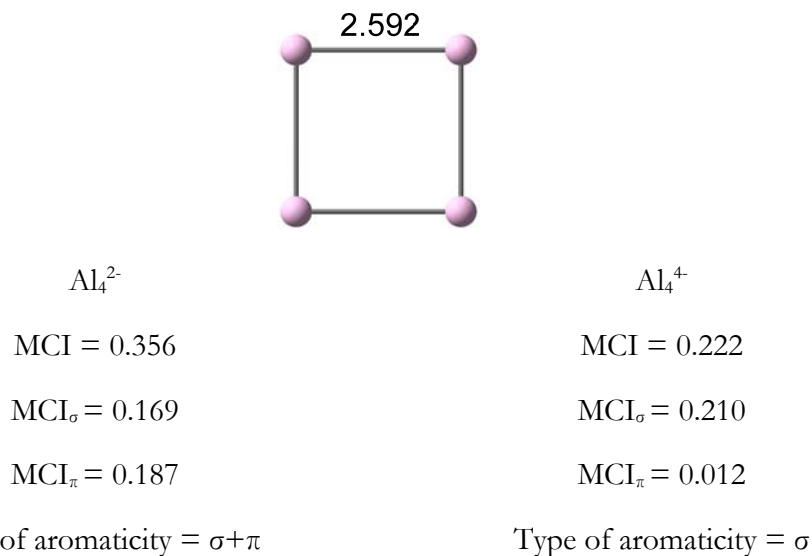
Figure 37. MCI, MCI_σ and MCI_π values of Al_4^{2-} and Al_4^{4-}. Values obtained from reference [106]. MCI values for Al_4^{4-} were calculated at the Al_4^{2-} geometry including two more electrons that go to an e_g orbital with π-antibonding character. Value in the geometry is a bond length expressed in Å.

Interpretation: On the one hand, for $C_5H_5^+$ all the multicenter indices are larger in the T_1 state confirming the Baird aromatic character of this species. On the other hand, for metal clusters, σ and π contributions of MCI have been calculated. Multifold ($\sigma + \pi$) aromaticity is detected for Al_4^{2-} as MCI_σ is similar to MCI_π. For Al_4^{4-}, MCI_σ is larger than MCI_π and therefore, the σ-aromaticity dominates.

Drawbacks: MCI is one of the best indicators of aromaticity.[234] Yet, the high computational cost and its large dependence on the level of calculation are the main problems of this electronic index.

2.3.3 Magnetic indices

The shielding tensor $\vec{\vec{\sigma}}$ describes the relation between external ($\vec{B}_{ext}$) and induced magnetic field ($\vec{B}_{ind}$):[242]

$$\vec{B}_{ind} = -\vec{\vec{\sigma}}\vec{B}_{ext} \tag{38}$$

The induced magnetic field at position $\vec{R}$ can be computed from the current density $\vec{J}(\vec{r})$ applying the Biot–Savart's law:

$$\vec{B}_{ind} = \frac{1}{c} \int \frac{\vec{J}(\vec{r}) \times (\vec{r} - \vec{R})}{\left|\vec{r} - \vec{R}\right|^3} d^3r \qquad (39)$$

Therefore, by using the two previous equations, the shielding tensor can be computed directly from the current density, which itself is induced by the external magnetic field $\vec{B}_{ext}$. The magnetic shielding tensors are composed of nine components (each associated with two axes) described by the three diagonal matrix elements in its principal axis system:

$$
\begin{array}{c|ccc}
 & x & y & z \\
\hline
x & xx & xy & xz \\
y & yx & yy & yz \\
z & zx & zy & zz \\
\end{array}
$$

The shielding constant is the isotropic value σ_{iso}, 1/3 of the trace of the shielding tensor (or the average of the principal tensor components xx, yy and zz):

$$\sigma_{iso} = \frac{1}{3}(\sigma_{11} + \sigma_{22} + \sigma_{33}) = \frac{1}{3}(\sigma_{XX} + \sigma_{YY} + \sigma_{ZZ}) \qquad (40)$$

In the equation 40, σ_{iso} is invariant with respect to rotation of principal axes. At this point, we have to introduce the nucleus-independent chemical shift (NICS), which is the negative of the shielding constant (the chemical shift with respect to vacuum). A positive shielding (negative NICS) means that the applied magnetic field is shielded, thus the induced field reduces the field (diamagnetic current), while a negative shielding (positive NICS) means that the induced field strengthens the applied magnetic field (paramagnetic current). NICS was first used by Buhl and van Wullen in 1995 when they were studying the electronic currents in fullerenes.[243] However, Schleyer and coworkers[155] were who first introduced explicitly the term of NICS as a magnetic-based descriptor of aromaticity.

The shielding tensor must be independent of the gauge origin. However, the number of basis functions is always limited in computations so that they strictly depend on the chemical shift on top of the gauge origin of the vector potential that describes the external magnetic field.[244] Hence, the choice of gauge is a practical problem for the calculation of magnetic properties.[245,246] Many different approaches exist to deal with this so-called gauge origin problem like the Gauge-Independent Atomic Orbital (GIAO)[247] or the Continuous Set of

Gauge Transformations (CSGT),[248–250] among others. These methods are integrated in most of the computational-based packages. It is worth mentioning that in case of *Gaussian*, magnetic shield tensors are obtained and therefore we must change their sign to obtain the NICS values.

As we have mentioned above, negative NICS values indicate evidence of aromaticity due to the presence of diamagnetic currents, while positive ones indicate antiaromaticity because of the paramagnetic rings. There are different ways to calculate NICS (also known as NICS$_{iso}$ or NICS$_{tot}$). NICS(0), which is attributed directly to NICS, is calculated in the center of a given ring (usually it coincides with the RCP) in its plane. NICS(1) reflects better the π-electron effects rather than NICS(0) and it is computed at 1Å above the plane of the ring. NICS$_{ZZ}$ is the isotropic shielding obtained from the out-of-plane tensor components corresponding to the principal axis perpendicular to the plane and thus we have the corresponding indicators NICS$_{ZZ}$(0) and NICS$_{ZZ}$(1).

$$NICS(0) = NICS(1) = -\sigma_{iso} \tag{41}$$

$$NICS_{ZZ}(0) = NICS_{ZZ}(1) = -\sigma_{ZZ} \tag{42}$$

NICS can be dissected into MOs.[251,252] Among the different present techniques, we mention CMO-NICS,[197] which is based on decomposition of total NICS into CMO contributions, defined as:

$$\sigma_{tot} = \sum_{i=1}^{occ} \sigma_{CMO_i} \tag{43}$$

Basically, applying this technique, one can obtain NICS$_{\pi}$(0)/NICS$_{\pi}$(1) as well as NICS$_{\pi ZZ}$(0)/NICS$_{\pi ZZ}$(1) where the isotropic shielding comes from the π contributions. Usually this method is applied for planar systems because in this case π-MOs are well defined. Nowadays, the NBO package[253] is one of the most powerful programs which allows dissecting NICS.

Example I: C_6H_6 and C_4H_4 as aromatic and antiaromatic molecules

$$C_6H_6 \qquad\qquad\qquad C_4H_4$$
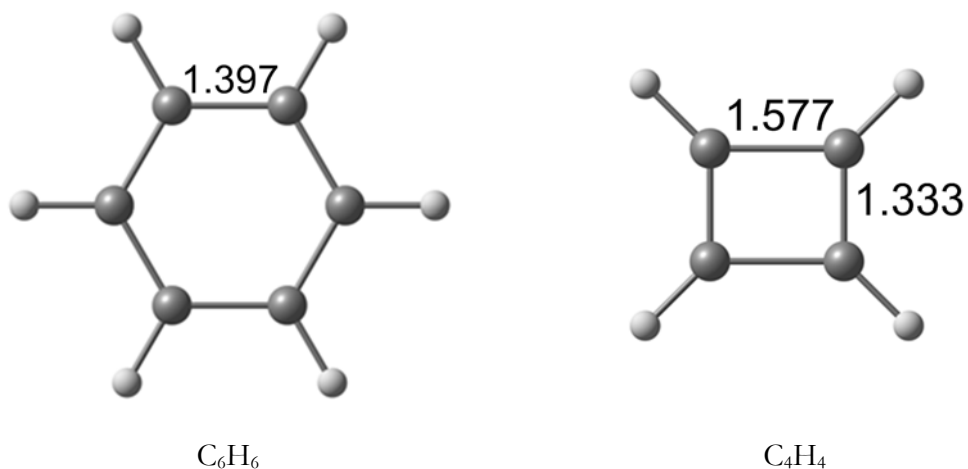
NICS(0) = -8.0	NICS(0)$_\pi$ = -23.4	NICS(0) = 26.4	NICS(0)$_\pi$ = 2.2
NICS(0)$_{ZZ}$ = -14.5	NICS(0)$_{\pi ZZ}$ = -35.8	NICS(0)$_{ZZ}$ = 110.2	NICS(0)$_{\pi ZZ}$ = 56.8
NICS(1) = -10.2	NICS(1)$_\pi$ = -11.4	NICS(1) = 17.5	NICS(1)$_\pi$ = 17.6
NICS(1)$_{ZZ}$ = -29.3	NICS(1)$_{\pi ZZ}$ = -29.1	NICS(1)$_{ZZ}$ = 55.8	NICS(1)$_{\pi ZZ}$ = 50.9

Figure 38. Magnetic-based indicators of benzene and CBD computed at B3LYP/6-311+G(d,p) geometry. Values in ppm. Values in the geometries are bond lengths expressed in Å.

Example II: Al_4^{2-} as a double ($\sigma+\pi$) aromatic metal cluster.
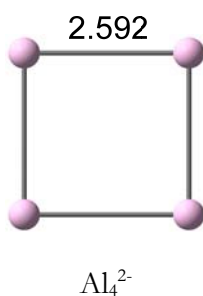
$$Al_4^{2-}$$

NICS(0) = -34.5	NICS(0)$_\pi$ = -21.7
NICS(0)$_{ZZ}$ = -66.1	NICS(0)$_\sigma$ = -12.2
NICS(1) = -27.4	NICS(1)$_{ZZ}$ = -54.9

Figure 39. Magnetic-based indicators of Al_4^{2-} computed at B3LYP/6-311+G(d,p) geometry obtained from reference [254]. Values in ppm. Value in the geometries is a bond length expressed in Å.

Interpretation: With regard to the organic systems, negative NICS values are detected for C_6H_6 revealing its diatropic character and thus, its aromaticity. C_4H_4, an antiaromatic molecule, shows signs of paratropicity due to the positive NICS values. In relation to Al_4^{2-}, the evidence of σ- and π-aromaticity is irrefutable due to the negative NICS values that are indicative of diatropicity.

Drawbacks: NICS values do not properly describe the trend of aromaticity when comparing rings with different size.[234] Besides, single NICS calculations should be avoided when describing the aromaticity of fused rings. In that case, $NICS_{XY}$ scans are more reliable. NICS in fused rings can incorporate the magnetic response of neighboring rings leading to spurious results.

2.3.4 Tests of aromaticity indicators

In 2008, Feixas *et al.*[234] proposed different aromaticity tests to analyze the advantages and drawbacks of a group of aromaticity descriptors. In particular, they suggested fifteen tests and applied ten indicators of aromaticity: HOMA, FLU, I_{ring}, I_{NG}, I_{NB}, MCI, NICS(0), NICS(1) and NICS(1)$_{ZZ}$. These tests include a variety of cases from simple benzene distortions to the study of chemical reactions.

Their results indicated that the best descriptors of aromaticity are the multicenter indices, especially the MCI, that passed all tests. Three recommendations were proposed from the application of the different indicators in the different tests: i) the indicators that depend on reference values such as HOMA and FLU should not be employed to study the aromaticity changes in chemical reactions; ii) comparing the aromatic character of rings with different sizes or with different atoms types in terms of NICS indices should be avoided; iii) even though electronic indices are generally considered reliable indices, PDI has problems to describe the aromatic character of rings with out-of-plane deformations.

2.4 Energy decomposition analysis (EDA)

The enormous importance of conjugation, hyperconjugation and aromaticity is reflected in the great number of different approaches that have been developed to estimate their relative strengths, not only in organic chemistry,[255,256] but in organometallic compounds[257] as well. Different methodologies have been discussed above but in this section we will only focus on

the energy decomposition analysis (EDA) which is strictly connected with the chemical bonding.

EDA was developed independently by Morokuma[258] and by Rauk and Ziegler.[259] This method has been proved to provide important and useful information about the nature of the chemical bonding.[193] The EDA decomposes the interaction energy (ΔE_{int}) between two fragments A and B in a molecule A–B into three terms: the electrostatic interaction between the charge densities of the fragments (ΔE_{elstat}), the exchange repulsion between the fragments due to Pauli's principle (ΔE_{Pauli}) and the energy gain due to orbital mixing of the fragments (ΔE_{orb}).

The EDA considers the formation of a molecule A–B with the corresponding wavefunction Ψ_{AB} and energy E_{AB} as the result of the interactions between fragments A^0 and B^0 in their electronic and geometric ground states Ψ_A^0 and Ψ_B^0 with energies E_A^0 and E_B^0, which are divided into several steps. In the first step, the fragments A^0 and B^0 are distorted from the equilibrium geometries and wavefunctions Ψ_A^0 and Ψ_B^0 to the geometries and electronic states Ψ_A and Ψ_B (with energies E_A and E_B), which they possess in the molecule A–B.[193] The total energy that is necessary to distort and electronically excite all fragments to this state is the preparation energy ΔE_{prep}:

$$\Delta E_{prep} = E_A - E_{A0} + E_B - E_{B0} \tag{44}$$

The focus of the EDA lies on the analysis of the ΔE_{int}, which is the difference between the energy of the molecule E_{AB} and the energies of the prepared fragments E_A and E_B:

$$\Delta E_{int} = E_{AB} - E_A - E_B \tag{45}$$

Then the total bonding energy (ΔE) is the sum of ΔE_{prep} and ΔE_{int}:

$$\Delta E = \Delta E_{prep} + \Delta E_{int} \tag{46}$$

In the first step of the bond formation according to the EDA, the distorted fragments with frozen charge densities A and B are brought from infinite separation to the position in the molecule. This state is the promolecule with the product wavefunction $\Psi_A\Psi_B$ and the energy E_{AB}^0. The interaction between the frozen charge densities of A and B at the equilibrium geometry of AB gives the quasiclassical Coulomb interaction ΔE_{elstat}:

$$\Delta \mathrm{E}_{elstat} = \sum_{\alpha \in A} \sum_{\beta \in B} \frac{Z_\alpha Z_\beta}{R_{\alpha\beta}} + \int dr V_B(r)\rho_A(r) + \int dr V_A(r)\rho_B(r)$$
$$+ \int \int dr_1 dr_2 \frac{\rho_A(r_1)\rho_B(r_2)}{r_{12}} \tag{47}$$

In the second step of the EDA, the product $\Psi_A\Psi_B$, which violates the Pauli principle, is antisymmetrized and renormalized to give an intermediate state Ψ^0 with the corresponding energy E^0. The energy difference between E^0_{AB} and E^0 is defined as exchange (Pauli) repulsion ($\Delta E_{\mathrm{Pauli}}$):

$$\Psi^0 = N\hat{A}\{\Psi_A\Psi_B\}$$
$$\Delta \mathrm{E}_{Pauli} = E^0_{AB} - E_0 \tag{48}$$

In the third step, Ψ^0 is relaxed to yield the final state Ψ_{AB} of the molecule A–B with the energy E_{AB}. The associated energy lowering comes from the orbital mixing, and thus, it can be identified as covalent contribution to the chemical bond. It is termed orbital interaction (ΔE_{orb}):

$$\Delta \mathrm{E}_{orb} = E_{AB} - E^0_{AB} \tag{47}$$

Finally, the summation of $\Delta E_{\mathrm{elstat}}$, $\Delta E_{\mathrm{Pauli}}$ and ΔE_{orb} gives the total interaction energy (ΔE_{int}):

$$\Delta \mathrm{E}_{int} = \Delta E_{elstat} + \Delta E_{Pauli} + \Delta E_{orb} \tag{49}$$

It is possible to decompose the orbital interaction ΔE_{orb} into contributions from orbitals, which belong to different irreducible representations Γ of the point group of the molecule:

$$\Delta E_{orb} = \sum_{\Gamma} \Delta E_\Gamma \tag{50}$$

The ΔE_{orb} term is always attractive as the total wavefunction is optimized during its calculation. Small repulsive values for contributions of irreducible representations to the total orbital interaction are due to numerical errors in the computation. Large repulsive values for orbital interactions always indicate a wrong setup of the fragments for the EDA calculation. The $\Delta E_{\mathrm{Pauli}}$ term is always repulsive as additional constraints are added to the wavefunction. The $\Delta E_{\mathrm{elstat}}$ term is usually attractive, but in special cases, it can yield repulsive contributions (*vide infra*).

The EDA calculations are usually performed in the framework of DFT and also their values depend on the functional that is used. In case of carrying out calculations with dispersion,

such as methods proposed by Grimme,[260,261] EDA is not being affected and the dispersion interaction appears as an extra term (ΔE_{disp}). Yet, if the dispersion interaction is part of the functional, then the EDA will change.

2.5 Noncovalent interactions (NCI) index

Noncovalent interactions are important in chemical and biological systems. Among the different systems which the noncovalent interactions can be present, it is worth mentioning the protein-ligand interactions,[262] the protein folding[262] or the packing of molecular crystals.[262] Yet, in these particular systems, the noncovalent interactions are weak. The most common noncovalent interactions are van der Waals interactions (vdW), steric clashes (SC) and hydrogen bonds (HB).

NCI analysis is a visual index that identifies noncovalent interactions using the electron density and its first derivative. NCI index[263] is given by,

$$ s = \frac{1}{2(3\pi^2)^{\frac{1}{3}}} \cdot \frac{|\nabla\rho|}{\rho^{\frac{4}{3}}} \tag{51} $$

where s is the reduced density gradient and ρ is the electron density. A crucial change in the reduced gradient between the interacting atoms is presented in weak inter- or intramolecular interactions producing density critical points between interacting fragments (Figure 40a,b). $s(\rho)$ is associated with each critical point.[263]

Troughs in s are dominated at low densities by ρ and tends to diverge except in the regions around a density critical point, where $\nabla\rho$ dominates, and s approaches zero. This behavior is depicted in Figure 40c,d, which shows that the main difference in the $s(\rho)$ plots between a monomer and a dimer is the steep trough at low density ($\rho \approx 0$). Searching for the points in real space giving rise to this feature, the noncovalent region clearly appears in the (supra)molecular complex as a green isosurface (Figure 40f).[263]
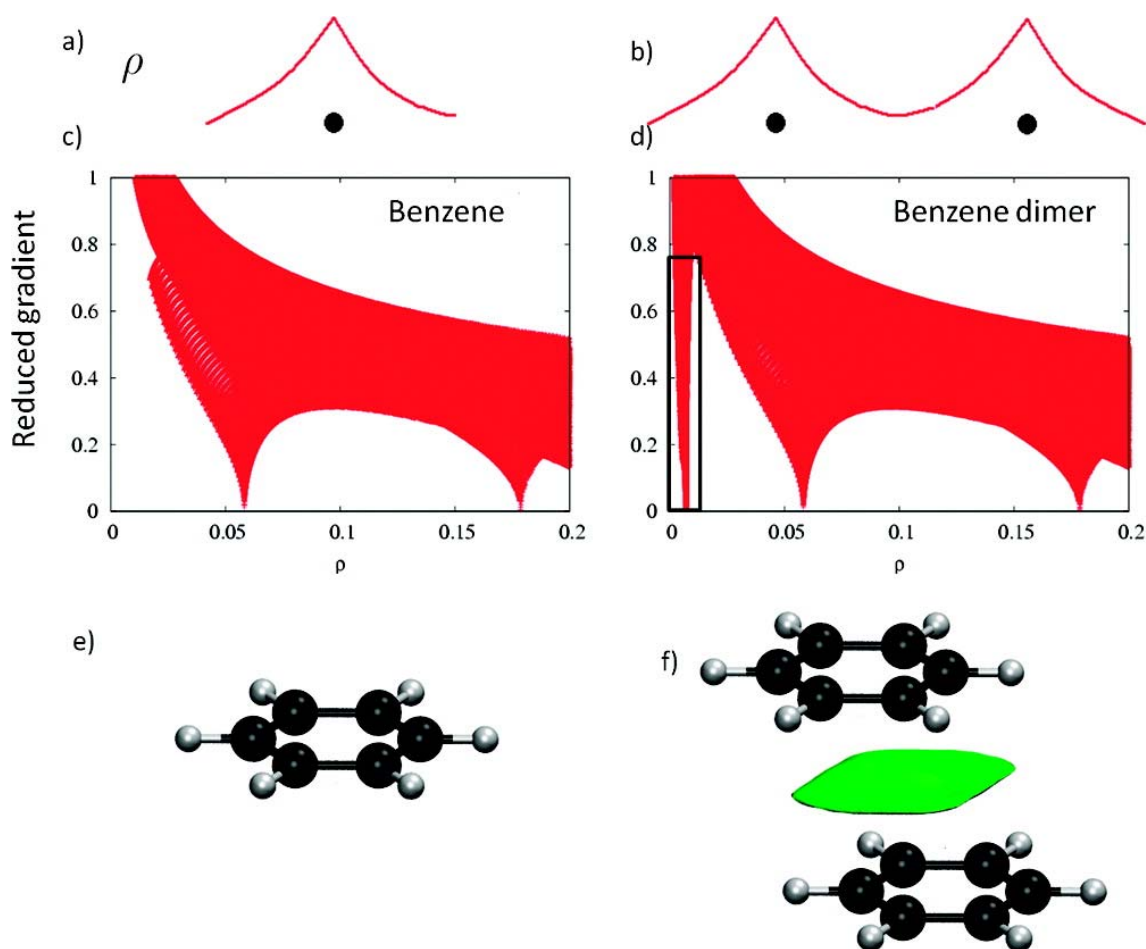
Figure 40. a) Representative behavior of atomic density. (b) Appearance of a $s(\rho(\vec{r}))$ singularity when two atomic densities approach each other. (c, d) Comparison of the reduced density behavior for the benzene monomer and dimer; a singularity in s appears at low density values in the dimer case. (e) Benzene monomer. (f) Appearance of an intermolecular interaction surface in the benzene dimer, associated with the additional singularity in the $s(\rho)$ plot. The isosurface was generated for $s = 0.7$ au and $\rho < 0.01$ au. Figure reproduced with permission from reference [263].

Second derivatives of the density ($\nabla^2\rho$), which are provided by the Hessian matrix (see section 2.1.1.1), are used to distinguish between attractive (favorable) and repulsive (unfavorable) interactions. To discriminate between them or characterize the strength of the interaction, the sign of the second eigenvalue (λ_2) is used. Interestingly, the λ_2 can be either positive or negative, depending on the interaction type. Bonding interactions, such as HB, are characterized by an accumulation of density perpendicular to the bond, and $\lambda_2 < 0$. Repulsion interactions, such as steric repulsion, produce density depletion, such that $\lambda_2 > 0$. Finally, vdW interactions are characterized by a negligible density overlap that gives $\lambda_2 \lesssim 0$.

Hence, NCI index can provide an image that indicates which type of interactions rules the molecule. For each type of interaction, NCIPLOT[263] assigns a color: blue for attractive interactions, green for weak interactions and red for repulsive interactions (Figure 41).
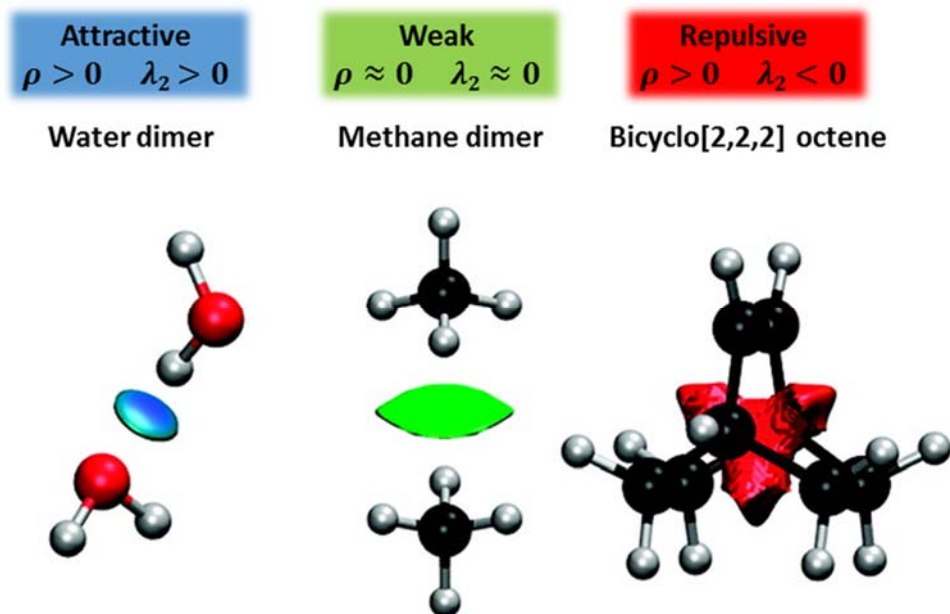
Figure 41. Attractive, weak and repulsive interactions for water dimer, methane dimer and bicyclo[2,2,2]octene. Figure adapted from reference [263].

CHAPTER 3: OBJECTIVES

The major aim of this thesis is to investigate the aromaticity of organic compounds and metal clusters. With respect to the former, the analysis has focused on the evaluation of aromaticity in their excited states by means of electron sharing indices. With respect to the metal clusters, even though their three-dimensional aromaticity is the main focus, the chemical bonding has also been analyzed in detail.

This thesis is further divided into three blocks that can be summarized in eight concrete objectives.

1. The main goal of the first block is the computational validation of the Glidewell-Lloyd's rule by means of DFT. For such aim, we analyse the molecular and electronic structure of 69 PCHs composed of different combinations of 4-, 6- and 8-MRs (Chapter 4).

2. The aim of the second block is the study of the aromaticity in the excited states in organic compounds. To achieve this goal, we propose the following objectives:

2.1. We analyze the effect of changing the spin ($S = 0$–6) in the DA cycloaddition between C_{60} and two different dienes, cyclopentadiene and isoindene using DFT. We advance that a regioselectivity inversion is occurred when going from the S_0 to the T_1 state. This study will reveal whether the aromaticity plays a role in the regioselectivity of the reaction or not. Moreover, experimental studies were carried out by Prof. N. Martin's group to corroborate them with our computational findings (Chapter 5.1).

2.2. We validate the fact that certain regions of the PES of the [2+2] photochemical conversion of norbornadiene (NBD) into quadricyclane (QC) at S_1 state can be influenced by homoaromaticity by means of MCI (Chapter 5.2).

2.3. Ottosson's group have attempted to combine the Baird's and Clar's rule to rationalize the triplet state energies of PAHs that have central $4n\pi$-electrons units (CBD, COT and PEN). To test their hypothesis, as part of my contribution, an aromaticity analysis has been carried out by means of FLU (Chapter 5.3).

3. The goal of the third block is based on three different works that involve aromaticity and chemical bonding studies on small metal clusters. The following objectives are enclosed:

3.1. We study the chemical bonding of the B_6^{2-} and Al_6^{2-} clusters. Al and B belong to group 13 but B_6^{2-} prefers the planar D_{2h} geometry, whereas Al_6^{2-} favours the O_h structure. Even though this has been already investigated, here we aim to provide a more detailed picture of the reasons for the observed geometry differences performing an EDA based on the turn-upside-down approach. $X_2Y_4^{2-}$ and $X_3Y_3^{2-}$ (X, Y = B, Al, Ga) mixed clusters have been also analysed (Chapter 6.1).

3.2. By means of MCI and NICS, we investigate the aromaticity of a series of octahedral metal clusters, O_h X_6^q (X = Li–C and Be–Si) with charges going from -2 to $+4$ and in $^{2S+1}A_{1g}$ electronic states with spin multiplicities ranging from the singlet (S = 0) to the septet (S = 3). First, we want to check whether a closed-shell structure or a half-filled shell with same spin electrons in O_h species is a sufficient requirement to generate aromaticity and, second, we aim to investigate the existence of a possible rule of aromaticity for octahedral compounds (Chapter 6.2).

3.3. O_h Li_6^+ (S=3/2) and O_h Be_6 (S=2) which have been treated in Chapter 6.2 possess NNAs that are typical of electrides. Thus, we investigate in detail the chemical bonding in these two metal clusters by means of the Laplacian of the electron density (Chapter 6.3).

3.4. Related to previously analyzed O_h Li_6^+ (S=3/2), we propose to analyse the chemical bonding of a series of lithium clusters, $^{2S+1}Li_n$ (n=3…5) with all the

possible spin combinations. Besides, using the Laplacian of the electron density, we attempt to design a receipt that allows us to classify whether a system behave like an electride, metal or a combination of both (Chapter 6.3).

CHAPTER 4: EXTENDED GLIDEWELL-LLOYD'S RULE[a]

In this chapter, DFT calculations are used to validate the Glidewell-Lloyd's rule. To this end, we analyze the molecular and electronic structure of different PCHs composed of different combinations of 4-MRs, 6-MRs and 8-MRs.

4.1 State-of-the-art

In sections 1.4.1 and 1.4.2, we mentioned that the Hückel's $(4n+2)\pi$-electron rule is strictly valid only for conjugated monocyclic systems and several attempts were made to extend this rule to PAHs. The most popular one was the Clar's π-sextet rule[19,60] which can be applied only to PAHs having 6-MRs, *i.e.*, benzenoid species. Yet, in 1984, Glidewell and Lloyd[25] proposed to extend the Clar rule to non-benzenoid PCHs.

Somewhat unexpectedly given the chemical importance of non-benzenoid PCHs,[55,264–267] Glidewell and Lloyd's rule is not widely known in the chemical community. To our knowledge, there are neither experimental nor theoretical works analyzing the soundness of this rule, except for the systems studied with the semiempirical MNDO method in the original manuscript by Glidewell and Lloyd.[25] We consider that the time is ripe to examine this rule in deeper detail. Thus, the main aim of this work is to study by means of DFT calculations the validity of this rule. To this end, we will analyze the molecular and electronic structure of 69 PCHs composed of different combinations of 4-MRs, 6-MRs and 8-MRs as shown in Scheme 4. We anticipate here that for most of the studied compounds (but not all) the Glidewell-Lloyd's rule is fully obeyed.

Scheme 4. The 69 PCHs in their closed-shell singlet states with the resonance structure that better defines them from the optimized molecular structure. Ring notation: A and B for 4-MR; C, D and E for 6-MR; F, G and H for 8-MR.

Mol. 45 · Mol. 46 · Mol. 47 · Mol. 48 · Mol. 49 · Mol. 50 · Mol. 51 · Mol. 52 · Mol. 53 · Mol. 54 · Mol. 55 · Mol. 56 · Mol. 57 · Mol. 58 · Mol. 59 · Mol. 60 · Mol. 61 · Mol. 62 · Mol. 63 · Mol. 64 · Mol. 65 · Mol. 66 · Mol. 67 · Mol. 68 · Mol. 69
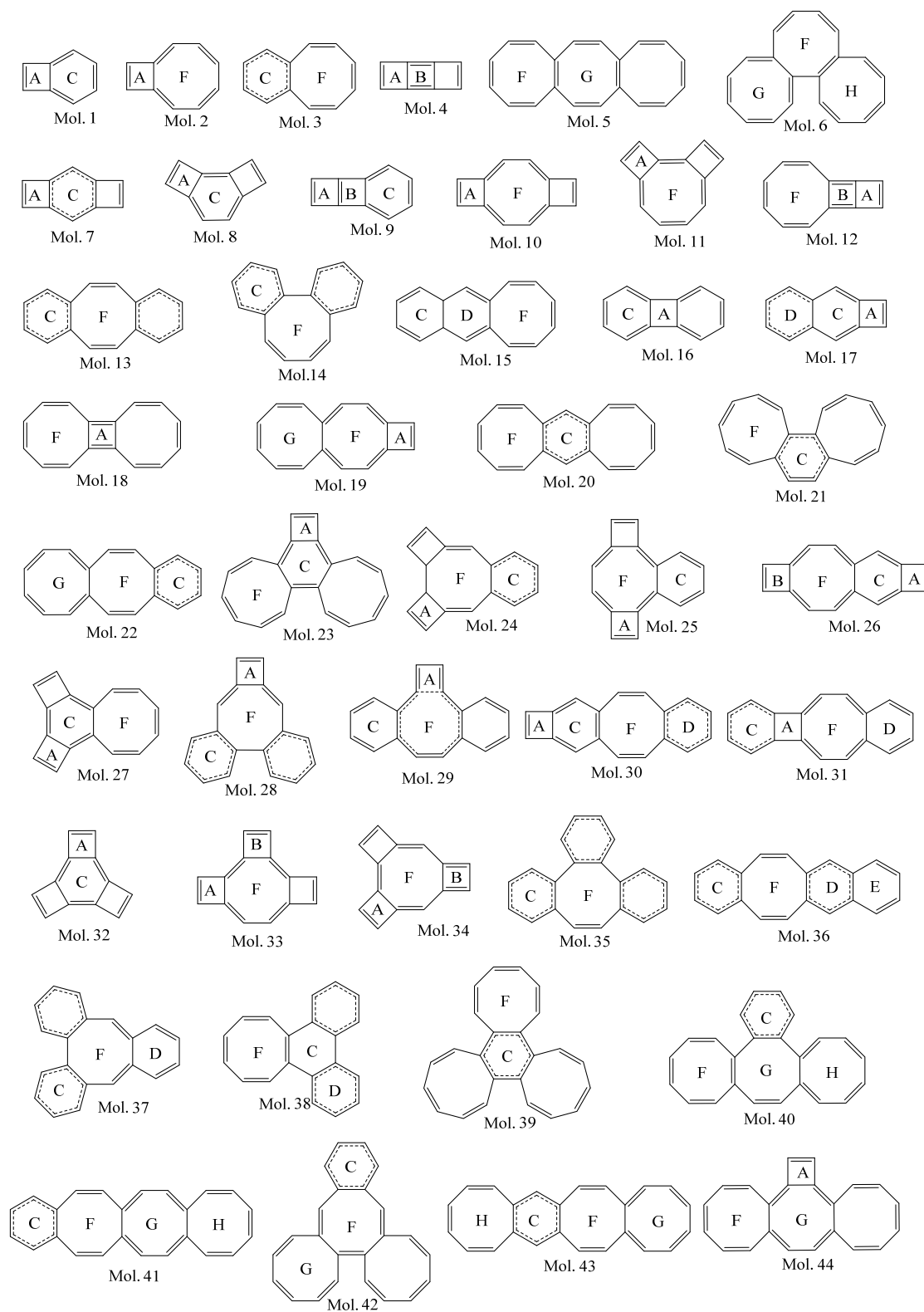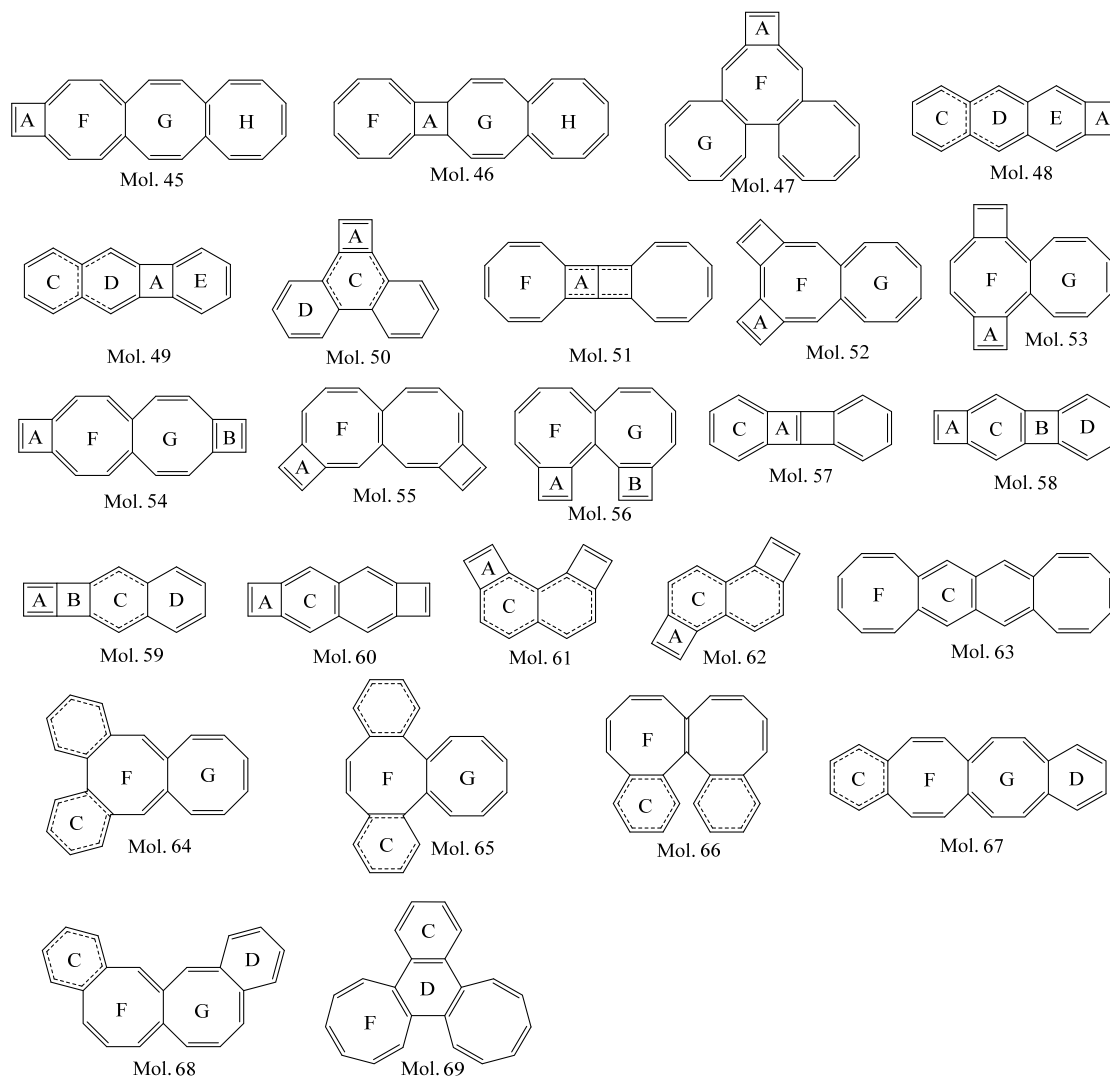
4.2 Results and discussion

The series of PCHs considered in our study is depicted in Scheme 4. We have included molecules having three and four fused rings containing all possible combinations of 4-MRs, 6-MRs, and 8-MRs with three additional requirements to keep a reasonable number of molecules treated: (1) the Lewis structure of the molecule (but not necessarily the molecule) has at least a C_2 symmetry axis; (2) molecules with junctions connecting three rings (highly strained situations) are not considered; and (3) combinations of only 6-MRs are not included because it is already well known that they follow Clar's rule[268] with only few exceptions (coronene could be one of them[175,269], although a recent study proves that Clar's model describes coronene better than other models[270]). In addition, we have also considered the combinations of a 4- and 6-MR, a 4- and 8-MR, and a 6- and 8-MR.

Scheme 4 depicts the covalent Lewis structure that more closely reproduces the geometry of the optimized species. In these structures, double bonds are depicted for the short bonds and single bonds for the long ones. In case we have a ring in which the largest difference between the shortest and longest bond lengths is equal or less than 0.05 Å, we have considered that we have an intermediate delocalized situation in between single and double bonds and we have represented these situations by dashed lines. For molecules with two or more 8-MRs (such as **Mol. 5**, **6**, **18**,…), we optimized all possible orientations of the non-planar 8-MRs. We found that relative energies of the different puckered conformers were in the range 0.3–1.5 kcal/mol. Given the small energy differences and similar geometrical features, we do not expect significant changes in the aromaticity of the rings when going from one to the other conformer.

By looking at the Lewis structures of Scheme 4, the conclusion is that most of the studied species follow the Glidewell–Lloyd rule, *i.e.*, π-electrons in conjugated polycyclic systems tend to form the smallest $4n + 2$ groups and to avoid the formation of the smallest 4n groups. This is the case, for instance, of bicyclodeca[6.2.0]pentaene (**Mol. 2**). The 10π-electrons are distributed 2π-electrons in the 4-MR and 8π-electrons in the 8-MR, avoiding placing 4π-electrons in the 4-MR. Comparison of C–C bond lengths in our optimized structure of **Mol. 2** and the X-ray structure[271] for a substituted derivative of **Mol. 2** (9,10-diphenylbicyclodeca[6.2.0]pentaene) shows that bond lengths differences are smaller than 0.023 Å (the maximum error occurs in the single bond of the 4-MR adjacent to the ring junction), thus providing confidence in our B3LYP/6-311G(d,p)-optimized geometries. However, there are some systems that do not follow the trend expected from the Glidewell–Lloyd's rule. In particular, **Mol. 12**, **18**, **29**, **34**, **51**, and **59** (9 % of the molecules in the set studied) break the rule. For instance, the 4-MR B of **Mol. 12** has 4π-electrons and this is not what one would expect from Glidewell–Lloyd's rule. One could argue that the 4-MR B of **Mol. 4** has also 4π-electrons but, in this case, there is no way to avoid having at least one 4-MR with 4π-electrons, and, therefore, the rule is obeyed. From the set of molecules that follow the Glidewell–Lloyd's rule, one can also extract interesting conclusions. For this reason, we divide this section into two parts. In the first part, we analyze the set of molecules that obey Glidewell–Lloyd's rule. In the second one, we discuss the reasons for the breakdown of the Glidewell–Lloyd's rule in the six particular cases found.

4.2.1 Polycyclic conjugated hydrocarbons that obey Glidewell–Lloyd's rule

Table 3 collects the relative energies of all isomers with the same ring types. The values of the MCI for all rings of the analyzed PCHs are given in Table 4 (values for HOMA and FLU indicators of aromaticity are collected in the SI of reference [272]). This table also contains the MCI values of CBD, benzene, and COT in the closed-shell singlet ground state and the lowest-lying triplet state for comparison purposes.

Table 3. The relative energies (kcal/mol) of subgroups of isomers that have the same ring-types. All species are considered in their low-lying singlet closed-shell states.

Systems	ΔE_{rel}	Systems	ΔE_{rel}
Mol. 6	0.00	**Mol. 42**	0.00
Mol. 5	3.71	**Mol. 41**	0.60
Mol. 8	0.00	**Mol. 40**	3.36
Mol. 7	17.02	**Mol. 43**	3.43
Mol. 9	42.32	**Mol. 39**	10.04
Mol. 10	0.00	**Mol. 46**	0.00
Mol. 11	2.54	**Mol. 45**	22.13
Mol. 12	48.12	**Mol. 44**	23.73
Mol. 14	0.00	**Mol. 47**	30.34
Mol. 13	0.17	**Mol. 49**	0.00
Mol. 15	7.75	**Mol. 48**	13.93
Mol. 16	0.00	**Mol. 50**	28.20
Mol. 17	9.43	**Mol. 52**	0.00
Mol. 18	0.00	**Mol. 55**	7.07
Mol. 19	23.49	**Mol. 53**	9.32
Mol. 22	0.00	**Mol. 56**	24.83
Mol. 20	1.17	**Mol. 51**	25.80
Mol. 21	3.96	**Mol. 54**	28.54
Mol. 24	0.00	**Mol. 58**	0.00
Mol. 25	16.20	**Mol. 60**	6.08
Mol. 26	32.76	**Mol. 62**	26.32
Mol. 27	44.17	**Mol. 57**	27.12
Mol. 28	0.00	**Mol. 61**	27.47
Mol. 31	17.89	**Mol. 59**	30.34
Mol. 30	22.69	**Mol. 64**	0.00
Mol. 29	23.52	**Mol. 63**	11.32
Mol. 33	0.00	**Mol. 65**	11.69
Mol. 34	22.33	**Mol. 69**	15.03
Mol. 35	0.00	**Mol. 68**	21.75
Mol. 36	8.52	**Mol. 67**	25.75
Mol. 38	17.55	**Mol. 66**	29.79
Mol. 37	24.99		

Table 4. The MCI values (units are electrons) for the rings in the closed-shell singlet state of the studied species and for CBD, benzene, and COT in closed-shell singlet and lowest-lying triplet states. Values computed at B3LYP/6-311G(d,p) level.

MCI	4-MR		6-MR			8-MR		
System	Ring A	Ring B	Ring C	Ring D	Ring E	Ring F	Ring G	Ring H
Mol. 1	0.0214		0.0507					
Mol. 2	0.0257					0.0002		
Mol. 3			0.0618			0.0008		
Mol. 4	0.0244	0.0398						
Mol. 5						0.0008	0.0007	
Mol. 6						0.0007	0.0001	0.0000
Mol. 7	0.0160		0.0601					
Mol. 8	0.0283		0.0150					
Mol. 9	0.0171	0.0259	0.0550					
Mol. 10	0.0299					0.0021		
Mol. 11	0.0294					0.0023		
Mol. 12	0.0338	0.0318				0.0029		
Mol. 13			0.0614			0.0006		
Mol. 14			0.0621			0.0005		
Mol. 15			0.0381	0.0333		0.0009		
Mol. 16	0.0213		0.0560					
Mol. 17	0.0265		0.0188	0.0505				
Mol. 18	0.0367					0.0041		
Mol. 19	0.0280					0.0012	0.0001	
Mol. 20			0.0518			0.0008		
Mol. 21			0.0531			0.0008		
Mol. 22			0.0585			0.0002	0.0008	
Mol. 23	0.0231		0.0351			0.0009		
Mol. 24	0.0285		0.0516			0.0013		
Mol. 25	0.0313		0.0136			0.0016		
Mol. 26	0.0293	0.0283	0.0091			0.0007		
Mol. 27	0.0308		0.0074			0.0029		
Mol. 28	0.0264		0.0590			0.0006		
Mol. 29	0.0093		0.0369			-0.0011		
Mol. 30	0.0230		0.0393	0.0616		0.0006		
Mol. 31	0.0185		0.0393	0.0155		-0.0004		
Mol. 32	0.0275		0.0059					
Mol. 33	0.0285	0.0277				0.0017		
Mol. 34	0.0290	0.0089				-0.0006		
Mol. 35			0.0623	0.0628		0.0003		
Mol. 36			0.0610	0.0337	0.0375	0.0006		
Mol. 37			0.0610	0.0101		0.0004		

MCI	4-MR		6-MR			8-MR		
System	Ring A	Ring B	Ring C	System	Ring A	Ring B	Ring C	System
Mol. 38			0.0150	0.0477		0.0008		
Mol. 39			0.0462			0.0008		
Mol. 40			0.0629			0.0008	0.0001	0.0008
Mol. 41			0.0587			0.0001	0.0007	0.0002
Mol. 42			0.0605			0.0004	0.0001	
Mol. 43			0.0497			0.0008	0.0001	0.0007
Mol. 44	0.0273					0.0003	0.0011	
Mol. 45	0.0282					0.0013	0.0002	0.0008
Mol. 46	0.0266					0.0013	0.0002	0.0007
Mol. 47	0.0272					0.0008	0.0007	
Mol. 48	0.0284		0.0371	0.0277	0.0125			
Mol. 49	0.0214		0.0456	0.0238	0.0558			
Mol. 50	0.0146		0.0210	0.0377				
Mol. 51	0.0385					0.0031		
Mol. 52	0.0277					0.0003	0.0007	
Mol. 53	0.0307					0.0020	0.0029	
Mol. 54	0.0278	0.0140				0.0010	-0.0007	
Mol. 55	0.0278					0.0013		
Mol. 56	0.0300	0.0147				0.0014	0.0003	
Mol. 57	0.0248		0.0517					
Mol. 58	0.0204	0.0230	0.0502	0.0518				
Mol. 59	0.0080	0.0074	0.0240	0.0299				
Mol. 60	0.0237		0.0304					
Mol. 61	0.0155		0.3144					
Mol. 62	0.0163		0.0303					
Mol. 63			0.0323			0.0009		
Mol. 64			0.0613			0.0004	0.0002	
Mol. 65			0.0551			-0.0002	-0.0002	
Mol. 66			0.0449			-0.0059		
Mol. 67			0.0107	0.0583		0.0002	0.0020	
Mol. 68			0.0616	0.0136		-0.0001	0.0006	
Mol. 69			0.0411	0.0276		0.0008		
CBD	0.0094							
benzene			0.0726					
COT						0.0009		
CBD triplet [a]	0.1257							
benzene triplet [a]			-0.0001					
COT triplet [a]						0.0275		

[a] Species in the lowest-lying triplet state.

The $4n+2$ Hückel's rule strictly holds for monocyclic systems like CBD or benzene. The breakdown of this rule in PAHs was already well recognized in the beginning of the 1950s.[273] A first attempt to extend the Hückel's $(4n+2)\pi$-electron rule from monocyclic annulenes to PAHs corresponded to Platt's ring perimeter model.[274] According to this model, PAHs can be divided into two parts: a perimeter and an inner core. The perimeter is considered as an annulene, and the inner core represents only a perturbation of the perimeter. The aromatic character of the PAH is that of the annulene of the perimeter as derived from Hückel's rule. Although this rule can explain the aromaticity of PAHs such as pyrene or coronene, it presents many exceptions in PCHs. For instance, bicyclodeca[6.2.0]pentaene (**Mol. 2**) with 10 π-electrons in its perimeter is antiaromatic (at least the 8-MR), despite following Hückel's rule. Other examples of the failure of the Platt's ring perimeter model are **Mol. 17**, **32**, **33**, or **34**. In other cases, the situation is less clear. For instance, **Mol. 24** should be considered antiaromatic according to the Platt's ring perimeter model but it has an antiaromatic 8-MR, an aromatic 6-MR, and two non-aromatic 4-MRs. In general, Platt's ring perimeter model fails to indicate aromaticity in PCHs.

Results on clamped benzenes and cyclooctatetraenes represent another source of interesting information. In general, significant bond length alternation is achieved when the benzene ring is annelated with clamping groups such as cyclopropa-, cyclobuta-, and CBD clamps.[275–278] However, as shown by Soncini *et al.*[275] using ring currents and by some of us[234,279,280] using different electronic, magnetic, and geometric indices of aromaticity, the aromatic character of the benzene ring changes only slightly. By comparing the clamping effect on a benzene ring of a CBD (**Mol. 1**) and COT (**Mol. 3**) clamps, one concludes that the CBD clamp localizes stronger than the COT ring. In the case of two clamped units attached to the benzene ring, the localization effect of two clamps is larger if they are located in meta than in para position. Comparison of isomers **24** and **27** provides support to the idea that 4-MRs when fused to 8-MRs result in more stable molecules than when clamped to 6-MRs (see **Table 3**). For three clamped rings, 4-MRs (**Mol. 32**) again have stronger localization effects than 8-MRs (**Mol. 39**). In all these cases, the more localized the 6-MRs, the lower their aromaticities, with the exception of rings **Mol. 20** and **21** that have similar aromaticities according to all indices. In biphenylene (**Mol. 16**), a 4-MR joins two 6-MRs. In this case, the localizing effect of the 4-MR is somewhat weaker than in **Mol. 1**. In fact, molecules having a 4-MR joining two 6- or 8-MRs are more stable than the corresponding isomers with an external 4-MR (compare in **Table 3**, for instance, **Mol. 16** and **Mol. 17**, **18** and **Mol. 19**, **30**

and **31**, **Mol. 44–47**, **Mol. 48** and **49**, and **Mol. 58–62**). Interestingly, **Mol. 18** that disobeys the Glidewell–Lloyd's rule is more stable than **Mol. 19** that follows it, in a similar manner as **Mol. 16** is more stable than **Mol. 17** (even though these latter two molecules they follow the rule). Another interesting case is given by **Mol. 31**, in which the 6-MR (ring C) fused to a 4-MR is more aromatic and has a more delocalized π-system than ring D with a clamped 8-MR. This result is somewhat unexpected from the effects of clamping 4- and 8-MRs discussed above. However, there is an explanation. There are two possibilities to locate a π-sextet in ring D. In one of them, one has to locate 4 π-electrons (two double bonds) in the 4-MR and this situation is unfavorable according to the Glidewell–Lloyd rule. Another option is to have π-sextets in rings D and C and 2 π-electrons in the 4-MR. However, this double bond in the 4-MR has to be located in the ring junction between the 8- and the 4-MR, and as we will see later, this situation is avoided as much as possible. Therefore, the most representative Lewis structure of **Mol. 31** is the one depicted in Scheme 4.

As already said, CBD clamps in benzene rings reduce their aromaticity. Interestingly, when fused to COT rings, the clamps most often decrease the antiaromaticity of these 8-MRs as indicated by the electronic indices of aromaticity (see MCI results for **Mol. 10–12**, **19**, **24**, **25**, **33**, **45**, **51**, **53–56**). Similarly, all indices of aromaticity show that 4-MRs increase their aromaticity as compared to CBD when fused to generate PCHs. The only exceptions correspond to ring B of **Mol. 34** and rings A and B of **Mol. 59**. These rings are found by MCI (but not by FLU nor HOMA) somewhat more antiaromatic than CBD. **Mol. 34** and **59** are two molecules that disobey Glidewell–Lloyd's rule and will be discussed in the next subsection.

With some exceptions, the aromaticity of all 4- and 8-MRs in the PCHs studied increases with respect to that of CBD and COT, while that of the 6-MRs decreases as compared to benzene. For 4-MRs, MCI values are in the range 0.007–0.398 e (reference value of CBD is 0.009 e), whereas MCIs of 6-MRs vary between 0.006 and 0.063 e (benzene reference value is 0.073 e) and for 8-MRs MCIs are found in between 0.000 and 0.0041 e (0.001 e is the reference value of COT). From these values, it becomes evident that the antiaromaticity of 8-MRs is quite constant, irrespective of the formal number of π-electrons (2, 4, 6, or 8) in the ring, whereas that of 4- and 6-MRs can change quite a lot depending on the PCH considered. It is worth mentioning that **Mol. 32** represents the only example in which, in a

given molecule, the 4-MRs are more aromatic than the 6-MR as shown by all indices used in this work.

It is well known that kinked polycyclic benzenoids are more stable than linear ones.[281] The paradigmatic example is phenanthrene that is more stable than anthracene by about 4–8 kcal/mol because of better π-interactions.[281] Apparently, the situation is reproduced when 6-MRs are replaced by 8-MRs and **Mol. 6** is more stable than **Mol. 5** by 3.7 kcal/mol at the B3LYP/6-311G(d,p) level of theory. It is likely that the reason is not because of better π-interactions in this case, since all 8-MRs of **Mol. 5** and **6** have similar antiaromaticities. Same situation is found when comparing **Mol. 7** and **8**. Again kinked **Mol. 8** is more stable than linear **Mol. 7**, in this case by 17.0 kcal/mol. From the aromaticity indices, it seems that **Mol. 7** is more aromatic than **Mol. 8**, and, therefore, the reason for the higher stability of **Mol. 8** is not likely to be better π-interactions. Although this kinked rule of stability seems to be quite general, in fact, it is not and, for instance, **Mol. 13** and **14** are isoenergetic or linear **Mol. 10** and **20** are more stable than kinked **Mol. 11** and **21** by 2.5 and 2.8 kcal/mol, respectively. An EDA would be needed to find the reason of the relative stabilities of these PCHs.

Finally, there are three molecules that follow the Glidewell–Lloyd rule in its low-lying closed-shell singlet state but for which the ground state is an open-shell singlet (O-SS) with the triplet being a low-lying excited state. These are molecules **Mol. 4**, **9**, and **57** that have three and two adjacent 4-MRs. In **Mol. 4**, one of the 4-MRs has 4 π-electrons. In **Mol. 9** and **57**, one of the 4-MRs has a double bond in the ring junction between two 4-MRs. In these molecules, the ring junction between two 4-MRs breaks and the molecule forms a biradical 6-MR with a structure analogous to that of p-benzyne (henceforth, we name these species with the prefix BR, see Scheme 5). For **BR-4**, the O-SS state is 7.0 more stable than the triplet (in p-benzyne this difference is about 4–6 kcal/mol[282]) and 57.9 more stable than the closed-shell singlet of **Mol. 4**. This situation was already discussed by Dewar and Li in 1974 comparing butalene (two fused 4-MRs) and p-benzyne using the MINDO/3 method.[283] The aromaticity of the 6-MR in the ground state of **BR-4** is significantly less than that of the 6-MR in **Mol. 1**. The same behavior is observed for **Mol. 9**. In that case, the O-SS state of **BR-9** is more stable by 2.7 and 61.3 kcal/mol than the triplet of **BR-9** and the closed-shell singlet states of **Mol. 9**, respectively. The higher stability of the O-SS with respect to the triplet is attributed to the existence of some 1,4-interaction in the benzyne ring.[282] For **BR-57**, the O-

SS is more stable than the triplet by 9.1 kcal/mol and more stable than the closed-shell singlet structure by 23.5 kcal/mol.

Scheme 5. The PCHs having an open-shell singlet (O-SS) biradical (BR) ground state with the resonance structure that better defines them from the optimized molecular structure.

Mol. BR-4
(O-SS biradical)

Mol. BR-9
(O-SS biradical)

Mol. BR-12
(O-SS biradical)

Mol. BR-51
(O-SS biradical)

Mol. BR-57
(O-SS biradical)

Mol. BR-59
(O-SS biradical)
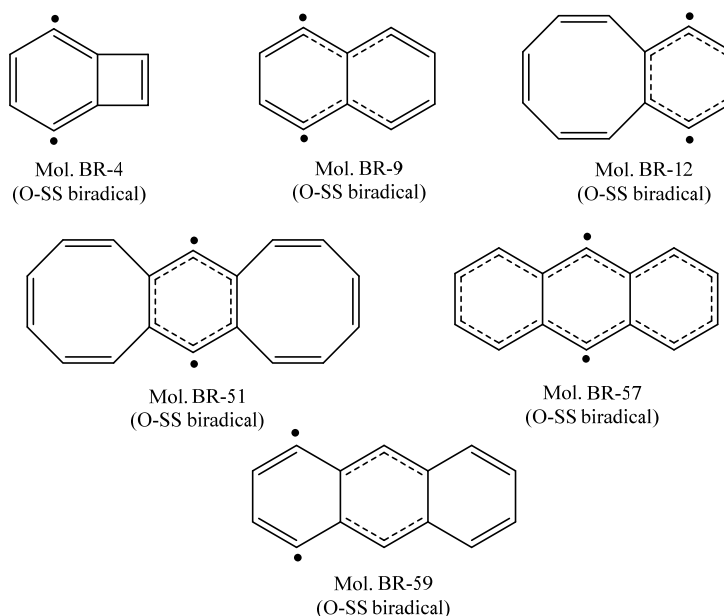
Let us finally discuss the case of **Mol. 54** and **56**. The most stable structure of molecules **Mol. 54** and **56** in their closed-shell singlet state is shown in black in Scheme 6. Alternative structures depicted in red in Scheme 6 are also minima. They are less stable than those in black by 1.7 and 4.9 kcal/mol, as expected from Glidewell–Lloyd rule. However, the closed-shell singlet state is not the ground state for these molecules. The ground state is an O-SS state that is by 4.3 and 3.2 kcal/mol more stable for **Mol. 54** and **56**, respectively, than the closed-shell singlet state. In the O-SS, the biradical character is located in rings B that become aromatic as expected from the Baird's rule.[20]

Scheme 6. In black, the most stable structure of **Mol. 54** and **56** in their closed-shell singlet state. In red, alternative structures of these molecules in their closed-shell singlet state.
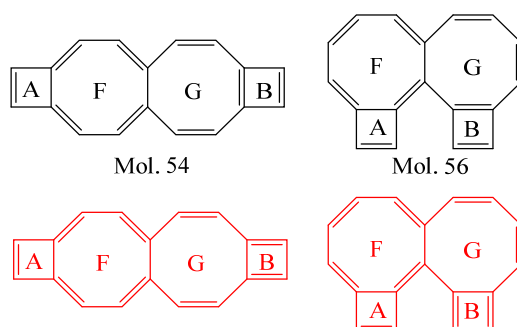
4.2.2 Polycyclic conjugated hydrocarbons that disobey Glidewell–Lloyd's rule

As commented above, in the set of molecules studied, there are six molecules disobeying the Glidewell–Lloyd rule in the closed-shell singlet state that are discussed in the following paragraphs. The expected structures for these molecules according to Glidewell–Lloyd's rule are displayed in Scheme 7.

Scheme 7. The predicted structure by Glidewell-Lloyd's rule of the studied PCHs that disobey this rule.
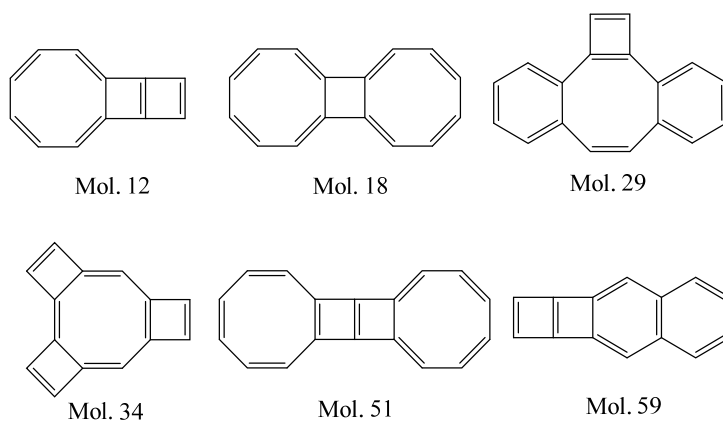
Mol. 12, **51**, and **59** have a similar behavior. In these cases, we have two adjacent 4-MRs that are fused to 6- or 8-MRs. In these systems, the expected Glidewell–Lloyd structure has a double bond located in the ring junction between two 4-MRs that destabilizes this situation. For this reason, they break the Glidewell–Lloyd prediction. For these systems, the O-SS state with a broken C–C ring junction between the 4-MRs (see Scheme 4) is the ground state, so one cannot strictly state that the Glidewell–Lloyd's rule is disobeyed in these molecules

because the closed-shell singlet state is an excited state. For these molecules in the closed-shell singlet state, the location of two double bonds in a 4-MR is less unfavorable than to place double bonds in between two 4-MRs as depicted in Scheme 7. It is likely that these two closed-shell singlet possibilities are not far in energy since compounds **Mol. 9** and **57** prefer to follow the Glidewell–Lloyd rule. For **Mol. 12**, **51**, and **59**, the O-SS ground state (*i.e.*, **BR-12**, **BR-51**, and **BR-59**, see Scheme 5) is more stable than the closed-shell singlet by 19.8, 7.4, and 28.0 kcal/mol, respectively. Besides, the O-SS is more stable than the triplet state for **BR-12** and **BR-51** (by 1.6 and 0.9 kcal/mol, respectively) but not for **BR-59** in which the triplet state is more stable than the O-SS by 10.1 kcal/mol.

Mol. 34 is similar to the group of three molecules discussed in the paragraph above. In the lowest-lying closed-shell singlet state, one of the 4-MRs (ring B) has formally 4 π-electrons. It is worth noting that this molecule is more stable by 4.6 kcal/mol in the O-SS state. The biradical character in this state is concentrated mainly in ring B that becomes Baird aromatic[67] (MCI in rings A and B of the ground state of **Mol. 34** is 0.031 and 0.053 e, respectively), thus stabilizing the system. In **Mol. 34**, the triplet state lies by 2.2 kcal/mol higher in energy than the O-SS ground state.

Because the ground state is not a closed-shell singlet, we consider that **Mol. 12**, **34**, **51**, and **59** do not represent "real" failures of the Glidewell–Lloyd rule. **Mol. 29** is a very particular case. To avoid placing a double bond in the ring junction between the 4- and 8-MR as expected from the Glidewell–Lloyd prediction (see Scheme 7), the molecule prefers to put 4 π-electrons in 4-MR A. As a consequence, the ring junction between rings A and F is elongated to 1.610 Å (Scheme 4). In this situation, one can consider that instead of rings A and F, one has a 10-MR with 10 π-electrons having Hückel aromaticity. This result is reinforced from the calculation of the MCI (0.003 e), FLU (0.017), and HOMA (0.553) that proves a certain aromatic character of the 10-MR. The ground state of this molecule is closed-shell singlet and, therefore, has to be considered a real example of failure of the Glidewell–Lloyd rule.

Finally, **Mol. 18** is an interesting case that does not follow Glidewell–Lloyd's rule either. The structure predicted by this rule is shown in Scheme 7. The preferred structure depicted in Scheme 4 avoids having two $4n$ large rings (8-MRs F) paying the price of having one small $4n$ ring (4-MR A).

Taking into account these results, one should reformulate the Glidewell–Lloyd rule by writing: "the total population of π-electrons in conjugated polycyclic hydrocarbons *that have a closed-shell singlet ground state* tends to form the smallest $4n + 2$ groups and to avoid the formation of the smallest $4n$ groups, *except in the case that avoiding formation of the smallest $4n$ groups results in the formation of a greater number of large $4n$ groups.*"

CHAPTER 5:

AROMATICITY IN THE

EXCITED STATES[a]

[a] This chapter is based on the following publications:

5.1) El Bakouri, O.; Garcia-Borràs, M.; M. Girón, R.; Filippone, S.; Martín, N.; Solà, M. On the regioselectivity of the Diels-Alder cycloaddition to C_{60} in high spin states. *To be submitted.*

5.2) Jorner, K.; Dreos, A.; Emanuelsson, R.; El Bakouri, O.; Fdez. Galván, I.; Börjesson, K.; Feixas, F.; Lindh, R.; Zietz, B.; Moth-Poulsen, K.; Ottosson, H. Unraveling factors leading to efficient norbornadiene–quadricyclane molecular solar-thermal energy storage systems. *Mater. Chem. A* **2017**, *5*, 12369.

5.3) Ayub, R.; El Bakouri, O.; Jorner, K.; Solà, M.; Ottosson, H. Can Baird's and Clar's Rules Combined Explain Triplet State Energies of Polycyclic Conjugated Hydrocarbons with Fused $4n\pi$- and $(4n + 2)\pi$-Rings? *J. Org. Chem.* **2017**, *82*, 6327.

5.1 On the regioselectivity of the Diels-Alder cycloaddition to C_{60} in high spin states

Controlling the regioselectivity in the exohedral functionalization of fullerenes and EMFs (fullerenes with metal atom(s) encapsulated) is essential to produce specific desired fullerene derivatives. In this work, using DFT calculations, we show that the regioselectivity of the DA cycloaddition of cyclopentadiene (Cp) to $^{2S+1}C_{60}$ changes from the usual [6,6] addition in the singlet ground state to the [5,6] attack in high spin states of C_{60}. Changes in the aromaticity of the 5-MRs and 6-MRs when going from singlet to high spin C_{60} provide a rationale to understand this regioselectivity change. Experimentally, however, we show that the DA cycloaddition of isoindene to triplet C_{60} yields the usual [6,6] adduct. Further DFT calculations and computational analyses give an explanation to this unanticipated experimental result by showing the presence of an intersystem crossing (ISC) close to the formed triplet biradical intermediate.

5.1.1 State-of-the-art

The functionalization of fullerenes and EMFs has attracted considerable attention in the last decades. The derivatization of these compounds helps to modulate their electronic and physicochemical properties generating fullerene and EMFs derivatives more suitable for practical applications.[284–289] Fullerenes undergo a variety of chemical reactions favored by their electron deficient nature, especially cycloadditions and nucleophilic additions.[290–295] Generally, the reactions in fullerenes take place in their singlet ground states. Less often,

however, the reaction can occur in high spin states. In some cases, this is because the ground state of the fullerene or EMF is a high spin state. High spin ground states in EMFs are attributed usually to the electronic structure of the metal cluster.[296–298] Although less common, some empty fullerene cages like C_{68} can also have high spin ground states.[299,300] The triplet ground state of C_{68} is attributed to the aromatic character of this electronic state as compared to the antiaromatic character of its singlet state.[299,301] In other cases, fullerenes can be photoexcited to higher spin states and the reaction takes place in these excited states. The photophysical and photochemical properties of $^3C_{60}$, which is the lowest-lying excited state of C_{60}, have been studied by several groups since 1991.[302–305] They proved that during the excitation of C_{60}, the ISC from the first singlet excited state to the first triplet excited state (S_1 to T_1) occurs with a high efficiency, mainly due to the small splitting between these two states as well as the large spin-orbital interaction in the spherical cage. The straightforward generation of the first triplet excited state of C_{60} opened the door to photochemical processes. For instance, the [2+2] photocycloadditions on fullerenes are common since the 90s.[306–309] In fact, fullerenes have been able to react photochemically with, among others, alkenes, enones, styrenes, *etc.*[310–317] The existence of a biradical intermediate was demonstrated in many of these reactions.[306–309,318–321] Moreover, several studies found that it is also possible to obtain DA adducts through the $^3C_{60}$ species.[322,323]

The multiple addition sites available in fullerenic cages makes the control of the regioselectivity in the chemical functionalization of fullerenes one of the most challenging aspects in fullerene chemistry.[324,325] Fullerenes following the IPR[326] have two types of bonds, namely, the [6,6] bonds in hexagon-hexagon ring junctions and the [5,6] bonds in the connection between an hexagon and a pentagon. Usually, the [6,6] bonds are more reactive than the [5,6] bonds in hollow fullerenes, while [5,6] additions are more common in EMFs.[327–329] In 2013, Garcia-Borràs *et al.* studied the changes in the regioselectivity of the exohedral functionalization of C_{60} after successive electron additions.[330] It was shown that the effect of successive reductions of C_{60} (C_{60}^{-q}, q = 0–6) dramatically changes the regioselectivity of the DA additions, from the usual [6,6] addition in neutral species to addition to the [5,6] bond when the number of electrons added to C_{60} is higher than four. This regioselectivity change was rationalized in terms of local aromaticity variations in the 5- and 6-MRs of the fullerene due to the reduction process. Electrons added to the cage accumulate in the 5-MRs that gain cyclopentadienyl anion character, increasing significantly their aromaticity. In this situation, addition to a [5,6] bond, which involves breaking the

aromaticity of a unique 5-MR, becomes more favorable than addition to a [6,6] bond that destroys the aromaticity of two 5-MRs (inset of Figure 42).

It is well known that the $C_5H_5^+$ has a triplet ground state.[331] The stability of this triplet state is justified by the so-called Baird's rule of aromaticity.[332,333] Taking this result into account, one could hypothesize that by increasing the spin of the fullerenic cage, the spin density may accumulate in the 5-MRs that may become more aromatic by getting more triplet cyclopentadienyl cation character. If this is true and from the results obtained in reduced C_{60}, it is likely that we may observe in C_{60} a change in the regioselectivity of the DA cycloaddition from [6,6] to [5,6] addition when increasing the spin of the fullerenic cage. The present study tests this hypothesis. Our aim is to analyze the effect of changing the spin (S = 0–6) in the DA cycloaddition between C_{60} and two different dienes, Cp and isoindene (indene). We explore different spin states (S from 0 to 6, the latter having 12 unpaired electrons, *i.e.*, one unpaired electron per 5-MR) with the aim to determine the spin state that must be reached to modulate the regioselectivity of the DA reaction. We anticipate that our computational results will show a dramatic change in the regioselectivity of the cycloaddition already for the triplet state. In parallel, we have carried out experiments to verify the calculations. Interestingly, experiments have not confirmed our predictions. Finally, we have performed additional calculations that justify the experimental outcome.

5.1.2 Results and discussion

This section is partitioned into two subsections. First, we perform a computational study of the DA cycloaddition of Cp to $^{2S+1}C_{60}$ (S = 0–6). And second, we discuss the experimental and computational results of the DA cycloaddition of isoindene to $^3C_{60}$.

5.1.2.1 The Diels-Alder cycloaddition of cyclopentadiene to $^{2S+1}C_{60}$ (S = 0–6). A computational study

The DA reaction between $^{2S+1}C_{60}$ and Cp can occur concertedly or stepwise (see Figure 42). Our results show that the reaction takes place concertedly only in the S_0 state. From S=1 to S=6, the process is stepwise and proceed *via* the formation of a high spin radical intermediate. In this intermediate, the carbon atom of the Cp that participates in the formation of the final adduct can be oriented to attack the C atom on the fullerene [6,6] bond and generate the

pro-int[6,6] intermediate or oriented towards the C atom of the [5,6] bond and form the pro-int[5,6]. These two intermediates are almost isoenergetic (energy differences of 0.27–0.54 kcal/mol) and the conversion from one intermediate to another takes place easily by rotation along the new formed C–C sigma bond ($\Delta E^{\ddagger}$=6.2–6.7 kcal/mol).
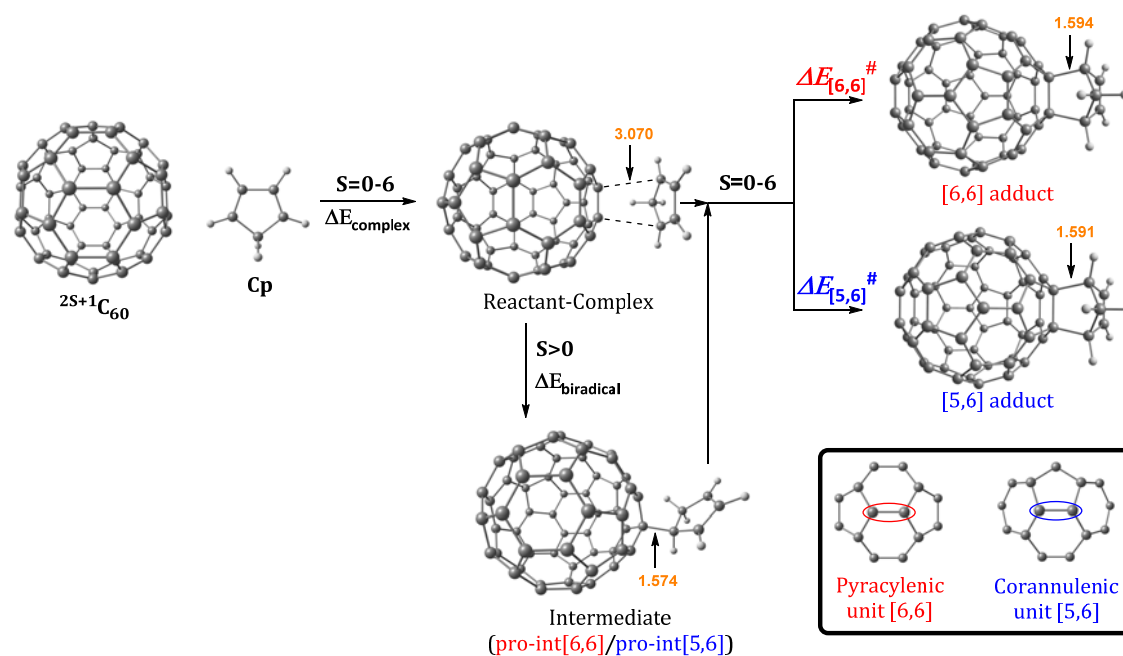
Figure 42. Schematic reaction mechanism of the DA reaction between $^{2S+1}C_{60}$ and Cp in the ground and high spin states. Bond distances (in Å) correspond to the reaction in the T_1 state.

Table 5 collects the Gibbs and electronic energy differences in reaction energies and energy barriers for the additions to the [5,6] and [6,6] bonds of $^{2S+1}C_{60}$. Positive values indicate that the [5,6] attack is thermodynamically or kinetically more favorable than the [6,6] addition. Figure 43 reports the difference in Gibbs reaction energy for the [5,6] and [6,6] additions as well as the aromaticity of the 5-MRs and 6-MRs measured in terms of MCI for the different studied spin states. In the S_0 state, our calculations indicate that the concerted [6,6] addition is thermodynamically and kinetically more favored than the [5,6] one as expected from previous theoretical studies.[327,328,330] This result is in agreement with experimental evidence[334,335] showing that the reaction takes place over the [6,6] bond with an activation energy of 6.9 kcal/mol (compared to $\Delta H^{\ddagger}$ = 10.2 kcal/mol at the B3LYP-D3/6-31G(d) level of theory calculated as the enthalpy difference between the transition state and the van der Waals reactant complex) and a reaction enthalpy of -19.8 ± 2.2 kcal/mol (ΔH_r = -23.5 kcal/mol with the B3LYP-D3/6-31G(d) method). Nevertheless, the regioselectivity changes drastically once $^3C_{60}$ is considered and the [5,6] addition becomes energetically favored.

Similar results are obtained for every other spin state (S=1–6). The reaction energy and energy barrier differences between [5,6] and [6,6] attacks for the different spin states given in Table 5 show that the inversion of the regioselectivity already occurs when going from $^1C_{60}$ to $^3C_{60}$ and it is maintained for the rest of the high spin states ($^{2S+1}C_{60}$ with S>0). Therefore, spin states of C_{60} with S = 1–6 favor the [5,6] addition both thermodynamically and kinetically even if the pro-int[6,6] is formed first. The barriers involving the transformation from pro-int[6,6] to pro-int[5,6] and to the adduct [5,6] are lower than the barrier corresponding to the formation of the [6,6] adduct from pro-int[6,6].

Table 5. B3LYP-D3/6-31G(d) Gibbs and electronic energy differences (kcal/mol) in reaction energies and energy barriers for the additions to the [6,6] and [5,6] bonds and for different spin states. Barriers calculated from the respective lowest in energy intermediate. Negative values indicate that the [6,6] addition is more favored than the [5,6] attack.

2S+1=	1	3	5	7	9	11	13
$\Delta\Delta E_R$ ([6,6]-[5,6])	-19.87	4.13	4.74	8.48	12.72	13.10	20.33
$\Delta\Delta E^{\ddagger}$ ([6,6]-[5,6])	-15.26	9.56	9.71	10.47	15.13	14.57	17.11
$\Delta\Delta G_R$ ([6,6]-[5,6])	-19.29	3.14	3.43	6.85	10.75	11.79	17.90
$\Delta\Delta G^{\ddagger}$ ([6,6]-[5,6])	-13.64	8.05	7.52	9.35	13.17	12.77	15.20
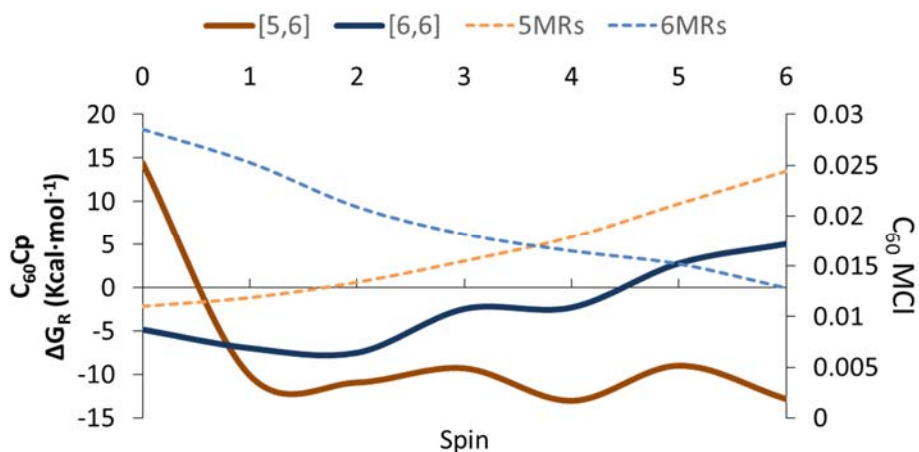
Figure 43. Schematic representation of the Gibbs reaction energies (kcal/mol) for the DA addition of Cp to the [6,6] and [5,6] bonds of $^{2S+1}C_{60}$ and average MCI values (dashed lines, in electrons) of the 5-MRs and 6-MRs in $^{2S+1}C_{60}$ for the different spin states studied. MCI for 5- and 6-MRs is obtained by averaging the MCI of all the 5-MRs (12 rings) and 6-MRs (20 rings) of C_{60}, respectively.

Changes in C–C bond distances and pyramidalization angles do not explain the inversion of the regioselectivity when going from singlet to high spin states. Pyramidalization angles

remain more or less the same and the [5,6] C–C bond distances are for all spin states studied larger than the [6,6] ones. The regioselectivity change can only be understood by analyzing the local aromaticity of the rings involved in the DA reaction. HOMA,[145,146] which is a geometric-based indicator of aromaticity that only takes into account the C–C bond distances, shows an increase of the aromaticity of the 5-MRs when the spin state increases, whereas for the 6-MRs it does not indicate a clear trend. As HOMA was developed for ground state species, it is likely that evaluation of aromaticity for the high spin systems is not accurate enough. Electronic indices are expected to be more reliable.[234,280,336,337] MCI and I_{NB} give the same tendency for the aromatic character of 5-MRs as HOMA does. Nevertheless, employing these electronic indices, we notice that the aromaticity of the 6-MRs decreases when the spin increases. Actually, the same trends were also observed when reducing C_{60} by adding up to six electrons to the carbon cage.[330] Our interpretation of this result is that 5-MRs become more aromatic by obtaining more triplet cyclopentadienyl cation character. Indeed, our results show that the spin density accumulates essentially in the 5-MRs of $^{2S+1}C_{60}$ (S =1–6). On the other hand, increasing the radical character of 6-MRs effectively reduces their aromaticity.

With this information, we can now rationalize the changes in the regioselectivity of the DA reaction between $^{2S+1}C_{60}$ and cyclopentadiene. Table 6 gathers the $^{2S+1}C_{60}$ MCI_{Pyr}, $^{2S+1}C_{60}$ MCI_{Cor}, $^{2S+1}C_{60}Cp$ MCI_{Pyr} and $^{2S+1}C_{60}Cp$ MCI_{Cor} values, where MCI is calculated summing the four rings involved in the corannulenic (MCI_{Cor}) or the pyracylenic unit (MCI_{Pyr}). ΔMCI is the difference between the sum of MCI of the rings of the pyracylenic/corannulenic unit in the product $^{2S+1}C_{60}Cp$ and the same sum in the reactant $^{2S+1}C_{60}$. And $\Delta\Delta MCI_{Pyr-Cor}$ in Table 6 corresponds to the difference in the loss of aromaticity measured with MCI between the [5,6] corannulenic addition and the [6,6] pyracylenic addition. A positive $\Delta\Delta MCI_{Pyr-Cor}$ value indicates that the reduction of the aromaticity due to a [5,6] attack is more important than that of the [6,6] addition and the other way around.

From the results of Table 5 and Table 6, we see that the [5,6] addition becomes more favorable when the $\Delta\Delta MCI_{Pyr-Cor}$ value decreases. Although there is not a perfect correlation (aromaticity change is not the only factor that intervenes and, for instance, spin density accumulation may be another important aspect to take into account), the trend is clear: when $\Delta\Delta MCI_{Pyr-Cor}$ decreases, $\Delta\Delta G_R$ and $\Delta\Delta G^\ddagger$ in Table 6 increase. As mentioned previously, 5-MRs become more aromatic when the spin state increases. The [5,6] addition (corannulenic

unit, Figure 42) disrupts the aromaticity of one 5-MR and three 6-MRs, whereas the [6,6] attack (pyracylenic unit, Figure 42) breaks the aromaticity of two 5-MRs and two 6-MRs. For the $^1C_{60}$, 6-MRs are more aromatic than 5-MRs, therefore it is more favorable the [6,6] addition that destroys the aromaticity of only two 6-MRs as compared to three in the [5,6] attack. On the other hand, for high spin states, the 5-MRs become more aromatic than the 6-MRs. In this situation, addition to a [5,6] bond becomes more favorable because it affects the aromaticity of only a single 5-MR.

Table 6. B3LYP-D3/6-311G(d)//B3LYP-D3/6-31G(d) MCI_{Pyr} and MCI_{Cor} indices (in 10^{-2} electrons), changes in MCI when going from reactants to products (ΔMCI) and their differences ($\Delta\Delta MCI_{(Pyr–Cor)}$) for the pyracylenic and corannulenic units for the different spin states.

2S+1=	1	3	5	7	9	11	13
$^{2S+1}C_{60}$ MCI_{Pyr}	5.63	5.89	5.25	5.20	5.64	6.02	6.46
$^{2S+1}C_{60}$ MCI_{Cor}	6.25	5.90	5.39	4.81	4.78	4.84	4.89
$^{2S+1}C_{60}Cp$ MCI_{pyr}	1.06	1.05	1.08	1.13	1.12	1.13	1.04
$^{2S+1}C_{60}Cp$ MCI_{Cor}	1.13	0.92	0.94	0.90	0.89	0.85	0.78
ΔMCI_{Pyr}	-4.57	-4.84	-4.17	-4.07	-4.52	-4.89	-5.41
ΔMCI_{Cor}	-5.11	-4.99	-4.44	-3.91	-3.88	-3.99	-4.09
$\Delta\Delta MCI_{(Pyr–Cor)}$	0.54	0.15	0.27	-0.16	-0.63	-0.90	-1.32

5.1.2.2 The Diels-Alder cycloaddition of isoindene to $^3C_{60}$

The computational results from the previous section indicate that DA cycloadditions involving $^3C_{60}$ should generate [5,6] adducts. Prompted by these results, we decided to validate these theoretical predictions experimentally. To this end, researchers in Prof. N. Martín's group performed the photochemically induced DA cycloaddition between $^3C_{60}$ and isoindene. In a previous work, Puplovskis *et al.* isolated the resulting [6,6] product from the DA reaction between $^1C_{60}$ and isoindene, which is prepared in situ from indene in refluxing *o*-dichlorobenzene (*o*-Cl$_2$C$_6$H$_4$).[338] Here, for the preparation of the [5,6] cycloadduct **1b**, we used photochemical conditions and temperatures below 40ºC to avoid the thermal cycloaddition. Derivative [6,6]closed **1a** was the sole monoadduct obtained with 4-39% yield depending on the reaction time (Scheme 8). On the other hand, the [5,6] adduct **1b** was not observed.
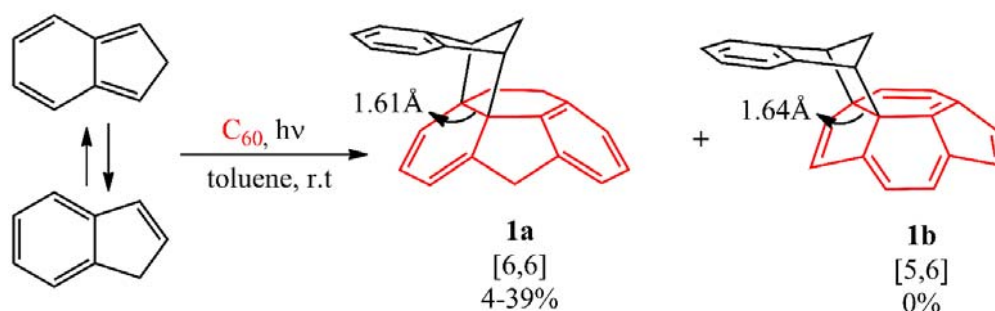
Scheme 8. The reaction between $^3C_{60}$ and isoindene. The [6,6]- and [5,6]-bond lengths correspond to the B3LYP-D3/6-31G(d).

Since experimental results appear in conflict with our theoretical prediction, we decided to analyze in more detail *via* computational methods the photochemical DA cycloaddition between $^3C_{60}$ and isoindene. Our aim was to see whether the use of a different diene (cyclopentadiene/isoindene) could explain the apparent disparity between experiments and computations. As previously found for cyclopentadiene, our calculations indicate that the DA addition of isoindene to C_{60} is concerted in the S_0 state and stepwise in the T_1 state. Table 7 collects Gibbs and electronic reaction energies and energy barriers for the [5,6] and [6,6] additions when the reaction takes places with isoindene (as well as with indene) in the S_0 and T_1 states. Generally, the lower energy barriers involved in the addition of isoindene indicate that this compound is more reactive than indene.

Table 7. Electronic reaction energies and energy barriers for the reaction between $^{2S+1}C_{60}$ and isoindene and indene. Energies in kcal/mol.

S	C_{60} + isoindene				C_{60} + indene			
	$\Delta E^{\ddagger}$ [5,6]	$\Delta E^{\ddagger}$ [6,6]	ΔE_R [5,6]	ΔE_R [6,6]	$\Delta E^{\ddagger}$ [5,6]	$\Delta E^{\ddagger}$ [6,6]	ΔE_R [5,6]	ΔE_R [6,6]
0	12.44	2.10	-28.52	-48.72	39.54	22.88	-5.88	-26.07
OS-S_0	1.54	-	-6.03	-26.22	-	-	-	-
1	6.83	16.70	-55.19	-49.05	20.72	27.12	-32.55	-26.13

Our results (Table 7) using isoindene as diene indicate that the formation of the [6,6] adduct is more exergonic and has a lower energy barrier than that of the [5,6] adduct in the S_0 state, whereas the opposite is found for the T_1 state. Therefore, the inversion of regioselectivity should also be occurring in this case but experimentally only the [6,6] adduct is obtained. At the first glance, computational and experimental results did not match. Nevertheless, it has been reported that $^1C_{60}$ can undergo ISC to $^3C_{60}$ with very high quantum yields.[302] Thus, if a

crossing point between the potential energy surfaces of the S_0 and T_1 states along the DA reaction exists, then it is likely that T_1 states can be deactivated through this ISC quite effectively.
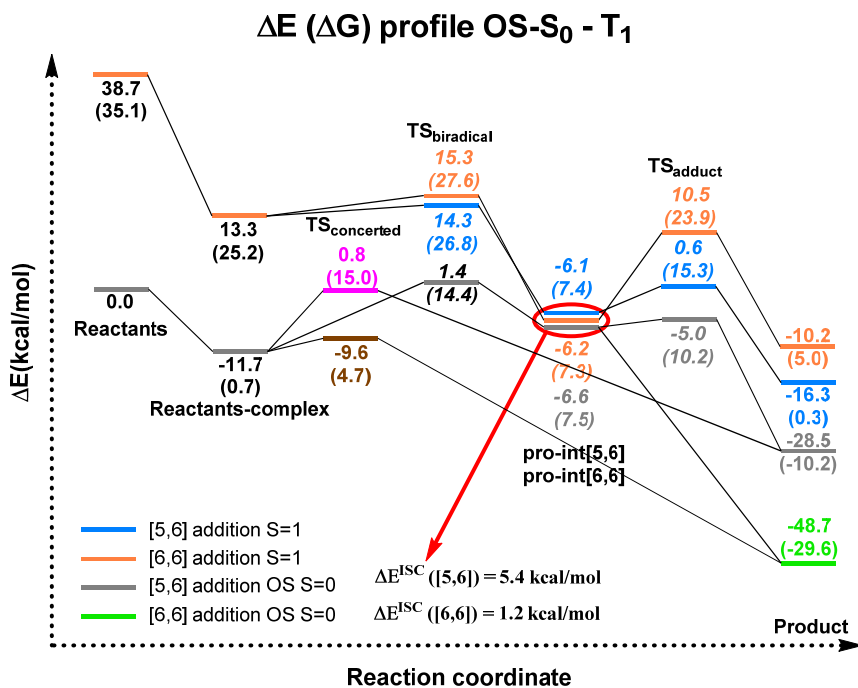
Figure 44. Electronic energy profiles (Gibbs energies in parenthesis) for the reaction between C_{60} and isoindene in the singlet, open-shell singlet, and triplet states at B3LYP-D3/6-31G(d) level. $\varDelta E^{ISC}$ is the necessary energy to reach the structure of the crossing point from the triplet state ($\varDelta E^{ISC}([5,6]) = E_{crossing}([5,6])-E_{pro\text{-}int}([5,6])^{T1}$; $\varDelta E^{ISC}([6,6]) = E_{crossing}([6,6])-E_{pro\text{-}int}([6,6])^{T1}$). Values in italics correspond to biradical open-shell singlet species.

At this point, it is difficult to predict if there is a crossing point or not because the mechanism is different (concerted and stepwise reaction for S_0 and T_1 states, respectively). So, we decided to compute the energy profile in the open-shell singlet potential energy surface (PES) for the stepwise mechanism (Figure 44). The closed- and open-shell singlet PESs coincide except in the region of the biradical intermediate. In the open-shell singlet case (Table 7), the predicted regioselectivity coincides with the closed-shell singlet state case, thus favoring the [6,6] addition, although differences in energy barriers for the two additions are smaller. In the open-shell singlet PES, we have been unable to locate the transition state of the [6,6] addition. A linear-transit calculation for the transformation of pro-int[6,6] to adduct has shown that it is a barrierless process. It is worth highlighting that the open-shell singlet character is detected only in $TS_{biradical}$, pro-int[5,6], pro-int[6,6], and TS_{adduct}[5,6] species. If we analyze the energy

profile (Figure 44) and the molecular structures shown in Figure 45, we observe that the pro-int[5,6] and pro-int[6,6] are the most suitable structures for being crossing state points. Indeed, the fact that these structures correspond to crossing points was confirmed using the Harvey's method to locate spin-crossing points.[339,340] The ISC energies ($\varDelta E^{ISC}$[5,6] and $\varDelta E^{ISC}$[6,6]) are calculated as the difference between the crossing point energy and the pro-int[5,6] or pro-int[6,6] energy in their T_1 state (Figure 44). $\varDelta E^{ISC}$([5,6]) and $\varDelta E^{ISC}$([6,6]) are 5.4 and 1.2 kcal/mol, respectively. Thus, based on our computations, when the pro-int[5,6] is formed in the T_1 state, it can fall to the open-shell S_0 state through an ISC by surmounting a barrier of 5.8 kcal/mol. Once the pro-int[5,6] is formed in the open-shell S_0 state, the [5,6] adduct can be formed (energy barrier is only $\varDelta E^{\ddagger} = 1.6$ kcal/mol) (Table 7). The transformation of pro-int[5,6]^{T1} to the [5,6]^{S0} adduct is exergonic by 17.6 kcal/mol. This means that this process could be reversible at 40 °C. Otherwise, if the pro-int[6,6] is formed first, it can be converted from T_1 to S_0 through an ISC with a barrier of only 1.2 kcal/mol to get the [6,6] adduct in a barrierless process. The transformation of pro-int[6,6]^{T1} to the [6,6]^{S0} adduct is exergonic by 36.9 kcal/mol and, therefore, it is an irreversible process. Therefore, our computational results indicate that the [6,6] adduct should be the major product formed in the DA of isoindene to $^3C_{60}$, as found experimentally due to the T_1 to S_0 relaxation when the biradical intermediate is formed.
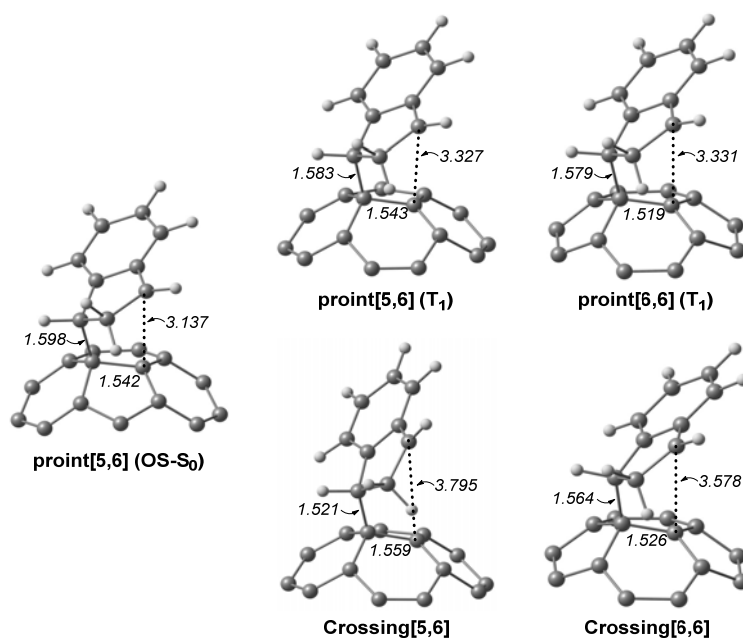
Figure 45. The molecular structure (distances in Å) of the biradical open-shell singlet and triplet intermediates and crossing points.

5.2 Unraveling Factors Leading to Efficient Norbornadiene-Quadricyclane Molecular Solar-Thermal Energy Storage Systems

The norbornadiene (NBD) to quadricyclane (QC) [2+2] photochemical reaction has been studied in collaboration with other authors using both computational and experimental methods. For this purpose **NBD-R₂** compounds with R = H, Me and *i*Pr have been synthetized and quantum yields have been measured. In the experiments, they observe an increase of the quantum yield along the increasing steric bulk added. For comparison, conical intersection (CI) structures and relaxation pathways have been calculated not only of **NBD-R₂** but also the **DA-R₂** model compound and **P-R₂** unsubstituted system. They have found interesting computational results that can explain the relative order of the experimental quantum yields based on relaxation from the respective CI structures. Their computational results conjecture that the reaction may be influenced by excited state S_1 or T_1 homoaromaticity. Indeed, our MCI calculations proves the previous fact.

5.2.1 State-of-the-art

Solar energy can be converted directly into latent chemical energy *via* several methods such as natural or artificial photosynthesis,[341,342] or photo-induced isomerization in chemical compounds – so-called molecular solar thermal systems (MOST)[343] like the norbornadiene-quadricyclane (NBD-QC)[344–346] molecule. A large fraction of the solar spectrum should be absorbed, the photoconversion must proceed with near unity quantum efficiency and the energy should be stored at a high energy density. Moreover, the photoisomer should be stable over time, the chemical compounds switchable for multiple cycles and the back-reaction from photoisomer to parent compound triggered externally by, *e.g.*, a solid state catalyst.

For the NBD-QC system (Figure 46), several of these requirements are fulfilled,[347] but unfortunately it only absorbs light below 300 nm.[348,349] NBD undergoes a photochemical [2+2]-cycloaddition reaction to form the strained high-energy QC isomer. Thermally, this reaction is forbidden according to the Woodward-Hoffmann rules[350] and the energy-releasing back-reaction from QC to NBD proceeds *via* a high-energy transition state of diradical character (experimental gas-phase activation energy of 33.5 kcal/mol).[351]
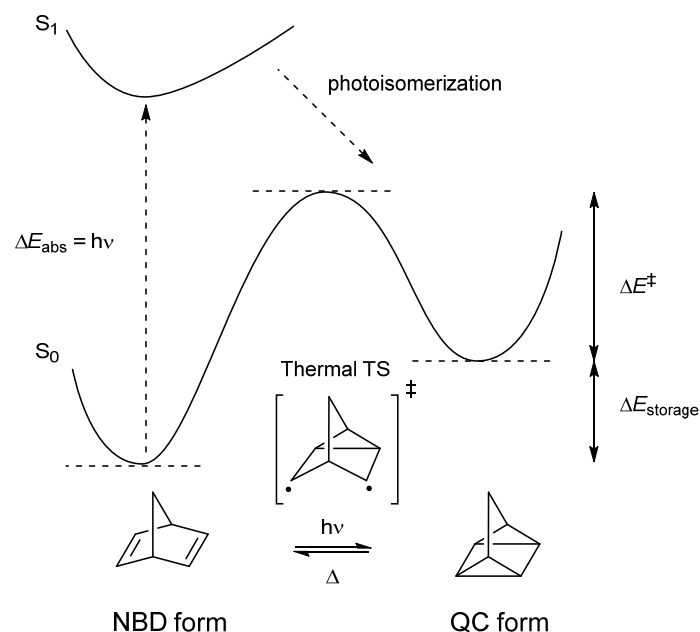
Figure 46. Schematic figure of the thermal and photochemical isomerization between NBD and QC. Shown are the excitation energy, ΔE_{abs}, storage energy, $\Delta E_{storage}$, and activation energy for thermal back reaction, $\Delta E^{\ddagger}$.

However, a challenge with the system is that all reported photoisomers of compounds with red-shifted absorption have too short lifetimes to be practically useful for long-term energy storage applications,[343,345,352] and the quantum yields are often well below unity.[346] It is therefore desirable to develop a detailed understanding of how the NBD-QC system can be chemically engineered with respect to absorption spectrum, quantum yield, energy storage and barrier for the thermal back-reaction. Herein this work reports how to disentangle and balance the different factors influencing the efficiency of the NBD-QC system. Figure 47 shows the NBD-QC systems investigated in this work.
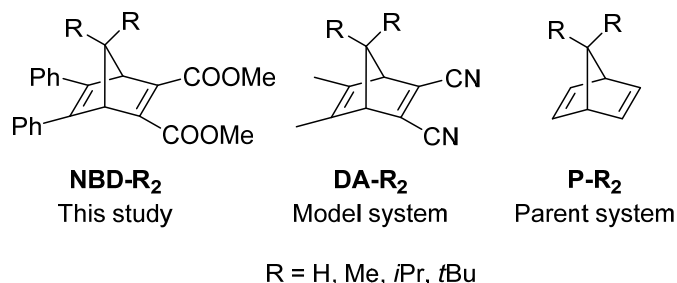
Figure 47. NBD-QC systems investigated in this study. DA-R_2, P-R_2 and NBD-tBu$_2$ are studied only computationally.

Even though a large amount of experiments and calculations have been done, in this thesis, we only discuss our contributions from the computational side. After a mapping of the S_1 surface, they suggest that homoaromaticity could have a significant role through the PES. In order to prove this hypothesis, we study the aromatic character along the PES by means of MCI, yet NICS have been also calculated as a magnetic index.

5.2.2 Results and discussion

First, it is essential to begin the discussion with the analysis of the PES performed by Prof. Ottosson's group. **NBD-H$_2$**, **DA-H$_2$** (as a model compound) and **P-H$_2$** (as an unsubstituted system) will be discussed. The **P-H$_2$** exhibits a symmetrical, rhombically distorted S_0/S_1 CI structure with C---C distances of 1.948 Å and **NBD-H$_2$** has one shorter bond which is almost fully formed (1.730 Å) while the other remains long (2.210 Å) (Figure 48). **DA-H$_2$** has the same behavior as **NBD-H$_2$**.

The CI preferentially leads back to the NBD isomer, in agreement with experiment. Interestingly, there are also shallow minima on the S_1 surface in between the Franck-Condon (FC) geometry and the CIs, but the depth (0.4 kcal/mol for **P-H$_2$**, 2.1 kcal/mol for **DA-H$_2$** and 3.2 kcal/mol for **NBD-H$_2$** with 3-SA-CASSCF(2,2)) is small compared to the excess energy from the FC point (29.0 kcal/mol for **P-H$_2$**, 28.2 kcal/mol for **DA-H$_2$** and 30.1 kcal/mol for **NBD-H$_2$** at the same level) and they are not likely to be populated significantly.

An overview of the PES for **NBD-H$_2$** is given in Figure 49. The PES of S_0 and S_1 states of NBD shows that once NBD is photoexcited from S_0 to S_1, it evolves through a barrierless process to a homoaromatic minimum and then it reaches the CI where it is deactivated to the S_0 PES. Therefore, the PES of Figure 49 shows that the photoexcitation reverts easily to ground state NBD and that explains the short lifetimes of photoexcited NBD (Figure 49).
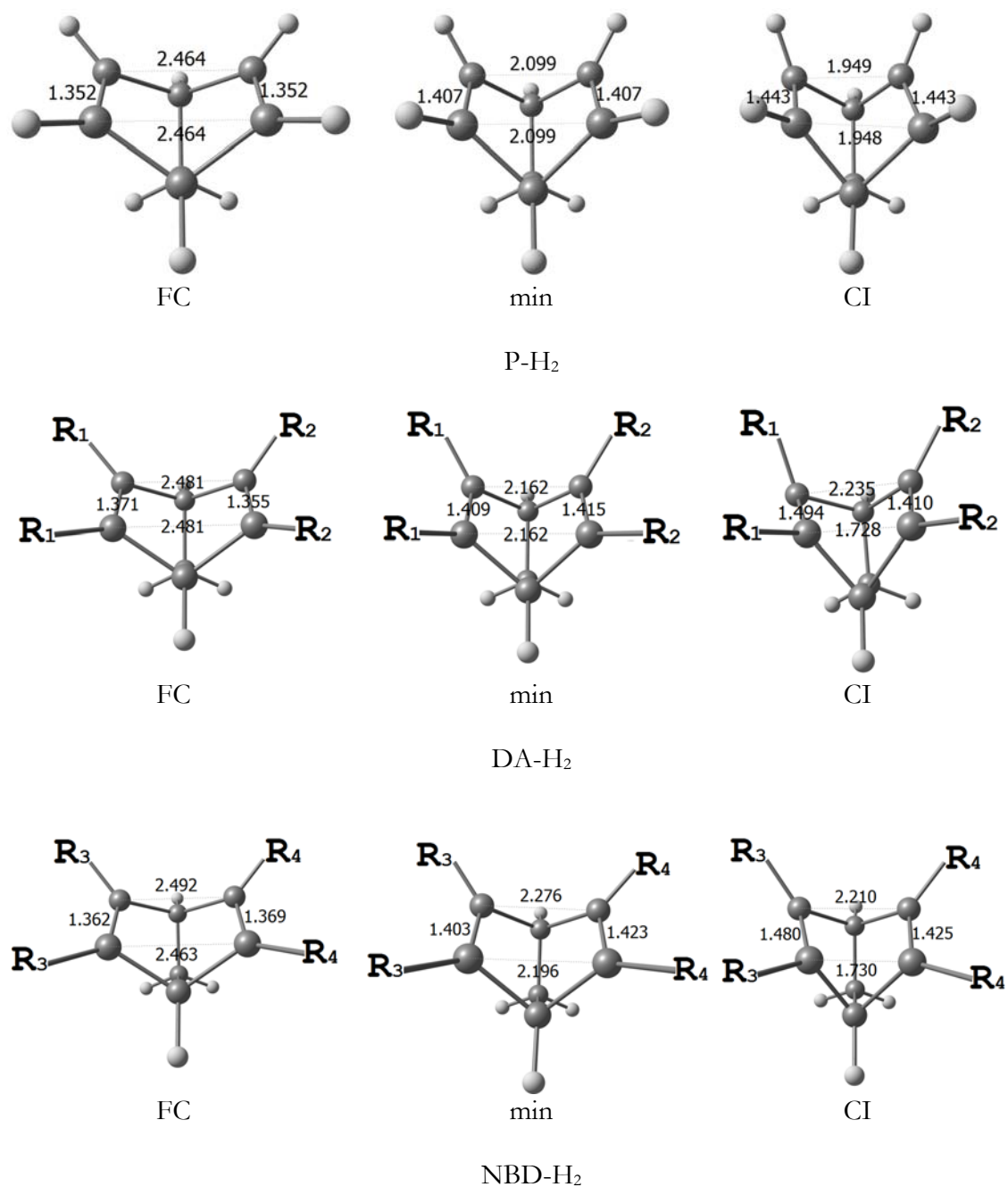
Figure 48. Frank-Condon (FC), minimum (min) and conical intersection (CI) geometries for P-H$_2$ (top), DA-H$_2$ and NBD-H$_2$ (bottom) at the 2-SA-CASSCF(2,2)/6-31G(d) level. R$_1$=CN, R$_2$=CH$_3$, R$_3$=COOH, R$_4$=Ph.
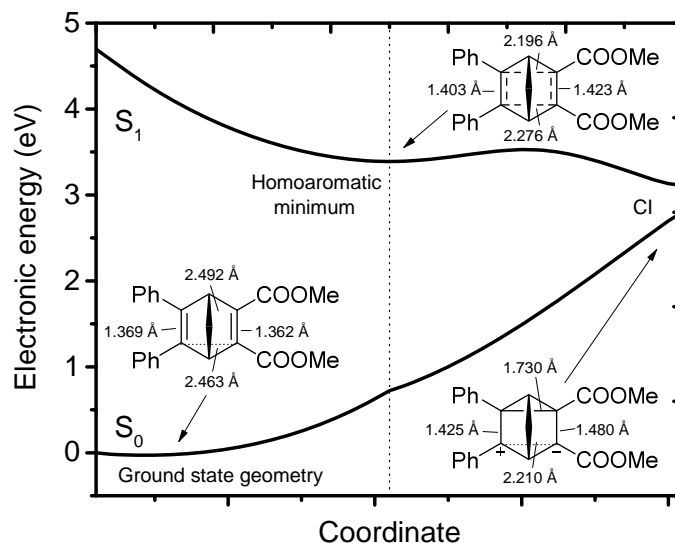
Figure 49. S_0 and S_1 energies for NBD-H_2 along the path from the optimized S_0 minimum to the optimized S_1 minimum to the CI at the 3-SA-CASSCF/6-31G(d) level. The points between the optimized structures have been obtained by linear interpolation in internal coordinates.

As we comment above, minimum energy potential (MEP) calculations have found a shallow minimum on S_1 at the CASSCF level. This minimum is not likely to affect the photoreactivity due to its shallow character, but its influence on the PES is likely important for the almost barrierless path to the CI. So one would wonder if this is a consequence of S_1 state Baird[20] homoaromaticity.[353] Or in another words, one also would wonder if this minimum could be stabilized by homoaromaticity in the S_1 state with four electrons in the cycle. To this end, we calculated MCI of the CASSCF wave functions at the S_1 minima of **P-H_2**, **DA-H_2** and **NBD-H_2**.[187,354] Figure 50 shows the trend of MCI between the FC region and the minimum for the S_1 state. The resulting values (0.032, 0.024 and 0.021) are large and approach that of the S_2 state CBD at its D_{2h} ground state geometry (0.049) which was previously assessed as clearly aromatic.[67] While the MCI values decrease from **P-H_2** to **DA-H_2** and **NBD-H_2**, the depth of the minima at the same time increases along with the increasing donor-acceptor character of the substituent (0.4 kcal/mol for **P-H_2**, 2.1 kcal/mol for **DA-H_2** and 3.2 kcal/mol for **NBD-H_2** at the CASSCF level). Therefore, the less S_1-homoaromatic compounds have the deeper minima. This finding is somewhat surprising because one would expect the opposite behavior that is the deeper minima should be the most S_1-homoaromatic. Actually, the electronic effect of substituents could be playing a role on the aromaticity or stability of these systems.
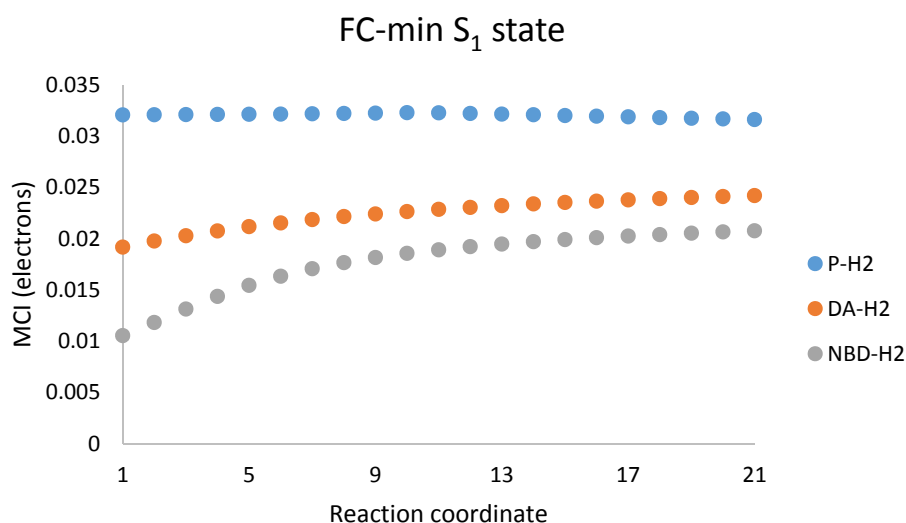
Figure 50. MCI values between the FC region and the minimum for NBD-H$_2$, DA-H$_2$ and P-H$_2$. Values in electrons.

5.3 Can Baird's and Clar's Rules be Combined to Rationalize Triplet State Energies of Polycyclic Conjugated Hydrocarbons with Fused 4nπ- and (4n+2)π-Rings?

Aromatic chameleons are compounds that have the ability to adjust their π-electron distribution so as to comply with the different rules of aromaticity in different electronic states. We now show that the fusion of the aromatic chameleonic units to benzene rings modifies the electronic properties of the compounds. An influence of triplet state aromaticity of central 4nπ-electron units is observed and, consequently, the most stabilized compounds retain Baird's quartets or octets, enabling outer benzene rings to adapt closed-shell singlet Clar's sextet character. Interestingly, as the number of aromatic cycles within a molecule increases the T$_1$ states goes to lower T$_1$ state energies. Different descriptors of aromaticity show that in the triplet states, the aromaticity of the central rings has a significant influence in lowering the triplet state energies of the molecules considered in the study. Yet, we are going to discuss only the FLU results.

5.3.1 State-of-the-art

π-Conjugated systems based on fused (4n+2)π- and 4nπ-electron cycles such as biphenylene and [N]phenylenes are interesting for applications in organic and molecular electronics.[355–358]

In their electronic ground (S_0) states the conjugated circuits of these compounds display properties that are intermediate between those of aromatic and antiaromatic systems, *i.e.*, they display partial aromaticity. Yet how do these compounds behave in their first electronically excited states, and can their properties be understood in qualitative terms? Such qualitative understanding should facilitate the identification of new compounds with useful properties for applications.

Actually, certain hydrocarbon compounds have been described as "aromatic chameleons" due to the ability to adjust their electronic structure so as to comply with Hückel's $4n+2$ rule for aromaticity in the S_0 state and Baird's $4n$ rule for aromaticity in the T_1 and S_1 states. [359–361] Biphenylene could tentatively be considered as an aromatic chameleon (Figure 51); in the S_0 state it can be influenced by a resonance structure with two 6π-electron benzene rings while in the T_1 state it can be described by four different Baird-aromatic resonance structures: one with a 12π-electron biradical perimeter (**T$_1$-I**), two equivalent ones with 8π-electron circuits (**T$_1$-III** and **T$_1$-III'**), and one with a central 4π-electron cycle (**T1-II**). Yet, biphenylene in its S_0 state can also be labeled as Hückel-antiaromatic, and previous computational studies indicated that biphenylene in this state has some antiaromatic character in the 12π-electron perimeter, and correspondingly, more localized C-C bonding.[362,363]
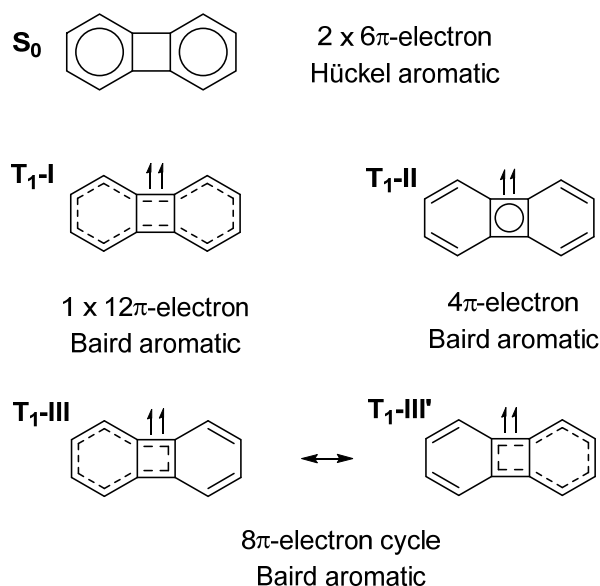
Figure 51. Aromatic resonance structures in the S_0 and T_1 states of biphenylene showing how it can act as an "aromatic chameleon" compound.
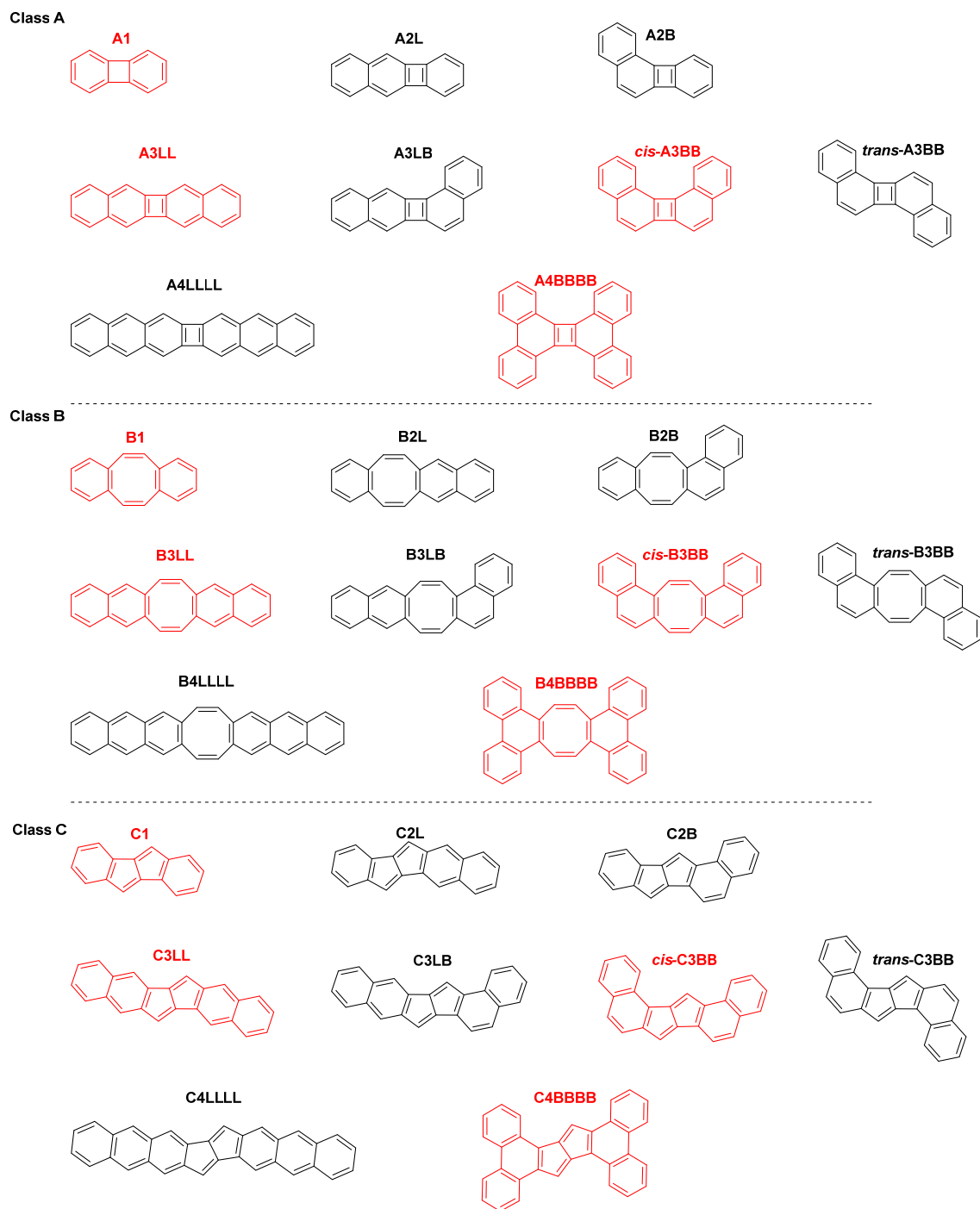
Figure 52. Classes of compounds studied. L: linear, B: bent.

We now investigate compounds with fused [4n+2]- and [4n]-conjugated circuits but with overall 4$n\pi$-electron perimeters, and we test if the T$_1$ state properties can be rationalized by usage of Baird's rule combined with Clar's rule. Remarkably, a linear correlation between the relative isomer energies (thermodynamic stability)[364] and excitation energies[365] with the number of Clar's π-sextets was reported for a series of heptabenzenoid isomers.

If a compound has both $(4n+2)\pi$- and $4n\pi$-electron rings we hypothesize that the isomer with the lowest energy in the T_1 state is that isomer which allows for the largest number of aromatic rings, *i.e.*, triplet diradical Baird-aromatic $4n\pi$-electron rings (π-quartets or π-octets) plus singlet closed-shell Hückel-aromatic π-sextet rings. If Baird's rule can be used together with Clar's rule and influence on the relative isomer energies in the T_1 state, then the different connectivity of various isomers should also have an impact on the T_1 state energies, $E(T_1)$. For this purpose, three central $4n\pi$-electron cycles (CBD, COT, and pentalene (PEN)) were considered (Figure 52), and we examine our working hypothesis that Clar's and Baird's rules can be used in combination. We particularly address the scope and limitations of this hypothesis.

5.3.2 Results and discussion

The three compound classes differ by the central unit being either a CBD, COT or PEN moiety. The influence of T_1 aromaticity is evaluated by the magnetic NICS and ACID indices, the electronic FLU index, and the geometric HOMA index. However, we now only focus our discussion on the FLU data. The rings in the various compounds are labeled so that the central $4n\pi$-electron ring is always ring *a*, or rings *a* and *a'* in case of pentalene, as shown in Figure 53. In case of symmetric compounds rings *a'*, *b'* and *c'* are equivalent to rings *a*, *b* and *c*, respectively. Even though a large set of systems have been investigated, we only now focus the discussion on a few representatives of them (in red, Figure 52).
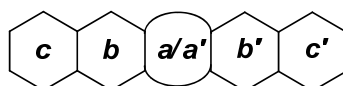
Figure 53. Labeling of different rings.

Biphenylene (**A1**) was suggested above to have an "aromatic chameleon" character (Figure 51).[64] Yet, is this labeling in accordance with computational results? The corresponding FLU values of ring *a* and *b* in the S_0 state are 0.0441 and 0.0052 (Table 8) for *a* and *b*, respectively. A near-zero value for *b* rings suggests a substantial aromaticity, contrasting the findings from NICS and ACID. The FLU value along the perimeter (0.0147) indicates that the π-electron delocalization is not particularly efficient through the perimeter and the most effective π-electron delocalization takes place locally in the 6-MRs with a FLU of 0.0052. Globally, FLU index (as well as HOMA, NICS and ACID) clarifies that the antiaromaticity of the *a* ring in

A1(S_0) is weaker than in the parent CBD (FLU=0.104) while the aromaticity of the *b* rings is reduced when compared to that of benzene (FLU=0.000).

Table 8. FLU and γ values computed for all the possible (local, semi-global, and global) circuits in S_0 and T_1 states for **A1**, **B1** and **C1**.

Compound	Electronic state	Circuit along perimeter of ring(s)	FLU	γ
A1	S_0	a	0.0441	
		b	0.0052	
		a+b	0.0220	-
		b+a+b'	0.0147	
	T_1	a	0.0382	0.3272
		b	0.0169	0.4140
		a+b	0.0157	0.5923
		b+a+b'	0.0082	1.0000
B1	S_0	a	0.0483	
		b	0.0011	
		a+b	0.0323	-
		b+a+b'	0.0243	
	T_1	a	0.0098	0.5816
		b	0.0150	0.0586
		a+b	0.0089	0.2228
		b+a+b'	0.0085	0.0118
C1	S_0	a+a	0.0340	
		b	0.0032	
		a+a'+b'	0.0224	-
		b+a+a'+b'	0.0160	
	T_1	a+a	0.0159	0.4865
		b	0.0131	0.5969
		a+a'+b'	0.0097	0.5369
		b+a+a'+b'	0.0066	0.6061

In the T_1 state, the FLU values of the CBD and benzene rings in **A1** are 0.0382 and 0.0169 (Table 8), respectively, revealing that when going from the S_0 to the T_1 state, the antiaromatic character of CBD decreases somewhat whereas the aromaticity of the 6-MR is significantly reduced. Due to its symmetry, **A1**(T_1) has three possible electronic circuits for $4n\pi$-electron delocalization; one global along the perimeter (FLU*bab'* = 0.0082; for comparison, FLU in the antiaromatic T_1 benzene molecule is 0.0238) and two semi-global which involves the CBD and one benzene ring (FLU*ab* = 0.0157). Besides, two local $(4n+2)\pi$ circuits corresponding to the two benzene rings (FLU*b* = 0.0169) are detected. The CBD ring (FLU*a* = 0.0382) in T_1 is antiaromatic. The FLU*bab'* is the lowest meaning that in the T_1 state the π-electron delocalization occurs most efficiently along the perimeter. Moreover, the γ*bab'* value of 1.00

(Table 8) of the perimeter circuit indicates Baird aromatic character and, consequently, the resonance structure **T₁-I** of Figure 51 is the one that best describes **A1**(T_1).
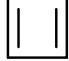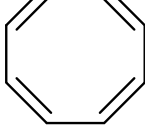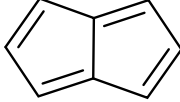
Interestingly, the DIs explain why FLU*bab* decreases and FLU*b* increases significantly from the S_0 to the T_1 state. In particular, the reason comes from 4-MR because their DIs are switched from the S_0 to the T_1 state so as to activate the perimeter π-electron delocalization circuit that was not efficient in the S_0 state (Figure 54). In the S_0 state, C1-C2 and C3-C4 DIs are 1.015 e, while C2-C3 and C4-C1 DIs are 1.215 e. For T_1 this trend is reversed, that is, DIs corresponding to C1-C2 and C3-C4 are 1.237 e while C2-C3 and C4-C1 DIs are 1.036 e. A DI close to 1.0 e is typical of single C-C bonds (Figure 54). It is interesting to see how the change from singlet to triplet state induces this change of DIs that activates the π-electron delocalization of the perimeter. Besides, from the DI analysis we can extract information of the local rings and the reason why FLU gives these particular values. In particular, FLU*a* is similar in the two states, FLU(S_0) = 0.0441 and FLU(T_1) = 0.0382 (Table 8), because of the simple reversing of the DIs (and bond distances). In terms of local aromaticity, the aromatic character of the 4-MR does not practically change according to FLU. However, the change on the DI is responsible for activating the perimeter ring current giving a global aromatic molecule. The 6-MR and the 4-MR share a C-C bond. In the case of T_1, the DI of this bond is 1.036, which makes the 6-MRs significantly less aromatic according to FLU. For S_0, the DI of this bond is 1.215, which is more similar to the value of aromatic molecules (Figure 54). Thus, the delocalization of the 6-MRs changes significantly from the S_0 (FLU*b* = 0.0052) to the T_1 state (FLU*b* = 0.0169) (Table 8). From the analysis of the DI it is clear that in the S_0 state there are two independent aromatic rings (6-MRs) connected by two single C-C bonds (DI close to 1), so the central 4-MR is non-aromatic or antiaromatic. On the other hand, in the T_1 state we have a large aromatic 12-MR, so the molecule is globally aromatic. Finally, the changes in aromaticity when going from the S_0 to the T_1 state are also apparent in the geometries.

DI in red
Bond distance in black
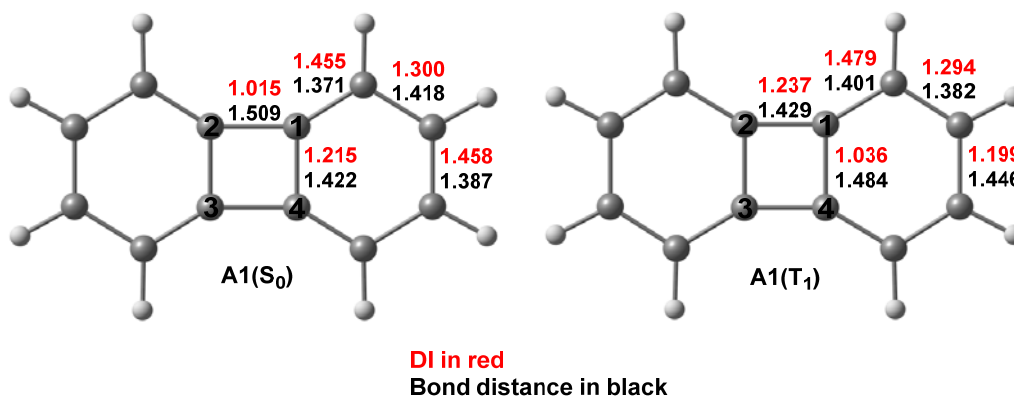
Figure 54. The delocalization indices (in e) and C-C bond lengths (in Å) of compound **A1** in the S_0 and T_1 states.

So is **A1** an aromatic chameleon compound? It is certainly influenced by Hückel-aromaticity in its S_0 state, although different aromaticity indices give different results as to the extent of this influence. Moreover, it is influenced by Baird-aromaticity in the T_1 state. Accordingly, **A1** has doubtlessly an aromatic chameleon character. Yet, can this character be increased in dibenzofused compounds having central 8π-electron units instead of a 4π-electron units?

Table 9. FLU_x and γ_x values of parent [$4n$]annulene in the T_1 state.

Compound	x	FLU_x	$\gamma_x = \Delta FLU_x / FLU_x$
	4	0.0100	1.7300
	8	0.0009	3.5556
	5,5	0.0033	1.8182

The various aromaticity measures applied to **B1** and **C1** in their S_0 and T_1 states also reveal aromatic chameleon features. The FLU values of 0.0011 and 0.0032 (Table 8), respectively, show strong representation of two aromatic benzene rings in both **B1**(S_0) and **C1**(S_0). In the T_1 state, the FLU index points out that the global π-electron delocalization through the perimeter is similarly effective in **A1** (T_1), **B1** (T_1) and **C1** (T_1) because the FLU*bab'* values are 0.0082, 0.0085 and 0.0066, respectively (Table 8). FLU values of parent [*4n*] annulenes are calculated at the same level for comparison to other compounds (Table 9). However, the γ

values show important differences between **A1** and **C1**, on one side, and **B1** on the other. While **A1** (T_1) and **C1** (T_1) have Baird-aromatic character in the perimeter ($\gamma_{bab'}$(**A1**) = 1.00, $\gamma_{bab'}$(**C1**) = 0.61), this is not the case for **B1** (T_1) ($\gamma_{bab'}$ = 0.01). Accordingly, **B1** (T_1) seems better represented by two Hückel-aromatic π-sextets in the $\boldsymbol{b}$ rings (FLU$_b$ = 0.0150, γ_b = 0.06) and a Baird-aromatic $\boldsymbol{a}$ ring (FLU$_a$ = 0.0098, γ_a = 0.58).

In conclusion, all three species **A1** – **C1** are influenced by Hückel-aromaticity in S_0 and by Baird-aromaticity in T_1, and can accordingly be labeled as aromatic chameleons. Now, having identified the tendency of these compounds to redistribute their electron density when going from S_0 to T_1, and to act as aromatic chameleons, how does this change upon further benzannelation? Such further benzannelation may impede the ability of the electronic structure readjustment in the T_1 state, but it may also depend on the connectivity (*vide infra*), and on the size of the central $4n\pi$-electron unit. An effect on the connectivity is indeed observed in the relaxed T_1 state energies as it will be seen next.

Prof. Ottosson's group have found that the $E(T_1)$ of classes **A3** and **C3** (Table 10), but not of class **B3**, show similar trends on the connectivity. The class **B3** presents weaker dependence of $E(T_1)$ on connectivity because of the non-planarity of these systems in the S_0 states, which results in weaker conjugation. Now, how do the variations in $E(T_1)$ among different isomers link with the connectivity and aromaticity? And how does it influence even larger benzannelated class A compounds?

If there is a variation in the $E(T_1)$ on the connectivity it should be visible in the relative isomer energies in the T_1 state. Moreover, our hypothesis is that an isomer which hosts a larger number of aromatic cycles, regardless if closed-shell π-sextets or triplet diradical π-quartets or π-octets, should have a lower relative energy than an isomer with less number of such units. Thus, we probe if Clar's rule can be extended to involve also $4n\pi$-electron circuits that are Baird-aromatic, and we first test the hypothesis on class A and subsequently on classes B and C. Will the correctness of the hypothesis and its applicability depend on the size of the $\boldsymbol{a}$ ring? In order to prove that hypothesis we have analysed the 3LL, *cis*-3BB and 4BBBB isomers. Generally, in all three classes, the $E(T_1)$ of *cis*-3BB isomer is smaller than the 3LL one. Besides, in the T_1 state, *cis*-3BB isomer is always more stable than the 3LL one.

Table 10. Relaxed triplet state energies $E(T_1)$ in eV at the (U)B3LYP/6-311G(d,p) level.

Class A		Class B		Class C	
	$E(T_1)$		$E(T_1)$		$E(T_1)$
A1	1.92	**B1**	1.74	**C1**	1.33
A2L	2.22	**B2L**	2.40	**C2L**	1.42
A2B	1.42	**B2B**	1.67	**C2B**	1.02
A3LL	2.75	**B3LL**	2.04	**C3LL**	1.43
A3LB	1.68	**B3LB**	1.74	**C3BL**	1.14
cis-**A3BB**	1.06	*cis*-**B3BB**	1.61	*cis*-**C3BB**	0.79
trans-A3BB	1.03	**trans-B3BB**	1.69	**trans-C3BB**	0.78
A4LLLL	1.70	**B4LLLL**	1.61	**C4LLLL**	1.30
A4BBBB	0.62	**B4BBBB**	1.93	**C4BBBB**	0.58

In terms of FLU, similar values are observed for **A3LL** and *cis*-**A3BB** in their T_1 states. In both cases, the outer benzene ring (FLU_c = 0.0077/0.0044), the naphthalene unit (FLU_{bc} = 0.009/0.0104) and the whole perimeter ($FLU_{cbab'c'}$ = 0.0068/0.0073) are the most efficient circuits for π-electron delocalization (Table 11). However, there are important differences according to γ. Thus, **A3LL** presents a high Baird-aromatic character in the outer benzene ring ($γ_c$ = 1.79) and a Hückel-aromatic character in the perimeter ($γ_{cbab'c'}$ = 0.06), whereas the outer benzene ring in *cis*-**A3BB** is basically Hückel aromatic ($γ_c$ = 0.12) and the perimeter is Baird aromatic ($γ_{cbab'c'}$ = 0.60).

So what is the reason for the T_1 state stabilization found in **A3BB**? It seems that FLU cannot explain the relaxed triplet energies trends. Yet, the ring currents provided by magnetic descriptors show different results (Figure 55). **A1** and **A3LL** display a global diamagnetic current and two Clar π-sextets, respectively. In case of *cis*-**A3BB**, besides from the diamagnetic ring current, two Clar π-sextets and a π-quartet are detected as well (Figure 55). In particular, according to Clar's rule, **I-A3LL** and **I-*cis*-A3BB** (Figure 55) should be the most stable structures and this is line with the magnetic descriptors. Actually, **A3LL** prefers two π-sextets instead of one π-quartet while *cis*-**A3LL** favors two π-sextets and one π-quartet

instead of only two π-sextets. Therefore, it is not obvious that our working hypothesis on usage of Baird's rule in a Clar's rule context is useful for the rationalization of the $E(T_1)$ of the **A3** isomers.

Table 11. FLU and γ values computed for all the possible (local, semi-global, and global) circuits in S_0 and T_1 states for **A3LL** and *cis*-**A3BB**.

Compound	Electronic state	Circuit along perimeter of ring(s)	FLU	γ
A3LL	S_0	a	0.0490	
		b	0.0182	
		c	0.0059	
		a+b	0.0292	-
		b+c	0.0114	
		b+a+b'	0.0227	
		c+b+a+b'+c'	0.0141	
	T_1	a	0.0384	0.3464
		b	0.0173	0.4138
		c	0.0077	1.7904
		a+b	0.0198	0.0015
		b+c	0.0090	0.7286
		b+a+b'	0.0135	0.3333
		c+b+a+b'+c'	0.0068	0.0624
cis-**A3BB**	S_0	a	0.0435	
		b	0.0070	
		c	0.0144	
		a+b	0.0257	-
		b+c	0.0071	
		b+a+b'	0.0198	
		c+b+a+b'+c'	0.0148	
	T_1	a	0.0345	0.3660
		b	0.0190	0.3088
		c	0.0044	0.1213
		a+b	0.0191	0.4442
		b+c	0.0104	0.3513
		b+a+b'	0.0139	0.5088
		c+b+a+b'+c'	0.0073	0.5970
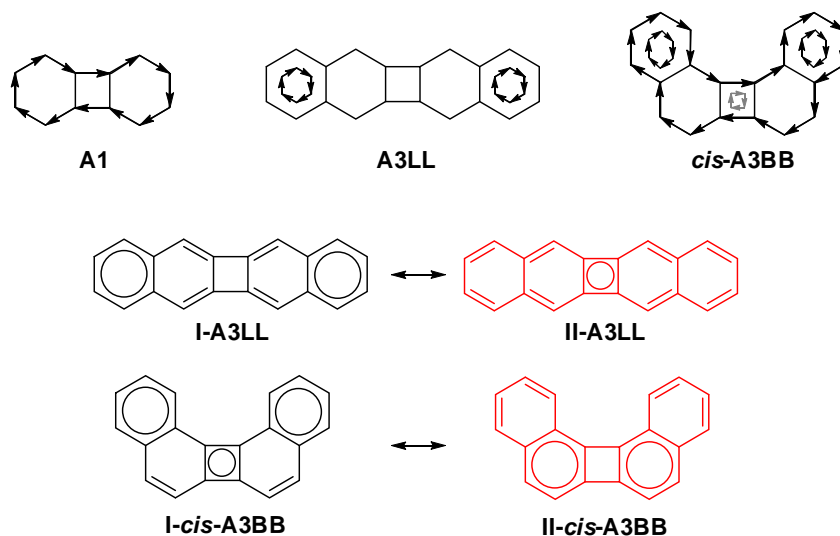
Figure 55. Schematic drawings of the ring current of **A1**, **A3LL** and ***cis*-A3BB** and resonance structures of **A3LL** and ***cis*-A3BB**. Red structures obey Clar's rule.

In this context, one can regard **A4BBBB**, a compound which could exhibit a particularly pronounced T_1 state stabilization and aromaticity since it is analogous to tetrabenzanthracene, *i.e.*, the fully benzenoid isomer among the heptabenzenoid PAHs. Compound **A4BBBB** has an $E(T_1)$ of 0.62 eV (Table 10), *i.e.*, 1.08 eV lower than that of **A4LLLL**. NICS$_{XY}$ scans and ACID plots reveal a global current along the perimeter, and additionally, localized currents in the π-sextets of the *c* rings as well as the π-quartet of the *a* ring (Figure 56).
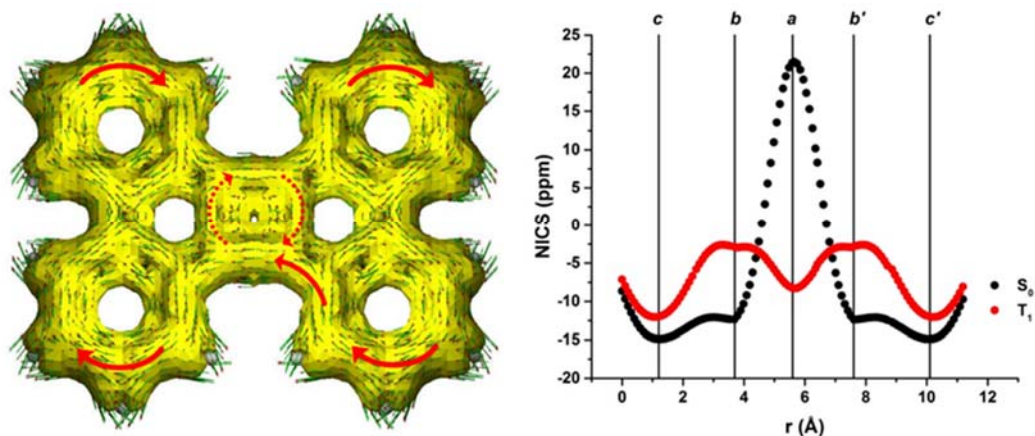
Figure 56. T_1 ACID plot and NICS$_{XY}$ scans of **A4BBBB**.

Table 12. FLU and γ values computed for all the possible (local, semi-global, and global) circuits in S_0 and T_1 states for **A4BBBB**, **B4BBBB**, and **C4BBBB**.

Compound	Electronic state	Circuit along perimeter of ring(s)	FLU	γ
A4BBBB	S_0	a	0.0434	
		b	0.0131	
		c	0.0077	
		a+b	0.0315	
		a+b+c	0.0296	
		b+c	0.0091	-
		c+b+c'	0.0073	
		b+a+b'	0.0220	
		c+b+a+b'+c'	0.0177	
		perimeter	0.0135	
	T_1	a	0.0307	0.4631
		b	0.0241	0.2473
		c	0.0043	0.1172
		a+b	0.0234	0.3941
		a+b+c	0.0210	0.3605
		b+c	0.0141	0.2562
		c+b+c'	0.0098	0.2656
		b+a+b'	0.0152	0.4043
		c+b+a+b'+c'	0.0122	0.3746
		perimeter	0.0084	0.3897
B4BBBB	S_0	a	0.0487	
		b	0.0209	
		c	0.0050	
		a+b	0.0425	
		a+b+c	0.0324	
		b+c	0.0134	-
		c+b+c'	0.0102	
		b+a+b'	0.0393	
		c+b+a+b'+c'	0.0269	
		perimeter	0.0208	
	T_1	a	0.0082	0.7583
		b	0.0250	0.1600
		c	0.0031	0.1180
		a+b	0.0152	0.2752
		a+b+c	0.0116	0.2781
		b+c	0.0153	0.1656
		c+b+c'	0.0111	0.1710
		b+a+b'	0.0188	0.1702
		c+b+a+b'+c'	0.0127	0.1756
		perimeter	0.0097	0.1808
C4BBBB	S_0	a+a	0.0326	
		b	0.0154	
		c	0.0059	
		a+a'+b'	0.0294	
		b+c	0.0102	
		c+b+c'	0.0080	
		c+b+a+a'+b'+c'	0.0194	-
		b+a+a'+b'	0.5858	
		perimeter	0.0152	

T_1	a+a	0.0119	0.7945
	b	0.0233	0.2657
	c	0.0036	0.0611
	a+a'+b'	0.0151	0.3697
	b+c	0.0142	0.2432
	c+b+c'	0.0102	0.2368
	c+b+a+a'+b'+c'	0.0113	0.2038
	b+a+a'+b'	0.0167	0.2186
	perimeter	0.0085	0.1893

For **A4BBBB**, FLU gives a different description as it indicates local Hückel-aromaticity in the *c* rings (FLU$_c$ = 0.0043, γ_c = 0.12) as well as semi-global (FLU$_{cbc'}$ = 0.0098, $\gamma_{cbc'}$ = 0.27) and global (FLU$_{perimeter}$ = 0.0083, $\gamma_{perimeter}$ = 0.39) circuits efficient for π-electron delocalization (Table 12). According to FLU, the perimeter has the highest Baird-aromatic character. In general, FLU fails to detect Baird aromaticity in the 4-MRs of T_1 states.

In terms of FLU (Table 12), **C4BBBB**(T_1) shows similar properties as **A4BBBB**(T_1). Specifically, the highest localization is found in the inner benzene ring (FLU$_b$ = 0.0241–0.0233) while the two outer benzene rings (FLU$_c$ = 0.0036-0.0043) are more Hückel aromatic. The phenanthrene moiety has also two semi-global circuits, the naphthalene one (**bc**) and the global one (**cbc'**). The latter (FLU$_{cbc'}$ = 0.0098-0.0102) is more delocalized than the former (FLU$_{bc}$ = 0.0142 - 0.0141). Finally, the most efficient circuit for π-electron delocalization is in the perimeter (FLU$_{perimeter}$ = 0.0084 - 0.0085) which has Hückel-aromatic character according to the γ value. The pentalene unit in **C4BBBB**(T_1) is more Baird aromatic than the 4-MR in **A4BBBB**(T_1) (FLU$_{aa'}$ = 0.0119 and $\gamma_{aa'}$ = 0.7945 *vs.* FLU$_a$ = 0.0307 and γ_a = 0.4631, respectively). On the other hand, **B4BBBB**(T_1) is best described as four Hückel π-sextets in the outer 6-MRs (FLU$_c$ = 0.0031) and one Baird π-octet in the 8-MR (FLU$_a$ = 0.0082 and γ_a = 0.7583).

Since it is known that CBD displays less extent of Baird-aromaticity in the T_1 state than larger [4*n*] annulenes, our hypothesis may work better in classes B and C with central 8π-electron units instead of the 4π-electron CBD cycle. As we comment above, FLU has not been calculated for all the systems but we decide to show the general behavior of the ring currents of **B3LL**, *cis*-**B3BB**, **C3LL** and *cis*-**C3BB** (Figure 57) which are provided by Prof. Ottosson's group.
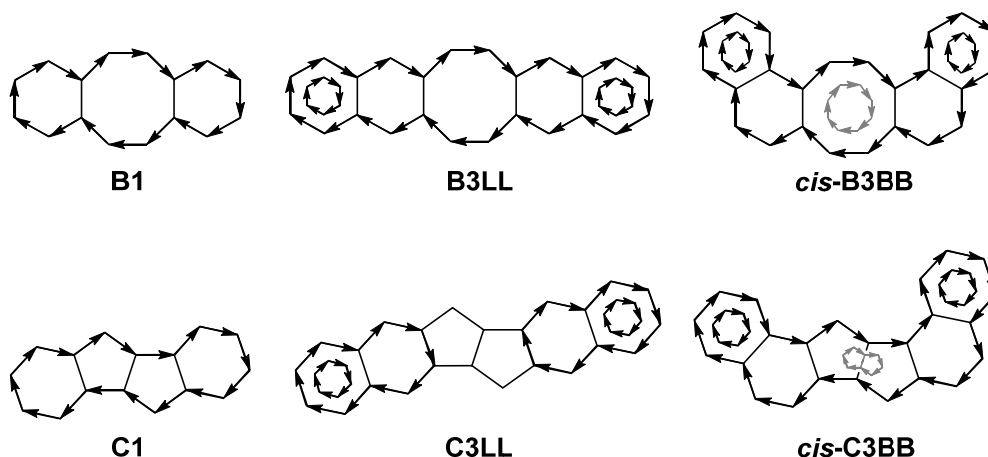
Figure 57. Schematic drawings of the ring current based on NICS$_{XY}$ scans and ACID plots.

B3LL(T$_1$) exhibits diamagnetic ring-currents going along the perimeter of the whole molecule (Figure 57). The ACID plots of ***cis*-B3BB**(T$_1$) show similar magnetic properties as ***cis*-A3BB**(T$_1$) with several different ring-currents; one that moves along the perimeter but also local diamagnetic ring-currents inside the ***c*** and ***a*** rings. The **B3** and **C3** isomers with bent connectivities are 17.0 and 7.3 kcal/mol more stable in their T$_1$ states than the corresponding linear isomers, which is smaller than found for the **A3** isomers (*vide supra*, 26.8 kcal/mol). However, these gains are now more clearly consequences of the existence of three local aromatic cycles in the bent isomers; two π-sextets in the ***c*** rings and one Baird-aromatic π-octet. Yet, the reason for the smaller gain in energy in T$_1$ when going from 3LL to 3BB isomers for class B and C than for class A seems connected to the gain of closed-shell Hückel-aromaticity in the ***c*** rings in the various compound classes.

CHAPTER 6: CHEMICAL

BONDING AND

AROMATICITY IN METAL

CLUSTERS[a]

[a]This chapter is based on the following publications:

6.1) El Bakouri, O.; Solà, M.; Poater, J. Planar *vs.* three-dimensional X_6^{2-}, $X_2Y_4^{2-}$, and $X_3Y_3^{2-}$ (X, Y = B, Al, Ga) metal clusters: an analysis of their relative energies through the turn-upside-down approach. *Phys. Chem. Chem. Phys.* **2016**, *18*, 21102.

6.2) El Bakouri, O.; Duran, M.; Poater, J.; Feixas, F.; Solà, M. Octahedral aromaticity in $^{2S+1}A_{1g}$ X_6^q clusters (X = Li–C and Be–Si, S = 0–3, and q = −2 to +4). *Phys. Chem. Chem. Phys.* **2016**, *18*, 11700.

6.3) El Bakouri, O.; Postils, V.; Garcia-Borràs, M.; Duran, M.; M. Luis, J.; Calvello, S.; Soncini, A.; Feixas, F.; Solà, M. Metallaelectrides: A molecular model for the metallic bonding. *To be submitted.*

6.4) El Bakouri, O.; Postils, V.; Feixas, F.; Solà, M.; Matito, E. Electride, metal, and metallaelectride behavior in lithium metal clusters. *To be submitted.*

6.1 Planar *vs.* three-dimensional X_6^{2-}, $X_2Y_4^{2-}$, and $X_3Y_3^{2-}$ (X, Y = B, Al, Ga) metal clusters: an analysis of their relative energies through the turn-upside-down approach

Despite B and Al belong to the same group 13 elements, the B_6^{2-} cluster prefers the planar D_{2h} geometry, whereas Al_6^{2-} favours the O_h structure. In this work, we analyse the origin of the relative stability of the D_{2h} and O_h forms in these clusters by means of an energy decomposition analysis based on the turn-upside-down approach. Our results show what causes the different trend observed is the orbital interaction energy term, which combined with the electrostatic component does (Al_6^{2-} and Ga_6^{2-}) or does not (B_6^{2-}) compensate the higher Pauli repulsion of the O_h form. Analysing the orbital interaction term in more detail, we find that the preference of B_6^{2-} for the planar D_{2h} form has to be attributed to two particular MO interactions. Our results are in line with a dominant delocalization force in Al clusters and the preference for more localized bonding in B metal clusters. For mixed clusters, we have found that those with more than two B atoms prefer the planar structure for the same reasons as for B_6^{2-}.

6.1.1 State-of-the-art

The electronic distribution of nanosized molecular clusters can be very different from that of the bulk state.[366] In fact, metals can exhibit isolating behaviour when reduced to small particles. Since the electronic properties of nanoparticles are quite different from those of the bulk, molecular clusters are expected to have a variety of electronic applications, such as single-electron transistors, diodes, and quantum dots.[367–369] The properties of clusters are

profoundly affected by the type of bonding they have. For some of these clusters one can expect an intermediate situation between covalent and metallic bonding. As modern technologies evolve towards the nanoscale, it becomes more important to have a more precise understanding of the bonding in these species to better tune their properties.

Among clusters, those made by group 13 atoms are particularly important.[370] Both B and Al belong to the same group 13, and thus present a similar electronic structure, $[He]2s^22p^1$ and $[Ne]3s^23p^1$, respectively. However, when they form small clusters, B clusters adopt a planar conformation as the equilibrium structure;[123,371–373] whereas Al clusters present a three-dimensional (3D) closed shape.[29,31,374,375] The most relevant examples are B_6^{2-} and Al_6^{2-} clusters, which were obtained experimentally as lithium salts in the form of LiB_6^- and $LiAl_6^-$.[375–377] B_6^{2-} adopts a planar D_{2h} geometry in its low-lying singlet state, whereas the Al_6^{2-} cluster is octahedral. Both shapes of the metal clusters are kept when lithium salts are formed.

The chemical bonding of B_6^{2-} and Al_6^{2-} has been widely analysed in previous studies.[375,378,379] In particular, Alexandrova *et al.*[379] highlighted the fact that B_6^{2-} is able to 2s–2p hybridize and to form 2c–2e B–B covalent localized bonds. On the other hand, 3s–3p hybridisation in the Al_6^{2-} cluster is more difficult due to larger s–p energy separation, which hampers the formation of directional covalent Al–Al bonds.[380] In this case, bonding comes from the combination of radial and tangential p-orbitals that result in extensive delocalisation.[381] Indeed, the Al_6^{2-} cluster displays octahedral aromaticity,[375,382] whereas planar D_{2h} B_6^{2-} is considered σ- and π-antiaromatic.[378,379,383,384] Thus, as pointed out by Alexandrova *et al.*,[379,385–387] covalent and delocalized bonding shows opposite effects in determining the molecular structure of many clusters. Huynh and Alexandrova analysed the whole series $B_nAl_{6-n}^{2-}$ (n = 0–6), from B_6^{2-} till Al_6^{2-} by substituting one B by Al each time, concluding that covalent bonding is a resilient effect that governs the cluster shape more than delocalisation does. Indeed, the planar structure of B_6^{2-} persists until n = 5, the reason being the strong tendency to form 2c–2e B–B bonds in case the cluster contains two or more B atoms.[379] Similar results were reported by Fowler and Ugalde in larger clusters of group 13. In particular, these authors found that B_{13}^+ prefers a planar conformation[388] in contrast to Al_{13}^-,[389] which adopts an icosahedral geometry. Interestingly, in closo boranes and substituted related species, like $B_6H_6^{2-}$ or $B_{12}I_{12}^{2-}$, the delocalized 3D structure is preferred. However, successive stripping of iodine in $B_{12}I_{12}^{2-}$ leads to a B_{12} planar structure with some localized 2c–2e B–B bonds.[390,391]

Similarly, for $B_6H_n^-$ clusters, the clusters are planar for n ≤ 3 and become three-dimensional for n ≥ 4.[392]
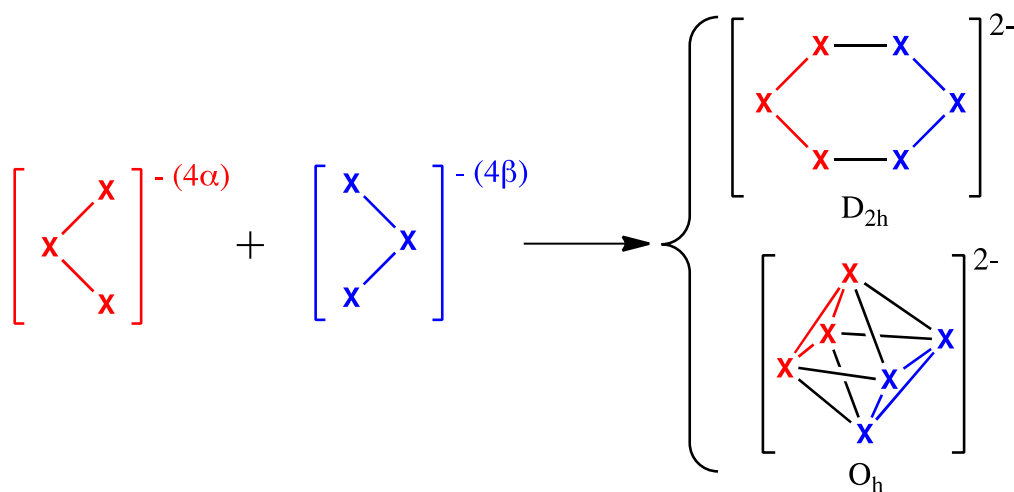
Scheme 9. D_{2h} and O_h structures of X_6^{2-} can be formed from C_{2v} X_3^- fragments.

As can be seen in Scheme 9, both 2D D_{2h} planar and 3D O_h geometries for X_6^{2-} (X = B, Al) can be obtained joining the same two X_3^- cluster fragments.[375,378] Therefore, X_6^{2-} species in D_{2h} and O_h geometries are particularly suitable for EDA[259,393–395] based on the turn-upside-down approach.[396–399] In this approach, two different isomers are formed from the same fragments and the bonding energy is decomposed into different physically meaningful components using an EDA. Differences in the energy components explain the reasons for the higher stability of the most stable isomer. For instance, using this method our group provided an explanation of why the cubic isomer of T_d geometry is more stable than the ring structure with D_{4h} symmetry for $(MX)_4$ tetramers (X = H, F, Cl, Br, and I) if M is an alkalimetal and the other way round if M belongs to group 11 transition metals.[398] Therefore, the application of this type of analysis to B_6^{2-} and Al_6^{2-} clusters will disclose the factors that make the planar D_{2h} structure more stable for boron and the octahedral one for aluminium. As said before, boron clusters favour localized covalent bonds whereas aluminium clusters prefer a more delocalized bonding. With the present analysis, we aim to provide a more detailed picture of the reasons for the observed differences. The analysis will be first applied to the above referred B_6^{2-} and Al_6^{2-} clusters, and then further complemented with Ga_6^{2-}. Finally, $X_2Y_4^{2-}$ and $X_3Y_3^{2-}$ (X, Y = B, Al, Ga) mixed clusters in their distorted D_{2h} planar and 3D D_{4h} geometries will also be discussed.

6.1.2 Results and discussion

We first focus on the homoatomic X_6^{2-} metal clusters with X = B, Al, and Ga. The optimized O_h and D_{2h} geometries at the BLYP-D3(BJ)/TZ2P level are depicted in Figure 58 with the main bond lengths and angles. As expected, B–B bond lengths (1.536–1.768 Å) are much shorter than those for Al–Al (2.574–2.912 Å) and Ga–Ga (2.526–2.898 Å). The similar Al–Al and Ga–Ga distances in X_6^{2-} metal clusters (X = Al, Ga) are not unexpected given the similar van der Waals radii of these two elements.[400] In addition, the X–X bond length connecting the two equivalent X_3^- fragments in O_h clusters is longer than in the D_{2h} systems.
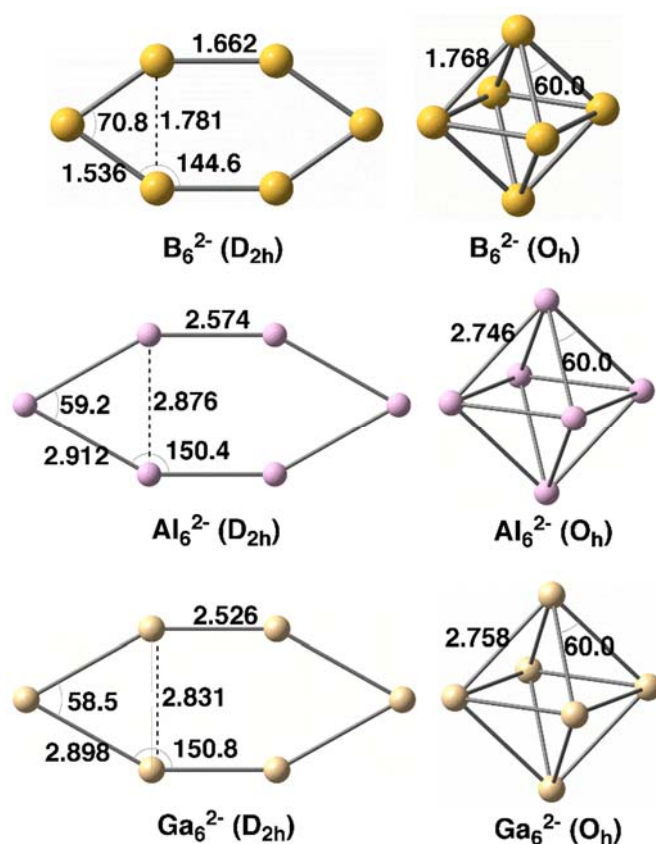
Figure 58. Geometries of X_6^{2-} metal clusters analysed with D_{2h} and O_h symmetries. Distances in Å and angles in degrees.

Table 13 encloses the energy differences between O_h and D_{2h} clusters. For B_6^{2-} D_{2h} symmetry is more stable than O_h by 67.5 kcal mol^{-1}, the latter not being a minimum.[379] Meanwhile the opposite trend is obtained in the other two metal clusters, for which O_h is lower in energy by 15.8 (Al_6^{2-}) and 9.3 kcal mol^{-1} (Ga_6^{2-}) than D_{2h} structures. These trends are confirmed by higher level CCSD(T)/aug-cc-pVTZ single point energy calculations at the same BLYP-D3(BJ)/TZ2P geometries (values also enclosed in Table 13). The relative energies of B_6^{2-},

Al_6^{2-}, and Ga_6^{2-} between O_h and D_{2h} symmetries are now -38.7, $+44.8$ and $+46.6$ kcal mol^{-1}, respectively. CCSD(T) values systematically favour O_h as compared to D_{2h} structures by about 20–30 kcal mol^{-1}. However, the qualitative picture remains the same.

Table 13. Relative energies of clusters between O_h and D_{2h} symmetries (in kcal·mol^{-1}); and aromatic MCI criterion.

Clusters		BLYP-D3(BJ)/TZ2P[a]		CCSD(T)/aug-cc-pVTZ[b]		MCI[c]	
		O_h	D_{2h}	O_h	D_{2h}	O_h	D_{2h}
X_6^{2-}	B_6^{2-}	67.5[e]	0.0[d]	38.7	0.0	0.062	-0.052
	Al_6^{2-}	0.0[d]	15.8[e]	0.0	44.8	0.077	0.068
	Ga_6^{2-}	0.0[f]	9.3[f]	0.0	46.6	0.083	0.071
		D_{4h}	D_{2h}	D_{4h}	D_{2h}	D_{4h}	D_{2h}
$X_2Y_4^{2-}$	$B_2Al_4^{2-}$	0.0[g]	15.9[g]	0.0	34.0	0.032	0.001
	$Al_2B_4^{2-}$	66.9[h]	0.0[g]	48.7	0.0	0.032	0.023
	$Al_2Ga_4^{2-}$	0.0[d]	13.0[h]	0.0	43.3	0.077	0.068
	$Ga_2B_4^{2-}$	79.4[g]	0.0[g]	47.1	0.0	0.047	0.042
	$Ga_2Al_4^{2-}$	0.0[d]	14.8[g]	0.0	48.2	0.074	0.072
		D_{3h}	C_{3v}	D_{3h}	C_{3v}	D_{3h}	C_{3v}
$X_3Y_3^{2-}$	$Al_3Ga_3^{2-}$	0.0[d]	13.2[h]	0.0	45.3	0.078	0.068

[a] $B_2Ga_4^{2-}$ (D_{2h}) has not been obtained because optimization breaks the symmetry; whereas $B_3Ga_3^{2-}$ and $B_3Ga_3^{2-}$ (O_h) have not been obtained because the strength of the B_3 unit causes the systems to be planar and to avoid a 3D geometry. [b] Single point energy calculations at BLYP-D3(BJ)/TZ2P geometries. [c] MCI calculated at the BLYP/aug-cc-pVDZ level of theory with the BLYP-D3(BJ)/TZ2P optimized geometries. [d] Local minima. [e] One imaginary frequency. [f] One small imaginary frequency due to numerical integration problems. [g] Two imaginary frequencies. [h] Three imaginary frequencies.

The aromaticity of these X_6^{2-} metal clusters was evaluated by means of the MCI electronic criterion. The six-membered MCIs are enclosed in Table 13. In all cases, the O_h system is more aromatic than the D_{2h} one, in agreement with the larger electronic delocalisation of the former, as discussed in 6.1.1.[382] MCI values confirm the octahedral aromaticity[382] of O_h Al_6^{2-} and the antiaromatic character of D_{2h} B_6^{2-}.[378,379,383,384] Interestingly, MCI values point out the clear aromatic character of all 3D clusters that do not contain boron (MCI = 0.074–0.077); whereas mixed $B_2Al_4^{2-}$, $Al_2B_4^{2-}$, and $Ga_2B_4^{2-}$-D_{4h} clusters containing boron atoms are less aromatic (MCI = 0.032–0.047). For planar structures, there are basically two groups of clusters. First, the group formed by B_6^{2-} and $B_2Al_4^{2-}$ has eight valence electrons distributed in two π-MOs and two σ-MOs (*vide infra*). Therefore, having four π-electrons and four σ-electrons, they are σ- and π-antiaromatic species. Second, the group formed by Al_6^{2-}, Ga_6^{2-},

$Al_2B_4^{2-}$, $Al_2Ga_4^{2-}$, $Ga_2B_4^{2-}$, and $Ga_2B_4^{2-}$ have eight valence electrons distributed in one π-MO and three σ-MOs (*vide infra*) and, therefore, they are σ- and π-aromatic species.

With the aim to obtain a deeper insight into the origin of 2D to 3D relative energies an energy decomposition analysis was performed, following the reaction presented in Scheme 9. As pointed out above, both systems can be constructed from two identical X_3^- anionic fragments, both in their quintet state in order to form the corresponding new bonds. Three of these bonds are of σ character, two tangential ($σ^T$) and one radial ($σ^R$), and one π character (see Figure 59). It must be pointed out that, very recently, Mercero *et al.* have proven the multiconfigurational character of some of the lowest-lying electronic states of Al_3^-.[380] In the case of the quintet state of Al_3^-, which is the fragment used in our calculations, the authors showed that the electronic configuration of the four valence electrons is also derived from the occupation of two σ-type tangential and one σ-type radial MOs arising from the $3p_x$ and $3p_y$ AOs, and one π-type orbital arising from the $3p_z$ ones. This quintet state was found to be dominated by one-single configuration with a coefficient of 0.92 in the multiconfigurational wavefunction.[380] Moreover, the energy difference between the ground state and the quintet state was almost the same when computed at DFT or at the MCSCF levels of theory.[380] This seems to indicate that DFT methods give reasonable results for this quintet state. Finally, the T_1 test[401] applied to clusters collected in Table 13 was found to be always less than 0.045, thus indicating the relatively low multiconfigurational character of these species. It is commonly accepted that CCSD(T) produces acceptable results for T_1 values as high as 0.055.[402]

The different terms of the EDA for B_6^{2-}, Al_6^{2-}, and Ga_6^{2-} clusters are enclosed in Table 14. First we notice that the total bonding energies (ΔE) are much larger for B_6^{2-} than for Al_6^{2-} or Ga_6^{2-}. For the former, ΔE are −100.2 (O_h) and −179.5 kcal mol⁻¹ (D_{2h}), whereas for the two latter are in between −19.0 and −38.1 kcal mol⁻¹. This trend correlates with the shorter B–B bond lengths mentioned above. Table 14 also encloses the relative EDA energies between the two clusters. The B_3^- fragment taken from the B_6^{2-} system in its D_{2h} symmetry is the one that suffers the largest deformation, *i.e.* the largest change in geometry with respect to the fully relaxed B_3^- cluster in the quintet state (ΔE_{prep} = 12.5 kcal mol⁻¹), whereas the rest of the systems present small values of ΔE_{prep} (0.0–1.7 kcal mol⁻¹). However, differences in ΔE are not due to preparation energies (indeed ΔE_{prep} values follow the opposite trend as ΔE), but to interaction energies (ΔE_{int}).

Table 14. EDA of singlet ground state X_6^{2-} (X = B, Al, and Ga) metal clusters with D_{2h} and O_h symmetries (in kcal·mol^{-1}), from two X_3^- fragments at their quintet state, computed at the BLYP-D3(BJ)/TZ2P level.

	B_6^{2-}			Al_6^{2-}			Ga_6^{2-}		
	$D_{2h}+D_{2h}$ →D_{2h}	O_h+O_h →O_h	$\Delta(\Delta E)$	$D_{2h}+D_{2h}$ →D_{2h}	O_h+O_h →O_h	$\Delta(\Delta E)$	$D_{2h}+D_{2h}$ →D_{2h}	O_h+O_h →O_h	$\Delta(\Delta E)$
ΔE_{int}	-192.0	-101.4	-90.6	-20.7	-39.8	19.1	-19.1	-31.0	11.9
ΔE_{Pauli}	533.5	735.3	-201.8	225.7	348.0	-122.3	269.6	384.5	-114.9
ΔV_{elstat}	-239.0	-291.9	52.9	-96.3	-166.5	70.2	-138.0	-207.5	69.5
ΔE_{oi}	-483.4	-542.8	59.4	-146.9	-217.4	70.5	-146.7	-203.4	56.7
ΔE_{disp}	-3.2	-2.1	-1.1	-3.2	-3.9	0.7	-4.0	-4.7	0.6
ΔE_{prep}	12.5	1.3	11.2	0.0	1.7	-1.7	0.1	1.4	-1.3
ΔE	-179.5	-100.2	-79.3	-20.7	-38.1	17.4	-19.0	-29.6	10.6

Thus, we focus on the decomposition of ΔE_{int} into ΔE_{Pauli}, ΔV_{elstat}, ΔE_{oi}, and ΔE_{disp} terms. As a general trend, in all three X_6^{2-} clusters ΔE_{Pauli} is larger for the O_h than the D_{2h} cluster ($\Delta(\Delta E_{Pauli}) = -201.8$, -122.3, and -114.9 kcal mol^{-1} for B_6^{2-}, Al_6^{2-}, and Ga_6^{2-}, respectively), so making it less stable. The overlaps between doubly occupied MOs are larger in the more compact O_h structure that, consequently, has larger ΔE_{Pauli}. The larger difference in ΔE_{Pauli} between the O_h and D_{2h} structures in the case of B_6^{2-} as compared to Al_6^{2-} and Ga_6^{2-} is attributed to the particularly short B–B distances that increase the overlap between doubly occupied MOs of each B_3^- fragment. At the same time, the O_h form presents larger (more negative) electrostatic interactions ($\Delta(\Delta V_{elstat}) = 52.9$, 70.2, and 69.5 kcal mol^{-1} for B_6^{2-}, Al_6^{2-}, and Ga_6^{2-}, respectively). It is usually the case that higher destabilising Pauli repulsions go with larger stabilising electrostatic interactions. The reason has to be found in the fact that both interactions increase in the absolute value when electrons and nuclei are confined in a relatively small space. The electrostatic interaction together with orbital interaction ($\Delta(\Delta E_{oi}) = 59.4$, 70.5, and 56.7 kcal mol^{-1} for B_6^{2-}, Al_6^{2-}, and Ga_6^{2-}, respectively) terms favour the O_h structure. However, in the case of O_h B_6^{2-}, $\Delta(\Delta V_{elstat})$ and $\Delta(\Delta E_{oi})$ cannot compensate $\Delta(\Delta E_{Pauli})$, which causes the D_{2h} system to be the lowest in energy. The opposite occurs for Al_6^{2-} and Ga_6^{2-}. Finally, the dispersion term almost does not affect the relative energies, as the difference in dispersion is only in the order of ca. 1.0 kcal mol^{-1}. Therefore, what causes the different trend observed for B_6^{2-} on one side, and Al_6^{2-} and Ga_6^{2-} on the other side is basically the ΔE_{oi} term, which combined with the ΔV_{elstat} component does (Al_6^{2-} and Ga_6^{2-}) or does not (B_6^{2-}) compensate the higher ΔE_{Pauli} of the O_h form.
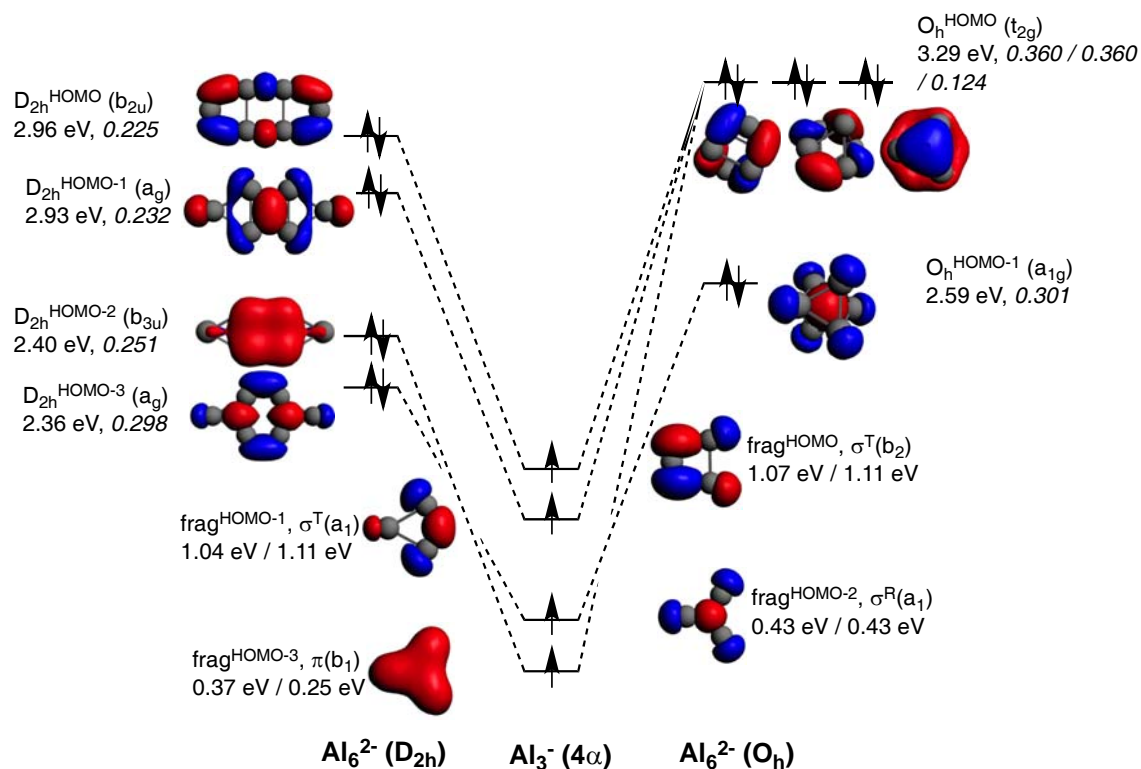
Figure 59. MO diagram corresponding to the formation of Al_6^{2-} in D_{2h} and O_h symmetries from two Al_3^- fragments in their quintet state. Energies of the molecular orbitals are enclosed (in eV), as well as the <SOMO|SOMO> overlaps of the fragments (values in italics). Energies of the fragments obtained from both D_{2h} (left) and O_h (right) symmetries are also enclosed.

The comparison of the MOs diagrams of B_6^{2-} and Al_6^{2-}, built from their X_3^- fragments, justify the trends of ΔE_{oi} (see Figure 59 and Figure 60). Both D_{2h} and O_h clusters are built from the same fragments; the only difference is that the two tangential $frag^{HOMO}(\sigma^T(b_2))$ and $frag^{HOMO-1}(\sigma^T(a_1))$ MOs of Al_3^- are degenerate when obtained from Al_6^{2-} in its O_h geometry, whereas they are not when generated from the D_{2h} system, although they still are very close in energy. As discussed from the EDA, O_h is more stable than D_{2h} because of more stabilizing electrostatic and orbital interactions, which compensate its larger Pauli repulsion. Figure 59 also encloses the overlaps for the interactions between the four SOMOs of the Al_3^- fragments to form the MOs of the metal clusters in both geometries. We take the Al_3^- fragments in their quintet states with three unpaired σ- and one unpaired π-electrons, all of them with spin α in one fragment and β in the other. A more negative ΔE_{oi} in O_h Al_6^{2-} is justified from the larger <SOMO|SOMO> overlaps, especially for $O_h HOMO(t_{2g},a)$ and $O_h HOMO(t_{2g},b)$ (0.360 compared to 0.225 and 0.232 for $D_{2h}HOMO(b_{2u})$ and $D_{2h}HOMO-1(a_g)$,

respectively). D_{2h} only presents a larger overlap for the π fragment orbital (0.251 for D_{2h}HOMO-2(b_{3u}) and 0.124 for O_hHOMO(t_{2g},c)). Meanwhile both of them have almost the same overlap for the combination of the radial MO ($σ^R$) fragment ($frag^{HOMO-2}$), with <SOMO|SOMO> = 0.298 and 0.301 for D_{2h}HOMO-3(a_g) and O_hHOMO-1(a_{1g}), respectively. Overall, the higher orbital interaction term of the O_h system can be explained by the larger <SOMO|SOMO> overlaps of two of the t_{2g} delocalized MOs for this cluster (see Figure 59). The energies of the occupied MOs of Al_6^{2-} formed are higher than those of the Al_3^- SOMOs because we move from a monoanionic fragment to a dianionic molecule.
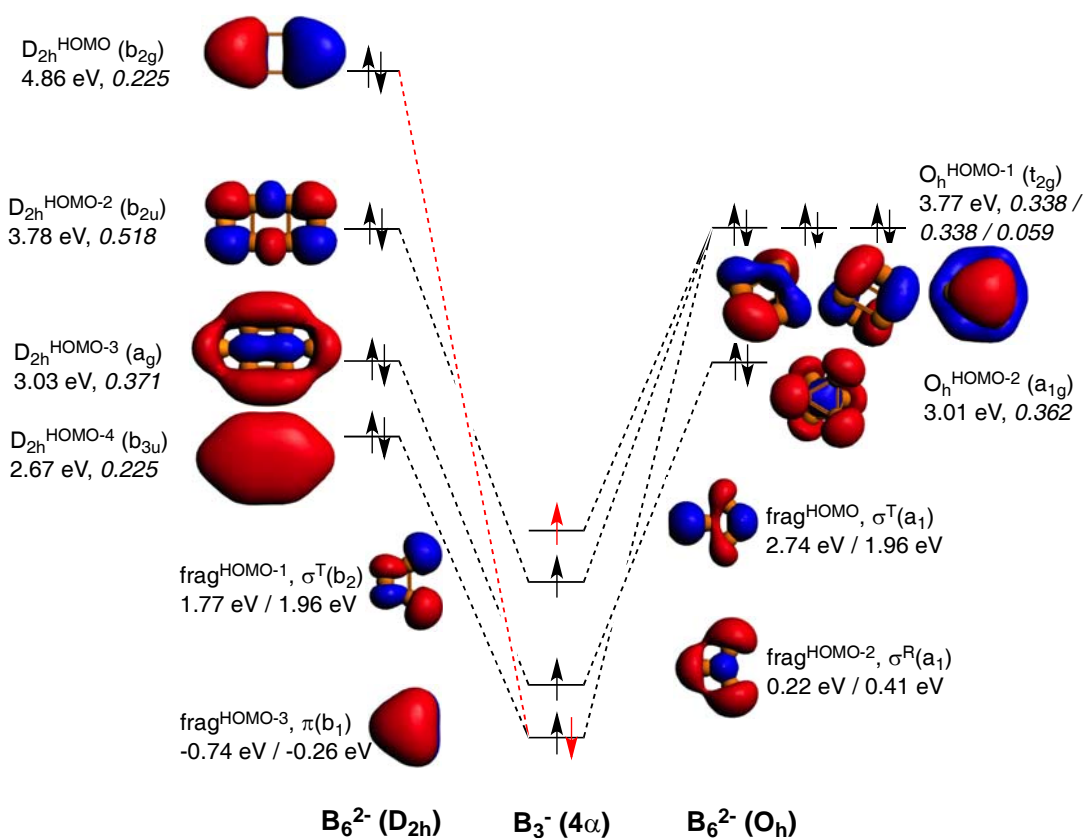
Figure 60. MO diagram corresponding to the formation of B_6^{2-} in D_{2h} and O_h symmetries from two B_3^- fragments in their quintet states. Electrons in red refer to the formation of B_6^{2-} (D_{2h}) from B_3^- fragments in their triplet state. In the triplet state, π(b_1) is doubly occupied, $σ^R$(a1) and $σ^T$(b_2) remain singly occupied, and the $σ^T$(a_1) becomes unoccupied. Energies of the molecular orbitals are enclosed (in eV), as well as the <SOMO|SOMO> overlaps of the fragments (values in italics). Energies of the fragments obtained from both D_{2h} (left) and O_h (right) symmetries are also enclosed.

Now it is the turn to visualize the MOs of B_6^{2-}. The fragments for B_6^{2-} are the same as those for Al_6^{2-} (see Figure 60). However, the first difference appears in the MOs for B_6^{2-} with D_{2h}

symmetry. In this case, it would be more reasonable to build the MOs of this molecule from two triplet (not quintet) B_3^- fragments. The reason is the different occupation of the MOs when compared to the D_{2h} Al_6^{2-} species. In D_{2h} B_6^{2-}, the HOMO corresponds to the antibonding π MO. To reach doubly occupied bonding (D_{2h}HOMO-4(b_{3u})) and antibonding (D_{2h}HOMO(b_{3g})) π MOs, the π MO (frag^{HOMO-3}) should be doubly occupied. Furthermore, the tangential σ^T(a_1) frag^{HOMO} does not participate in any occupied MO of this metal cluster and only generates virtual MOs. Consequently, MOs of B_6^{2-} are better formed from two B_3^- fragments in their triplet state (see red electron in Figure 60). On the other hand, B_6^{2-} with O_h follows the same trend as Al_6^{2-}, and in this case the same SOMOs in their quintet state are involved. At this point, it is worth mentioning that, as pointed out by Mercero *et al.*, due to the strong multiconfigurational character of this species, one must be cautious with the electronic configuration, especially for the triplet state, as radial and tangential MOs are very close in energy.[380]

To make results comparable, Table 14 gathers the EDA of O_h and D_{2h} B_6^{2-} from two B_3^- fragments in their quintet states. Also in this case ΔE_{oi} is more favourable for O_h than for D_{2h}, however, at a lower extent when compared to Al_6^{2-}. There are two main reasons for such a decrease of the strength of ΔE_{oi} in O_h compared to D_{2h}. First, and more importantly, because the D_{2h}HOMO-2(b_{2u}) formed presents a much larger <SOMO|SOMO> overlap than O_hHOMO-1(t_{2g}) (0.518 in the former *vs.* 0.338 in the latter). In particular, this D_{2h}HOMO−2(b_{2u}) MO contributes to the 2c–2e B–B localized bonds that are related to the larger covalent character of this structure. And second, because the π-interaction between the two π-SOMO fragments is much larger in the case of D_{2h} (0.225 *vs.* 0.059 for D_{2h} and O_h, respectively). Nevertheless, these two more favourable orbital interactions are not enough to surpass the ΔE_{oi} term of the O_h cluster. However, as compared to Al_6^{2-}, for B_6^{2-} the $\Delta(\Delta E_{oi})$ term favours the O_h system to a less extent and cannot compensate the higher ΔE_{Pauli} term of the O_h form, thus making the planar geometry to be more stable in this case. This is related to the determinant force of the formed covalent bonding, involving more localized MOs than for Al_6^{2-}. Such a larger covalent component in B_6^{2-} is also supported by the covalent character of the interaction between the two fragments calculated as % covalency = ($\Delta E_{oi}/(\Delta E_{oi} + \Delta V_{elstat} + \Delta E_{disp})$) × 100. This formula results in B_6^{2-}: 65–67% (O_h, D_{2h}), Al_6^{2-}: 56–60% (O_h, D_{2h}), and Ga_6^{2-}: 49–51% (O_h, D_{2h}); thus confirming again the larger covalency found in B_6^{2-}.

Just to conclude this section, we must point out that the whole EDA and turn-upside-down analyses were performed with fragments in their quintet state. However, as we commented before this is not the most reasonable way to build B_6^{2-} in D_{2h} symmetry. Table 15 contains the EDA for O_h and D_{2h} B_6^{2-} systems using B_3^- fragments in their triplet states. Results show that although the different terms are larger in the absolute value, the trends discussed above are not affected, and the D_{2h} cluster is favoured mainly because of smaller Pauli repulsions.

Table 15. EDA of B_6^{2-} metal cluster with D_{2h} and O_h symmetries (in kcal·mol^{-1}), from two B_3^- fragments at their triplet state, computed at the BLYP-D3(BJ)/TZ2P level.

B_6^{2-}	$D_{2h} + D_{2h} \rightarrow D_{2h}$	$O_h + O_h \rightarrow O_h$	$\Delta(\Delta E)$
ΔE_{int}	-84.9	-50.5	-34.4
ΔE_{Pauli}	451.8	1169.5	-717.7
ΔV_{elstat}	-180.9	-447.6	266.7
ΔE_{oi}	-352.7	-770.4	417.7
ΔE_{disp}	-3.2	-2.1	-1.1
ΔE_{prep}	0.2	11.8	-11.7
ΔE	-84.8	-38.7	-46.1

Mixed metal clusters

In this section, we analyse the $X_2Y_4^{2-}$ clusters with X, Y = B, Al, Ga and X ≠ Y (see Figure 61). The relative energies of the planar and 3D forms are also enclosed in Table 13. In all cases, the D_{2h} system is preferred when the cluster incorporates four B atoms; otherwise the 3D D_{4h} geometry is the lowest in energy. In particular, the D_{2h} symmetry is much more stable for $Al_2B_4^{2-}$ and $Ga_2B_4^{2-}$ by 66.9 and 79.4 kcal mol^{-1}, respectively. On the other hand, when B is not the predominant atom, the D_{4h} cluster is more stable by about 9–16 kcal mol^{-1}. As for the homoatomic metal clusters, at the CCSD(T) level, the same trend is obtained, although the D_{4h} system is stabilized with respect to the D_{2h} one by 20–30 kcal mol^{-1}. It is important to note that the D_{4h} and D_{2h} systems are not always the most stable for the $X_2Y_4^{2-}$ clusters. For instance, for $Al_2B_4^{2-}$, a C_2 geometry is the most stable form and, for $B_2Al_4^{2-}$, a C_{2v} structure is the lowest in energy.[379] However, we are not interested here in finding the most stable structure for each cluster but to discuss the reasons why in some cases 2D clusters are preferred over 3D and the other way round. Finally, $Al_3Ga_3^{2-}$ also prefers an O_h geometry by 13.2 kcal mol^{-1}. Unfortunately, this latter relative energy cannot be compared to those of $B_3Al_3^{2-}$ or $B_3Ga_3^{2-}$ because the strength of the localized bonding between three B

atoms prevents the optimization of their 3D structures. In this context, it is worth mentioning that Alexandrova and coworkers[387] found in X_3Y_3 (X = B, Al, Ga; Y = P, As) clusters that the lighter elements prefer 2D structures, whereas the heavier ones favour 3D geometries.

Table 16. Energy decomposition analysis (EDA) of all mixed metal clusters with planar and 3D symmetries (in kcal·mol^{-1}), from two fragments at their quintet states, computed at the BLYP-D3(BJ)/TZ2P level.

		ΔE_{int}	$\Delta E_{\mathrm{Pauli}}$	$\Delta V_{\mathrm{elstat}}$	ΔE_{oi}	ΔE_{disp}
$B_2Al_4^{2-}$	D_{4h}	-52.1	440.1	-202.7	-285.7	-3.9
	D_{2h}	-40.4	243.4	-98.1	-182.5	-3.3
	ΔE	11.7	-196.7	104.6	103.2	0.6
$Al_2B_4^{2-}$	D_{4h}	-75.1	584.0	-251.7	-404.1	-3.3
	D_{2h}	-139.6	556.6	-238.6	-454.5	-3.3
	ΔE	-64.6	-27.4	13.2	-50.4	0.0
$Al_2Ga_4^{2-}$	D_{4h}	-35.0	381.2	-201.0	-210.6	-4.6
	D_{2h}	-19.2	283.1	-147.1	-151.4	-3.8
	ΔE	15.8	-98.1	53.8	59.3	0.8
$Ga_2B_4^{2-}$	D_{4h}	-83.8	590.4	-262.5	-408.2	-3.5
	D_{2h}	-157.5	540.0	-225.6	-468.6	-3.2
	ΔE	-73.7	-50.4	36.8	-60.4	0.3
$Ga_2Al_4^{2-}$	D_{4h}	-38.4	370.1	-188.0	-216.1	-4.3
	D_{2h}	-20.6	218.0	-90.8	-144.4	-3.6
	ΔE	17.8	-152.0	97.3	71.7	0.8
$Al_3Ga_3^{2-}$	D_{3h}	-36.8	381.0	-197.8	-215.7	-4.2
	C_{3v}	-20.7	254.4	-122.8	-148.7	-3.6
	ΔE	16.1	-126.6	75.0	67.0	0.6

The EDA was also performed for this series of six mixed metal clusters (see Table 16) with the aim to further understand the determinant force towards the most stable cluster. For the $X_2Y_4^{2-}$ clusters, the EDA was carried out taken YXY^- fragments in their quintet states. For $Al_3Ga_3^{2-}$, the fragments were Al_3^- and Ga_3^- in the quintet state too. For those systems for which the out-of-plane geometry is the most stable, the combination of more favourable electrostatic and orbital interactions, even though presenting larger Pauli repulsion, gives the explanation to the trend observed. This is the same behaviour already discussed above for both Al_6^{2-} and Ga_6^{2-} systems. On the other hand, when D_{2h} symmetry is the cluster lower in energy, as for $Al_2B_4^{2-}$ and $Ga_2B_4^{2-}$ metal clusters, even though the D_{4h} system presents more stable electrostatic interaction, now the orbital interactions in combination with less unfavourable Pauli repulsion favour the D_{2h} symmetry. This latter behaviour differs from

that of B_6^{2-}, for which the orbital interactions also favour the O_h symmetry, thus making Pauli repulsion the determinant factor towards the preference for planar D_{2h} B_6^{2-}.
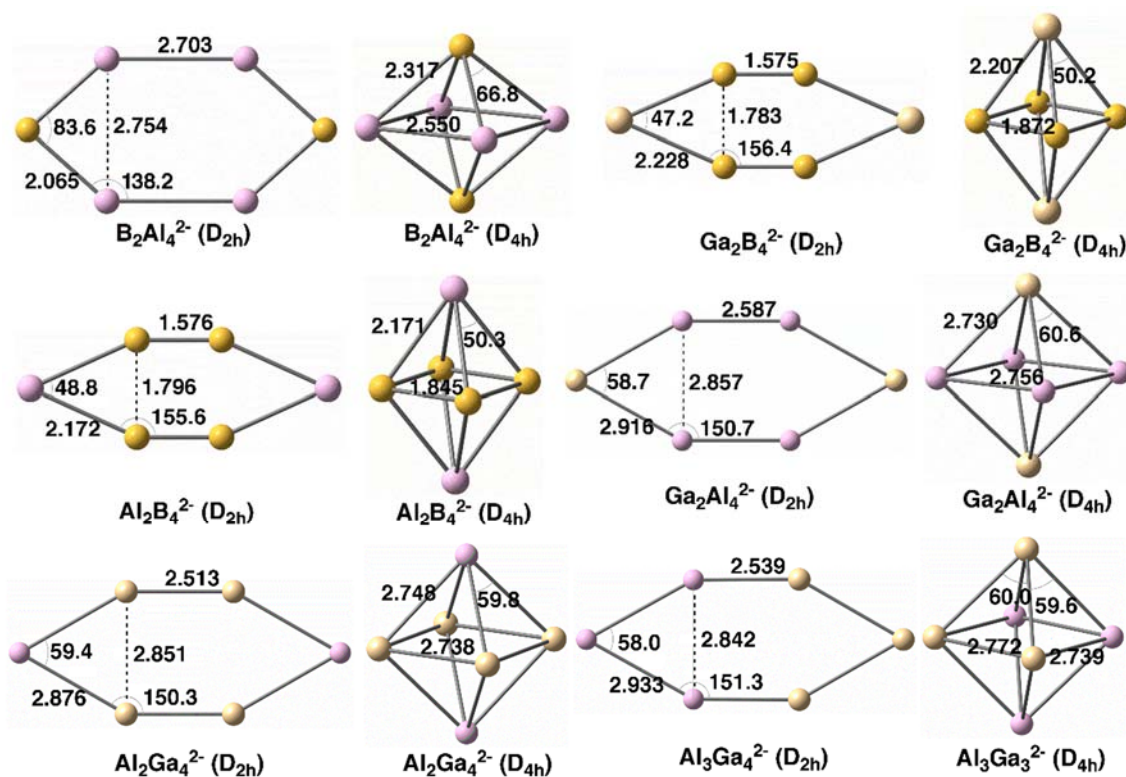
Figure 61. Geometries of mixed metal clusters analysed with planar and 3D geometries. Distances in Å and angles in degrees.

6.2 Octahedral aromaticity in $^{2S+1}A_{1g}$ X_6^q clusters (X = Li–C and Be–Si, S = 0–3, and q = −2 to +4)

The (anti)aromaticity of planar metal clusters can be easily detect because in these cases we can distinguish the π and σ MOs. Extending this concept to three-dimensional systems in metal clusters has been very challenging since we cannot trust anymore in the MOs because the π and σ separation is blurry. However, similar to the spherical rules for fullerenes, specific rules have been proposed to predict the aromaticity in three-dimensional metal clusters (section 1.4.4). Yet, due to the availability of electronic and magnetic descriptors of aromaticity, one could easily quantify the aromaticity of a 3D system and then, according to this information, one could try to design a general rule for analogous systems.

In all examples of known 3D aromaticity[16,18] the systems described as aromatic (section 6.2.1) have a closed-shell or a half-filled shell with same spin electronic structure. These two types

of electronic structures seem to offer good prospects of aromaticity.[403] Thus, we have followed this recipe in the quest for aromatic species with octahedral symmetry. Our search includes all species of the type O_h X_6^q (X = Li–C and Be–Si) with charges going from −2 to +4 and in $^{2S+1}A_{1g}$ electronic states with spin multiplicities ranging from the singlet (S = 0) to the septet (S = 3). We have not included atoms from the groups 15 to 18 due to the little tendency of the atoms of these groups to form clusters. It is worth emphasizing that our aim is not to find the lowest lying isomer for the $^{2S+1}A_{1g}$ X_6^q species but to analyse octahedral species with two objectives. First, we want to check whether a closed-shell structure or a half-filled shell with same spin electrons in O_h species is a sufficient requirement to generate aromaticity and, second, we aim to investigate the existence of a possible rule of aromaticity for octahedral compounds analogous to the Wade–Mingos rule for closo borane compounds.

6.2.1 State-of-the-art

A few octahedral systems have been described as aromatic. To our knowledge only five cases have been reported, namely, the $B_6H_6^{2-}$ closo borane cluster,[404] the eight σ-electron H_6^{2-} species,[405] and the metalloaromatic[374,406] Be_6 in the quintet state[407] and the singlet Au_6^{2-} and Al_6^{2-} clusters.[375,403] Experimentally, however, only the O_h $B_6H_6^{2-}$ and Al_6^{2-} clusters have been observed, the latter in the form of $LiAl_6^-$.[375] Interestingly, as we have seen in the previous section, B_6^{2-} that is valence isoelectronic with Al_6^{2-} has a planar D_{2h} molecular structure and it is antiaromatic.[378,383] Hyunh and Alexandrova studied the $B_{6-n}Al_n^{2-}$ (n = 0–6) systems and found that the planar structure of B_6^{2-} persists until n = 5.[379] M_6Li_2 (M = Cu, Ag, Au) with pseudo-O_h symmetry were also found to be aromatic.[381] It is worth noting that O_h Si_6^{2-}, which is valence isoelectronic with $B_6H_6^{2-}$, was found to be antiaromatic according to NICS(0) values.[404]

6.2.2 Results and discussion

Combination of the four valence ns and np AOs of atom X in an O_h $^{2S+1}A_{1g}$ X_6^q species leads to twenty-four MOs. Figure 62 depicts the sixteen lowest-lying MOs present in O_h $^{2S+1}A_{1g}$ X_6^q clusters. The same MOs with the same shape and energetic ordering were reported by Schleyer *et al.* for O_h Si_6^{2-}.[404] From these orbitals, one could propose the series 2, 8, 12, 14, 20, 26, 32… as the magic numbers that lead to closed-shell aromatic species. For open-shell

clusters, the magic numbers would be 1, 5, 10, 13, 17, 23, 29… Unfortunately, these series of magic numbers cannot be generalized because the energetic order of the MOs shown in Figure 62 changes depending on the X atoms and the multiplicity and the charge of the O_h $^{2S+1}A_{1g}$ X_6^q clusters. The $2a_{1g}$ and $1t_{2g}$ MOs always become more stable than the $1e_g$ ones for the clusters of the second period (X = Li, Be and B). Moreover, in some clusters the $2a_{1g}$ are more stable than the $1t_{2g}$ and in other cases is the other way round. Basically, the energy difference between $1e_g$, the radial $2a_{1g}$, and the tangential $1t_{2g}$ is small and the ordering of the different orbitals changes from one cluster to another. This leads to the first conclusion of this work: it is not possible to derive a general rule for octahedral aromaticity similar to those of spherical aromaticity. Interestingly, however, the first two shells ($1a_{1g}$ and $1t_{1u}$) are always the same for all clusters analysed. Therefore, for a small number of valence electrons, the magic numbers 2 and 8 (closed-shell) or 1 and 5 (open-shell) for octahedral aromaticity hold and they are the same as those found in spherical[28,84,85] and cubic aromatic species[121].
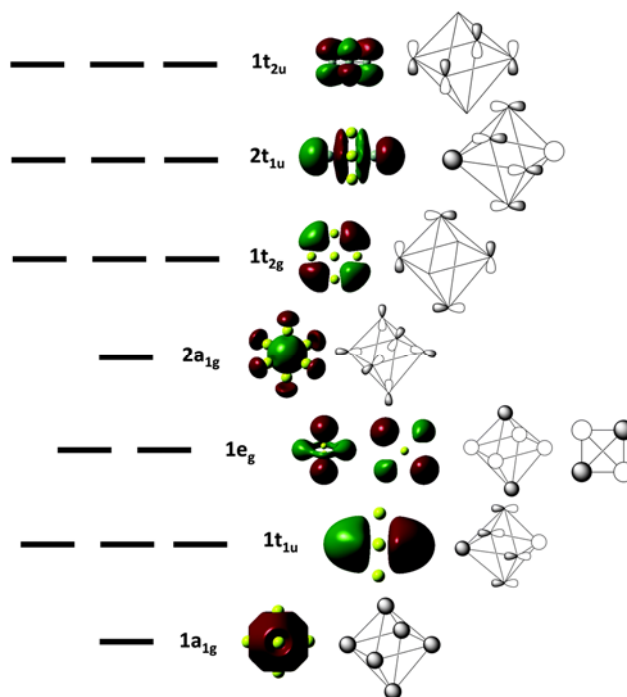
Figure 62. Schematic MO energy levels for a typical octahedral cluster.

Nevertheless, we decided to look for octahedral aromatic species by generating clusters with closed shells or half-filled shells with same spin electrons. To this end, we constructed all clusters with formula X_6^q (X = Li–C and Be–Si) having $^{2S+1}A_{1g}$ electronic states and with charges going from −2 to +4 and spin multiplicities ranging from the singlet to the septet (S = 0, 1/2, 1…3). Table 17 gathers all clusters with a combination of charge and spin that (i)

lead to an electronic closed shell or a half-filled shell with same spin electronic configurations and (ii) are minima in the PES. For instance, for $^{2S+1}A_{1g}$ C_6^q, all clusters found with octahedral symmetry are n-order saddle points. As a whole, we found twenty-three O_h $^{2S+1}A_{1g}$ X_6^q clusters that are minima but not necessarily the global minimum. Moreover, three out of these twenty-three minima have a negative energy of atomization (Table 17). These clusters are metastable, *i.e.*, the system is energetically stabilized by dissociation into atomic fragments in their lowest-lying states but with a Coulombic barrier for the dissociation, as found for instance in the N_2^{2+} compound[408,409] or in the dissociation of Ge_4^{2+} into two Ge_2^+ fragments.[410]

As can be seen in Table 17, the X–X bond distance generally increases from the second to the third period X atoms and for the same period decreases in the order group 1 > group 2 > group 13 > group 15. Not unexpectedly, the X–X bond distance decreases following the same tendency of the atomic radius of X atoms. In addition, the large bond distances of alkali metals can be attributed to the low number of valence electrons that occupy the lowest-lying bonding orbitals that leads to structures with relatively low dissociation energies. This is the case of Li_6^+ in the $^4A_{1g}$ state that has five valence electrons fully occupying the $1a_{1g}$ orbital and half filling the degenerate $1t_{1u}$ orbitals. This cluster has a dissociation energy to $5Li + Li^+$ of only 123.5 kcal mol^{-1}.

The lack of all-metal and semimetal aromatic clusters that can serve as reference systems (like benzene does in classical aromatic organic molecules) makes the measure of aromaticity in these systems difficult.[106,406] Indeed, most of the current available methods to quantify aromaticity have been designed to measure the aromaticity of organic 2D molecules and take benzene or other aromatic organic molecules as a reference in their definitions. Moreover, computation of energetic-based indicators such as resonance energies or ASE[139] is challenging for these clusters also because of the lack of appropriate reference systems.[105,411] For this reason, MCI and NICS are probably to date the most suitable indicators of metalloaromaticity.[254,406] In Table 17 we have gathered the MCI involving the six X atoms of the octahedron (MCI$_6$), four equatorial X atoms (MCI$_4$), and three X atoms in the face of the octahedron (MCI$_3$). We have also computed the NICS in the centre of the octahedron (NICS(0)$_6$) and in the centre of an octahedron face (NICS(0)$_3$). Finally, we have collected the PDIs that are the DIs between opposed axial atoms in the octahedron.

Table 17. Molecular structures of octahedral clusters $^{2S+1}A_{1g}X_6{}^q$ that are minima on the PES. Values of X–X bond distance in Å, MCI and PDI in electrons, NICS in ppm, and ΔE_{atom} in kcal/mol. ΔE_{atom} is the atomization energy of cluster to the most stable atomic fragments.[a]

System	q	Spin	Electronic state	d_{X-X}	MCI_6	MCI_4	MCI_3	$NICS(0)_6$	$NICS(0)_3$	PDI	ΔE_{atom}
Li_6	1	S=3/2	$^4A_{1g}$	3.007	0.068	0.038	0.078	-19.17	-14.07	0.260	123.5
		S=5/2	$^6A_{1g}$	3.112	0.069	0.035	0.077	-18.63	-13.72	0.258	61.2
Be_6	-2	S=3	$^7A_{1g}$	2.129	0.061	0.055	0.137	-58.66	-45.88	0.584	130.1
	-1	S=3/2	$^4A_{1g}$	2.050	0.121	0.066	0.175	-35.72	-17.16	0.656	205.9
	0	S=2	$^5A_{1g}$	2.040	0.080	0.054	0.158	-31.54	-15.38	0.603	156.9
	2	S=0	$^1A_{1g}$	2.135	0.140	0.068	0.158	-50.45	-37.13	0.521	136.5
	3	S=1/2	$^2A_{1g}$	2.267	0.097	0.054	0.136	-43.21	-33.00	0.461	-25.2
B_6	0	S=1	$^3A_{1g}$	1.675	0.085	0.060	0.174	-72.97	-53.40	0.769	488.8
	2	S=0	$^1A_{1g}$	1.628	0.109	0.063	0.196	-47.64	-24.90	0.800	381.3
	3	S=1/2	$^2A_{1g}$	1.677	0.072	0.039	0.175	-36.67	-19.02	0.742	59.8
	4	S=0	$^1A_{1g}$	1.745	0.035	0.015	0.152	-22.98	-10.93	0.682	-37.3
Na_6	-2	S=0	$^1A_{1g}$	3.605	0.022	0.035	0.078	-17.79	-16.99	0.330	41.4
		S=3	$^7A_{1g}$	3.890	0.064	0.032	0.054	4.50	6.74	0.236	0.9
	1	S=3/2	$^4A_{1g}$	3.602	0.061	0.038	0.064	-20.12	-15.64	0.237	100.1
Mg_6	-2	S=0	$^1A_{1g}$	3.439	0.056	0.029	0.071	14.48	17.04	0.367	14.8
		S=3	$^7A_{1g}$	3.096	0.057	0.063	0.105	-52.10	-44.09	0.511	-20.4
	0	S=0	$^1A_{1g}$	3.702	0.001	0.003	0.031	10.99	10.53	0.286	12.6
	2	S=1	$^3A_{1g}$	3.411	0.017	0.022	0.060	-3.11	-0.30	0.329	40.05
Al_6	-2	S=0	$^1A_{1g}$	2.710	0.081	0.087	0.125	-80.73	-68.12	0.678	250.0
		S=3	$^7A_{1g}$	2.865	0.038	0.030	0.120	15.74	8.61	0.573	205.3
	2	S=2	$^5A_{1g}$	2.948	0.046	0.049	0.078	-24.86	-18.88	0.491	106.6
Si_6	-2	S=0	$^1A_{1g}$	2.485	0.023	0.030	0.165	10.08	-14.73	0.772	527.0
	1	S=3/2	$^4A_{1g}$	2.461	0.055	0.054	0.146	-43.57	-48.33	0.726	565.8

[a] For instance, in $Mg_6{}^{2+}$ we have considered the atomization into $5Mg + Mg^{2+}$ rather than to $4Mg + 2Mg^+$ because the former has a lower energy.

This index is analogous to the PDI used as a measure of aromaticity in 6-MRs of PAHs.[188,412]

Among all systems gathered in Table 17, the aromaticity of $^1A_{1g}$ $Al_6{}^{2-}$ was studied previously and it has been concluded that this cluster is aromatic.[375,379] The relatively large MCI_6, MCI_4, MCI_3, and PDI values and the negative $NICS(0)_6$ and $NICS(0)_3$ provide further support to

the aromatic character of this cluster. Values of the different indices of this system are used as a reference to discuss the rest of the series. Interestingly, $^1A_{1g}$ Al_6^{2-} has the largest MCI_4 and the most negative $NICS(0)_6$ and $NICS(0)_3$ values. The CMO–NICS contributions collected in Figure 63a show that all occupied orbitals of Al_6^{2-} exhibit strong diamagnetic character. On the other hand, the largest PDI and MCI_3 correspond to $^1A_{1g}$ B_6^{2+}, whereas the system with the highest MCI_6 is found for $^1A_{1g}$ Be_6^{2+}. Linear correlations between the different indices analysed, which are given in Table 18, indicate that in most cases correlations are rather poor. The best linear correlations among different indices are $NICS(0)_6$–$NICS(0)_3$ ($R^2 = 0.88$), PDI–MCI_3 ($R^2 = 0.82$), $NICS(0)_6$–MCI_4 ($R^2 = 0.71$) and $NICS(0)_3$–MCI_4 ($R^2 = 0.66$).

Table 18. Linear coefficients of determination (R^2) between the different computed indices including all the possible combinations.

R^2	MCI_6	MCI_4	MCI_3	$NICS(0)_6$	$NICS(0)_3$	PDI
MCI_6	1.00					
MCI_4	0.58	1.00				
MCI_3	0.33	0.31	1.00			
$NICS(0)_6$	0.37	0.71	0.30	1.00		
$NICS(0)_3$	0.20	0.66	0.26	0.88	1.00	
PDI	0.09	0.22	0.82	0.25	0.26	1.00

Somewhat surprisingly from the fact that usually the MCI is lower when the number of atoms involved in the measure increases, in most cases MCI_6 of $^{2S+1}A_{1g}$ X_6^q clusters in Table 17 are greater than MCI_4. In contrast, as expected, PDI is always larger than MCI_3 and this index in turn is larger than MCI_4. If we assume that systems with relatively large electronic indices ($MCI_6 > 0.02$; $MCI_4 > 0.02$; $MCI_3 > 0.05$, and PDI > 0.20) and negative $NICS(0)_6$ and $NICS(0)_3$ values are aromatic, then sixteen out of the twenty three species listed in Table 17 are aromatic, $^1A_{1g}$ Mg_6 is antiaromatic, and the six clusters left are in the border between aromatic and antiaromatic species and we can classify them as non-aromatic. Therefore, we can conclude that in general, but not always, a closed-shell or a half-filled shell with same spin electronic configurations in octahedral species leads to aromatic clusters. It is worth noting that, as Table 17 shows, all second period octahedral compounds (*e.g.* Li, Be, and B) are aromatic while nonaromatic and antiaromatic species are only observed for compounds formed by elements of the third period. Let us finally discuss in more detail the five following clusters that deserve further comments: Li_6^+, Be_6, Mg_6, Al_6^{2-}, and Si_6^{2-}.

Li_6^+ has two possible electronic configurations with half-filled shells with same spin electrons, namely, $1a_{1g}^2 1t_{1u}^3$ (S = 3/2, $^4A_{1g}$) and $1a_{1g}^1 1t_{1u}^3 2a_{1g}^1$ (S = 5/2, $^6A_{1g}$) with atomization energies of 123.5 and 61.2 kcal mol^{-1}, respectively. The energy difference between these two electronic states is 62.3 kcal mol^{-1}, $^4A_{1g}$ being the most stable. In these states, the X–X distance and the aromaticity parameters are similar. From the aromatic indicators of Table 17, one can classify these clusters as moderately aromatic. Neither $^4A_{1g}$ nor $^6A_{1g}$ of octahedral Li_6^+ is the ground state for this cluster. Indeed, the most stable isomer for Li_6^+ at the CCSD(T)/cc-pVDZ level has a C_{2v} structure and an atomization energy of 142.6 kcal mol^{-1} (23.8 kcal mol^{-1} per atom).[413] This C_{2v} structure with S = 1/2 is not aromatic at all (MCI$_6$ = 0.006 e; NICS(0)$_6$ = 44.70 ppm; PDI = 0.241 e at B3LYP/6-311G++(3df,3pd)).

The electronic state of the octahedral Be_6 cluster is $^5A_{1g}$. Aromaticity descriptors in Table 17 denote a clear aromatic character for this species. The presence of twelve valence electrons instead of five in $^4A_{1g}$ Li_6^+ makes the Be–Be bond stronger (atomization energy is 156.9 kcal mol^{-1}) and the Be–Be distance shorter (2.040 Å). The electronic configuration is $1a_{1g}^2 1t_{1u}^6 2a_{1g}^1 1t_{2g}^3$, the highest-lying four valence electrons being same spin electrons half-filling the $2a_{1g}$ and $1t_{2g}$ MOs. Like for $^4A_{1g}$ Li_6^+, the $^5A_{1g}$ Be_6 state is an excited state for Be_6, although this conclusion depends on the level of calculation. Indeed, Be_6 is the first Be cluster the ground state of whom is controversial[414,415] and for some methods the O_h $^5A_{1g}$ is the ground state.[407] Different authors have pointed out the following ground states: O_h $^5A_{1g}$,[407] D_{3d} $^3A_{1g}$,[416,417] C_{2v} $^1A_1$,[416] C_{2h} ^3A_u,[378] and D_{2h} ^1A_g.[414,416] All CCSD calculations favour the D_{2h} ^1A_g state.[414,416] In this most stable D_{2h} ^1A_g electronic state the cluster can be considered non-aromatic (MCI$_6$ = 0.089 e; NICS(0)$_6$ = 3.72 ppm; PDI = 0.532 e at B3LYP/6-311G++(3df,3pd)).

$^1A_{1g}$ Mg_6 is a particular case for its long X–X distance (3.702 Å). The electronic configuration is $1a_{1g}^2 1t_{1u}^6 e_g^4$. Its positive NICS and low values of electronic indices indicate antiaromatic character. CMO–NICS results of Figure 63 show that the antiaromatic character is mainly due to the contribution from $1e_g$ orbitals. The lack of aromaticity in this octahedral closed-shell $^1A_{1g}$ Mg_6 species is somewhat surprising and the reasons for this unexpected behaviour are unclear. However, there are other examples of similar situations. For instance, borazine has an electronic structure similar to benzene and should be aromatic according to Hückel's rule but it is not.[418–420]

Al_6^{2-} has two possible electronic configurations. One that is a closed-shell, $1a_{1g}^2 1t_{1u}^6 1e_g^4 2a_{1g}^2 1t_{2g}^6$ (S = 0, $^1A_{1g}$), and another one with two half-filled shells with same spin electrons, $1a_{1g}^2 1t_{1u}^6 1e_g^4 2a_{1g}^2 1t_{2g}^3 2t_{1u}^3$ (S = 3, $^7A_{1g}$). The energy difference between these two electronic states is 44.7 kcal mol^{-1}. The $^1A_{1g}$ Al_6^{2-} cluster was studied previously and it was concluded that this cluster is aromatic.[375,379] Our indicators also support this conclusion. On the other hand, the $^7A_{1g}$ Al_6^{2-} cluster with positive NICS and low electron sharing indices is classified as non-aromatic. It is worth noting that, with the exception of Mg_6^{2-}, closed-shell electronic structures ($^1A_{1g}$) are found to be more aromatic than open-shell ones.

(a) (b)

CMO-NICS$_6$(0)

	CMO-NICS$_6$(0)
$1t_{2g}$	-7.7
$2a_{1g}$	-8.5
$1e_g$	-4.2
$1t_{1u}$	-8.2
$1a_{1g}$	-12.6

$^1A_{1g}$ Al_6^{2-}

	CMO-NICS$_6$(0)
$1e_g$	18.2
$1t_{1u}$	-4.9
$1a_{1g}$	-8.8

$^1A_{1g}$ Mg_6

(c)

	CMO-NICS$_6$(0)	**CMO-NICS$_3$(0)**
$2t_{1u}$	30.0	18.6+18.6+10.8=48.0
$1t_{2g}$	-9.9	-10.7+-8.4+-9.9=-27.0
$2a_{1g}$	-6.4	-4.0
$1e_g$	-0.3	-0.6
$1t_{1u}$	-7.6	-7.5+-6.2+-9.8=-23.5
$1a_{1g}$	-14.3	-8.6
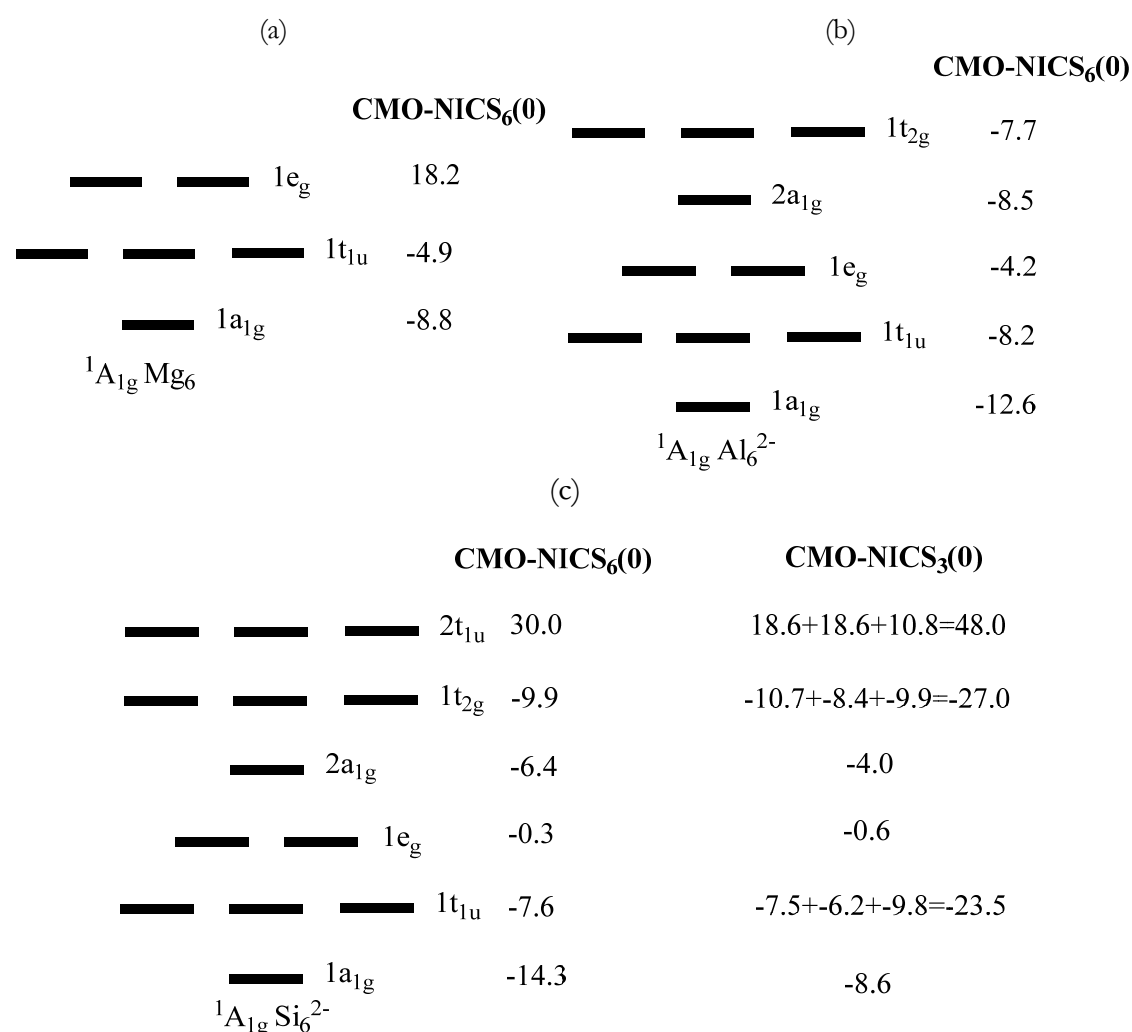
$^1A_{1g}$ Si_6^{2-}

Figure 63. MO-NICS$_6$(0) decomposition for a) Mg_6, b) Al_6^{2-} and c) Si_6^{2-} in their $^1A_{1g}$ electronic states. Contributions of the core MOs are not included.

For the $^1A_{1g}$ Si_6^{2-} cluster, the octahedral geometry is the most stable.[421] This cluster was detected experimentally in time-of-flight mass spectra as Si_6Na_2.[422] As said in the Introduction the octahedral $^1A_{1g}$ Si_6^{2-} cluster with electronic configuration $1a_{1g}^2 1t_{1u}^6 1e_g^4 2a_{1g}^2 1t_{2g}^6 2t_{1u}^6$ was

found to be antiaromatic according to NICS(0)$_6$ values.[404] We also obtain positive NICS(0)$_6$ values, although NICS(0)$_3$ are negative. CMO–NICS contributions to NICS(0)$_6$ of Figure 63 show that positive values come from the filled 2t$_{1u}$ MOs. [404,423] This situation resembles that of the Al$_3$H$_3^{2-}$ cluster in which the tangential orbitals contribute with positive CMO–NICS to the total NICS(0) value.[424,425] The negative NICS(0)$_3$ value in the ^{1}A$_{1g}$ Si$_6^{2-}$ cluster appears due to an important reduction of the antiaromatic character of the 2t$_{1u}$ orbitals when calculated in the face of the octahedron. The computed MCI$_6$ and MCI$_4$ for ^{1}A$_{1g}$ Si$_6^{2-}$ are not particularly large but not negligible either. MCI$_3$ gives a significantly large value which is in line with the negative NICS(0)$_3$ value. These results could indicate a certain degree of electron delocalisation among the atoms that form the faces of the octahedron but this electron sharing is not extended among the six atoms of the system. As a whole, we classify this system in the border between aromatic and antiaromatic clusters, *i.e.*, as a non-aromatic species.

6.3 Metallaelectrides

The study of the molecular and electronic structure of octahedral ^{4}A$_{1g}$ Li$_6^+$ and ^{5}A$_{1g}$ Be$_6$ species shows that the chemical bonding in these molecules resembles that of the solid metals where metal cations are surrounded by a "sea" of valence electrons. The presence of a large number of highly delocalized NNAs indicate that we are dealing with new border species that are halfway between electrides and metals. We propose the term metallaelectrides to refer to this new type of electrides.

6.3.1 State-of-the-art

A solid electride is an ionic substance in which confined electrons trapped in a cavity serve as anions.[426,427] Because of the presence of these loosely bound anionic electrons, solid electrides have particular properties such as high non-linear optical behaviour,[428,429] large magnetic susceptibility,[430] or high reducing power.[426,427] To date, twelve (four inorganic and eight organic) solid electrides have been reported; three out of these twelve are stable at room temperature.[431–433] Molecular electrides are another type of electrides that have an electron (or a significant portion of an electron) that cannot be assigned to any nucleus of the molecule and that it is relatively well localized in the molecular space. In a recent work by some researchers of our group,[434] five molecular electrides were characterized using three

different criteria that provide support to the presence of an isolated electron, namely, i) the existence of a NNA of the electron density, ii) the presence of an ELF basin in the same region of the NNA, and iii) negative values of the Laplacian of the electron density ($\nabla^2\rho$) in the NNA. This study also showed that the mere existence of NNAs with negative values of $\nabla^2\rho$ were enough to characterize an electride.[434] These criteria apply except when the NNAs are located in the close vicinity of an atom because in this case the isolated nature of the electron is dubious.[434]

The term molecular cluster refers to a relatively small aggregation of atoms or molecules. Clusters are homo- or heteroatomic nanoparticles that behave as a link between the atom or the molecule and the bulk material, thus constituting an intermediate phase of matter.[435] They exhibit characteristics of both forms of matter (atom and bulk) and, consequently, they have specific properties that depend crucially on their size. Some clusters with closed-shell or same-spin half-filled electronic structure are particularly stable because they are aromatic.[403] This is the case of Li_3^+ or Li_4^{2+}[107] that follow the $4n+2$ Hückel's rule,[436] the $B_{12}H_{12}^{2-}$ that obeys the $2n+2$ Wade-Mingos criterion,[16,18] the C_{60}^{10+} and C_{80}^{8+} that satisfy the $2(n+1)^2$ Hirsch formula[28] or the C_{60}^- (S=11/2) that fulfills the $2n^2+2n+1$ (S=$n+1/2$)[40] rule. With this idea in mind, in the previous section we have looked for aromatic molecular clusters with octahedral symmetry (see section 6.2).[382] By serendipity, we found that O_h Li_6^+ (S=3/2) and Be_6 (S=2) have a unique electronic structure that resembles that of the metals.[382] These systems have more NNAs than atoms and have all (or most of the) valence electrons located in these NNAs. Because of the presence of NNAs characteristic of electrides and the resemblance of their chemical bonding nature to the metallic bonding with extensive electron delocalization of valence electrons, we propose to name this particular class of electrides as *metallaelectrides*. The main aim of this work is to report the properties of the Li_6^+ (S=3/2) and Be_6 (S=2) metallaelectrides. Except otherwise stated, the results discussed below are obtained with the UB3LYP/aug-cc-pVTZ method. Spin contamination at this level of theory was found to be negligible for the two species studied. It is worth mentioning that we decided not to use the ELF to characterize the studied systems because there is not a unique way to represent ELF in open-shell species[202,437–440] like in the present high spin metal cluster. Instead, we use the negative values of the Laplacian of the electron density that provide a direct measure of the electron density accumulation in the real space.[181,441]

6.3.2 Results and discussion

Li_6^+ with S=3/2 has a perfect octahedral symmetry with the Li–Li distance ranging from 3.006 to 3.156 Å for the different levels of theory we have used (UB3LYP, UBP86, UM06-2X, UMP2, UCCSD; 6-31G(d), 6-31+G(d), 6-311G(d,p), 6-311+G(d,p), cc-pVDZ, cc-pVTZ, aug-cc-pVDZ, aug-cc-pVTZ). Our best estimate is the 3.087 Å obtained at the UCCSD/aug-cc-pVTZ level. Although the Li clusters are usually difficult to describe due to the diffuse nature of the valence electron and the multiconfigurational character of their wavefunctions,[441] $O_h(^4A_{1g})$ Li_6^+ is reasonably well-described at the monoconfigurational level. Indeed, the T_1 test[401] at the UCCSD/aug-cc-pVTZ//QCISD/aug-cc-pVTZ level for this system gives 0.042, which is below the recommended threshold for open-shell species.[442] The five valence electrons occupy the a_{1g} and t_{1u} MOs, the latter ones being half-filled with three same spin electrons (see Figure 64). The three unpaired t_{1u} electrons provide what is called no-pair ferromagnetic bonding.[443] O_h Li_6^+ (S=3/2) is an excited state for the cationic hexamer of Li.
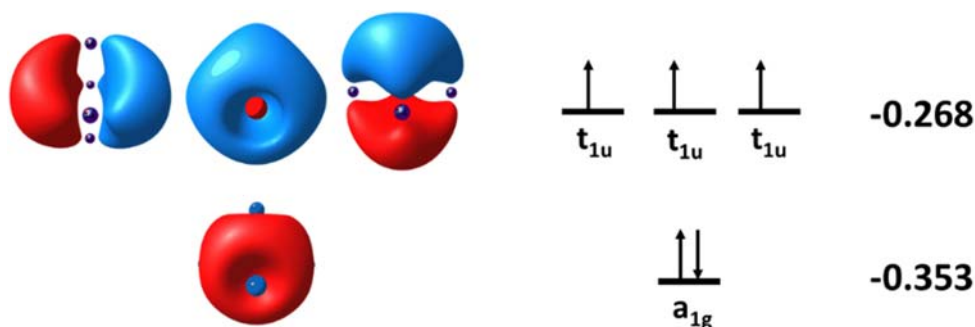
Figure 64. Schematic MO energy levels (energies in eV) of $^4A_{1g}$ Li_6^+ (S=3/2).

The ground state for this species, which is by 20.7 kcal/mol more stable at the UCCSD/aug-cc-pVTZ//B3LYP/aug-cc-pVTZ level, is the $C_{2v}(^2A_1)$ state, whereas the $D_{2h}(^2B_{2u})$ is only by 0.6 kcal/mol higher than the lowest in energy C_{2v} structure (Table 19). $C_{2v}(^2A_1)$ and $D_{2h}(^2B_{2u})$ are almost degenerate states with octahedral distorted geometries. Previous studies with the coupled-cluster method found the $C_{2v}(^2A_1)$ as the ground state,[413,444] whereas MRD-CI calculations favoured the $D_{2h}(^2B_{2u})$.[445]

Table 19. Relative energies of the structures of Li_6^+ (S=1/2, 3/2) at CCSD(T)/aug-cc-pVTZ//B3LYP/aug-cc-pVTZ geometry. Energies are expressed in kcal/mol.

Li_6^+	Isomer	ΔE
S=½	O_h	0.00
	C_{2v}	-20.69
	D_{2h}	-20.08
S=3/2	O_h	-9.38

The QTAIM analysis of $O_h(^4A_{1g})$ Li_6^+ provides the picture shown in Figure 65 obtained with the UB3LYP/aug-cc-pVTZ method. As can be seen, this species has eight NNAs located in the faces of the octahedral structure. The presence of NNAs is not a frequent feature of molecular densities. Although NNAs are typically found in the interstitial regions of the Li clusters,[446] $O_h(^4A_{1g})$ Li_6^+ represents the first example of a molecule with more NNAs than nuclei. Previous results on Li_2, Li_4, and Li_6 show that these clusters have 1, 2, and 3 NNAs respectively.[205,206,447] For the diatomic Li_2 molecule, the Li–Li distance at which these NNAs appear was found to be in the range 2.15–3.45 Å.[447] We checked the number of NNAs in $O_h(^4A_{1g})$ Li_6^+ with different functionals, correlated methods, and basis sets and in all cases we found that the number of NNAs was either 8 or 12. In the latter case, the NNAs are located in the centre of the Li–Li edges of the octahedron. The change in the number of NNAs is not unexpected due to the extremely flat profile of the electron density in this species.[448] Our best estimate is provided by the UCCSD/aug-cc-pVTZ density that gives eight NNAs. The population of these NNAs at the UB3LYP/aug-cc-pVTZ level is 0.43 e and its degree of localization is 22%.

Figure 65 plots an isosurface of $\nabla^2\rho$ that showing the presence of regions of negative Laplacian of the electron density located around the NNAs. One can analyze the isosurfaces of the alpha and beta electrons contributions to the Laplacian of the electron density ($\nabla^2\rho_\alpha$ and $\nabla^2\rho_\beta$). Since the number of alpha valence electrons in this open-shell system (4 e) is not equal to the number of the beta ones (1 e), different $\nabla^2\rho_\alpha$ and $\nabla^2\rho_\beta$ isosurfaces are expected (Figure 66). In O_h Li_6^+ (S=3/2), the alpha electrons are highly delocalized around NNAs, while the beta electron is even more delocalized and located in the centre of the octahedron. At high $\nabla^2\rho_\alpha$ isosurface values one can distinguish twelve regions (situated between each pair of Li atoms) with electron density. However, the regions where the NNAs are located (face

regions) are more delocalized than edge regions. In fact, at the large negative values of the Laplacian, the Laplacian in the face regions is not visible and it is only present in the twelve edge regions split (Figure 66). Interestingly, these findings show that the electron density in the NNAs is quite delocalized according to QTAIM analysis. On the other hand, for an isosurface of -0.002 a.u., one is able to distinguish a single region in the isosurface of $\nabla^2\rho_\beta$. However, at more negative isosurface values, this isosurface is bisected into twelve regions, the same number as the $\nabla^2\rho_\alpha$ isosurface. Remarkably, the beta region is more delocalized than the alpha ones (Figure 66).[449]
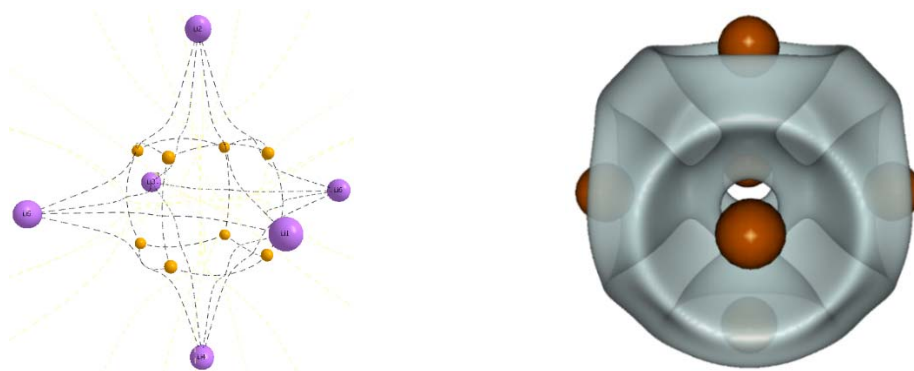
Figure 65. $^4A_{1g}$ Li_6^+ (S=3/2) at B3LYP/aug-cc-pVTZ. Location of NNA (in yellow) obtained by QTAIM analysis (on the left) and Laplacian of the electron density ($\nabla^2\rho$, isosurface is -0.0005 a.u.) (on the right).

Therefore, most valence electrons in O_h Li_6^+ (S=3/2) are located far from nuclei and are quite delocalized. The energetic cost of moving the valence electrons away from nuclei is offset by avoiding repulsive Pauli effects due to core electrons and by lowering the kinetic energy.[450,451] Moreover, Dale and coworkers[448] demonstrated that NCI plots are ideal to reveal the presence of confined electrons in solid electrides. These electrons are located in regions of low electron density with low reduced-gradient values and, consequently, they are disclosed in the NCI maps. Figure 67a plots one of these maps that show the presence of a green region indicating the existence of a week attractive interaction between the interstitial regions around the NNAs position and the nuclei. The values of the isotropic static electronic polarizability ($\overline{\alpha}_{ee}(0;0)$ = 308.1 a.u.) and of the second hyperpolarizability ($\gamma_I^e(0;0,0,0)$ = 3.66x10^5 a.u.) are rather high for such a small molecule as usually found in electrides. For symmetry reason, the first hyperpolarizability is zero. All these results provide strong support to the classification of $O_h(^4A_{1g})$ Li_6^+ as a metallaelectride.
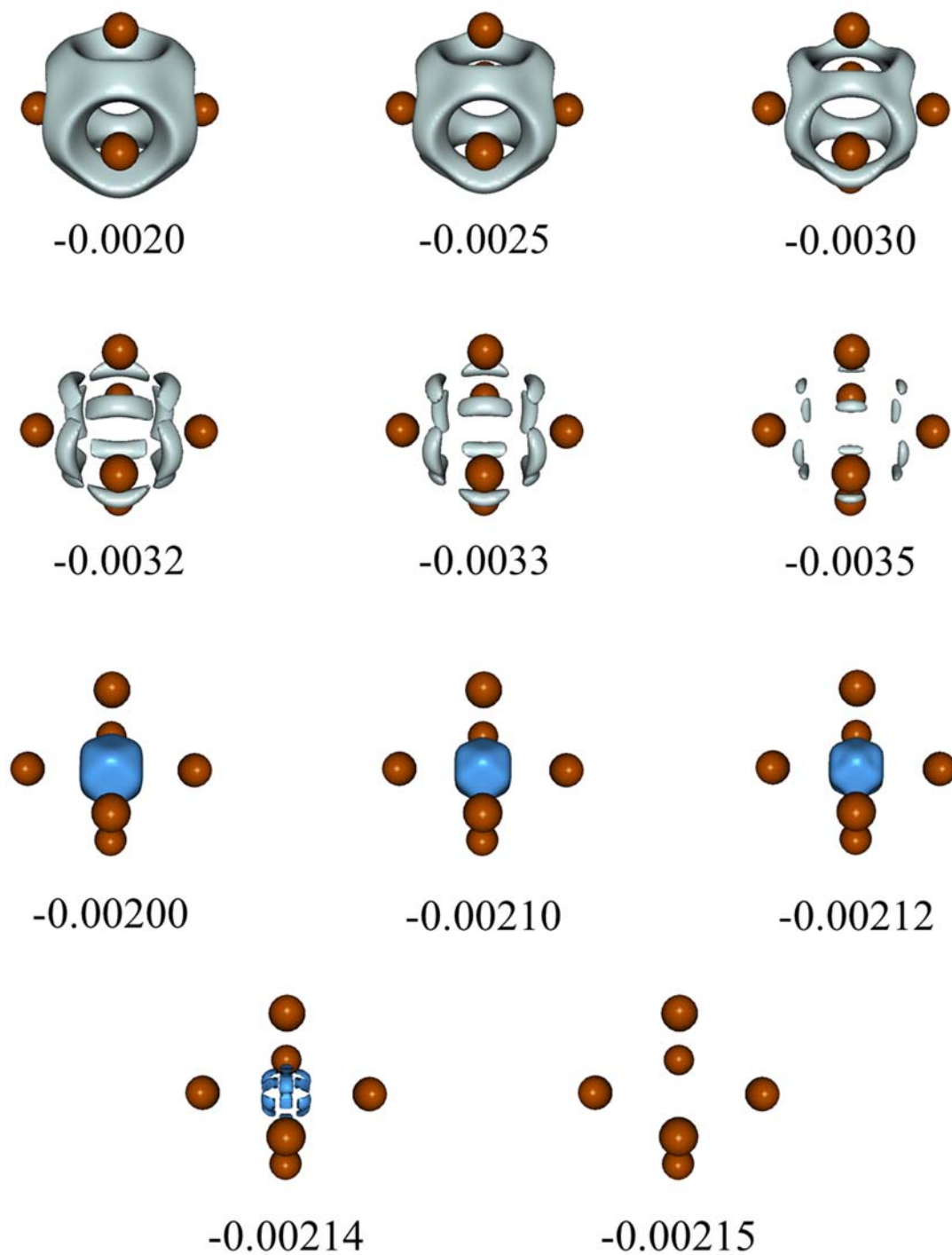
Figure 66. $^4A_{1g}$ Li_6^+ (S=3/2). $\nabla^2\rho_\alpha$ (in gray) and $\nabla^2\rho_\beta$ (in blue). Isosurfaces given in a.u.

a)   b)
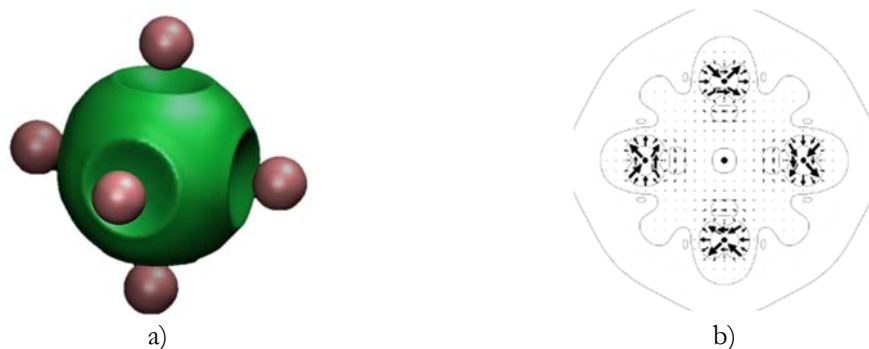
Figure 67. $^4A_{1g}$ Li_6^+ (S=3/2). a) Noncovalent interactions (NCI, isosurface of 0.2). b) Magnetic field along C_4. Contributions to current densities of all electrons (top) in a plane containing the four equatorial atoms.

As discussed in the previous paragraphs, the electronic configuration of $O_h(^4A_{1g})$ Li_6^+ is compatible with an aromatic molecule. In fact, with five valence electrons, this species with $n=1$ follows the $2n^2+2n+1$ ($n = S+1/2$)[40] rule for open-shell spherical aromatic species. The NICS in the center of the octahedron and in the center of the faces is −19.4 and −14.2 ppm, respectively, thus denoting a 3D aromatic species. The MCI for six Li atoms is 0.068, both almost identical to that of benzene (0.072 at the B3LYP/6-311++G(d,p) level)[279]. The shape of the Laplacian of the electron density and the metalloaromatic character[374,406] of this species prove the presence of delocalized electrons in the interstitial regions of the octahedron in the $O_h(^4A_{1g})$ Li_6^+ species. We were curious whether this electronic structure can result in strong ring currents, so we calculated the current density maps with the Coupled-perturbed Restricted Open-Shell Hartree-Fock (CROHF) method[452] with a cc-pVDZ basis set. Plots in Figure 67b represent the all-electron electronic linear response to a magnetic field oriented along the C_4 axis. A clockwise (counterclockwise) circulation corresponds to a paratropic (diatropic) current. Two main characteristics of the observed ring currents are: (i) a delocalized diatropic "ring" current located within the polyhedron molecular volume where the overlap between radial-2p atomic functions is maximal, and (ii) a set of well-localized paratropic circulations centered about the nuclear sites. Inside the octahedron, a delocalized diatropic current is observed, fully originating from a $t_{1u} \rightarrow t_{2g}$ translationally allowed transition due to the top spin-up electrons in $O_h(^4A_{1g})$ Li_6^+. Besides that, on the planes containing either equatorial atoms or a triangular face paratropic localized currents become an important feature of the maps. As evident from the decomposition into orbital currents, the top t_{1u} spin-up electrons play an important role in the description of these localized but

somewhat weak currents in Li_6^+, due to the mixed paratropic $t_{1u} \rightarrow t_{1u}$ and diatropic $t_{1u} \rightarrow t_{2g}$ character of the current contribution from these electrons.

Be_6 with S =2 has a perfect octahedral structure like $^4A_{1g}$ Li_6^+. The presence of 12 valence electrons instead of 5 in $^4A_{1g}$ Li_6^+ makes the bond stronger and the Be–Be distance shorter with values in between 2.037 and 2.092 Å for the different levels of theory we have used. Our best estimate is the UCCSD/aug-cc-pVTZ value of 2.063 Å. At this level of theory, the T_1 test value of 0.016 shows that $^5A_{1g}$ Be_6 has monoconfigurational character. The highest-lying four valence electrons have the same spin and half-fill the a_{1g} and t_{2g} MOs (see Figure 68).
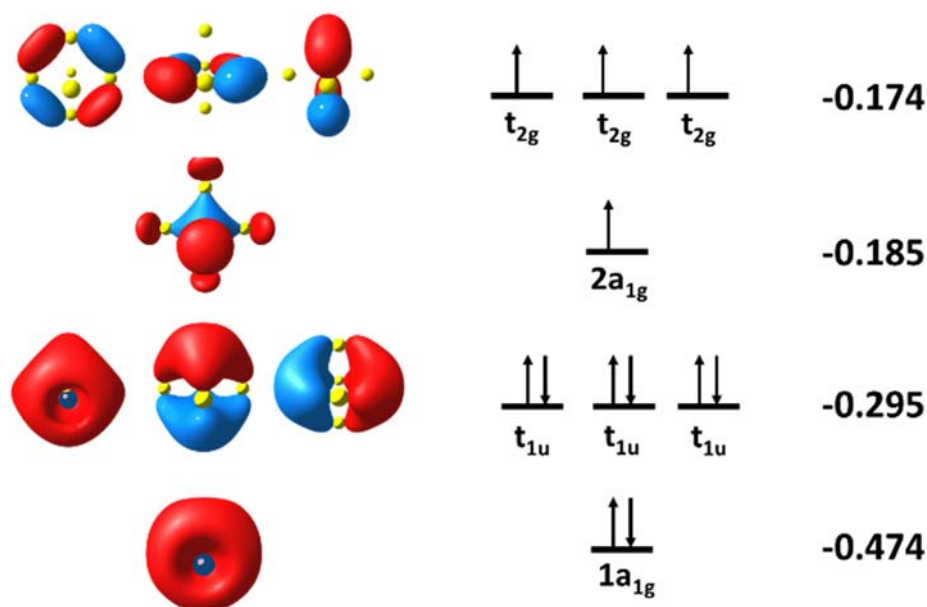
Figure 68. Schematic MO energy levels (energies in eV) of $^4A_{1g}$ Be_6 (S=2).

Like for $^4A_{1g}$ Li_6^+, the $^5A_{1g}$ Be_6 state is an excited state for Be_6. With the UCCSD/aug-cc-pVTZ//QCISD/aug-cc-pVTZ method, the ground state is the $D_{2h}(^1A_g)$ state. The $C_{2v}(^1A_1)$ is less stable by only 0.2 kcal/mol. With respect to the ground state, the $^5A_{1g}$ Be_6 state lies only 4.1 kcal/mol higher in energy (Table 20). Be_6 is the first Be cluster the ground state of whom is controversial.[414,415] Depending on the level of calculation used, different authors have pointed out the following ground states: $O_h(^5A_{1g})$,[407] $D_{3d}(^3A_{1g})$,[416,417] $C_{2v}(^1A_1)$,[416] $C_{2h}(^3A_u)$,[378] and $D_{2h}(^1A_g)$,[414,416] although all CCSD calculations favour the D_{2h} ^1A_g state.[414,416] Calculated enthalpies at 298 K locate the $^5A_{1g}$ Be_6 state at only 2.1 kcal/mol with respect to the $D_{2h}(^1A_g)$ ground state. This means that production of $^5A_{1g}$ Be_6 cluster in collimated supersonic cluster beams cannot be discarded.

Table 20. Relative energies of the structures of Be_6 (S=0, 1, 2) at CCSD(T)/aug-cc-pVTZ//B3LYP/aug-cc-pVTZ geometry. Energies are expressed in kcal/mol.

Be_6	Isomer	ΔE
S=0	O_h	0.00
	D_{2h}	-49.19
	C_{2v}	-48.96
S=1	O_h	-14.60
	D_{3d}	-37.02
	C_i	-36.36
S=2	O_h	-45.06

The UB3LYP/aug-cc-pVTZ QTAIM plot of $O_h(^5A_{1g})$ Be_6 electron density is given in Figure 69. As in $O_h(^4A_{1g})$ Li_6^+, the total number of NNAs depend on the level of calculation. In the case of $O_h(^5A_{1g})$ Be_6, the located NNAs are 12 or 20 depending on the level of theory used. At the UB3LYP/aug-cc-pVTZ levels of theory there are 20 NNAs. For Be_2, the Be–Be distance at which these NNAs appear is more narrow than in Li_2 (2.36–2.45 Å). The Be–Be distance in $^5A_{1g}$ Be_6 is somewhat shorter. The population of these NNAs at the UB3LYP/aug-cc-pVTZ level is 0.01 e for the NNAs in the faces and of only 0.51 e for the NNAs of the edges. The latter have a degree of localization of 17%.
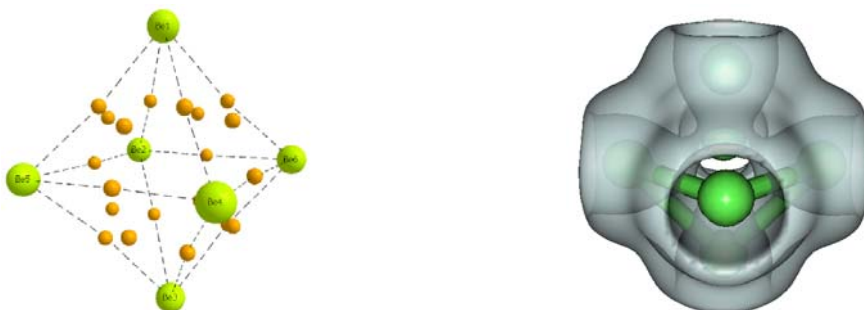

Figure 69. $^5A_{1g}$ Be_6 (S=2). Location of NNA (in yellow) obtained by QTAIM analysis (on the left) and Laplacian of the electron density ($\nabla^2\rho$, isosurface is -0.0005 a.u.) (on the right).
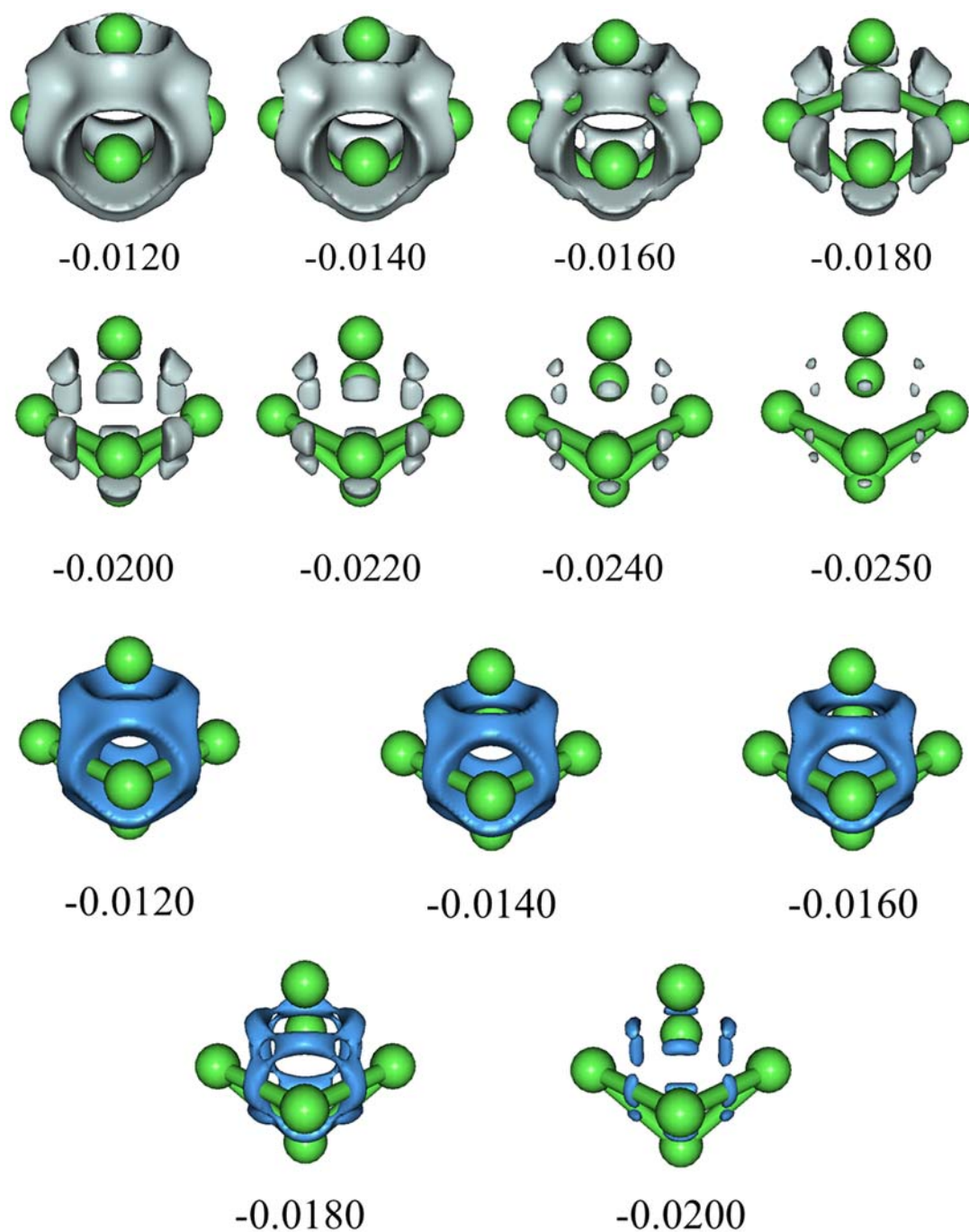
Figure 70. $^5A_{1g}$ Be$_6$ (S=2). $\nabla^2\rho_\alpha$ (in gray) and $\nabla^2\rho_\beta$ (in blue). Isosurfaces given in a.u.

The isosurface of $\nabla^2\rho$ depicted in Figure 69 indicates the presence of regions of negative Laplacian of the electron density located around the NNAs. Generally, the isosurface of $\nabla^2\rho_\alpha$ is quite similar to that of the $O_h(^4A_{1g})$ Li$_6^+$ species. Yet, the only difference between the two metal clusters is the positioning of the isosurface of $\nabla^2\rho_\alpha$ which, in the case of $O_h(^5A_{1g})$ Be$_6$, is more displaced out of the centre of the octahedral structure (Figure 70). The $\nabla^2\rho_\beta$

isosurface is analogous to $\nabla^2\rho_\alpha$ and they only slightly differ in the location of the isosurface. From the $\nabla^2\rho_\alpha$ and $\nabla^2\rho_\beta$ isosurfaces for $O_h(^5A_{1g})$ Be$_6$, one can distinguish twelve regions which coincide on the position of the (12) NNAs that are located in the edges. Regarding the regions where the (8) faced NNAs are situated, a localized surface is not found because actually they are less localized than the bonded NNAs regions (Figure 70). In fact, the previous result makes sense because, according to QTAIM, the faced NNA is more delocalized than in the edges.

Figure 71a plots the NCI map for $O_h(^5A_{1g})$ Be$_6$ that shows a blue region due to the presence of a attractive interaction between the interstitial regions around the NNAs position and the Be atoms. The values of the isotropic static electronic polarizability ($\overline{\alpha}_{ee}(0;0)$ = 157.9 a.u.) and of the second hyperpolarizability ($\gamma_I^e(0;0,0,0)$ = 2.85x10^5 a.u.) are somewhat smaller than those found for $O_h(^4A_{1g})$ Li$_6^+$, still high enough to consider $O_h(^5A_{1g})$ Be$_6$ as a molecule with metallaelectride characteristics. All indicators of aromaticity point out that the aromaticity of $O_h(^5A_{1g})$ Be$_6$ is higher than that of $O_h(^4A_{1g})$ Li$_6^+$. Indeed, NICS in the centre of the octahedron and in the centre of the faces is –31.2 and –15.3 ppm, respectively, and the MCI for the three Be atoms forming a face of the octahedron is 0.158 e and for the six Be atoms is 0.080. The current density maps obtained with the CROHF/cc-pVDZ method (see Figure 71b) show similar currents in $O_h(^5A_{1g})$ Be$_6$ and $O_h(^4A_{1g})$ Li$_6^+$, the former being more intense. Again the main diamagnetic transition corresponds to the $t_{1u} \rightarrow t_{2g}$ transition that in $O_h(^5A_{1g})$ Be$_6$ is strengthened by the small energy gap between these orbitals.

a)   b)

Figure 71. $^4A_{1g}$ Be$_6$ (S=2). a) Noncovalent interactions (NCI, isosurface of 0.2). b) Magnetic field along C$_4$. Contributions to current densities of all electrons (top) in a plane containing the four equatorial atoms.

6.3.3 On-going results and discussion about the chemical bonding of electrides

In the previous study (sections 6.3.1 and 6.3.2), we have introduced for the first time the term *metallaelectride* to refer to systems that resemble metals but also show typical features of electrides. That is, systems like $^4A_{1g}$ Li_6^+ possess NNAs as electrides but these NNAs present high electron delocalization. In contrast, TCNQ-Li_2 and Li_2 are characterized as molecular electrides due to the highly localized nature of the NNA between the two Li atoms.[434] As we can observe, the degree of localization and delocalization of the NNA gives information about the bonding nature of a system.

Li_2 and $O_h(^4A_{1g})$ Li_6^+ present significant structural differences and also the two species have different spin state. As we have seen above, a closed-shell species such as Li_2 is a molecular electride with a highly localized NNA, while an open-shell system like $O_h(^4A_{1g})$ Li_6^+ gives rise to a metallaelectride with highly delocalized NNA (see section 6.3.2). Several lithium clusters with different spin states have been studied although they have not been classified as electrides before. Could we find more lithium-based systems that behave like electrides and metallaelectrides among simple lithium clusters? To investigate that, we have analyzed the chemical bonding nature of different lithium clusters, Li_n (n=2…5), exploring all the possible spin combinations.

Firstly, we have to identify the global minimum of each Li_n (n=2…5) at different spin states. We should take into account that the number of molecular conformations increases with the size of the system. Ideally we should work only with global minimum structures because local minima may offer completely different bonding patterns. Indeed, the global minima of most of them have already been reported in the literature. Thus, we have used these structures as a reference. Nevertheless, for the non-reported cases, we have performed a qualitative search of their global minimum using Car-Parrinello molecular dynamics simulations.[453] The method combines molecular dynamics simulation and density-functional theory to efficiently explore the PES of lithium clusters. The most stable minima observed in the simulation was selected as a starting point for geometry optimization. Table 21 collects a list of all the lithium clusters studied in their respective global minima together with the point group. Figure 72 shows the optimized molecular structure at the (U)B3LYP/aug-cc-pVTZ level of theory of each of these systems. QTAIM studies have been performed at the same level of theory.

Table 21. Lithium clusters ($^{2S+1}Li_n$) that have been studied with all the possible spin state (S) combinations and their symmetry. The number of NNAs of each species has been provided as well as the number of electrons (Ne_{NNA}) and the percentage of electron localization ($\%LI_{NNA}$) of each NNA.

Li_n cluster	Spin	Symmetry	NNA	Ne_{NNA}	$\% LI_{NNA}$
Li$_2$	S=0	D$_{\infty h}$	1	0.98	49%
	S=1	D$_{\infty h}$	0	-	-
Li$_3$	S=1/2	C$_{2v}$^{454}	1	1.57	55%
	S=3/2	D$_{3h}$^{443}	3	0.43x3	35%
Li$_4$	S=0	D$_{2h}$^{454}	3	1.23x3	56%
	S=1	D$_{2d}$^{a}	1	2.30	59%
	S=2	T$_d$^{455}	4	0.56x4	33%
Li$_5$	S=1/2	C$_{2v}$^{444,454}	3	0.65/1.21x2	40%/52%
	S=3/2	D$_{3h}$^{454}	2	1.53x2	41%
	S=5/2	C$_{4v}$^{443}	4	0.63x4	27%

a) Structure that has been found using quantum dynamics.

To characterize the bonding features of all these clusters, a QTAIM analysis has been performed to detect the number and position of NNAs in each molecule. According to that, we observe that the number of NNA differs with the size of the molecule as well as the spin state (Table 21). At first glance, we can see that all the cases present at least one NNA except for D$_{\infty h}$ ^{3}Li$_2$. It is worth highlighting that in most of the cases a BCP between two lithium atoms is not detected. The same behavior can be observed for RCPs.

As we mentioned above, to classify a compound as an electride it must fulfill five conditions: high values of non-linear optical properties (NLOP), the presence of a NNA, the manifestation of an ELF basin around the position of a NNA and negative values of $\nabla^2\rho$ in the NNA. But, according to the results of the previous sections, we must add an extra condition regarding the properties of the NNA: they should show significant electron localization. In the case that the NNA is present but shows significant electron delocalization with other regions of the molecule, we cannot classify the compound as an electride and, therefore, we suggest labelling the compound as a metallaelectride.
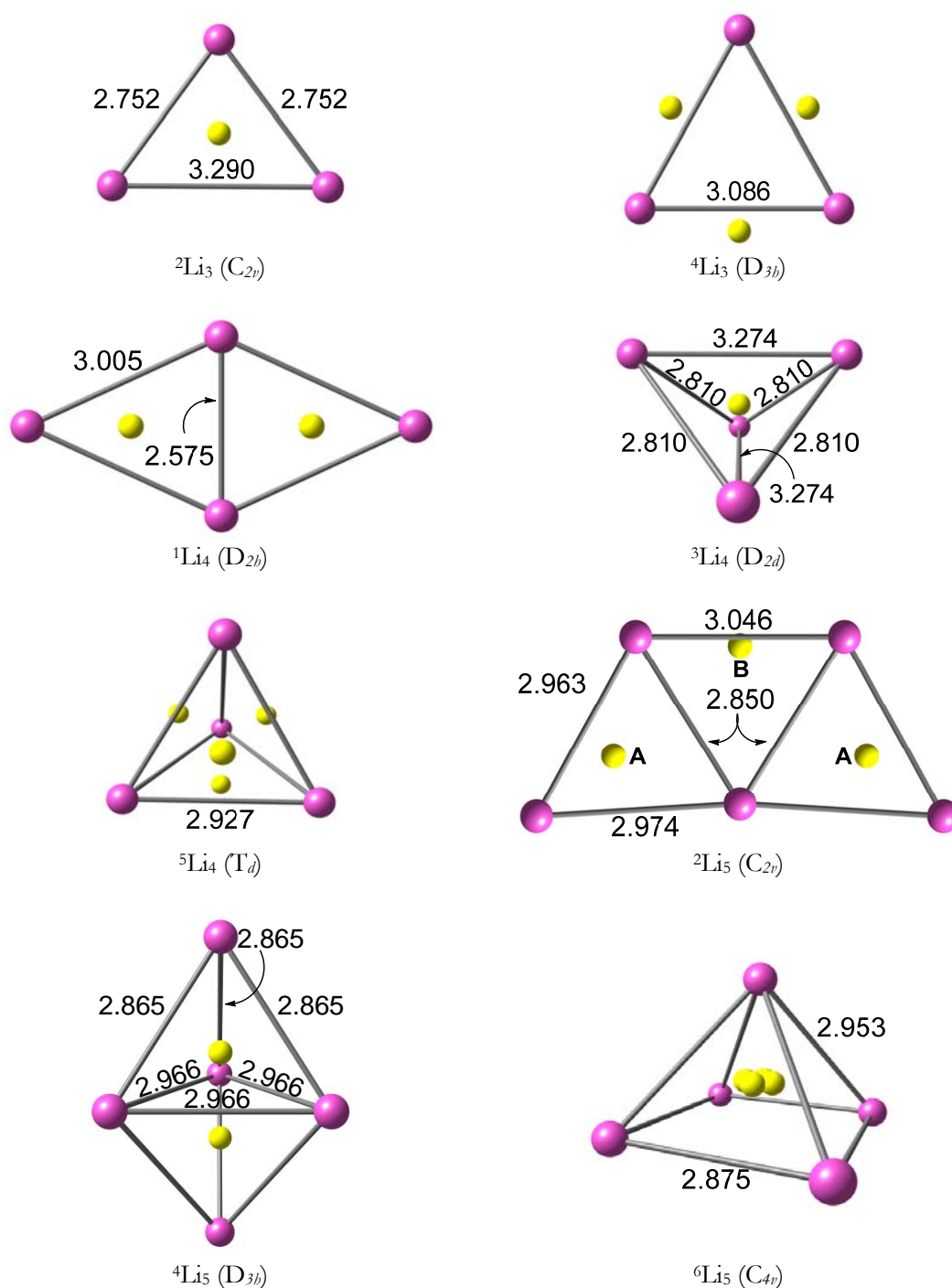
Figure 72. Molecular structure of $^{2S+1}Li_n$ clusters (n=3…5; S=0…5/2) optimized at (U)B3LYP/aug-cc-pVTZ level. NNAs are highlighted in yellow.

In the present work, all these conditions that were previously suggested to classify a molecule as an electride are satisfied for all the systems. Thus, all present electride character. However, the degree of localization/delocalization of NNAs differs depending on the system. Even though ELF gives us a qualitative picture of the electron pair distribution, in section 6.3.2 we

have found that the current definition is not adequate enough when describing quantitatively open-shell systems such as $^1A_{1g}$ Li_6^+ (S=3/2). For that reason, we decided to analyze the isosurface of the $\nabla^2\rho$ because the plot gives more insight physically sound than ELF. Again, we are also going to split $\nabla^2\rho$ into alpha ($\nabla^2\rho_\alpha$) and beta ($\nabla^2\rho_\beta$) contributions to identify regions with electron localization and delocalization, respectively.

$^2Li_3$ has one NNA with a localization of 88% according to QTAIM. According to $\nabla^2\rho_\alpha$ plot, two delocalized regions are detected and one localized region appears in the $\nabla^2\rho_\beta$ picture (Figure 73). Interestingly, the $\nabla^2\rho_\beta$ region is located around the NNA and it is not disappearing till we find an isosurface of 0.006 au. Instead, the $\nabla^2\rho_\alpha$ region is more concentrated in the two regions, thus causing that it does not disappear till higher isovalues (0.006). Yet, at low isovalues, the $\nabla^2\rho_\alpha$ plot shows electron density regions around the NNA but they disappear sooner (0.002-0.0025 au). Those observations lead to the next conclusion: the electron density around the NNA is more concentrated (or stays at high isovalues) in the beta density ($\nabla^2\rho_\beta$) which means that the NNA is highly localized and this is actually supported by the 88% shown by the localization index (LI) (see section 2.2). The results indicate that the β electron corresponds to a localized electron typical of an electride. So this species can be categorized as an electride.
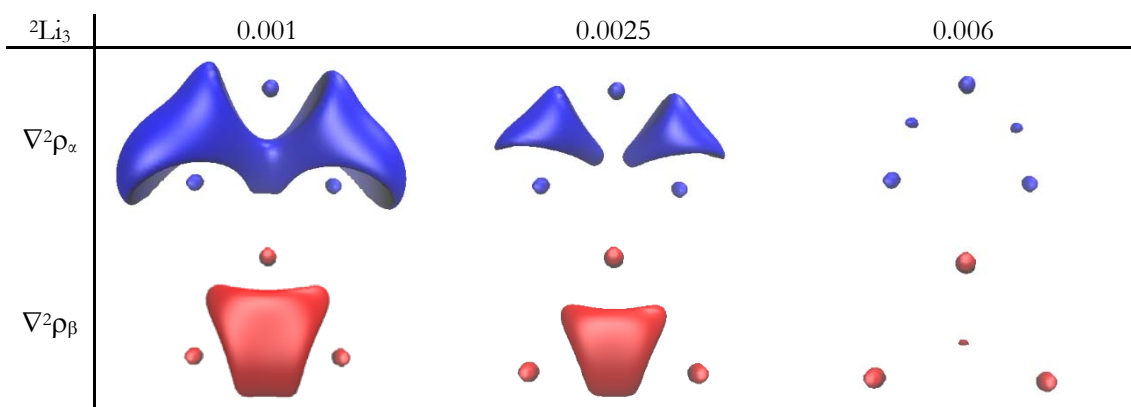
Figure 73. $\nabla^2\rho_\alpha$ and $\nabla^2\rho_\beta$ plots for $^2Li_3$. Isosurfaces given in a.u.

$^4Li_3$ presents three NNAs with a localization of 35%. In this case, we only have unpaired (alpha) electrons. So the $\nabla^2\rho_\alpha$ isosurface alone will provide the information about the whole behavior of the molecule because valence beta electrons are not present (Figure 74). The $\nabla^2\rho_\alpha$ plot distinguishes three regions strongly delocalized that remain at high isovalues of the Laplacian of the electron density (0.006 a.u.). Remarkably, these regions are positioned

around the NNAs. Hence the $\nabla^2\rho_\alpha$ isosurface explains the low degree of localization (35%) that is detected by the QTAIM analysis. In that sense, we can conclude that NNAs are highly delocalized and, thus, the system can be classified as a metallaelectride.

$^4Li_3$	0.001	0.0025	0.006
$\nabla^2\rho_\alpha$			
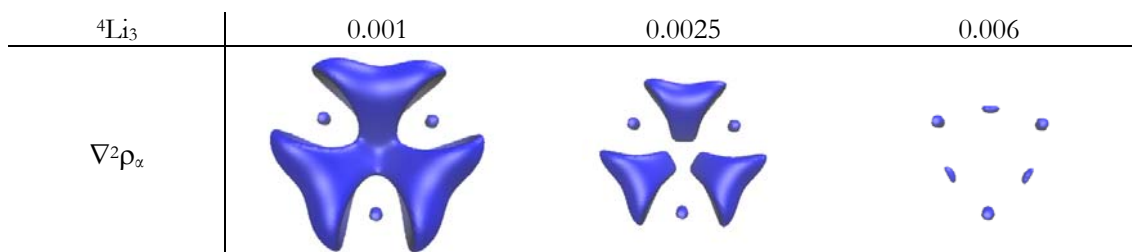
Figure 74. $\nabla^2\rho_\alpha$ plot for $^4Li_3$. Isosurfaces given in a.u.

$^1Li_4$ presents two NNAs with a localization of 56%. The $\nabla^2\rho_\alpha$ and $\nabla^2\rho_\beta$ plots are the same since we have a closed-shell system. The $\nabla^2\rho$ isosurface shows two regions that persist until an isovalue of 0.006 a.u around the positions of the NNAs (Figure 75). Even though the LI values indicate low localization, and it is higher than in the $^4Li_3$ case, $\nabla^2\rho$ proves that the NNAs have more localization than delocalization. So $^1Li_4$ can be described as a 2-fold molecular electride, with two electrons acting as electrides.

$^1Li_4$	0.001	0.0025	0.005
$\nabla^2\rho_\alpha/\nabla^2\rho_\beta$			
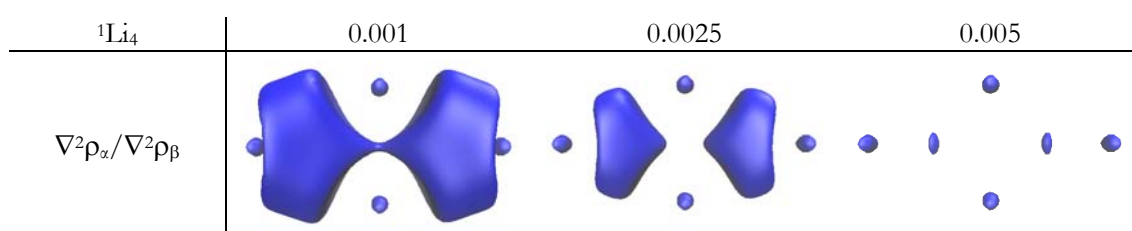
Figure 75. $\nabla^2\rho_\alpha$ and $\nabla^2\rho_\beta$ plots for $^1Li_4$. Isosurfaces given in a.u.

$^3Li_4$ has one NNA which is 59% localized according to the QTAIM analysis. The $\nabla^2\rho_\alpha$ isosurface presents four delocalized regions while the $\nabla^2\rho_\beta$ plot, which provides signs of localization, shows only one region around the position of the NNA that persists at an isovalue of 0.006 (Figure 76). In fact, this behavior resembles the one observed in $^2Li_3$, so $^3Li_4$ should be considered a molecular electride as well, yet the percentage of localization is much lower (59%) than in the previous state.
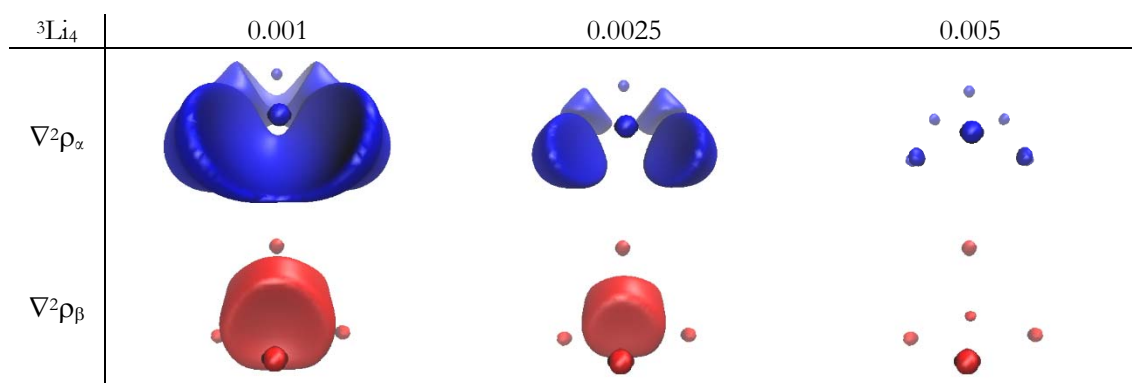
Figure 76. $\nabla^2\rho_\alpha$ and $\nabla^2\rho_\beta$ plots for ${}^3Li_4$. Isosurfaces given in a.u.

${}^5Li_4$ possesses four NNAs, which are located on the faces of the tetrahedron structure. They have a degree of localization of 33%. It is a compound that only has alpha valence electrons. The $\nabla^2\rho_\alpha$ plot shows four delocalized regions which are located around the NNAs (Figure 77). Therefore, ${}^5Li_4$, like ${}^4Li_3$, should be described as a metallaelectride due to the high delocalization presented by the NNAs.
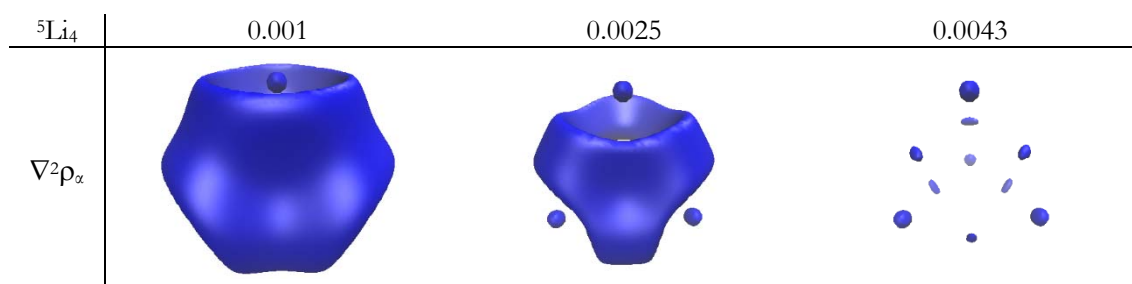
Figure 77. $\nabla^2\rho_\alpha$ plot for ${}^5Li_4$. Isosurfaces given in a.u.

${}^2Li_5$ has three NNAs, two of them (NNA_A) with a localization of 52% and the other one (NNA_B) with 40%. From the $\nabla^2\rho_\alpha$ isosurfaces, one can clearly distinguish three regions which are located nearby the NNAs. Two of these regions (A) disappear sooner (near the NNA_A, Figure 72) than the other one (B) (near the NNA_B, Figure 72) and therefore that would be indicative that the delocalized character of NNA_B is stronger than NNA_A (Figure 78). Even though the latter results indicate clearly that the two NNA_A have a localized character, $\nabla^2\rho_\beta$ evidences that the species presents delocalization around the NNA_A according to $\nabla^2\rho_\beta$ plots. Taking all these findings, we conclude that ${}^2Li_5$ should be described as a mix of an electride (β electrons) and a metallaelectride (α electrons).
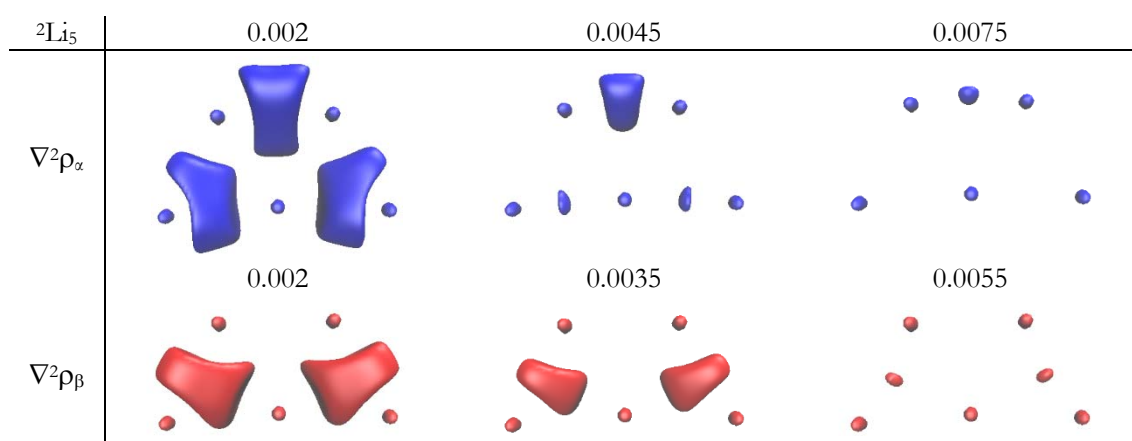
Figure 78. $\nabla^2\rho_\alpha$ and $\nabla^2\rho_\beta$ plots for $^2Li_5$. Isosurfaces given in a.u.

$^4Li_5$ has two NNAs with a localization of 41%. $\nabla^2\rho_\alpha$ plot displays delocalized regions far from the NNAs while $\nabla^2\rho_\beta$ shows a localized region in the center of the molecule around both NNAs (Figure 79). This localized region is peculiar because, at high isovalues, it does not split into two regions as one would expect. Maybe the reason for this is that the NNAs are too close compared to other molecules. Interestingly, the most significant delocalization takes place between these two NNAs as the delocalization of 21% shows. Thus, one can conclude that the NNAs are strongly localized according to $\nabla^2\rho_\beta$ plots and do not have any particular role in the electronic delocalization. Then, clearly, we should label $^4Li_5$ as an electride.
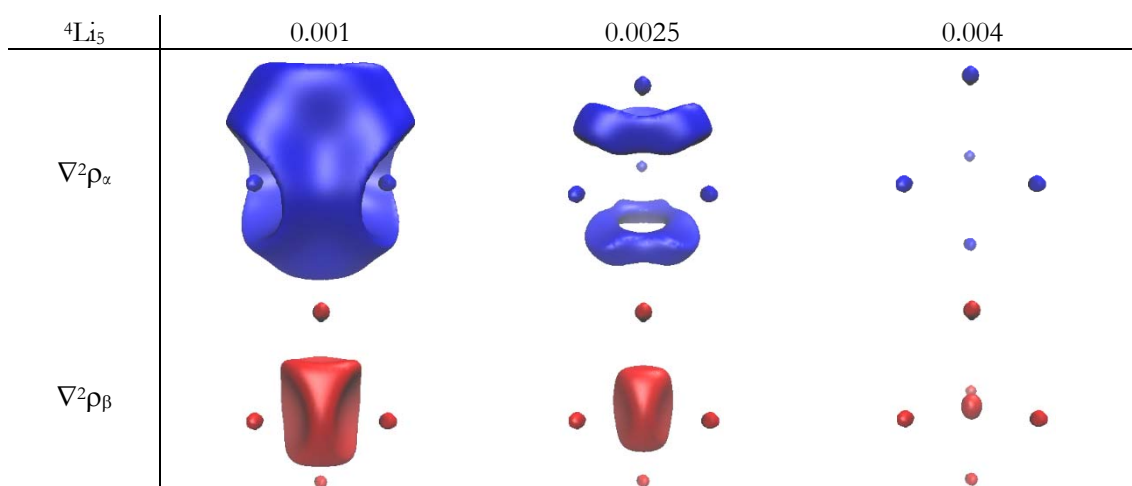
Figure 79. $\nabla^2\rho_\alpha$ and $\nabla^2\rho_\beta$ plots for $^4Li_5$. Isosurfaces given in a.u.

$^6Li_5$ has four NNAs which are located in the center of the molecule with a localization of 27%. According to the $\nabla^2\rho_\alpha$ isosurface, four delocalized regions can be distinguished but

they are quite displaced from the positions of the NNAs (Figure 80). Besides, the NNAs are situated close to each other and the DI between each pair is between 7–10%. Could these NNAs be an artifact? To prove that one must assess the stability of the system with different methodology. If they are artifacts, we cannot describe this species as a metallaelectride. Towards that situation, we decide to label it as a metal because we actually have a "sea" of electrons surrounding the molecule (delocalization) where the NNAs are not involved.

$^{6}Li_5$	0.002	0.004	0.0045
$\nabla^2\rho_\alpha$			
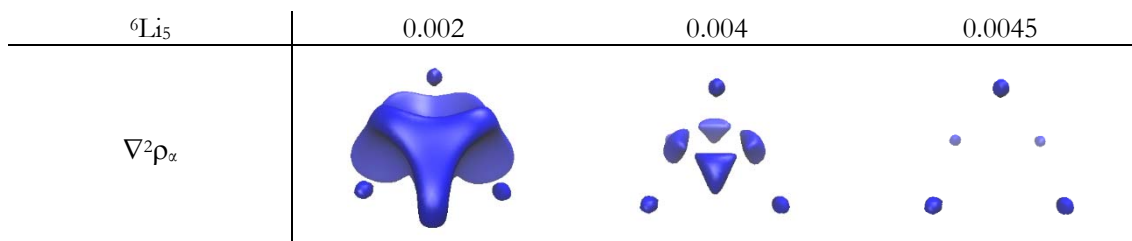
Figure 80. $\nabla^2\rho_\alpha$ plots for $^{6}Li_5$. Isosurfaces given in a.u.

In conclusion, from the previous analysis we observe that closed-shell systems are, in general, described as electrides, while high spin species are classified as metallaelectrides. On the other hand, the compounds that present paired and unpaired electrons show a mix of both properties. Yet, $^{6}Li_5$ is more like a metal, even though it possesses two NNAs. Figure 81 shows a general scheme of the results discussed previously. Clearly, one can see that these molecules can be classified in one group or another depending on the behavior of the electron density, the number of unpaired electrons and NNAs. First, for $^{1}Li_4$ and $^{2}Li_5$, which are considered an electride or a mixture of both properties, respectively, their electron localization and delocalization behave similarly. On the other hand, $^{2}Li_3$, $^{3}Li_4$ and $^{4}Li_5$ share the same behavior, that is, electron localization regions are really concentrated close to the NNAs while the other regions are more delocalized. Finally, for $^{4}Li_3$, $^{5}Li_4$ and $^{6}Li_5$, the electron delocalization is the most important feature while the localization does not exist. In the latter cases, the electron delocalization coincides with the position around the NNAs like $^{4}Li_3$ and $^{5}Li_4$ and, therefore, we are talking about metallaelectrides. Yet when the electron delocalization is not found around the NNAs, like the case of $^{6}Li_5$, we must refer to it as a metal.
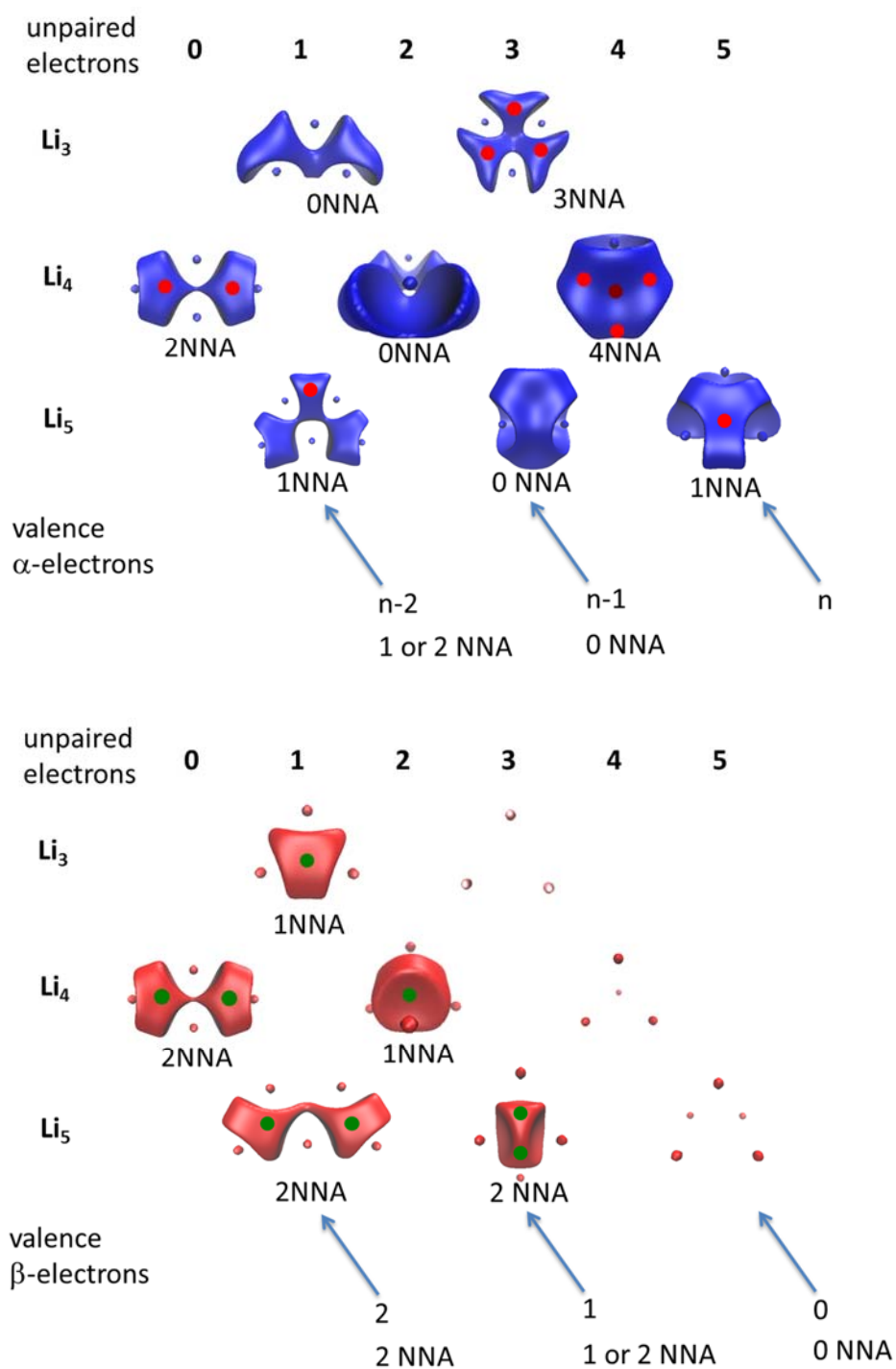
Figure 81. $\nabla^2\rho_\alpha$ and $\nabla^2\rho_\beta$ plots for all systems that have been studied. Red and green dots symbolize the position of the NNAs. Isosurface of 0.001 is used (a.u.).

CHAPTER 7: GENERAL

CONCLUSIONS

The main conclusions of this thesis can be organized in three groups of applications:

<u>Extension and validation of the Glidewell-Lloyd's rule</u>

<u>First:</u>

We have investigated the validity of the Glidewell–Lloyd rule in 69 PCHs composed of different combinations of 4-, 6-, and 8-MRs. Our results indicate that most of PCHs in their ground (or lowest-lying) closed-shell singlet state obey the rule. We found three types of situations in which the Glidewell–Lloyd rule breaks down. First, compounds having two or more adjacent CBD rings fused to 6- or 8-MRs. Second, conjugated polycyclic systems that try to avoid as much as possible the presence of double bonds in ring junctions. And third, there is the situation of **Mol. 18** that places 4π-electrons in one CBD ring to avoid placing 8π-electrons in two COT rings. Therefore, we propose a minor modification of the Glidewell–Lloyd rule to include this case. In this new formulation, the rule states: "*the total population of π-electrons in conjugated polycyclic systems that have a closed-shell singlet ground state tends to form the smallest 4n + 2 groups and to avoid the formation of the smallest 4n groups, except in the case that avoiding formation of the smallest 4n groups results in the formation of a greater number of large 4n groups*".

<u>Aromaticity in the excited states</u>

<u>Second:</u>

DFT calculations have revealed the most favored product in high spin states of DA reaction between C_{60} and Cp is the [5,6] adduct, whereas in the ground state is the [6,6] product. This

regioselectivity inversion is mainly attributed to the change of the aromatic character of the molecular cage. Yet, experimentally, we obtain the [6,6] adduct instead of the [5,6] one from the DA reaction between isoindene and photo-excited $^3C_{60}$. So the regioselectivity does not change. Computations explain the experimental observations by showing that that in the T_1 state the reaction goes through an ISC to reach the S_0 state and then the reaction ends in the ground state giving the [6,6] product.

Third:

MCI calculations have proved the existence of excited state homoaromaticity between the FC region and the minimum along the photochemical conversion of QC to NBQ at S_1 state. This finding is observed in the real system (NBD-R_2) as well as in the parent system (PA-H_2) and in the model system (DA-H_2). That explains why Prof. Ottosson's group found a shallow minimum at CASSCF level of theory.

Fourth:

FLU has been used as an electronic descriptor to quantify the local and global aromaticity of some PAHs in their S_0 and T_1 states, yet HOMA and magnetic indices have been also computed by other authors. In general, this study reveals that Clar's rule can be extended to the T_1 state if it is connected to Baird's rule. All aromatic descriptors agree with the fact that, in a set of isomeric PAHs having a central $4n\pi$-electron unit, the most stable isomer is the one that has the largest number of combined Baird quartets/octets and Clar sextets. Hence, due to the combination of Baird's rule with Clar's rule, we are able to explain the order in triplet energies of PAHs.

Aromaticity and chemical bonding of metal clusters

Fifth:

We showed that the preference of B_6^{2-} for the planar D_{2h} form is due to two particular MO interactions. From one side the D_{2h}HOMO-2(b_{2u}) formed from two tangential SOMO $\sigma^T(b_2)$ orbitals, is related to localized covalent bonding, and has a much more important weight in B_6^{2-} than in Al_6^{2-}, proving the dominant localized covalent character in the former. And the second determinant interaction is that of π character. In the case of O_hHOMO-1(t_{2g}) for B_6^{2-}, its formation from two π-SOMO orbitals is much less favourable than for Al_6^{2-}. This result

is in line with a dominant delocalization force in Al clusters and more localized bonding in B metal clusters. For mixed clusters, we have found that those with more than two B atoms prefer the planar structure for the same reasons as discussed for B_6^{2-}.

<u>Sixth:</u>

We have found fifteen new octahedral clusters that have octahedral aromaticity. Yet, in general but not always closed-shells or open-shells half-filled with the same spin electronic configurations with octahedral symmetry have aromatic character with large ESIs and negative NICS values. So an electronic configuration with a closed-shell or an open-shell half-filled with the same spin electrons is not a sufficient condition for aromaticity. Finally, a rule for octahedral aromaticity cannot be proposed because the ordering of the MOs changes from one O_h system to another.

<u>Seventh:</u>

We have identified two species ($O_h(^4A_{1g})$ Li_6^+ and $O_h(^5A_{1g})$ Be_6) with more NNAs than nuclei and with all or almost all valence electrons located in these NNAs. Their chemical bonding resembles that of solid metals[206] where the array of metal cations are surrounded by a "sea" of valence electrons (electron-sea model), and consequently, we suggest that these species can be used as molecular models for the study of the metal bonding. The presence of high delocalized NNAs and delocalized regions provided by the negative values of the Laplacian of the electron density indicate that we are dealing with metallaelectrides instead of molecular electrides.

<u>Eighth:</u>

We have studied the chemical bonding of a series of lithium clusters that possess NNAs in order to show the discrepancies between an electride and a metallaelectride. By means of the Laplacian of the electron density, we study the localisation versus the delocalisation of the systems towards the NNA. Thus, we find that low spin species tend to act as electrides (due to the high localization), whereas high spin compounds behave like a metal (because of the high delocalization of NNAs). Even though, we have found these two extreme cases, some of the lithium clusters in their intermediate spin state have a mix of both electride and metallaelectride character. Finally, $^6Li_5$ is the only case that can be described as a metal and not as a metallaelectride because the delocalisation is not around the position of the NNA.

References

(1)   Solà, M. In *Encyclopedia of physical organic chemistry*; Wang, Z., Ed.; John Wiley & Sons, Weinhelm, 2017; pp 511–542.

(2)   Chen, Z.; Wannere, C. S.; Corminboeuf, C.; Puchta, R.; Schleyer, P. von R. *Chem. Rev.*, **2005**, *105*, 3842–3888.

(3)   McNaught, A. D.; Wilkinson, A. *IUPAC Compendium of Chemical Terminology: Gold Book*; 2014.

(4)   Faraday, M. *Phil. Trans. R. Soc. Lon.*, **1825**, *115*, 440–446.

(5)   Kekulé, A. *Bulletin Mensuel de la Société Chimique de Paris*, **1865**, *3*, 98–110.

(6)   Erlenmeyer, E. *Ann. Chem.*, **1866**, *137*, 327–359.

(7)   Willstätter, R.; Waser, E. *Ber. Dtsch. Chem. Ges.*, **1911**, *44*, 3423–3445.

(8)   Crocker, E. C. *J. Am. Chem. Soc.*, **1922**, *44*, 1618–1630.

(9)   Armit, J. W.; Robinson, R. *J. Chem. Soc. Trans.*, **1925**, *127*, 1604–1618.

(10)   Hückel, E. *Z. Phys.*, **1931**, *70*, 204–286.

(11)   Pauling, L.; Sherman, J. *J. Chem. Phys.*, **1933**, *1*, 606–617.

(12)   Calvin, M.; Wilson, K. W. *J. Am. Chem. Soc.*, **1945**, *67*, 2003–2007.

(13)   Heilbronner, E. *Tetrahedron Lett.*, **1964**, *5*, 1923–1928.

(14)   Breslow, R. *Chem. Eng. News*, **1965**, *43*, 90–100.

(15)   Wade, K. *Electron-deficient Compounds*; Nelson and Sons, Ltd.: London, 1971.

(16)   Wade, K. *J. Chem. Soc. D Chem. Commun.*, **1971**, 15, 792–793.

(17)   Mingos, D. M. P. *Nat. Phys. Sci.*, **1972**, *236*, 99–102.

(18)   Mingos, D. M. P. *Acc. Chem. Res.*, **1984**, *17*, 311–319.

(19)   Clar, E. *The Aromatic Sextet*; Wiley: New York, 1972.

(20)   Baird, N. C. C. *J. Am. Chem. Soc.*, **1972**, *94*, 4941–4948.

(21)   Aihara, J. *J. Am. Chem. Soc.*, **1978**, *100*, 3339–3342.

(22)   Bursten, B. E.; Fenske, R. F. *Inorg. Chem.*, **1979**, *18*, 1760–1765.

(23)   Thorn, D. L.; Hoffmann, R. *Nouv. J. Chim.*, **1979**, *3*, 39–45.

(24)   Dewar, M. J. S. *Bull. Soc. Chim. Belg.*, **1979**, *88*, 957–967.

(25)   Glidewell, C.; Lloyd, D. *Tetrahedron*, **1984**, *40*, 4455–4472.

(26)   Shaik, S. S.; Hiberty, P. C. *J. Am. Chem. Soc.*, **1985**, *107*, 3089–3095.

(27)   Kroto, H. W.; Heath, J. R.; O'Brien, S. C.; Curl, R. F.; Smalley, R. E. *Nature*, **1985**, *318*, 162–163.

(28) Hirsch, A.; Chen, Z.; Jiao, H. *Angew. Chem. Int. Ed.*, **2000**, *39*, 3915–3917.

(29) Li, X.; Kuznetsov, A. E.; Zhang, H.-F.; Boldyrev, A. I.; Wang, L.-S. *Science*, **2001**, *291*, 859–861.

(30) King, R. B. *Inorg. Chim. Acta*, **2003**, *350*, 126–130.

(31) Kuznetsov, A. E. *Science*, **2003**, *300*, 622–625.

(32) Ajami, D.; Oeckler, O.; Simon, A.; Herges, R. *Nature*, **2003**, *426*, 819–821.

(33) Wannere, C. S.; Corminboeuf, C.; Wang, Z.-X.; Wodrich, M. D.; King, R. B.; Schleyer, P. v. R. *J. Am. Chem. Soc.*, **2005**, *127*, 5701–5705.

(34) Tsipis, C. A.; Karagiannis, E. E.; Kladou, P. F.; Tsipis, A. C. *J. Am. Chem. Soc.*, **2004**, *126*, 12916–12929.

(35) Huang, X.; Zhai, H.-J.; Kiran, B.; Wang, L.-S. *Angew. Chem. Int. Ed.*, **2005**, *117*, 7417–7420.

(36) Zhai, H.-J.; Averkiev, B. B.; Zubarev, D. Y.; Wang, L.-S.; Boldyrev, A. I. *Angew. Chem. Int. Ed.*, **2007**, *46*, 4277–4280.

(37) Averkiev, B. B.; Boldyrev, A. I. *J. Phys. Chem. A*, **2007**, *111*, 12864–12866.

(38) Soncini, A.; Fowler, P. W. *Chem. Phys. Lett.*, **2008**, *450*, 431–436.

(39) Rappaport, S. M.; Rzepa, H. S. *J. Am. Chem. Soc.*, **2008**, *130*, 7613–7619.

(40) Poater, J.; Solà, M. *Chem. Commun.*, **2011**, *47*, 11647–11649.

(41) Schaller, G. R.; Topić, F.; Rissanen, K.; Okamoto, Y.; Shen, J.; Herges, R. *Nat. Chem.*, **2014**, *6*, 608–613.

(42) Mitscherlich, E. *Ann. der Pharm.*, **1834**, *9*, 39–48.

(43) Kekulé, A. *Ann. Chem.*, **1866**, *137*, 129–196.

(44) Hofmann, A. W. *Proc. R. Soc. Lond.*, **1856**, *8*, 1–3.

(45) Pauling, L. *J. Chem. Phys.*, **1936**, *4*, 673–677.

(46) Hückel, E. *Z. Phys.*, **1931**, *72*, 310–337.

(47) Von E.Doering, W.; Knox, L. H. *J. Am. Chem. Soc.*, **1954**, *76*, 3203–3206.

(48) Mucke, E.-K.; Schönborn, B.; Köhler, F.; Herges, R. *J. Org. Chem.*, **2011**, *76*, 35–41.

(49) Higashino, T.; Soya, T.; Kim, W.; Kim, D.; Osuka, A. *Angew. Chem. Int. Ed.*, **2015**, *54*, 5456–5459.

(50) Lim, J. M.; Yoon, Z. S.; Shin, J.-Y.; Kim, K. S.; Yoon, M.-C.; Kim, D. *Chem. Commun.*, **2008**, 3, 261–273.

(51) Shin, J.-Y.; Kim, K. S.; Yoon, M.-C.; Lim, J. M.; Yoon, Z. S.; Osuka, A.; Kim, D. *Chem. Soc. Rev.*, **2010**, *39*, 2751–2767.

(52) Breslow, R. *Acc. Chem. Res.*, **1973**, *6*, 393–398.

(53) Breslow, R.; Brown, J.; Gajewski, J. J. *J. Am. Chem. Soc.*, **1967**, *89*, 4383–4390.

(54) Clar, E. *Polycyclic Hydrocarbons*; London: Academic, 1964.

(55) Randić, M. *Chem. Rev.* , **2003**, *103*, 3449–3605.

(56) Ruiz-Morales, Y. *J. Phys. Chem. A*, **2004**, *108*, 10873–10896.

(57) Schulman, J. M.; Disch, R. L. *J. Phys. Chem. A*, **1999**, *103*, 6669–6672.

(58) Cyrański, M. K.; Stepién, B. T.; Krygowski, T. M. *Tetrahedron*, **2000**, *56*, 9663–9967.

(59) Portella, G.; Poater, J.; Bofill, J. M.; Alemany, P.; Solà, M. *J. Org. Chem.*, **2005**, *70*, 2509–2521.

(60) Solà, M. *Front. Chem.*, **2013**, *1*, 22.

(61) Matsumoto, A.; Suzuki, M.; Kuzuhara, D.; Hayashi, H.; Aratani, N.; Yamada, H. *Angew. Chem. Int. Ed.*, **2015**, *54*, 8175–8178.

(62) Petty, M. C.; Bryce, M. R.; Bloor, D. *An introduction to molecular electronics*; Oxford University Press: Oxford, 1995.

(63) Matsumoto, A.; Suzuki, M.; Hayashi, H.; Kuzuhara, D.; Yuasa, J.; Kawai, T.; Aratani, N.; Yamada, H. *Chem. Eur. J.*, **2016**, *22*, 14462–14466.

(64) Rosenberg, M.; Dahlstrand, C.; Kilså, K.; Ottosson, H. *Chem. Rev.*, **2014**, *114*, 5379–5425.

(65) Karadakov, P. B. *J. Phys. Chem. A*, **2008**, *112*, 7303–7309.

(66) Karadakov, P. B. *J. Phys. Chem. A*, **2008**, *112*, 12707–12713.

(67) Feixas, F.; Vandenbussche, J.; Bultinck, P.; Matito, E.; Solà, M. *Phys. Chem. Chem. Phys.*, **2011**, *13*, 20690–20703.

(68) Breslow, R.; Chang, H. W.; Hill, R.; Wasserman, E. *J. Am. Chem. Soc.*, **1967**, *89*, 1112–1119.

(69) Saunders, M.; Berger, R.; Jaffe, A.; McBride, J. M.; O'Neill, J.; Breslow, R.; Hoffmann, J. M.; Perchonock, C.; Wasserman, E. *J. Am. Chem. Soc.*, **1973**, *95*, 3017–3018.

(70) Wörner, H. J.; Merkt, F. *Angew. Chem. Int. Ed.*, **2006**, *45*, 293–296.

(71) Papadakis, R.; Ottosson, H. *Chem. Soc. Rev.*, **2015**, *44*, 6472–6493.

(72) Papadakis, R.; Li, H.; Bergman, J.; Lundstedt, A.; Jorner, K.; Ayub, R.; Haldar, S.; Jahn, B. O.; Denisova, A.; Zietz, B.; Lindh, R.; Sanyal, B.; Grennberg, H.; Leifer, K.; Ottosson, H. *Nat. Commun.*, **2016**, *7*, 12962.

(73) Stone, A. J.; Wales, D. J. *Chem. Phys. Lett.*, **1986**, *128*, 501–503.

(74) Banhart, F.; Kotakoski, J.; Krasheninnikov, A. V. *ACS Nano*, **2011**, *5*, 26–41.

(75) Migani, A.; Blancafort, L.; Robb, M. A.; DeBellis, A. D. *J. Am. Chem. Soc.*, **2008**, *130*, 6932–6933.

(76) Migani, A.; Leyva, V.; Feixas, F.; Schmierer, T.; Gilch, P.; Corral, I.; Gonzalez, L.; Blancafort, L. *Chem. Commun.*, **2011**, *47*, 6383–6385.

(77)   Forés, M.; Duran, M.; Solà, M. *Chem. Phys.*, **2000**, *260*, 53–64.

(78)   Exelby, R.; Grinter, R. *Chem. Rev.*, **1965**, *65*, 247–260.

(79)   Ortiz-Sánchez, J. M.; Gelabert, R.; Moreno, M.; Lluch, J. M. *J. Phys. Chem. A*, **2006**, *110*, 4649–4656.

(80)   Ortiz-Sánchez, J. M.; Gelabert, R.; Moreno, M.; Lluch, J. M. *J. Chem. Phys.*, **2008**, *129*, 214308.

(81)   Gutiérrez-Arzaluz, L.; Cortés-Guzman, F.; Rocha-Rinza, T.; Peón, J. *Phys. Chem. Chem. Phys.*, **2015**, *17*, 31608–31612.

(82)   Cuma, M.; Scheiner, S.; Kar, T. *J. Mol. Struct.*, **1999**, *467*, 37–49.

(83)   Forés, M.; Duran, M.; M. Solà, A.; Adamowicz, L. . *Phys. Chem. A*, **1999**, *103*, 4413–4420.

(84)   Chen, Z.; Jiao, H.; Hirsch, A.; Thiel, W. *J. Mol. Model.*, **2001**, *7*, 161–163.

(85)   Bühl, M.; Hirsch, A. *Chem. Rev.*, **2001**, *101*, 1153–1184.

(86)   Kroto, H. W. *Nature*, **1987**, *329*, 529–531.

(87)   García Borràs, M. PhD thesis: Structure and reactivity of endohedral (metallo)fullerenes, Universitat de Girona, 2015.

(88)   Garcia-Borràs, M.; Osuna, S.; Swart, M.; Luis, J. M.; Solà, M. *Chem. Commun.*, **2013**, *49*, 1220–1222.

(89)   Bingel, C. *Chem. Ber.*, **1993**, *126*, 1957–1959.

(90)   Hirsch, A.; Brettreich, M. *Fullerenes: Chemistry and Reactions*; John Wiley & Sons: Weinheim, 2006.

(91)   Garcia-Borràs, M.; Cerón, M. R.; Osuna, S.; Izquierdo, M.; Luis, J. M.; Echegoyen, L.; Solà, M. *Angew. Chem. Int. Ed.*, **2016**, *55*, 2374–2377.

(92)   Garcia-Borràs, M.; Osuna, S.; Swart, M.; Luis, J. M.; Echegoyen, L.; Solà, M. *Chem. Commun.*, **2013**, *49*, 8767–8769.

(93)   Garcia-Borràs, M.; Osuna, S.; Swart, M.; Luis, J. M.; Solà, M. *Angew. Chem. Int. Ed.*, **2013**, *52*, 9275–9278.

(94)   Kiely, A. F.; Haddon, R. C.; Meier, M. S.; Selegue, J. P.; Brock, C. P.; Patrick, B. O.; Wang, G.-W.; Chen, Y. *J. Am. Chem. Soc.*, **1999**, *121*, 7971–7972.

(95)   Winstein, S. *J. Am. Chem. Soc.*, **1959**, *81*, 6524–6525.

(96)   Elliott, G. P.; Roper, W. R.; Waters, J. M. *J. Chem. Soc., Chem. Commun.*, **1982**, 14, 811–813.

(97)   Gausa, M.; Kaschner, R.; Lutz, H. O.; Seifert, G.; Meiwes-Broer, K.-H. *Chem. Phys. Lett.*, **1994**, *230*, 99–102.

(98)   Li, X.-W.; Pennington, W. T.; Robinson, G. H. *J. Am. Chem. Soc.*, **1995**, *117*, 7578–7579.

(99) Li, X.; Zhang, H.-F.; Wang, L.-S.; Kuznetsov, A. E.; Cannon, N. A.; Boldyrev, A. I. *Angew. Chem. Int. Ed.*, **2001**, *40*, 1867–1870.

(100) Dewar, M. J. S. *J. Am. Chem. Soc.*, **1984**, *106*, 669–682.

(101) Kuznetsov, A. E.; Corbett, J. D.; Wang, L.-S.; Boldyrev, A. I. *Angew. Chem. Int. Ed.*, **2001**, *40*, 3369–3372.

(102) Kuznetsov, A. E.; Boldyrev, A. I.; Li, X.; Wang, L.-S. *J. Am. Chem. Soc.*, **2001**, *123*, 8825–8831.

(103) Fowler, P. W. W.; Havenith, R. W. A. W. A.; Steiner, E. *Chem. Phys. Lett.*, **2001**, *342*, 85–90.

(104) Jusélius, J.; Straka, M.; Sundholm, D. *J. Phys. Chem. A*, **2001**, *105*, 9939–9944.

(105) Boldyrev, A. I.; Kuznetsov, A. E. *Inorg. Chem.*, **2002**, *41*, 532–537.

(106) Feixas, F.; Matito, E.; Duran, M.; Poater, J.; Solà, M. *Theor. Chem. Acc.*, **2011**, *128*, 419–431.

(107) Alexandrova, A. N.; Boldyrev, A. I. *J. Phys. Chem. A*, **2003**, *107*, 554–560.

(108) Havenith, R. W. A.; De Proft, F.; Fowler, P. W.; Geerlings, P. *Chem. Phys. Lett.*, **2005**, *407*, 391–396.

(109) Bishop, D. M.; Chaillet, M.; Larrieu, K.; Pouchan, C. *Mol. Phys.*, **1984**, *51*, 179–183.

(110) Jiménez-halla, J. O. C.; Matito, E.; Blancafort, L.; Robles, J.; Solà, M. *J. Comput. Chem.*, **2009**, *30*, 2764–2776.

(111) Kuznetsov, A. E.; Boldyrev, A. I. *Chem. Phys. Lett.*, **2004**, *388*, 452–456.

(112) Tsipis, C. A. *Coord. Chem. Rev.*, **2005**, *249*, 2740–2762.

(113) Giri, S.; Roy, D. R.; Duley, S.; Chakraborty, A.; Parthasarathi, R.; Elango, M.; Vijayaraj, R.; Subramanian, V.; Islas, R.; Merino, G.; Chattaraj, P. K. *J. Comput. Chem.*, **2010**, *31*, 1815–1821.

(114) Chi, X. X.; Liu, Y. *Int. J. Quantum Chem.*, **2007**, *107*, 1886–1896.

(115) Ivanov, A. S.; Zhang, X.; Wang, H.; Boldyrev, A. I.; Gantefoer, G.; Bowen, K. H.; Černušák, I. *J. Phys. Chem. A*, **2015**, *119*, 11293–11303.

(116) Lipscomb, W. N.; Pitochelli, A. R.; Hawthorne, M. F. *J. Am. Chem. Soc.*, **1959**, *81*, 5833–5834.

(117) Lipscomb, W. N. *Boron Hydrides*; W. A. Benjamin: New York, 1963.

(118) Klanberg, F.; Eaton, D. R.; Guggenberger, L. J.; Muetterties, E. L. *Inorg. Chem.*, **1967**, *6*, 1271–1281.

(119) Knoth, W. H.; Miller, H. C.; England, D. C.; Parshall, G. W.; Muetterties, E. L. *J. Am. Chem. Soc.*, **1962**, *84*, 1056–1057.

(120) Poater, J.; Solà, M.; Viñas, C.; Teixidor, F. *Angew. Chem. Int. Ed.*, **2014**, *53*, 12191–12195.

(121) Cui, P.; Hu, H.-S.; Zhao, B.; Miller, J. T.; Cheng, P.; Li, J. *Nat. Commun.*, **2015**, *6*, 6331.

(122) Sergeeva, A. P.; Popov, I. A.; Piazza, Z. A.; Li, W.-L.; Romanescu, C.; Wang, L.-S.; Boldyrev, A. I. *Acc. Chem. Res.*, **2014**, *47*, 1349–1358.

(123) Zhai, H.-J. H.-J.; Alexandrova, A. N.; Birch, K. A.; Boldyrev, A. I.; Wang, L.-S. L.-S. *Angew. Chem. Int. Ed.*, **2003**, *42*, 6004–6008.

(124) Sergeeva, A. P.; Zubarev, D. Y.; Zhai, H.-J.; Boldyrev, A. I.; Wang, L.-S. *J. Am. Chem. Soc.*, **2008**, *130*, 7244–7246.

(125) Sergeeva, A. P.; Averkiev, B. B.; Zhai, H.-J.; Boldyrev, A. I.; Wang, L.-S. *J. Chem. Phys.*, **2011**, *134*, 224304.

(126) Romanescu, C.; Harding, D. J.; Fielicke, A.; Wang, L.-S. *J. Chem. Phys.*, **2012**, *137*, 14317.

(127) Huang, W.; Sergeeva, A. P.; Zhai, H.-J.; Averkiev, B. B.; Wang, L.-S.; Boldyrev, A. I. *Nat. Chem.*, **2010**, *2*, 202–206.

(128) Romanescu, C.; Galeev, T. R.; Li, W.-L.; Boldyrev, A. I.; Wang, L.-S. *Acc. Chem. Res.*, **2013**, *46*, 350–358.

(129) Romanescu, C.; Galeev, T. R.; Li, W.-L.; Boldyrev, A. I.; Wang, L.-S. *Angew. Chem. Int. Ed.*, **2011**, *50*, 9334–9337.

(130) Li, W.-L.; Romanescu, C.; Galeev, T. R.; Piazza, Z. A.; Boldyrev, A. I.; Wang, L.-S. *J. Am. Chem. Soc.*, **2012**, *134*, 165–168.

(131) Galeev, T. R.; Romanescu, C.; Li, W.-L.; Wang, L.-S.; Boldyrev, A. I. *Angew. Chem. Int. Ed.*, **2012**, *51*, 2101–2105.

(132) Romanescu, C.; Galeev, T. R.; Sergeeva, A. P.; Li, W.-L.; Wang, L.-S.; Boldyrev, A. I. *J. Organomet. Chem.*, **2012**, *721–722*, 148–154.

(133) Min, X.; Popov, I. A.; Pan, F.; Li, L.; Matito, E.; Sun, Z.; Wang, L.; Boldyrev, A. I. *Angew. Chem. Int. Ed.*, **2016**, *55*, 5531–5535.

(134) Tsipis, A. C. *Phys. Chem. Chem. Phys.*, **2009**, *11*, 8244–8261.

(135) Robilotto, T. J.; Bacsa, J.; Gray, T. G.; Sadighi, J. P. *Angew. Chem. Int. Ed.*, **2012**, *51*, 12077–12080.

(136) Kuwabara, T.; Guo, J. D.; Nagase, S.; Saito, M. *Angew. Chem. Int. Ed.*, **2014**, *53*, 434–438.

(137) Blanchard, S.; Fensterbank, L.; Gontard, G.; Lacôte, E.; Maestri, G.; Malacria, M. *Angew. Chem. Int. Ed.*, **2014**, *53*, 1987–1991.

(138) Popov, I. A.; Pan, F.-X.; You, X.-R.; Li, L.-J.; Matito, E.; Liu, C.; Zhai, H.-J.; Sun, Z.-M.; Boldyrev, A. I. *Angew. Chem. Int. Ed.*, **2016**, *55*, 15344–15346.

(139) Cyrański, M. K. *Chem. Rev.*, **2005**, *105*, 3773–3811.

(140) Hehre, W. J.; McIver, R. T.; Pople, J. A.; Schleyer, P. v. R. *J. Am. Chem. Soc.*, **1974**, *96*, 7162–7163.

(141) Hehre, W. J.; Ditchfield, R.; Radom, L.; Pople, J. A. *J. Am. Chem. Soc.*, **1970**, *92*, 4796–4801.

(142) Schleyer, P. von R.; Pühlhofer, F. *Org. Lett.*, **2002**, *4*, 2873–2876.

(143) Fernández, I.; Frenking, G. *Faraday Discuss.*, **2007**, *135*, 403–421.

(144) Julg, A.; François, P. *Theor. Chim. Acta*, **1967**, *8*, 249–259.

(145) Kruszewski, J.; Krygowski, T. M. M. *Tetrahedron Lett.*, **1972**, *13*, 3839–3842.

(146) Krygowski, T. M. *J. Chem. Inf. Model.*, **1993**, *33*, 70–78.

(147) Więckowski, T.; Krygowski, T. M. *Can. J. Chem.*, **1981**, *59*, 1622–1629.

(148) Krygowski, T. M.; Anulewicz, R.; Kruszewski, J.; IUCr. *Acta Crystallogr. Sect. B Struct. Sci.*, **1983**, *39*, 732–739.

(149) Bird, C. W. *Tetrahedron*, **1985**, *41*, 1409–1414.

(150) Bird, C. W. *Tetrahedron*, **1986**, *42*, 89–92.

(151) Krygowski, T. M.; Ciesielski, A.; Bird, C. W.; Kotschy, A. *J. Chem. Inf. Model.*, **1995**, *35*, 203–210.

(152) Raczyńska, E. D.; Hallman, M.; Kolczyńska, K.; Stępniewski, T. M. *Symmetry*, **2010**, *2*, 1485–1509.

(153) Mallion, R. B. *Pure Appl. Chem.*, **1980**, *52*, 1541–1548.

(154) Gomes, J. A. N. F.; Mallion, R. B. *Chem. Rev.*, **2001**, *101*, 1349–1384.

(155) Schleyer, P. v. R.; Maerker, C.; Dransfeld, A.; Jiao, H.; van Eikema Hommes, N. J. R. *J. Am. Chem. Soc.*, **1996**, *118*, 6317–6318.

(156) Lazzeretti, P. *Phys. Chem. Chem. Phys.*, **2004**, *6*, 217–223.

(157) Stanger, A. *J. Org. Chem.*, **2006**, *71*, 883–893.

(158) Stanger, A. *Chem. Eur. J.*, **2006**, *12*, 2745–2751.

(159) Jiménez-Halla, J. O. C.; Matito, E.; Robles, J.; Solà, M. *J. Organomet. Chem.*, **2006**, *691*, 4359–4366.

(160) Geuenich, D.; Hess, K.; Köhler, F.; Herges, R. *Chem. Rev.*, **2005**, *105*, 3758–3772.

(161) Coriani, S.; Lazzeretti, P.; Malagoli, M.; Zanasi, R. *Theor. Chim. Acta*, **1994**, *89*, 181–192.

(162) Steiner, E.; Fowler, P. W. *J. Phys. Chem. A*, **2001**, *105*, 9553–9562.

(163) Havenith, R. W. A.; Fowler, P. W. *Phys. Chem. Chem. Phys.*, **2006**, *8*, 3383.

(164) Jusélius, J.; Sundholm, D.; Gauss, J. *J. Chem. Phys.*, **2004**, *121*, 3952–3963.

(165) Fliegl, H.; Taubert, S.; Lehtonen, O.; Sundholm, D. *Phys. Chem. Chem. Phys.*, **2011**, *13*, 20500–20518.

(166) Fliegl, H.; Sundholm, D.; Taubert, S.; Jusúlius, J.; Klopper, W. *J. Phys. Chem. A*, **2009**,

113, 8668–8676.

(167)   De Proft, F.; Geerlings, P. *Chem. Rev.*, **2001**, *101*, 1451–1464.

(168)   Merino, G.; Vela, A.; Heine, T. *Chem. Rev.*, **2005**, *105*, 3812–3841.

(169)   Poater, J.; Duran, M.; Solà, M.; Silvi, B. *Chem. Rev.*, **2005**, *105*, 3911–3947.

(170)   Matito, E.; Solà, M. *Coord. Chem. Rev.*, **2009**, *253*, 647–665.

(171)   Feixas, F.; Matito, E.; Poater, J.; Solà, M. *Chem. Soc. Rev.*, **2015**, *44*, 6434–6451.

(172)   Foster, J. P.; Weinhold, F. *J. Am. Chem. Soc.*, **1980**, *102*, 7211–7218.

(173)   Reed, A. E.; Curtiss, L. A.; Weinhold, F. *Chem. Rev.*, **1988**, *88*, 899–926.

(174)   Zubarev, D. Y.; Boldyrev, A. I. *Phys. Chem. Chem. Phys.*, **2008**, *10*, 5207–5217.

(175)   Zubarev, D. Y.; Boldyrev, A. I. *J. Org. Chem.*, **2008**, *73*, 9251–9258.

(176)   Savin, A.; Nesper, R.; Wengert, S.; Fassler, T. F. *Angew. Chem. Int. Ed. Engl.*, **1997**, *36*, 1809–1832.

(177)   Oña, O. B.; Alcoba, D. R.; Torre, A.; Lain, L.; Torres-Vega, J. J.; Tiznado, W. *J. Phys. Chem. A*, **2013**, *117*, 12953–12958.

(178)   Oña, O. B.; Alcoba, D. R.; Tiznado, W.; Torre, A.; Lain, L. *Int. J. Quantum Chem.*, **2013**, *113*, 1401–1408.

(179)   Oña, O. B.; Torres-Vega, J. J.; Torre, A.; Lain, L.; Alcoba, D. R.; Vásquez-Espinal, A.; Tiznado, W. *Theor. Chem. Acc.*, **2015**, *134*, 28.

(180)   Bader, R. F. W. *Atoms in Molecules: A Quantum Theory*; Clarendon: Oxford, 1990.

(181)   Bader, R. F. W. *Chem. Rev.*, **1991**, *91*, 893–928.

(182)   Johnson, E. R.; Keinan, S.; Mori-Sánchez, P.; Contreras-García, J.; Cohen, A. J.; Yang, W. *J. Am. Chem. Soc.*, **2010**, *132*, 6498–6506.

(183)   Fradera, X.; Poater, J.; Simon, S.; Duran, M.; Solà, M. *Theor. Chem. Acc.*, **2002**, *108*, 214–224.

(184)   Bader, R. F. W.; Stephens, M. E. *J. Am. Chem. Soc.*, **1975**, *97*, 7391–7399.

(185)   Fradera, X.; Austen, M. A.; Bader, R. F. W. *J. Phys. Chem. A*, **1999**, *103*, 304–314.

(186)   Giambiagi, M.; de Giambiagi, M. S.; dos Santos, C. D.; de Figueiredo, A. P. *Phys. Chem. Chem. Phys.*, **2000**, *2*, 3381–3392.

(187)   Bultinck, P.; Ponec, R.; Van Damme, S. *J. Phys. Org. Chem.*, **2005**, *18*, 706–718.

(188)   Poater, J.; Fradera, X.; Duran, M.; Solà, M. *Chem. Eur. J.*, **2003**, *9*, 400–406.

(189)   Matito, E.; Duran, M.; Solà, M. *J. Chem. Phys.*, **2005**, *122*, 14109.

(190)   Garcia-Borràs, M.; Osuna, S.; Luis, J. M.; Swart, M.; Solà, M. *Chem. Soc. Rev.*, **2014**, *43*, 5089–5105.

(191)   Garcia-Borràs, M.; Osuna, S.; Luis, J. M.; Solà, M. *Chem. Commun.*, **2017**, *53*, 4140–

4143.

(192) Boldyrev, A. I.; Kuznetsov, A. E. *Inorg. Chem.*, **2002**, *41*, 532–537.

(193) Hopffgarten, M. von; Frenking, G. *WIREs Comput. Mol. Sci.*, **2012**, *2*, 43–62.

(194) Bickelhaupt, F. M.; Baerends, E. J. In *Reviews in Computational Chemistry*; Lipkowitz, K. B., Boyd, D. B., Eds.; Wiley-VCH: New York, 2000; Vol. 15, pp 1–86.

(195) Fernández, I.; Frenking, G. *Chem. Eur. J.*, **2007**, *13*, 5873–5884.

(196) Poater, J.; Feixas, F.; Bickelhaupt, F. M.; Solà, M. *Phys. Chem. Chem. Phys.*, **2011**, *13*, 20673–20681.

(197) Heine, T.; Schleyer, P. v. R.; Corminboeuf, C.; Seifert, G.; Reviakine, R.; Weber, J. *J. Phys. Chem. A*, **2003**, *107*, 6470–6475.

(198) Castro, A. C.; Osorio, E.; Jiménez-Halla, J. O. C.; Matito, E.; Tiznado, W.; Merino, G. *J. Chem. Theory Comput.*, **2010**, *6*, 2701–2705.

(199) Taubert, S.; Sundholm, D.; Jusélius, J. *J. Chem. Phys.*, **2011**, *134*, 54123.

(200) Quandt, A. *Valency and Bonding. A Natural Bond Orbital Donor–Acceptor Perspective. By Frank Weinhold and Clark Landis.*; 2006; Vol. 7.

(201) Mulliken, R. S. *J. Chem. Phys.*, **1955**, *23*, 1833–1840.

(202) Becke, A. D.; Edgecombe, K. E. *J. Chem. Phys.*, **1990**, *92*, 5397–5403.

(203) Mayer, I.; Salvador, P. *Chem. Phys. Lett.*, **2004**, *383*, 368–375.

(204) Salvador, P.; Mayer, I. *J. Chem. Phys.*, **2004**, *120*, 5046–5052.

(205) Gatti, C.; Fantucci, P.; Pacchioni, G. *Theor. Chim. Acta*, **1987**, *72*, 433–458.

(206) Cao, W. C.; Gatti, C.; McDougall, P. J.; Bader, R. F. W. *Chem. Phys. Lett.*, **1987**, *141*, 380–385.

(207) Bader, R. F. W. *J. Phys. Chem. A*, **1998**, *102*, 7314–7323.

(208) Cioslowski, J.; Mixon, S. T. *J. Am. Chem. Soc.*, **1992**, *114*, 4382–4387.

(209) Cioslowski, J.; Mixon, S. T. *Can. J. Chem.*, **1992**, *70*, 443–449.

(210) Poater, J.; Solà, M.; Bickelhaupt, F. M. *Chem. Eur. J.*, **2006**, *12*, 2889–2895.

(211) Poater, J.; Solà, M.; Bickelhaupt, F. M. *Chem. Eur. J.*, **2006**, *12*, 2902–2905.

(212) Bader, R. F. W. *Chem. Eur. J.*, **2006**, *12*, 2896–2901.

(213) Pendás, A. M.; Francisco, E.; Blanco, M.; Gatti, C. *Chem. Eur. J.*, **2007**, *13*, 9362–9371.

(214) Biegler-König, F.; Schönbohm, J. *J. Comput. Chem.*, **2002**, *23*, 1489–1494.

(215) AIMAll (Version 14.11.23). T. A. Keith, TK Gristmill Software: Overland Park KS, USA, 2017 (aim.tkgristmill.com).

(216) AIMPAC program package. J. Cheeseman, T. A. Keith, R. F. W. Bader, McMaster University, Hamilton: Ontario 1992.

(217) Hirshfeld, F. L. *Theor. Chim. Acta*, **1977**, *44*, 129–138.

(218) Bultinck, P.; Van Alsenoy, C.; Ayers, P. W.; Carbó-Dorca, R. *J. Chem. Phys.*, **2007**, *126*, 144111.

(219) Bultinck, P.; Cooper, D. L.; Neck, D. Van. *Phys. Chem. Chem. Phys.*, **2009**, *11*, 3424–3429.

(220) Francisco, E.; Martín Pendás, A.; Blanco, M. A. *J. Chem. Theory Comput.*, **2006**, *2*, 90–102.

(221) Matito, E.; Solà, M.; Salvador, P.; Duran, M. *Faraday Discuss.*, **2007**, *135*, 325–345.

(222) Salvador, P.; Ramos-Cordoba, E. *APOST-3D*. Institute of Computational Chemistry and Catalysis, University of Girona: Girona, Catalonia, Spain.

(223) Coulson, C. A. *Proc. R. Soc. A Math. Phys. Eng. Sci.*, **1939**, *169*, 413–428.

(224) Fulton, R. L.; Mixon, S. T. *J. Phys. Chem.*, **1993**, *97*, 7530–7534.

(225) Mayer, I. *Chem. Phys. Lett.*, **1983**, *97*, 270–274.

(226) Mayer, I. *Int. J. Quantum Chem.*, **1984**, *26*, 151–154.

(227) Mayer, I. *Int. J. Quantum Chem.*, **1986**, *29*, 73–84.

(228) Mayer, I. *Int. J. Quantum Chem.*, **1986**, *29*, 477–483.

(229) Bader, R. F. W. *Acc. Chem. Res.*, **1985**, *18*, 9–15.

(230) Bader, R. F. W.; Stephens, M. E. *J. Am. Chem. Soc.*, **1975**, *97*, 7391–7399.

(231) Giambiagi, M.; de Giambiagi, M. S.; Mundim, K. C. *Struct. Chem.*, **1990**, *1*, 423–427.

(232) Bochicchio, R.; Ponec, R.; Torre, A.; Lain, L. *Theor. Chem. Acc.*, **2001**, *105*, 292–298.

(233) Feixas, F.; Solà, M.; Barroso, J. M.; Ugalde, J. M.; Matito, E. *J. Chem. Theory Comput.*, **2014**, *10*, 3055–3065.

(234) Feixas, F.; Matito, E.; Poater, J.; Solà, M. *J. Comput. Chem.*, **2008**, *29*, 1543–1554.

(235) Bader, R. F. W.; Streitwieser, A.; Neuhaus, A.; Laidig, K. E.; Speers, P. *J. Am. Chem. Soc.*, **1996**, *118*, 4959–4965.

(236) Matito, E.; Feixas, F.; Solà, M. *J. Mol. Struct.*, **2007**, *811*, 3–11.

(237) Jorner, K.; Feixas, F.; Ayub, R.; Lindh, R.; Solà, M.; Ottosson, H. *Chem. Eur. J.*, **2016**, *22*, 2793–2800.

(238) Cioslowski, J.; Matito, E.; Solà, M. *J. Phys. Chem. A*, **2007**, *111*, 6521–6525.

(239) Gutman, I.; Milun, M.; Trinajstic, N. *J. Am. Chem. Soc.*, **1977**, *99*, 1692–1704.

(240) Bultinck, P.; Rafat, M.; Ponec, R.; Van Gheluwe, B.; Carbó-Dorca, R.; Popelier, P. *J. Phys. Chem. A*, **2006**, *110*, 7642–7648.

(241) Matito, E. *Phys. Chem. Chem. Phys.*, **2016**, *18*, 11839–11846.

(242) Corminboeuf, C.; Heine, T.; Seifert, G.; Schleyer, P. v. R.; Weber, J. *Phys. Chem. Chem.*

Phys., **2004**, *6*, 273–276.

(243) Bühl, M.; van Wüllen, C. *Chem. Phys. Lett.*, **1995**, *247*, 63–68.

(244) Gregor, T.; Mauri, F.; Car, R. *J. Chem. Phys.*, **1999**, *111*, 1815–1822.

(245) Lipscomb, W. N. *Adv. Magn. Reson.*, **1966**, *2*, 137–176.

(246) Hegstrom, R. A.; Lipscomb, W. N. *J. Chem. Phys.*, **1968**, *48*, 809–811.

(247) Wolinski, K.; Hilton, J. F.; Pulay, P. *J. Am. Chem. Soc.*, **1990**, *112*, 8251–8260.

(248) Keith, T. A.; Bader, R. F. W. *Chem. Phys. Lett.*, **1992**, *194*, 1–8.

(249) Keith, T. A.; Bader, R. F. W. *Chem. Phys. Lett.*, **1993**, *210*, 223–231.

(250) Cheeseman, J. R.; Trucks, G. W.; Keith, T. A.; Frisch, M. J. *J. Chem. Phys.*, **1996**, *104*, 5497–5509.

(251) Schleyer, P. v. R.; Jiao, H. J.; van Eikema Hommes, N. J. R.; Malkin, V. G.; Malkina, O. L. *J. Am. Chem. Soc.*, **1997**, *119*, 12669–12670.

(252) Schleyer, P. v. R.; Manoharan, M.; Wang, Z. X.; Kiran, B.; Jiao, H. J.; Puchta, R.; van Eikema Hommes, N. J. R. *Org. Lett.*, **2001**, *3*, 2465–2468.

(253) Glendening, E. D.; Badenhoop, J. K.; Reed, A. E.; Carpenter, J. E.; Bohmann, J. A.; Morales, C. M.; Landis, C. R.; Weinhold, F. *NBO 6.0 program, Theor. Chem. Inst. Dep. Chem. Univ. Wisconsin, Madison, Wisconsin*, **2013**.

(254) Feixas, F.; Jiménez-Halla, J. O. C.; Matito, E.; Poater, J.; Solà, M. *J. Chem. Theory Comput.*, **2010**, *6*, 1118–1130.

(255) Kovács, A.; Esterhuysen, C.; Frenking, G. *Chem. Eur. J.*, **2005**, *11*, 1813–1825.

(256) Krapp, A.; Bickelhaupt, F. M.; Frenking, G. *Chem. Eur. J.*, **2006**, *12*, 9196–9216.

(257) Frenking, G.; Wichmann, K.; Fröhlich, N.; Loschen, C.; Lein, M.; Frunzke, J.; Rayón, V. M. *Coord. Chem. Rev.*, **2003**, *238*, 55–82.

(258) Morokuma, K. *J. Chem. Phys.*, **1971**, *55*, 1236–1244.

(259) Ziegler, T.; Rauk, A. *Theor. Chim. Acta*, **1977**, *46*, 1–10.

(260) Grimme, S. *J. Comput. Chem.*, **2004**, *25*, 1463–1473.

(261) Grimme, S. *J. Comput. Chem.*, **2006**, *27*, 1787–1799.

(262) Panigrahi, S. K.; Desiraju, G. R. *Proteins*, **2007**, *67*, 128–141.

(263) Contreras-García, J.; Johnson, E. R.; Keinan, S.; Chaudret, R.; Piquemal, J.-P.; Beratan, D. N.; Yang, W. *J. Chem. Theory Comput.*, **2011**, *7*, 625–632.

(264) Vol'pin, M. E. *Russ. Chem. Rev.*, **1960**, *29*, 129–160.

(265) Ginsburg, D.; Baker, W. *Non-benzenoid aromatic compounds*; Interscience Publishers: California, 1959.

(266) Breslow, R. *Chem. Rec.*, **2014**, *14*, 1174–1182.

(267) Miyoshi, H.; Nobusue, S.; Shimizu, A.; Tobe, Y. *Chem. Soc. Rev.*, **2015**, *44*, 6560–6577.

(268) Portella, G.; Poater, J.; Solà, M. *J. Phys. Org. Chem.*, **2005**, *18*, 785–791.

(269) Popov, I. A.; Boldyrev, A. I. *European J. Org. Chem.*, **2012**, *2012*, 3485–3491.

(270) Kumar, A.; Duran, M.; Solà, M. *J. Comput. Chem.*, **2017**, *38*, 1606–1611.

(271) Kabuto, C.; Oda, M. *Tetrahedron Lett.*, **1980**, *21*, 103–106.

(272) El Bakouri, O.; Poater, J.; Feixas, F.; Solà, M. *Theor. Chem. Acc.*, **2016**, *135*, 205.

(273) Roberts, J. D.; Streitwieser, A.; Regan, C. M. *J. Am. Chem. Soc.*, **1952**, *74*, 4579–4582.

(274) Platt, J. R. *J. Chem. Phys.*, **1949**, *17*, 484–495.

(275) Soncini, A.; Havenith, R. W. A. W. A.; Fowler, P. W. W.; Jenneskens, L. W. W.; Steiner, E. *J. Org. Chem.*, **2002**, *67*, 4753–4758.

(276) Frank, N. L. L.; Baldridge, K. K. K.; Siegel, J. S. S. *J. Am. Chem. Soc.*, **1995**, *117*, 2102–2103.

(277) Fowler, P. W.; Havenith, R. W. A.; Jenneskens, L. W.; Soncini, A.; Steiner, E. *Chem. Commun.*, **2001**, *22*, 2386–2387.

(278) Grant Hill, J.; Karadakov, P. B.; Cooper, D. L. *Mol. Phys.*, **2006**, *104*, 677–680.

(279) Feixas, F.; Matito, E.; Poater, J.; Solà, M. *J. Phys. Chem. A*, **2007**, *111*, 4513–4521.

(280) Solà, M.; Feixas, F.; Jiménez-Halla, J. O. C.; Matito, E.; Poater, J. *Symmetry*, **2010**, *2*, 1156–1179.

(281) Poater, J.; Visser, R.; Solà, M.; Bickelhaupt, F. M. *J. Org. Chem.*, **2007**, *72*, 1134–1142.

(282) Poater, J.; Bickelhaupt, F. M.; Solà, M. *J. Phys. Chem. A*, **2007**, *111*, 5063–5070.

(283) Dewar, M. J. S.; Li, W.-K. *J. Am. Chem. Soc.*, **1974**, *96*, 5569–5571.

(284) Martin, N.; Sanchez, L.; Illescas, B.; Perez, I. *Chem. Rev.*, **1998**, *98*, 2527–2547.

(285) Wang, S.-J.; Li, Y.; Wang, Y.-F.; Wu, D.; Li, Z.-R. *Phys. Chem. Chem. Phys.*, **2013**, *15*, 12903–12910.

(286) Miura, T.; Tao, R.; Shibata, S.; Umeyama, T.; Tachikawa, T.; Imahori, H.; Kobori, Y. *J. Am. Chem. Soc.*, **2016**, *138*, 5879–5885.

(287) Rudolf, M.; Kirner, S. V.; Guldi, D. M. *Chem. Soc. Rev.*, **2016**, *45*, 612–630.

(288) Schroeder, B. C.; Li, Z.; Brady, M. A.; Faria, G. C.; Ashraf, R. S.; Takacs, C. J.; Cowart, J. S.; Duong, D. T.; Chiu, K. H.; Tan, C.-H.; Cabral, J. T.; Salleo, A.; Chabinyc, M. L.; Durrant, J. R.; McCulloch, I. *Angew. Chem. Int. Ed.*, **2014**, *53*, 12870–12875.

(289) Martín, N.; Altable, M.; Filippone, S.; Martín-Domenech, A. *Synlett*, **2007**, *2007*, 3077–3095.

(290) Hirsch, A. *The Chemistry of Fullerenes*; Thieme: Stuttgart, 1994.

(291) Hirsch, A. *Top. Curr. Chem.*, **1999**, *199*, 1–65.

(292) Hirsch, A.; Brettreich, M. *Fullerenes: Chemistry and Reactions*; Wiley & Sons: Weinheim, 2005.

(293) Thilgen, C.; Herrmann, A.; Diederich, F. *Angew. Chem. Int. Ed. Engl.*, **1997**, *36*, 2269–2280.

(294) Diederich, F. N. *Pure Appl. Chem.*, **1997**, *69*, 395–400.

(295) Martín, N.; Elliott, B.; Hudson, J. S.; Amirkhanian, A.; Echegoyen, L.; Guldi, D. M.; Vázquez, E.; Prato, M.; Zhu, D.; Imahori, H.; Fukumuzi, S.; Nagase, S. *Chem. Commun.*, **2006**, *12*, 2093–2104.

(296) Romero, E. L.; Echegoyen, L. *J. Phys. Org. Chem.*, **2016**, *29*, 781–792.

(297) Fu, W.; Zhang, J.; Fuhrer, T.; Champion, H.; Furukawa, K.; Kato, T.; Mahaney, J. E.; Burke, B. G.; Williams, K. A.; Walker, K.; Dixon, C.; Ge, J.; Shu, C.; Harich, K.; Dorn, H. C. *J. Am. Chem. Soc.*, **2011**, *133*, 9741–9750.

(298) Dai, X.; Han, J.; Gao, Y.; Wang, Z. *ChemPhysChem*, **2014**, *15*, 3871–3876.

(299) Dang, J.-S.; Zheng, J.-J.; Wang, W.-W.; Zhao, X. *Inorg. Chem.*, **2013**, *52*, 4762–4764.

(300) Tan, Y.-Z.; Chen, R.-T.; Liao, Z.-J.; Li, J.; Zhu, F.; Lu, X.; Xie, S.-Y.; Li, J.; Huang, R.-B.; Zheng, L.-S. *Nat. Commun.*, **2011**, *2*, 420.

(301) Amsharov, K. Y.; Ziegler, K.; Mueller, A.; Jansen, M. *Chem.-Eur. J.*, **2012**, *18*, 9289–9293.

(302) Hung, R. R.; Grabowski, J. J. *J. Phys. Chem.*, **1991**, *95*, 6073–6075.

(303) Wasielewski, M. R.; O'Neil, M. P.; Lykke, K. R.; Pellin, M. J.; Gruen, D. M. *J. Am. Chem. Soc.*, **1991**, *113*, 2774–2776.

(304) Arbogast, J. W.; Darmanyan, A. P.; Foote, C. S.; Diederich, F. N.; Whetten, R. L.; Rubin, Y.; Alvarez, M. M.; Anz, S. J. *J. Phys. Chem.*, **1991**, *95*, 11–12.

(305) Wang, Y. *J. Phys. Chem.*, **1992**, *96*, 764–767.

(306) Vassilikogiannakis, G.; Orfanopoulos, M. *J. Am. Chem. Soc.*, **1997**, *119*, 7394–7395.

(307) Hatzimarinaki, M.; Vassilikogiannakis, G.; Orfanopoulos, M. *Tetrahedron Lett.*, **2000**, *41*, 4667–4670.

(308) Vassilikogiannakis, G.; Hatzimarinaki, M.; Orfanopoulos, M. *J. Org. Chem.*, **2000**, *65*, 8180–8187.

(309) Wilson, S. R.; Kaprinidis, N.; Wu, Y.; Schuster, D. I. *J. Am. Chem. Soc.*, **1993**, *115*, 8495–8496.

(310) Wilson, S. R. R.; Kaprinidis, N.; Wu, Y. H.; Schuster, D. I. I. *J. Am. Chem. Soc.*, **1993**, *115*, 8495–8496.

(311) Vassilikogiannakis, G.; Orfanopoulos, M. *J. Am. Chem. Soc.*, **1997**, *119*, 7394–7395.

(312) Vassilikogiannakis, G.; Orfanopoulos, M. *Tetrahedron Lett.*, **1997**, *38*, 4323–4326.

(313) Vassilikogiannakis, G.; Chronakis, N.; Orfanopoulos, M. *J. Am. Chem. Soc.*, **1998**, *120*, 9911–9920.

(314) Vassilikogiannakis, G.; Orfanopoulos, M. *J. Org. Chem.*, **1999**, *64*, 3392–3393.

(315) Hatzimarinaki, M.; Vassilikogiannakis, G.; Orfanopoulos, M. *Tetrahedron Lett.*, **2000**, *41*, 4667–4670.

(316) Vassilikogiannakis, G.; Hatzimarinaki, M.; Orfanopoulos, M. *J. Org. Chem.*, **2000**, *65*, 8180–8187.

(317) Hatzimarinaki, M.; Roubelakis, M. M.; Orfanopoulos, M. *J. Am. Chem. Soc.*, **2005**, *127*, 14182–14183.

(318) Vassilikogiannakis, G.; Orfanopoulos, M. *Tetrahedron Lett.*, **1997**, *38*, 4323–4326.

(319) Vassilikogiannakis, G.; Chronakis, N.; Orfanopoulos, M. *J. Am. Chem. Soc.*, **1998**, *120*, 9911–9920.

(320) Vassilikogiannakis, G.; Orfanopoulos, M. *J. Org. Chem.*, **1999**, *64*, 3392–3393.

(321) Hatzimarinaki, M.; Roubelakis, M. M.; Orfanopoulos, M. *J. Am. Chem. Soc.*, **2005**, *127*, 14182–14183.

(322) Mikami, K.; Matsumoto, S.; Tonoi, T.; Okubo, Y.; Suenobu, T.; Fukuzumi, S. *Tetrahedron Lett.*, **1998**, *39*, 3733–3736.

(323) Mikami, K.; Matsumoto, S.; Okubo, Y.; Fujitsuka, M.; Ito, O.; Suenobu, T.; Fukuzumi, S. *J. Am. Chem. Soc.*, **2000**, *122*, 2236–2243.

(324) Osuna, S.; Swart, M.; Solà, M. *Phys. Chem. Chem. Phys.*, **2011**, *13*, 3585–3603.

(325) Popov, A. A.; Yang, S.; Dunsch, L. *Chem. Rev.*, **2013**, *113*, 5989–6113.

(326) Kroto, H. W. *Nature*, **1987**, *329*, 529–531.

(327) Solà, M.; Mestres, J.; Martí, J.; Duran, M. *Chem. Phys. Lett.*, **1994**, *231*, 325–330.

(328) Fernández, I.; Solà, M.; Bickelhaupt, F. M. *Chem. – A Eur. J.*, **2013**, *19*, 7416–7422.

(329) Osuna, S.; Valencia, R.; Rodríguez-Fortea, A.; Swart, M.; Solà, M.; Poblet, J. M. *Chem. Eur. J.*, **2012**, *18*, 8944–8956.

(330) Garcia-Borràs, M.; Osuna, S.; Swart, M.; Luis, J. M.; Solà, M. *Chem. Commun.*, **2013**, *49*, 1220–1222.

(331) Saunders, M.; Berger, R.; Jaffe, A.; McBride, J. M.; O'Neill, J.; Breslow, R.; Hoffmann, J. M.; Perchonock, C.; Wasserman, E.; Hutton, R. S.; Kuck, V. J. *J. Am. Chem. Soc.*, **1973**, *95*, 3017–3018.

(332) Baird, N. C. *J. Am. Chem. Soc.*, **1972**, *94*, 4941–4948.

(333) Ottosson, H. *Nat. Chem.*, **2012**, *4*, 969–971.

(334) Pang, L. S. K.; Wilson, M. A. *J. Phys. Chem.*, **1993**, *97*, 6761–6763.

(335) Giovane, L. M.; Barco, J. W.; Yadav, T.; Lafleur, A. L.; Marr, J. A.; Howard, J. B.; Rotello, V. M. *J. Phys. Chem.*, **1993**, *97*, 8560–8561.

(336) Feixas, F.; Jiménez-Halla, J. O. C.; Matito, E.; Poater, J.; Solà, M. *J. Chem. Theory Comput.*, **2010**, *6*, 1118–1130.

(337) Zhao, L.; Grande-Aztatzi, R.; Foroutan-Nejad, C.; Ugalde, J. M.; Frenking, G. *ChemistrySelect*, **2017**, *2*, 863–870.

(338) Puplovskis, A.; Kacens, J.; Neilands, O. *Tetrahedron Lett.*, **1997**, *38*, 285–288.

(339) Harvey, J. N.; Aschi, M.; Schwarz, H.; Koch, W. *Theor. Chem. Acc.*, **1998**, *99*, 95–99.

(340) Poli, R.; Harvey, J. N.; Kraatz, H.-B.; Poli, R.; Cundari, T. R. *Chem. Soc. Rev.*, **2003**, *32*, 1–8.

(341) Magnuson, A.; Anderlund, M.; Johansson, O.; Lindblad, P.; Lomoth, R.; Polivka, T.; Ott, S.; Stensjö, K.; Styring, S.; Sundström, V.; Hammarström, L. *Acc. Chem. Res.*, **2009**, *42*, 1899–1909.

(342) Berardi, S.; Drouet, S.; Francàs, L.; Gimbert-Suriñach, C.; Guttentag, M.; Richmond, C.; Stoll, T.; Llobet, A.; Mallouk, T. E.; Fontecave, M.; Artero, V. *Chem. Soc. Rev.*, **2014**, *43*, 7501–7519.

(343) Lennartson, A.; Roffey, A.; Moth-Poulsen, K. *Tetrahedron Lett.*, **2015**, *56*, 1457–1465.

(344) Philippopoulos, C.; Economou, D.; Economou, C.; Marangozis, J. *Ind. Eng. Chem. Prod. Res. Dev.*, **1983**, *22*, 627–633.

(345) Gray, V.; Lennartson, A.; Ratanalert, P.; Börjesson, K.; Moth-Poulsen, K.; Majundar, A.; Vollhardt, K. P. C.; Sealman, R. A. *Chem. Commun.*, **2014**, *50*, 5330–5332.

(346) Quant, M.; Lennartson, A.; Dreos, A.; Kuisma, M.; Erhart, P.; Börjesson, K.; Moth-Poulsen, K. *Chem. Eur. J.*, **2016**, *22*, 13265–13274.

(347) Jorner, K.; Dreos, A.; Emanuelsson, R.; El Bakouri, O.; Fdez. Galván, I.; Börjesson, K.; Feixas, F.; Lindh, R.; Zietz, B.; Moth-Poulsen, K.; Ottosson, H. *J. Mater. Chem. A*, **2017**, *5*, 12369–12378.

(348) Yoshida, Z. *J. Photochem.*, **1985**, *29*, 27–40.

(349) Kucharski, T. J.; Tian, Y.; Akbulatov, S.; Boulatov, R. *Energy Environ. Sci.*, **2011**, *4*, 4449–4472.

(350) Woodward, R. B.; Hoffmann, R. *The Conservation of Orbital Symmetry*; Verlag Chemie: Weinheim, 1970.

(351) Qin, C.; Zhao, Z.; Davis, S. R. *J. Mol. Struct. (THEOCHEM)*, **2005**, *728*, 67–70.

(352) Dubonosov, A. D.; Bren, V. A.; Chernoivanov, V. A. *Russ. Chem. Rev.*, **2002**, *71*, 917–927.

(353) Ikezawa, H.; Kutal, C.; Yasufuku, K.; Yamazaki, H. *J. Am. Chem. Soc.*, **1986**, *108*, 1589–1594.

(354) Matito, E. ESI-3D: El. Institute of Computational Chemistry: Girona 2006.

(355) Schneebeli, S.; Kamenetska, M.; Foss, F.; Vazquez, H.; Skouta, R.; Hybertsen, M.; Venkataraman, L.; Breslow, R. *Org. Lett.*, **2010**, *12*, 4114–4117.

(356) Denis, P. A. *J. Phys. Chem. C*, **2014**, *118*, 24976–24982.

(357) Fukazawa, A.; Oshima, H.; Shimizu, S.; Kobayashi, N.; Yamaguchi, S. *J. Am. Chem.*

Soc., **2014**, *136*, 8738–8745.

(358) Yuan, C.; Saito, S.; Camacho, C.; Kowalczyk, T.; Irle, S.; Yamaguchi, S. *Chem. Eur. J.*, **2014**, *20*, 2193–2200.

(359) Möllerstedt, H.; Piqueras, M. C.; Crespo, R.; Ottosson, H. *J. Am. Chem. Soc.*, **2004**, *126*, 13938–13939.

(360) Jorner, K.; Emanuelsson, R.; Dahlstrand, C.; Tong, H.; Denisova, A. V.; Ottosson, H. *Chem. Eur. J.*, **2014**, *20*, 9295–9303.

(361) Dahlstrand, C.; Rosenberg, M.; Kilså, K.; Ottosson, H. *J. Phys. Chem. A*, **2012**, *116*, 5008–5017.

(362) Bich, V. T.; Bini, R.; Salvi, P. R.; Marconi, G. *Chem. Phys. Lett.*, **1990**, *175*, 413–418.

(363) Zimmermann, R. *J. Mol. Struct.*, **1996**, *377*, 35–46.

(364) Zhu, J.; Dahlstrand, C.; Smith, J. R.; Villaume, S.; Ottosson, H. *Symmetry*, **2010**, *2*, 1653–1682.

(365) Balaban, A. T.; Klein, D. J. *J. Phys. Chem. C*, **2009**, *113*, 19123–19133.

(366) Hu, Y.; Wagener, T. J.; Gao, Y.; Meyer, H. M.; Weaver, J. H. *Phys. Rev. B*, **1988**, *38*, 3037–3044.

(367) Wang, B.; Wang, H.; Li, H.; Zeng, C.; Hou, J. G.; Xiao, X. *Phys. Rev. B*, **2000**, *63*, 35403.

(368) Torma, V.; Reuter, T.; Vidoni, O.; Schumann, M.; Radehaus, C.; Schmid, G. *ChemPhysChem*, **2001**, *2*, 546–548.

(369) Barnett, R. N.; Cleveland, C. L.; Häkkinen, H.; Luedtke, W. D.; Yannouleas, C.; Landman, U. *Eur. Phys. J. D*, **1999**, *9*, 95–104.

(370) Aldridge, S.; Downs, A. J. *The Group 13 Metals Aluminium, Gallium, Indium and Thallium: Chemical Patterns and Peculiarities*; John Wiley & Sons, Ltd: Chichester, 2011.

(371) Alexandrova, A. N.; Boldyrev, A. I. *Inorg. Chem.*, **2004**, *43*, 3588–3592.

(372) Alexandrova, A. N.; Birch, K. A.; Boldyrev, A. I. *J. Am. Chem. Soc.*, **2003**, *125*, 10786–10787.

(373) Alexandrova, A. N.; Boldyrev, A. I.; Zhai, H.-J.; Wang, L.-S. *Coord. Chem. Rev.*, **2006**, *250*, 2811–2866.

(374) Boldyrev, A. I.; Wang, L.-S. *Chem. Rev.*, **2005**, *105*, 3716–3757.

(375) Kuznetsov, A. E.; Boldyrev, A. I.; Zhai, H.-J.; Li, X.; Wang, L.-S. *J. Am. Chem. Soc.*, **2002**, *124*, 11791–11801.

(376) Thomas, O. C.; Zheng, W.-J.; Lippa, T. P.; Xu, S.-J.; Lyapustina, S. A.; Bowen, K. H. *J. Chem. Phys.*, **2001**, *114*, 9895–9900.

(377) Alexandrova, A. N.; Boldyrev, A. I.; Zhai, H.-J.; Wang, L.-S. *J. Chem. Phys.*, **2005**, *122*, 54313.

(378) Alexandrova, A. N.; Boldyrev, A. I.; Zhai, H.-J.; Wang, L.-S.; Steiner, E.; Fowler, P.

W. *J. Phys. Chem. A*, **2003**, *107*, 1359–1369.

(379) Huynh, M. T.; Alexandrova, A. N. *J. Phys. Chem. Lett.*, **2011**, *2*, 2046–2051.

(380) Mercero, J. M.; Matito, E.; Ruipérez, F.; Infante, I.; Lopez, X.; Ugalde, J. M. *Chem. Eur. J.*, **2015**, *21*, 9610–9614.

(381) Corminboeuf, C.; Wannere, C. S.; Roy, D.; King, R. B.; Schleyer, P. v R. *Inorg. Chem.*, **2006**, *45*, 214–219.

(382) El Bakouri, O.; Duran, M.; Poater, J.; Feixas, F.; Solà, M. *Phys. Chem. Chem. Phys.*, **2016**, *18*, 11700–11706.

(383) Ma, J.; Li, Z.; Fan, K.; Zhou, M. *Chem. Phys. Lett.*, **2003**, *372*, 708–716.

(384) Yang, L.-M.; Wang, J.; Ding, Y.-H.; Sun, C.-C. *Phys. Chem. Chem. Phys.*, **2008**, *10*, 2316–2320.

(385) Alexandrova, A. N. *Chem. Phys. Lett.*, **2012**, *533*, 1–5.

(386) Alexandrova, A. N.; Nayhouse, M. J.; Huynh, M. T.; Kuo, J. L.; Melkonian, A. V; Chavez, G.; Hernando, N. M.; Kowal, M. D.; Liu, C.-P. *Phys. Chem. Chem. Phys.*, **2012**, *14*, 14815–14821.

(387) Alexandrova, A. N.; Nechay, M. R.; Lydon, B. R.; Buchan, D. P.; Yeh, A. J.; Tai, M.-H.; Kostrikin, I. P.; Gabrielyan, L. *Chem. Phys. Lett.*, **2013**, *588*, 37–42.

(388) Fowler, J. E.; Ugalde, J. M. *J. Phys. Chem. A*, **2000**, *104*, 397–403.

(389) Fowler, J. E.; Ugalde, J. M. *Phys. Rev. A - At. Mol. Opt. Phys.*, **1998**, *58*, 383–388.

(390) Farràs, P.; Vankova, N.; Zeonjuk, L. L.; Warneke, J.; Dülcks, T.; Heine, T.; Viñas, C.; Teixidor, F.; Gabel, D. *Chem. Eur. J.*, **2012**, *18*, 13208–13212.

(391) Fagiani, M. R.; Liu Zeonjuk, L.; Esser, T. K.; Gabel, D.; Heine, T.; Asmis, K. R.; Warneke, J. *Chem. Phys. Lett.*, **2015**, *625*, 48–52.

(392) Olson, J. K.; Boldyrev, A. I. *J. Phys. Chem. A*, **2013**, *117*, 1614–1620.

(393) Kitaura, K.; Morokuma, K. *Int. J. Quantum Chem.*, **1976**, *10*, 325–340.

(394) Morokuma, K. *Acc. Chem. Res.*, **1977**, *10*, 294–300.

(395) Ziegler, T.; Rauk, A. *Inorg. Chem.*, **1979**, *18*, 1558–1565.

(396) El-Hamdi, M.; Tiznado, W.; Poater, J.; Solà, M. *J. Org. Chem.*, **2011**, *76*, 8913–8921.

(397) El-Hamdi, M.; El Bakouri El Farri, O.; Salvador, P.; Abdelouahid, B. A.; El Begrani, M. S.; Poater, J.; Solà, M. *Organometallics*, **2013**, *32*, 4892–4903.

(398) El-Hamdi, M.; Solà, M.; Frenking, G.; Poater, J. *J. Phys. Chem. A*, **2013**, *117*, 8026–8034.

(399) Islas, R.; Poater, J.; Matito, E.; Solà, M. *Phys. Chem. Chem. Phys.*, **2012**, *14*, 14850–14859.

(400) Alvarez, S. *Dalt. Trans.*, **2013**, *42*, 8617–8636.

(401) Lee, T. J.; Taylor, P. R. *Int. J. Quantum Chem., Quant. Chem. Symp.*, **1989**, *S23*, 199–207.

(402) Martin, J. M. L. *Energ. Stable Mol. React. Intermed.*, **1999**, 373–417.

(403) Chen, Z.; Neukermans, S.; Wang, X.; Janssens, E.; Zhou, Z.; Silverans, R. E.; King, R. B.; Schleyer, P. von R.; Lievens, P. *J. Am. Chem. Soc.*, **2006**, *128*, 12829–12834.

(404) King, R. B.; Heine, T.; Corminboeuf, C.; Schleyer, P. v R. *J. Am. Chem. Soc.*, **2004**, *126*, 430–431.

(405) Jiao, H.; Schleyer, P. von R.; Glukhovtsev, M. N. *J. Phys. Chem.*, **1996**, *100*, 12299–12304.

(406) Feixas, F.; Matito, E.; Poater, J.; Solà, M. *WIREs Comput. Mol. Sci.*, **2013**, *3*, 105–122.

(407) Srinivas, S.; Jellinek, J. *J. Chem. Phys.*, **2004**, *121*, 7243–7252.

(408) Edwards, A. K.; Wood, R. M. *J. Chem. Phys.*, **1982**, *76*, 2938–2942.

(409) Wetmore, R. W.; Boyd, R. K. *J. Phys. Chem.*, **1986**, *90*, 5540–5551.

(410) Díaz-Cervantes, E.; Poater, J.; Robles, J.; Swart, M.; Solà, M. *J. Phys. Chem. A*, **2013**, *117*, 10462–10469.

(411) Zhan, C.-G.; Zheng, F.; Dixon, D. A. *J. Am. Chem. Soc.*, **2002**, *124*, 14795–14803.

(412) Poater, J.; Fradera, X.; Duran, M.; Solà, M. *Chem. Eur. J.*, **2003**, *9*, 1113–1122.

(413) Temelso, B.; Sherrill, C. D. *J. Chem. Phys.*, **2005**, *122*, 64315.

(414) Šulka, M.; Labanc, D.; Kováč, M.; Pitoňák, M.; Černušák, I.; Neogrády, P. *J. Phys. B At. Mol. Opt. Phys.*, **2012**, *45*, 85102.

(415) Heaven, M. C.; Merritt, J. M.; Bondybey, V. E. *Annu. Rev. Phys. Chem.*, **2011**, *62*, 375–393.

(416) Zhao, Y.; Li, N.; Xu, W. G.; Li, Q. S. *Int. J. Quantum Chem.*, **2007**, *107*, 81–91.

(417) Beyer, M. K.; Kaledin, L. A.; Kaledin, A. L.; Heaven, M. C.; Bondybey, V. E. *Chem. Phys.*, **2000**, *262*, 15–23.

(418) Maslowsky, E. *Coord. Chem. Rev.*, **2011**, *255*, 2746–2763.

(419) Islas, R.; Chamorro, E.; Robles, J.; Heine, T.; Santos, J. C.; Merino, G. *Struct. Chem.*, **2007**, *18*, 833–839.

(420) Charistos, N. D.; Papadopoulos, A. G.; Sigalas, M. P. *J. Phys. Chem. A*, **2014**, *118*, 1113–1122.

(421) Takahashi, M.; Kawazoe, Y. *Chem. Phys. Lett.*, **2006**, *418*, 475–480.

(422) Kishi, R.; Iwata, S.; Nakajima, A.; Kaya, K. *J. Chem. Phys.*, **1997**, *107*, 3056–3070.

(423) Corminboeuf, C.; King, R. B.; Schleyer, P. von R. *ChemPhysChem*, **2007**, *8*, 391–398.

(424) Mercero, J. M.; Piris, M.; Matxain, J. M.; Lopez, X.; Ugalde, J. M. *J. Am. Chem. Soc.*, **2009**, *131*, 6949–6951.

(425) Mercero, J. M.; Boldyrev, A. I.; Merino, G.; Ugalde, J. M. *Chem. Soc. Rev.*, **2015**, *44*, 6519–6534.

(426) Dye, J. L.; Redko, M. Y.; Huang, R. H.; Jackson, J. E. In *Advances in Inorganic Chemistry*; Rudi van, E., Kristin, B.-J., Eds.; Academic Press, 2006; Vol. 59, pp 205–231.

(427) Dye, J. L. *Acc. Chem. Res.*, **2009**, *42*, 1564–1572.

(428) Garcia-Borràs, M.; Solà, M.; Luis, J. M.; Kirtman, B. *J. Chem. Theory Comput.*, **2012**, *8*, 2688–2697.

(429) He, H.-M.; Li, Y.; Sun, W.-M.; Wang, J.-J.; Wu, D.; Zhong, R.-L.; Zhou, Z.-J.; Li, Z.-R.; Botek, E.; Yamaguchi, K. *Dalt. Trans.*, **2016**, *45*, 2656–2665.

(430) Dale, S. G.; Johnson, E. R.; Onishi, T.; Takano, Y.; Shigeta, Y.; Nagao, H.; Yoshioka, Y.; Yamaguchi, K.; Yamaguchi, K.; Dabo, I. *Phys. Chem. Chem. Phys.*, **2016**, *18*, 27326–27335.

(431) Matsuishi, S.; Toda, Y.; Miyakawa, M.; Hayashi, K.; Kamiya, T.; Hirano, M.; Tanaka, I.; Hosono, H. *Science*, **2003**, *301*, 626–629.

(432) Redko, M. Y.; Jackson, J. E.; Huang, R. H.; Dye, J. L. *J. Am. Chem. Soc.*, **2005**, *127*, 12416–12422.

(433) Lee, K.; Kim, S. W.; Toda, Y.; Matsuishi, S.; Hosono, H. *Nature*, **2013**, *494*, 336–340.

(434) Postils, V.; Garcia-Borràs, M.; Solà, M.; Luis, J. M.; Matito, E. *Chem. Commun.*, **2015**, *51*, 4865–4868.

(435) Johnston, R. L. *Atomic and Molecular Clusters*; Taylor & Francis: New York, 2002.

(436) Hückel, E. *Z. Elektrochemie*, **1937**, *43*, 752–788.

(437) Kohout, M.; Savin, A. *Int. J. Quantum Chem.*, **1996**, *60*, 875–882.

(438) Melin, J.; Fuentealba, P. *Int. J. Quantum Chem.*, **2003**, *92*, 381–390.

(439) Pilmé, J. *J. Comput. Chem.*, **2017**, *38*, 204–210.

(440) Silvi, B. *J. Phys. Chem. A*, **2003**, *107*, 3081–3085.

(441) Alexandrova, A. N.; Boldyrev, A. I.; Li, X.; Sarkas, H. W.; Hendricks, J. H.; Arnold, S. T.; Bowen, K. H. *J. Chem. Phys.*, **2011**, *134*, 44322.

(442) Rienstra-Kiracofe, J. C.; Allen, W. D.; Schaefer, H. F. *J. Phys. Chem. A*, **2000**, *104*, 9823–9840.

(443) Danovich, D.; Shaik, S. *Acc. Chem. Res.*, **2014**, *47*, 417–426.

(444) Alexandrova, A. N.; Boldyrev, A. I. *J. Chem. Theory Comput.*, **2005**, *1*, 566–580.

(445) Boustani, I.; Pewestorf, W.; Fantucci, P.; Bonaić-Koutecký, V.; Koutecký, J. *Phys. Rev. B*, **1987**, *35*, 9437–9450.

(446) Silvi, B.; Gatti, C. *J. Phys. Chem. A*, **2000**, *104*, 947–953.

(447) Pendás, A. M.; Blanco, M. A.; Costales, A.; Sánchez, P. M.; Luaña, V. *Phys. Rev. Lett.*, **1999**, *83*, 1930–1933.

(448) Dale, S. G.; Otero-de-la-Roza, A.; Johnson, E. R. *Phys. Chem. Chem. Phys.*, **2014**, *16*, 14584–14593.

(449) Rousseau, R.; Marx, D. *Chem. Eur. J.*, **2000**, *6*, 2982–2993.

(450) Singh, D. J.; Krakauer, H.; Haas, C.; Pickett, W. E. *Nature*, **1993**, *365*, 39–42.

(451) Neaton, J. B.; Ashcroft, N. W. *Nature*, **1999**, *400*, 141–144.

(452) Soncini, A. *J. Chem. Theory Comput.*, **2007**, *3*, 2243–2257.

(453) Car, R.; Parrinello, M. *Phys. Rev. Lett.*, **1985**, *55*, 2471–2474.

(454) Tai, T. B.; Nhat, P. V.; Nguyen, M. T.; Li, S.; Dixon, D. A. *J. Phys. Chem. A*, **2011**, *115*, 7673–7686.

(455) De Visser, S. P.; Danovich, D.; Wu, W.; Shaik, S. *J. Phys. Chem. A*, **2002**, *106*, 4961–4969.